Evaluation of the Performance of Multi-Component Cementitious Composites:

Multi-Scale Experimental Characterization and Numerical Simulation

by

Aashay Arora

A Dissertation Presented in Partial Fulfillment
of the Requirements for the Degree
Doctor of Philosophy

Approved October 2018 by the
Graduate Supervisory Committee:

Narayanan Neithalath, Chair
Subramaniam Rajan
Barzin Mobasher
Nikhilesh Chawla
Christian G. Hoover

ARIZONA STATE UNIVERSITY

December 2018

ABSTRACT

Being a remarkably versatile and inexpensive building material, concrete has found tremendous use in development of modern infrastructure and is the most widely used material in the world. Extensive research in the field of concrete has led to the development of a wide array of concretes with applications ranging from building of skyscrapers to paving of highways. These varied applications require special cementitious composites which can satisfy the demand for enhanced functionalities such as high strength, high durability and improved thermal characteristics among others.

The current study focuses on the fundamental understanding of such functional composites, from their microstructural design to macro-scale application. More specifically, this study investigates three different categories of functional cementitious composites. First, it discusses the differences between cementitious systems containing interground and blended limestone with and without alumina. The interground systems are found to outperform the blended systems due to differential grinding of limestone. A novel approach to deduce the particle size distribution of limestone and cement in the interground systems is proposed. Secondly, the study delves into the realm of ultra-high performance concrete, a novel material which possesses extremely high compressive-, tensile- and flexural-strength and service life as compared to regular concrete. The study presents a novel first principles-based paradigm to design economical ultra-high performance concretes using locally available materials. In the final part, the study addresses the thermal benefits of a novel type of concrete containing phase change materials. A software package was designed to perform numerical simulations to analyze temperature profiles and thermal stresses in concrete structures containing PCMs.

The design of these materials is accompanied by material characterization of cementitious binders. This has been accomplished using techniques that involve measurement of heat evolution (isothermal calorimetry), determination and quantification of reaction products (thermo-gravimetric analysis, x-ray diffraction, micro-indentation, scanning electron microscopy, energy-dispersive x-ray spectroscopy) and evaluation of pore-size distribution (mercury intrusion porosimetry). In addition, macro-scale testing has been carried out to determine compression, flexure and durability response. Numerical simulations have been carried out to understand hydration of cementitious composites, determine optimum particle packing and determine the thermal performance of these composites.

DEDICATION

I dedicate this thesis to mummy and papa who have sacrificed so much to get me here, to Bauji who always believed in me and whose stories inspired me to never give up, to Nandu tauji in whose footsteps I follow, and to all my family members and close friends who have stood by me in the toughest of times

ACKNOWLEDGMENTS

The completion of this dissertation would not have been possible without the support and assistance of my family, friends and colleagues. I thank all of you for your patience, support and understanding.

I would like to gratefully acknowledge my advisor Dr. Narayanan Neithalath for his guidance, support, and motivation throughout my research endeavor. Without his encouragement and enthusiasm this dissertation would not have been possible. I would also like to thank my committee members Dr. Subramaniam Rajan, Dr. Barzin Mobasher Dr. Nikhilesh Chawla and Dr. Christian G. Hoover for their guidance and taking the time to examine this work.

I would like to extend special thanks to Kirk Vance who was my mentor when I embarked on this journey at ASU. I would like to thank my colleagues Akash, Sumanta, Matt, Pu, Vikram, Yiming, Canio, Joey, Robert, Bilal, Naman, Sooraj, Anand, Hussam, Emily and Loukham for making my time as a PhD student most memorable. I would also like to thank the graduate and undergraduate students who I have had the pleasure to work with to accomplish my research and for all their help and guidance during the completion of my dissertation.

I would like to thank the laboratory support staff: Peter Goguen, Jeff Long, and Kenneth Witczak for all their assistance throughout this project.

Finally, I would like to thank Arizona State University and the Ira A. Fulton Schools of Engineering for providing me with the resources which enabled the completion of this PhD.

TABLE OF CONTENTS

PAGE

CHAPTER PAGE

CHAPTER PAGE

CHAPTER PAGE

LIST OF TABLES

Table Page

LIST OF FIGURES

Figure Page

Figure Page

Figure Page

Figure Page

Figure Page

Figure Page

Figure Page

Figure Page

CHAPTER 1

INTRODUCTION

1.1 Background

Cement is a remarkable man-made material and has had a significant impact on human development in the last few decades. The ease of availability of raw materials, inexpensive cost of production, ability to gain strength over time and long-lasting service life has led to a revolution in the fast-growing infrastructure sector. It has been such an essential material that the growth of nations and economies has been found to be directly correlated with their cement consumption and demand (Davidson, n.d.). The GDP versus cement consumption graph is a striking visual representation of a country's stage of development. The global volumes of cement consumption have doubled over the last decade from 1.8 bn tonne in 2002 to 3.7 bn tonne in 2012 (Armstrong 2013). Cement is the major ingredient in concrete, which is used as the basic building material for construction. Concrete has been recognized as a great building material ever since the dawn of human civilization. The earliest known man-made structures made out of concrete were built in 6500 BC in the regions of modern day Syria and Jordan. Some of world's most notable historic structures have been made out of concrete. The Great Pyramid of Giza and the Great Wall of China are examples of concrete structures that have stood the test of time. The Pantheon in Rome built around 2600 years ago is still the largest unreinforced concrete dome structure in the world. In all of these structures, concrete developers used crude materials such as gypsum, limestone, crushed rice, clay etc. with minimal processing. With the advent of modern technology, it is now possible to make immense quantities of concrete with precision quality control and at

extremely affordable costs to make the modern concrete forms that we have in this day and age. Some of the modern concrete marvels include the Itaipu gravity dam located on the border of Brazil and Paraguay, Burj Khalifa, the tallest building in the world in Saudi Arabia, Millau Viaduct, the highest bridge in the world and the 102-mile-long Danyang–Kunshan Grand Bridge in China.

Because of its versatile nature, concrete researchers often go out of their way to look for novel and more effective ways to make concrete better. Each of the projects described above used a different composition of concrete, where concrete is modified using several alternative materials to create a functional concrete composite that is best suitable for the application. The design of such a concrete composite depends on several factors – the availability of raw materials, architectural design of the structure, type of loading experienced by the structure, compressive and flexural strength required, environmental conditions, structural life expectancy, project cost etc. With several limiting factors on every construction project and a multitude of emerging uses of concrete, functional concrete composites have found their way into the scientific discussion most appropriately. These composite materials are cement-based materials with high volume replacement of cement by supplementary cementitious materials, cement-less materials with alternative replacement materials and non-hydraulic cementitious materials.

The current study focuses on the replacement of cement with alternate cementitious materials including fillers such as limestone and supplementary cementitious materials such as fly ash, blast furnace slag, metakaolin and silica fume, in order to achieve certain

functional goals such as ultra-high strength and durability, improved thermal response of concrete infrastructure.

1.2 Research Approach

The early stages of the study began with exploring the effect of fineness in the reactivity of two commercial interground portland limestone cements having the same limestone content. The fineness effect was distinctly observed at early ages and the interground system with a higher fineness was able to reach higher early age strengths. The increase in consumption of limestone was evaluated using thermo-gravimetric analysis. Further, the performance of these interground cements was compared to those of blended limestone systems, where limestone of four different median sizes was mixed with ordinary portland cement to create blends in an attempt to match the particle size distribution of the PLCs. The interground systems were found to outperform the blended systems, which was hypothesized to be due to the differential grinding of cement and limestone in the interground systems. In order to determine the unknown PSDs of clinker and limestone in the interground PLCs, a novel method was proposed which helps in better design of blended mixtures to achieve performance equivalence as those of the PLCs.

It was recognized that limestone is capable of chemically combining with the aluminate phases in the cementitious materials to form carboaluminates that further densify the microstructure and consequently improve the properties. Therefore, a combination of limestone and slag was utilized as OPC replacement in order to develop binders that contain higher levels of cement replacement, yet result in performance-equivalent concretes. In addition to the alumina content in slag (which is higher than that in OPC but significantly

lower than those in fly ash or metakaolin) that facilitates limestone-aluminate synergistic reactions, slag demonstrates cementitious (albeit slow) and pozzolanic reactivity. The synergistic effects of limestone and slag were explored in detail with respect to their contributions to the formation of hydration products and the development of strength and pore structure. The synergistic effect of slag and limestone was confirmed by the linear correlation between the consumption of carbonates and the formation of AFmc phase in the pastes. The presence of limestone resulted in an increased strength in ternary OPC mixtures containing slag and limestone as compared to the binary OPC-slag blends.

The understanding of cement hydration and the chemistry of supplementary cementitious materials was used in the formulation of ultra-high performance concretes, a special class of cementitious materials that show very high mechanical properties and enhanced durability. The study was focused on designing the binder phase of ultra-high performance concretes (UHPC) from commonly available cement replacement (fly ash, slag, microsilica, metakaolin) and fine filler (limestone) materials. A packing algorithm was used to extract the number density, mean centroidal distance, and coordination number of the microstructure. Similarly, rheological studies on the pastes provided yield stress, plastic viscosity, and min-slump spread. Using a combination of strategically designed packing and flow criteria, a total of 8 ternary and quaternary blends were selected for characterization out of 32 initial mixture compositions. The highly efficient microstructural packing in these mixtures and better workability that facilitated dispersion of particles to enhance the reactivity resulted in beneficial pore structure and mechanical properties. 28-day compressive strengths more than 90 MPa were obtained for some mortars while all the mixtures showed strengths of more

than 80 MPa at 28 days. Proposed experimental works include (a) developing superior ultra-high performance binders using metakaolin and silica fume in combination with fine limestone and (b) developing ultra-high performance concretes using locally available materials by using aggregate and paste optimization techniques.

In addition to the experimental investigation, computer simulations were also carried out to model the early-age performance of special cementitious binders. When subjected to an increase in temperature, phase change materials (PCMs) transition from solid to liquid state, thus allowing them to act as a latent heat storage medium. This behavior presents a unique opportunity to utilize PCMs as a strategy to mitigate early- and later-age thermal cracking in concrete structures. A one-dimensional finite difference model was used for a hydrating concrete pavement with considerations of mixture proportions, member geometry, and structural and thermal (environmental) boundary conditions. Significant reductions in early-age hydration heat release were observed when PCMs were incorporated in the pavement concretes, as replacement for the cement paste or fine aggregates. The simulations predicted a 6°C-to-10°C reduction in peak temperature when the concrete contained approximately 5% by volume of PCM, either as a replacement of fine aggregates or of the cement paste, therefore reducing the thermal stresses in the concrete and leading to a significant reduction in the probability of cracking. Curling stresses are a major concern in mature pavements which lead to thermal fatigue and cracking and ultimately reduction in the service life of pavements. Simulations on mature pavements containing PCMs showed a 4 °C to 6 °C reduction in the peak value of temperature differential in the pavement containing PCM when compared with a plain concrete pavement. This led to a comparable reduction in the

curling stress values. Simulations were run on concrete pavements located in hotter climate of Phoenix, Arizona and cooler climate of San Francisco, California and it was found that the selection of appropriate PCM transition temperature is extremely important to increase its effectiveness in different climatic conditions. PCM with a transition temperature of 35 ^{o}C was more effective in Phoenix, whereas PCM with a transition temperature of 24 ^{o}C was more appropriate for San Francisco.

As a result of this work, it was identified that there are several variables that play a key role in determining the optimum amount and type of PCM to be used in a climatic condition. In addition, the incorporation of PCM would benefit all concrete structures by reducing the amount of thermal fatigue. Therefore, a software tool MATRICEs was developed to simulate the effect of PCMs in concrete structures. The software is in the early stages of development and currently MATRICEs version 1.0 is capable to modeling the thermal response of concrete bridge decks and pavements with variable climatic conditions considering the concrete mix design, hydration parameters and mechanical strength development.

1.1.1 Research Objectives

This study has been focused on understanding the fundamental early age behavior of composite cementitious binder systems, consisting of supplementary cementitious materials such as slag, fly ash, metakaolin, silica fume and inert fillers such as limestone. Experimental investigation techniques as well as computational modeling were employed to study the early age behavior. Experimental work was carried out using advanced microstructural

characterization techniques such as isothermal calorimetry, thermo-gravimetric analysis, mercury intrusion porosimetry, dynamic shear rheology and X-ray diffraction.

The objectives of the study in these sections are:

a. Comparative investigation of interground and blended limestone cements,
b. Characterization of ternary binders containing slag and limestone, and exploring the synergy between limestone and aluminous source slag,
c. First principles-based approach to the development of ultra-high-performance binders and concretes, and their characterization, and
d. Exploring the significance of incorporating phase change materials in concrete for mitigation of early age thermal cracking in pavements and bridge decks.

1.1.2 Research Significance

With the rapid growth of economies over the past few decades, global cement consumption has risen four-fold in the last 30 years and is predicted to rise to about 4.4 billion metric tons in 2020. The production of ordinary portland cement is a highly energy intensive process which involves heating raw materials at temperatures as high as 1200ºC. Besides that, the calcination of limestone used to produce cement emits carbon dioxide, a greenhouse gas responsible for global warming. According to a 2016 report on global CO_2 emissions (Olivier et al. 2016), the cement industry accounts for approximately 8% of the global carbon emissions. The environmental impact, particularly the significant emission of greenhouse gases associated with the manufacture of ordinary portland cement (OPC) (Worrell et al. 2001), has deemed it necessary to design concrete infrastructure using high-volume replacement of cement with alternate cementitious materials including fillers such as

limestone and supplementary cementitious materials such as fly ash, blast furnace slag, metakaolin and silica fume. The research presented in this study dives into the realm of sustainable concrete design to introduce novel cementitious systems which provide the same or better properties than conventional OPC. The use of sustainable concrete in infrastructure, thus, not only reduces the environmental impact of the cement industry, but at the same time also has significant potential in reducing material costs in construction projects.

1.1.3 Report Outline

The dissertation consists of eight research papers that have been published, submitted or going to be submitted for publication. These papers are presented in Chapters 3-10. The overall report is divided into two major sections – (A) novel concrete mixtures and their early age performance, and (B) modeling of early age performance of novel concrete mixtures. Chapters 3-8 belong to the first section and Chapters 9 – 10 belong to the second section. The overall organization of the thesis is shown below.

Chapter 1 gives a brief introduction about the study and presents the background on functional cementitious composites. The definition of functional cementitious composites is explained along with the relevance to the work done in this study. The research objectives are identified, and a chapter outline is presented.

Chapter 2 presents a thorough literature review pertaining to all four objectives of the study.

Chapter 3 reports a comparative investigation on blended and interground limestone cements. The effect of cement replacement using limestone in these two different ways is

brought out by studying the hydration, pore structure and strength development of the cement-limestone systems.

Chapter 4 explores a novel methodology to extract the individual particle size distributions of limestone and cement from an interground cement/limestone composite cement. The hydration of binary cement-limestone systems is modeled using a three-dimensional cement hydration modeling tool.

Chapter 5 brings out the limestone-aluminate synergy in slag containing high volume cement replacement binders. The chapter provides a characterization of the cement and cement-slag binders in the presence of limestone using several available techniques and discusses how a favorable limestone-alumina synergy can lead to performance equivalent binders.

Chapters 6-8 present a series of studies to implement a novel multi-scale design strategy to design ultra-high performance concrete mixtures.

Chapter 6 discusses the methodology to design ultra-high performance binders that incorporate conventional cement replacement materials, and achieve a high degree of microstructural packing and desirable rheology for flowable concrete.

Chapter 7 presents a holistic material design of ultra-high performance concrete by coupling the efficient design for ultra-high performance binders with an optimized aggregate distribution to attain the maximum packing density.

Chapter 8 presents the compression and flexural response of the ultra-high performance concretes designed in the previous chapter. It also discusses the evaluation of homogenized micro-mechanical response of ultra-high performance binder using micro-indentation.

Chapter 9 presents a numerical simulation study to evaluate the thermal response of concrete pavements that contain phase change materials. The study employs a one-dimensional finite difference method to determine the spatio-temporal temperature profile of a concrete pavement and utilizes that to further analyze the thermal stresses and cracking probability in concrete pavements.

Chapter 10 presents a comprehensive software package for modeling and analysis of thermal stresses in concrete structures. The chapter describes the software documentation and theory behind the computation of thermal strains and stresses in a diverse array of concrete structures.

Chapter 11 goes over the conclusions and recommendations for future work beyond this thesis.

CHAPTER 2

LITERATURE REVIEW

This literature review is divided into two parts. The first part covers the multi-component cement replacement systems and goes over the research conducted in the field of supplementary cementitious materials and high-volume cement replacement using SCMs. It discusses ultra-high performance concretes and their design in terms of strength, durability and cost. The second part discusses briefly about the science of phase change materials and reviews the research conducted in the field of incorporation of phase change materials in concrete.

2.1 Cement Replacement by SCMs

2.1.1 Background

As in any conventional cementitious system, ordinary portland cement (OPC) constitutes the major binding material in concrete. In addition to OPC, several waste/by-product materials containing reactive aluminosilicates (industrial by-products such as fly ash and slag, and natural pozzolans) are used because of their potential to enhance the mechanical and durability properties of concretes. Partial cement replacement materials such as fly ash, silica fume and metakaolin (Figure 2-1) are generally used in the cement and concrete industry in large amounts (Kosmatka et al., 2002). The mechanisms by which these materials improve the properties of cementitious systems is well known. These materials react with the soluble calcium hydroxide (CH) produced as a result of OPC hydration, resulting in secondary calcium silicate hydrate (C-S-H) gel. This increases the volume of solid products in the

material structure and refines the pore structure, thereby enabling strength enhancement and increased resistance to the passage of deleterious agents such as chlorides and sulfates.

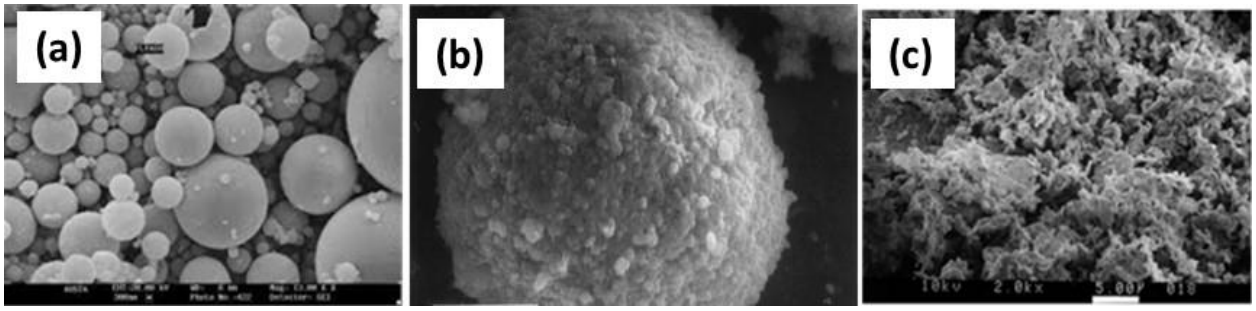

Figure 2-1: Micrographs of: (a) fly ash, (b) silica fume (Mitchell et al., 1998), and (c) metakaolin as supplementary cementitious materials (SCMs).

These materials are referred to as supplementary replacement materials (SCMs). The common materials used to replace cement in concrete are described in this section.

2.1.2 Fly Ash

Fly ash (FA) is a by-product of coal fired electric power plants. Depending on the amount of calcium present in the fly ash, it can be classified as high calcium (Class C) or low calcium (Class F) fly ash. Class F fly ash is more common in Arizona. Due to their spherical shape (Figure 2-1 (a)), FA particles have been shown to improve the workability of concrete. FA is also a pozzolanic material, which means that it reacts with the by-product of cement hydration (i.e. calcium hydroxide) to form its own hydration product, thereby improving concrete properties. However, it is notable that the pozzolanic reaction of fly ash (in general, Class F FA) is a slow process, and thus the effects of FA on early age reaction kinetics, setting, and strength development becomes an important consideration in designing concrete systems. Fly ash blended with other cement replacement materials such as silica

fume and metakaolin has been shown to provide accelerated early age property development (Vance et al., 2013a). It has been well documented (Nochaiya et al., 2010; Richardson, 1999) that FA lowers the heat of hydration, enhances the amount of hydration products (C-S-H gel), and thus improves the mechanical properties and durability of concrete, when used as a partial cement replacement. In general, the replacement levels of cement by Class F FA in concrete ranges from 10-30% (by mass), while Class C FA can be used in higher amounts. The use of high volumes of fly ash in cementitious systems or the use of geo-polymeric systems (where OPC is not used at all; rather fly ash is the sole cementing medium, aided by high concentration of alkali hydroxides and silicates) (Garcia-Lodeiro et al., 2011) have also been studied.

2.1.3 Silica Fume

Silica fume (SF), one of the most popular pozzolanic materials used in concrete, is a by-product of the manufacturing of silicon and silicon alloys (Malhotra et al., 1987). The fine particle size of silica fume (lower by an order or magnitude or more as compared to OPC) results in SF acting as nucleation sites for cement hydration, thereby enhancing the rates of reaction during the early stages of hydration (Cheng-yi and Feldman, 1985). Silica fume is available in densified and undensified states; the dry densified one being more common in use. Although densified silica fume increases the bulk density, researchers have shown there is some degree of agglomeration between the particles which influences the workability and properties of concrete (Boddy et al., 2000; Bonen and Diamond, 1992; Mitchell et al., 1998; Nagataki et al., 1994). The enhancement in mechanical properties when SF is used, is attributed to the matrix densification and pore size refinement as a result of consumption of

calcium hydroxide (Bayasi and Zhou, 1993; Igarashi et al., 2005; Mazloom et al., 2004; Poon et al., 2006; Rao, 2003; Yajun and Cahyadi, 2003). The very high reactivity of SF, aided by its small particle size and high amounts of reactive silica, results in faster property development than other partial cement replacement materials. This can be noticed from the strength activity indices of cementitious systems containing SF or FA as can be noticed from Figure 2-2 (Neithalath et al., 2009). An even finer version of silica fume, termed as nano-silica is also used sometimes for special applications. While the very small particle sizes undoubtedly increase the reactivity in the system, the dispersion of mixtures containing such particles is a challenge, even when very high amounts of dispersion-helping chemical admixtures are used. The agglomeration of these particles sometimes causes undesirable effects in mechanical properties.

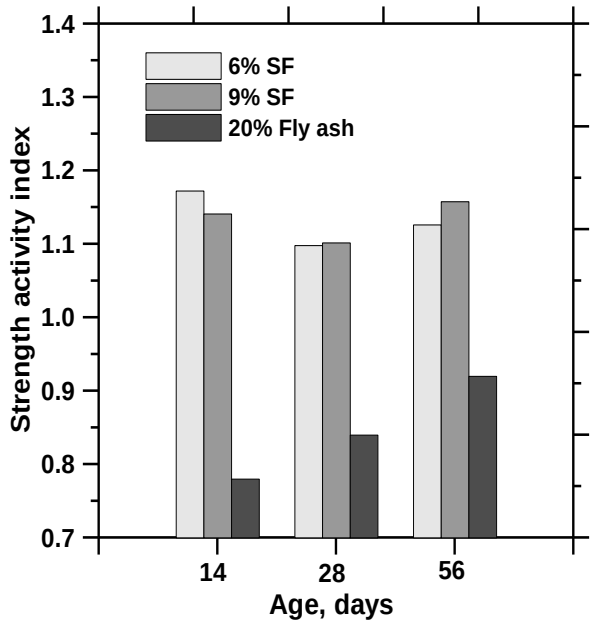

Figure 2-2: Strength activity indices of cementitious mortars containing SF or FA (Neithalath et al., 2009)

2.1.4 Metakaolin

Metakaolin (MK) is a pozzolanic material produced by the thermal processing of kaolin clay (Gruber et al., 2001). Metakaolin has an amorphous structure (see Figure 2-1) consisting mostly of aluminosilicates, and forms C-S-H gel on reaction with calcium hydroxide produced from cement hydration. Metakaolin has been shown to be more reactive than fly ash and other similar pozzolanic materials due to its higher surface area and greater alumina content (Poon et al., 2001). The higher reactivity, along with the reduction in cement content, leads to increase in heat of hydration per unit mass of cement (Figure 2-3(a)) (Vance et al., 2013a). The enhanced pozzolanic activity consumes more calcium hydroxide and forms more C-S-H than what is typical with other cement replacement materials such as fly ash. This is shown through thermal analysis results in Figure 2-3(b) (Vance et al., 2013a). The net result is an increase in the amount of hydration products, refinement of the pore structure, and consequent improvement in the mechanical properties and durability of concrete (Antoni et al., 2012; Kadri et al., 2011; Paiva et al., 2012; Poon et al., 2001; Shekarchi et al., 2010; Vance et al., 2013a).

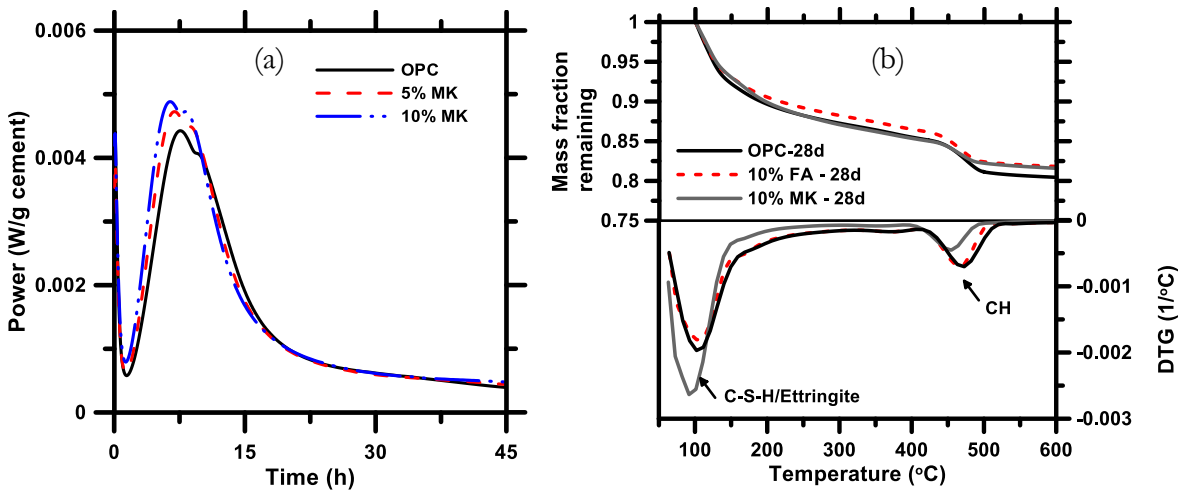

Figure 2-3: (a) Reduction in heat of hydration when cement is partially replaced by MK, (b) thermal analysis results showing reduction in CH and increase in C-S-H when MK replaces part of cement (Vance et al., 2013a)

2.1.5 Limestone

The use of limestone as a partial cement replacement material has been on the rise in recent years. Portland limestone cements are used in several countries including the U.S. ASTM C 595 has defined a Type IL cement that can include up to 15% of limestone powder as a partial cement replacement material (Tennis et al., 2011). The use of appropriate size ranges of limestone powder results in better particle packing and thus improves the properties. Limestone powder can chemically interact with the aluminate phases in cement to form a carboaluminate phase (Arora et al., 2016b, 2016a; Das et al., 2015; Kumar et al., 2013; Puerta-Falla et al., 2016; Vance et al., 2013a, 2015a). Previous work (Vance et al., 2013a) has shown that fine limestone in the presence of metakaolin or fly ash, enhances the amount of C-S-H gel formed even as early as 28 days, and has a beneficial impact in strength

development as shown in Figure 2-4. This is a significant result, since it provides the rationale for using fine limestone in combination with other SCMs, which has the potential to improve the sustainability of concrete.

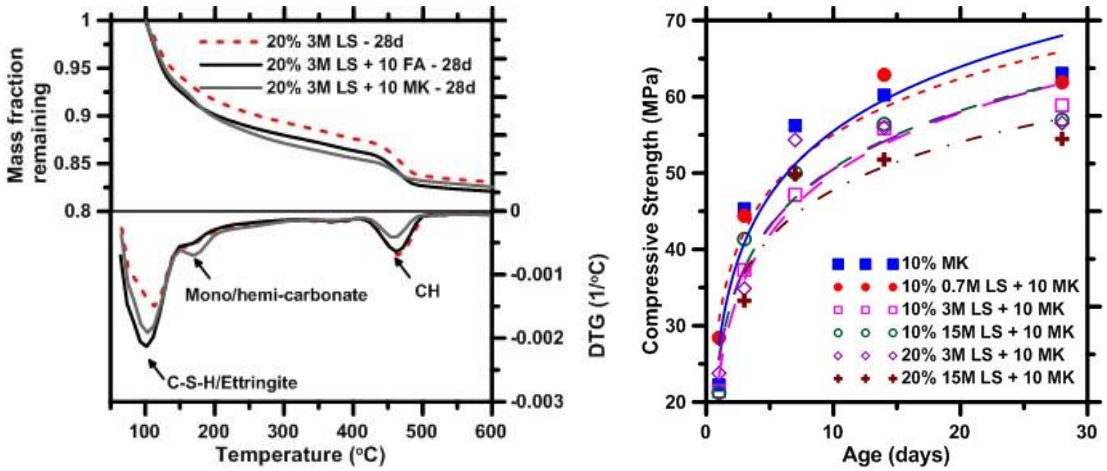

(a) (b)

Figure 2-4: (a) Thermal analysis results showing reduction in CH and increase in C-S-H when MK or FA in combination with limestone replaces part of cement, and (b) strength development of limestone-metakaolin systems (Vance et al., 2013a)

2.1.6 Microstructure Packing and Hydration Modeling

The microstructure of a cementitious system plays a significant role in determining the hydration, porosity and strength development properties of the macro-scale concrete. As such, the particle size distribution and fineness of constituent materials can be used to construct virtual microstructures and study the interactions of particles. Improved mechanical and durability properties of cementitious systems are a result of proper mixture proportioning that includes a low w/b ratio and the use of several materials that help refine the pore structure. The pozzolanic materials provide increased hydration and refinement of the pore structure, causing the microstructure in these systems to densify, as explained in the

previous sections of this chapter. Use of a proper size distribution of solid particles can help increase the packing density of the microstructure, which beneficially influences the mechanical and durability properties of the material. This is schematically depicted in Figure 2-5 ("Fillers in Action: How to Achieve High Particle Loadings" 2015). Since packing in the matrix can be controlled by judicious selection of powders with appropriate particle sizes, it is a better means to design and produce economical concrete mixtures, rather than the use of expensive high-reactivity materials. In this manner, a particle-packing based mixture proportioning ensures economy and sustainability.

(Stovall, de Larrard, and Buil 1986) presented a model for packing density of multi-sized grains. The model expresses the packing density as a function of the fractional solid volume of each size of grain present. In many packing models, it is assumed that there is at least one dominant sized particle group (that has the highest packing density) among the various grain sizes present. By sequentially considering each class of particles as dominant, a series of packing density functions can be obtained. The minimum packing density can then be conservatively taken to be the packing density of the mixture (De Larrard 1999; Lecomte 2006a). The packing density functions can be represented as:

$$\gamma_i = \frac{\beta_i}{1-(1-\beta_i)\sum_{j=1}^{i} v_j - \sum_{j=i+1}^{n} v_j} \quad (1)$$

where γ_i is the virtual packing density of the mixture when class i is dominant, β_i is the virtual packing density of grains of class i, v_j is the volume fraction of grains of class j, and n is the

total number of grain classes. Refer to (De Larrard 1999) for more details including the formulation and mathematical expressions that define packing-based mixture design.

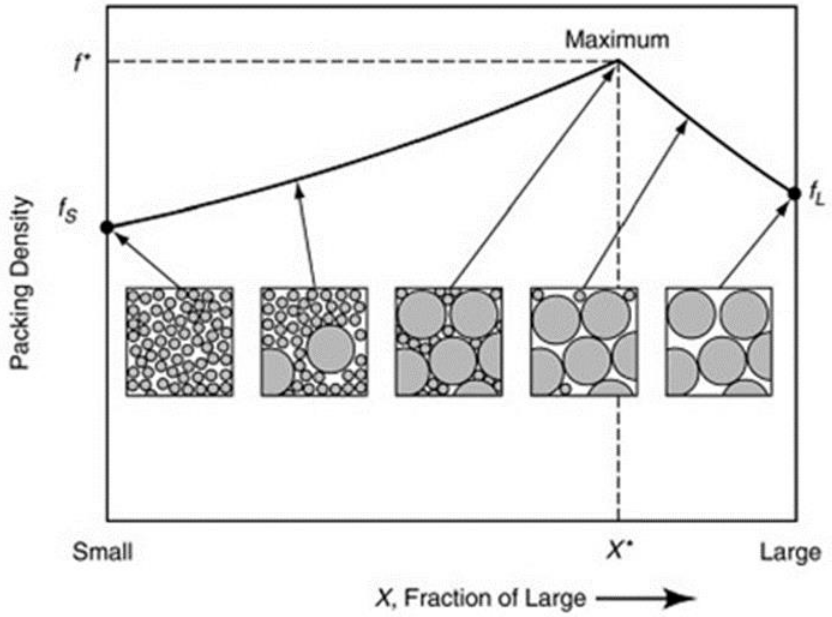

Figure 2-5: Schematic illustration of packing density as a fraction of larger particles in the mix ("Fillers in Action," 2015).

Virtual packing density is defined as the maximum packing density, which can be achieved by placing each particle one by one, in appropriate positions in a representative volume. In reality, it is not possible to control the positions of the grains, and therefore the distribution of the particles is random. For any random packing arrangement, a value called the actual packing density can be calculated (De Larrard 1999). Previous research (Vance, Kumar, et al. 2013) has indicated that packing densities can be calculated computationally by placing

spheres (that represent the actual particles[1]) in representative volume elements (RVEs) as shown in Figure 2-6. Virtual 3-dimensional (3D) microstructures can be created using the particle size distributions of the powders present in the mixture.

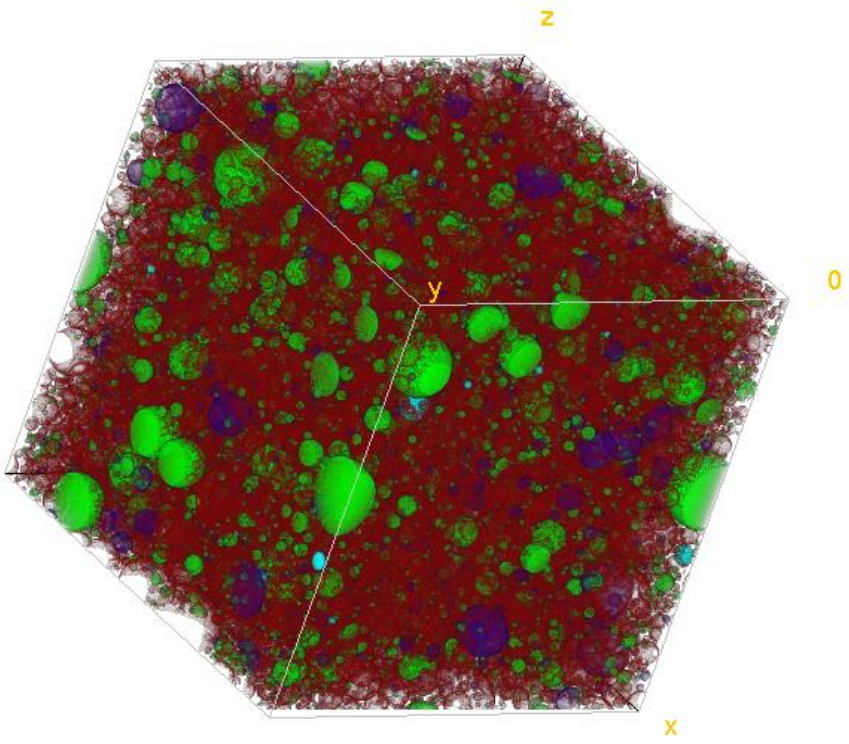

Figure 2-6: A 3D system in which spheres of different sizes are packed

Several microstructural parameters can be calculated from these microstructures to characterize and distinguish between different cementitious systems. The parameters include packing density, number density, contact fraction, mean centroidal distance, coordination

[1] Though many of the cementitious materials, with the exception of fly ash, are not spherical, the spherical particle assumption is widely used in computational materials science. This is to ensure that the simulations run in a reasonable amount of time in a relatively high-powered computer or a cluster. Assigning realistic particle shapes require orders of magnitude larger computational time, and the refinement in the results have not justified that choice, in past studies.

number, cumulative averaged cumulative number among others. Packing density is referred to as the volume fraction occupied by particles in the representative volume. The packing density is a function of the water-to-binder ratio of the cement paste. Number density is calculated as the number of particles in a unit volume. The number density values increase as OPC is substituted by finer constituents such as microsilica, fine limestone and metakaolin. Mean centroidal distance is a measure of the degree of packing of the microstructure. It is calculated as the normalized average distance from the surface of a particle to the surface of its nearest neighbors. The calculated distance is normalized with respect to the packing fraction of the particles in the microstructure. This is essential when comparing microstructures with different packing fraction values. Nearest neighbors are considered as all the particles that lie partially or wholly in the radial field of a particle in the microstructure, defined as a sphere of radius ($r + r_{50}/2$). Here 'r' is the radius of the particle, and r_{50} is the median radius of the microstructure obtained using the cumulative particle size distribution of the paste. The coordination number (CN) is an averaged quantity calculated as the number of neighbors as a function of the distance from the surface of any particle in the microstructure. The number of neighbors is counted as the particles that lie partially or wholly at a distance 'd' from the surface of a particle of radius 'r', where 'd' varies from 0 to r/2. Following with this definition, a particle with a higher radius will have a larger spatial field and therefore a higher number of particles as neighbors. Therefore, an averaged CN profile may be more useful to characterize the entire microstructure and compare between two different microstructures. Such a quantity is defined as the cumulative averaged coordination number (CACN). Quantification of the interactions through contact fractions

is useful to obtain a perspective on the reaction rates in the mixtures. The particle contact fraction is calculated as the fraction of nearest neighbor pairs in the microstructure. For instance, in a binary system containing cement and limestone, the cement-limestone contact fraction is calculated as the ratio of the total number of contacts between cement and limestone to the total number of contacts in the system (which includes cement-cement, limestone-limestone, and cement-limestone contacts).

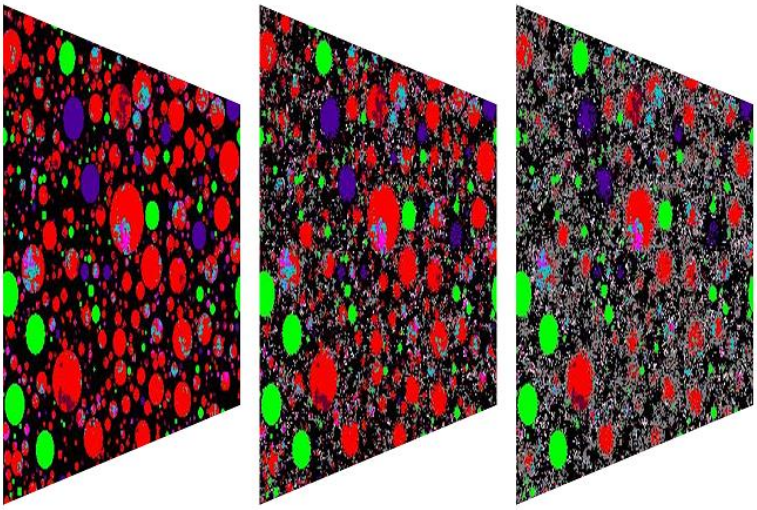

Figure 2-7: Evolution of hydration in OPC as a function of number of cycles. From the left, images correspond to 0, 100 and 400 cycles of hydration, corresponding respectively to t=0, t=4 hours and t=56 hours.

The virtual microstructures developed can be used to study the evolution of hydration products in cementitious systems. While several models are available in literature (Williamson 1972; Pommersheim and Clifton 1979; Navi and Pignat 1996; Lothenbach and Winnefeld 2006; Thomas et al. 2011), this research uses a cellular automata-based cement hydration model (D. P. Bentz 2005) to study cement paste hydration. The powder

constituents are considered as spherical particles and assigned properties such as reaction rates, heat of hydration, dissolution rate according to values obtained in literature. When the virtual microstructure initiate the contact with water, hydration products are formed probabilistically based on the rules of cellular automata. Figure 2-7 shows three sectioned images of a 300-micron RVE containing OPC after 0, 4 and 56 hours of simulated hydration. The voids are shown in black and the hydration products can be identified in grey. The cement phases C_3S,C_2S, C_3A and C_4AF are indicated in white, maroon, purple and turquoise respectively. The blue and violet colors indicate gypsum content in form of hemihydrate and di-hydrate in the cement.

2.2 Ultra-High Performance Concrete

2.2.1 Background

Ultra-High Performance Concrete (UHPC) is a special type of concrete designed to demonstrate exceptional strength, ductility, and durability properties. The high compressive strength of UHPC enables reduction in cross section and self-weight of reinforced concrete structures. UHPC is constituted by employing a well-defined size distribution of particles (both fine particles including cement replacement materials such as silica fume, and fine and coarse aggregates), fibers, and a very low water-to-binder ratio (w/b) (0.2-to-0.3). The very low w/b demands the use of higher-than-normal amounts of chemical admixtures including high range water reducers and viscosity modifiers. This complex mixture formulation, which is often proprietary in nature, leads to a significant increase in the cost of production of UHPC. Development of economical, yet optimally performing UHPC mixtures is a major challenge for many users including State Departments of Transportation.

While the 28-day compressive strength of conventional concrete ranges from 4000-7000 psi and that of high performance concrete lies between 7000 psi and 14000 psi, the compressive strength of UHPC is in the order of 20000-24000 psi. The significantly higher tensile strength (1000-1500 psi) and bending strength also set UHPC apart from conventional concrete, and even traditional high-performance concrete. In addition, the use of a high dosage rate (of the order of 1%-3% equivalent steel fibers) of fibers in UHPC increases the ductility of the member, in addition to allowing to withstand tension and bending loads without any passive or active reinforcement. The use of a low w/b, coupled with optimal particle packing, significantly increases the durability properties of UHPC by resisting the ingress of moisture and other deleterious ions such as chlorides and sulfates. These special properties of UHPC have been utilized for the construction of several transportation structures as well as the connections for precast elements in the U.S and Canada. Figure 2-8 shows the first UHPC bridge in the U.S. which was built in Iowa, and the casting of longitudinal connections between precast bridge girders in the state of New York.

Figure 2-8: (a) The first UHPC bridge constructed in the U.S (in Wapello County, IA), (b) casting of longitudinal connections between deck-bulb-tee girders (Route 31 Bridge, Lyons NY). Both figures courtesy of FHWA.
(https://www.fhwa.dot.gov/publications/research/infrastructure/structures/11038/)

Structural applications requiring enhanced mechanical performance are candidates for UHPC (Attar et al., 2000; Porteneuve et al., 2001; Schiessl et al., 2004; Schrefler et al., 2002). The precursors of UHPC include high performance concretes (HPC) (Ahlborn et al., 2011), polymer modified concretes (Birchall et al., 1983), and reactive powder concrete (Cheyrezy et al., 1995; Dugat et al., 1996; Feylessoufi et al., 1996; Philippot et al., 1996; Richard and Cheyrezy, 1995; Zanni et al., 1996) among others. While HPC has been, and still is, rather popular, its performance requirements are generally lower than those specified for UHPC. The Portland Cement Association defines UHPC as 'a high-strength, ductile material formulated by combining portland cement, silica fume, quartz flour, fine silica sand, high-range water reducer, water, and steel or organic fibers'. This is a rather prescriptive definition, which is not strictly correct since some of these components might not be needed to obtain desired performance levels. ACI Committee 239 on UHPC defines it as 'concrete that has a minimum specified compressive strength of 150 MPa (22,000 psi) with specified durability, tensile ductility and toughness requirements; fibers are generally included to achieve the specified requirement'. FHWA has a rather generic and inclusive definition of UHPC: 'a cementitious composite material composed of an optimized gradation of granular constituents, a water-to-cementitious materials ratio less than 0.25, and a high percentage of discontinuous internal fiber reinforcement'. The mechanical properties of UHPC include compressive strength greater than 22,000 psi (150 MPa), and sustained post-cracking tensile strength greater than 720 psi (5 MPa) (B. Graybeal, 2011; Russell and Graybeal, 2013).

2.2.2 Particle Packing-Based Mixture Proportioning of UHPC

To gain extremely high compressive strengths, a dense particle packing of aggregates and cement paste is one of the most important considerations while designing UHPC mixtures. (Stroeven and Stroeven, 1999) showed that for dense mono-sized particles at two different grain fractions, the volumetric packing density exhibits an oscillatory phenomenon as shown in Figure 2-9. Note that the dashed lines in the top of Figure 2-9 at 2 and 14 mm from the interface, represent the simulated particle dispersion of the bottom images in Figure 2-9. It can be noted that there is an increase in the fractional density at the interface when binary particles are used. Such an understanding is useful in selecting particle sizes of aggregates for mixtures such as UHPC where packing must be increased for optimal performance.

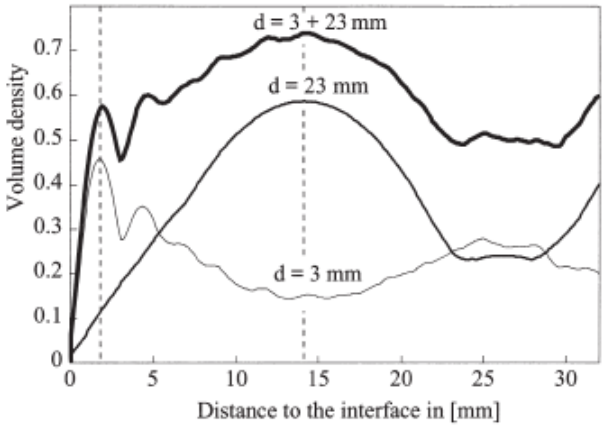

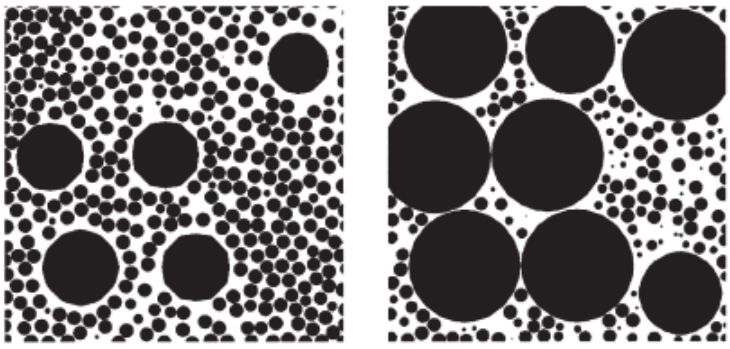

Figure 2-9: Volume fraction of a bimodal particle mixture of sand and gravel as a function of the distance to a rigid interface (A. Kumar, Oey, Kim, et al. 2013)

Other models for particle packing also exist. Yu et al. (2014) employed the Andreasen and Andreasen particle packing model to produce a dense UHPC with a binder content of about 650 kg/m^3. The Funk and Dinger packing theory was used by (Le et al. 2015) in order to determine the grading of aggregates for self-compacting high performance concrete. While these models also provide adequate capabilities with respect to packing, they employ several assumptions (e.g., size distribution of all grain classes are the same, the ratio of largest to smallest particle size is limited to a certain value etc.). The virtual packing density-based model chosen for the present work eliminates many of those assumptions and provides a scientific methodology for mixture design, which is repeatable and robust.

The degree of hydration is rather low in UHPC systems due to the low w/b ratios. It was suggested that filler materials (e.g. limestone, quartz powder) and nanoparticles (nano silica, for example) can be used to improve the workability of the mixture and accelerate the cement hydration process by acting as nucleation sites (Camiletti, Soliman, and Nehdi 2012; W. Li et al. 2015). (Sobolev 2004) proposed models for high performance concrete that calculate the appropriate water-to-cement ratio required for a specific compressive strength. This work suggests that the optimal water reducing admixture[2]-to-silica fume ratio for

[2] High-range water reducing admixtures are also referred to as superplasticizers. They are typically made from polycarboxylate polymers which act as dispersants to improve the flow characteristics of the concrete mixture. Not all superplasticizers provide efficient workability, as shown by Ghafari et al. (2015), who tested 7 different types of superplasticizers and determined that the ideal type of superplasticizer limits the formation of air voids.

achieving ultra-dense packing and high fluidity of the system is 1:10. Though there are concerns as to how this exact number was arrived at, it is reasonable to assume, based on the fineness of silica fume, that a higher water reducing admixture dosage would be warranted with higher silica fume content.

Table 2-1 gives an overview of the constituents in UHPC and their amounts in a typical UHPC mixture design, as reported in several studies (Yazıcı et al. 2008; Tafraoui et al. 2009; C. Wang et al. 2012; Elrahman and Hillemeier 2014; Yu, Spiesz, and Brouwers 2014a, 2015; Yoo and Yoon 2015; Kay Wille and Boisvert-Cotulio 2015; Alkaysi et al. 2016).

Table 2-1 Typical proportions of materials used for UHPC

Materials in UHPC Binder phase	Amount (% by weight)
Cement	25 – 45
Silica Fume	5 – 15
Metakaolin	0 – 10
Fly Ash	5 - 25
Sand	35 – 45
Quartz	5 – 15
Water	3 – 10
Fiber	0 – 6

2.2.3 Hydration and Microstructure

It is important to evaluate the hydration of the binding materials in UHPC systems since the property development is intimately related to the degree of hydration and the resultant

microstructure. Understanding the hydration in these systems also provide indications of heat release and potential cracking probabilities, as well as degrees of reaction of the component materials.

Reda et al. 1999) conducted microstructural investigations on carbon fiber reinforced UHPC using scanning electron microscopy (SEM) and X-ray diffraction (XRD). They detected a very dense and uniform microstructure in the UHPC pastes with a very small interfacial transition zone. XRD studies showed no trace of calcium hydroxide, which was attributed to the highly efficient pozzolanic reactions of silica fume/silica flour present in the mixtures. (Ghafari et al. 2012) also studied the microstructure of UHPC using SEM and quantified the density of the microstructure using sorptivity tests and porosity measurements. They found that the UHPC mixture containing nano-silica had a much-refined pore structure, resulting in a lower amount of water absorption as compared to the reference UHPC mixture. In addition, the incorporation of nano-silica also resulted in lower volume of capillary pores, which was measured using porosimetry, and confirmed with SEM analysis.

2.2.4 Mechanical Properties

The key mechanical property of interest for UHPC is its compressive strength, even though the need to consider many other important parameters have been laid out. All definitions of UHPC specifically state the need for high compressive strengths.

Compressive strength testing of UHPC is generally carried out in accordance with ASTM C39/C39M or EN 12390-3. The modulus of elasticity is determined using ASTM C469/C469M or EN 12390-13. The specimen size has been found to have a significant influence on the strength of UHPC. For instance, (Magureanu et al. 2012) found that the

flexural strength of 40 x 40 x 160 mm (1.57 x 1.57 x 6.29 in.) prisms was 1.47 times higher than that of 100 x 100 x 300 mm (3.94 x 3.94 x 11.81 in.) prisms. Skazlić et al. (2008) also observed a 21 % increase in cylinder compressive strength for a specimen size of 70 × 140 mm (2.75 × 5.50 in) compared to that of 100 × 200 mm (3.94 × 7.87 in). This was attributed to a higher probability of encountering larger size flaws in larger sized specimens. Further, it has been found that the addition of steel fibers changes the failure mode of UHPC specimens from complete damage or sudden explosion to a somewhat ductile behavior. The higher the fiber factor, $V_f \ell_f / d_f$ (V_f is the fiber volume fraction, ℓ_f is the fiber length, and d_f is the fiber diameter), the more pronounced is the change in the failure mode (Bencardino et al. 2008). Wille et al. (2011a) investigated the direct tensile behavior of ten different fiber reinforced UHPC (also referred to as UHPFRC) mixtures containing either smooth, deformed, or twisted fibers. They found that the use of deformed fibers resulted in higher tensile strengths as compared to smooth fibers, which was attributed to an improvement in the fiber-matrix mechanical bond through fiber deformation.

To compute the elastic modulus of the sample during a compression test, in addition to its post peak response, a closed loop strain-controlled test should be employed; however, the use of axial strain during the softening region may not result in good quality results because of energy release and snap back. These features of the test would result in sudden failure of the specimen. It is recommended the complete stress-strain curve of UHPC be obtained using a two-stage process. During the first stage, the axial strain is used as the control parameter and prior to reaching the peak load, the mode of control is changed to the circumferential strain (Ariño and Mobasher 1999).

The tensile strength of UHPC, both before and after tensile cracking, is significantly higher than that of normal concrete (B. A. Graybeal 2006). The capacity to retain a non-negligible and reliable tensile resistance in the post-cracking regime is a distinct feature of fiber reinforced concrete. Wille et al. (2011b) showed that addition of 1.5% deformed fibers by volume results in a 60% higher post-cracking tensile strength than comparable UHPFRC with smooth steel fibers. Therefore, the experimental identification of post-cracking tensile behavior and defining parameters to suitably characterize UHPFRC from a design perspective is of the utmost importance. Many experimental tensile tests, direct or indirect, have been used; however, no tensile test standard has been established to date.

Curing methods such as steam and heat curing have been found to enhance the compressive strength of UHPC. Prem et al. (2015) found that heat cured samples showed 1.5 times increase in 28-day compressive strengths as compared to steam cured and water cured samples, both of which had similar 28-day strengths. This was also confirmed in a different study (Magureanu et al. 2012) which found that the compressive strength of the steel fiber-reinforced concrete at 371 days was 1.34 times higher for the heat-treated specimens stored in water as compared to the water-cured specimens. A FHWA study (B. A. Graybeal 2006) reported that steam based treatment of UHPC significantly enhances the material properties. Three steam-based treatments: steam, delayed steam, and tempered steam, were compared with a curing treatment that did not involve steam after casting.

Flexural testing is carried out using ASTM C78/C78M or C1609/C1609M under four-point bending, or alternately by center-point loading using ASTM C293/C293M. If only maximum flexural strength is of interest, ASTM C78/C78M or C293/C293M can be used. If toughness

or load-deflection behavior after matrix failure is also of interest, ASTM C1609/C1609M is appropriate. Flexural strength results obtained in load-controlled testing according to ASTM C78/C78M may differ from those obtained using the deflection-controlled procedures of ASTM C1609/C1609M. A study by FHWA showed that the ASTM C1018 prism flexure test provided means of comparing the post-cracking tensile behavior of various UHPFRCs (B. A. Graybeal 2006). The European Standard EN 14651, specifies, for FRC with fibers up to 2.4 in. (60 mm) long, a 6 in. x 6 in. x 22 in. (150 mm x 150 mm x 550 mm) beam specimen, with a 1 in. (25 mm) deep notch at mid-span, with a test span of 20 in. (500 mm), and a center point loading configuration. The test can be performed in displacement control mode but the CMOD is measured with a clip gauge.

Two parameter fracture method (TPFM) can be used to characterize the fracture properties of UHPC. The fracture parameters such as the critical stress intensity factor (K_{IC}^{S}) and the critical crack tip opening displacement ($CTOD_C$), can be calculated from three-point bend tests on notched beams as shown in Figure 2-10(a). TPFM involves the use of the loading and unloading compliances, peak load, specimen and notch geometry, and a geometry correction factor, to determine the values of K_{IC}^{S} and $CTOD_C$. A typical load-CMOD plot is shown in Figure 2-10(b) with the loading and unloading compliances.

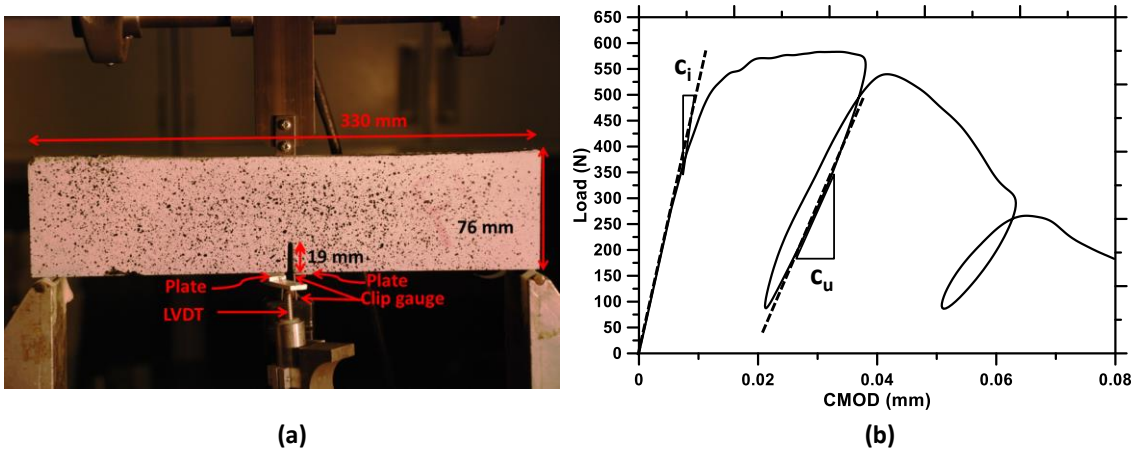

Figure 2-10: (a) Experimental setup for the notched beam fracture test, and (b) a typical load-CMOD plot showing loading and unloading compliances (Das et al. 2015)

In addition to the ASTM and EN standards discussed, there are many other standards available to evaluate the flexural properties of fiber reinforced cementitious systems such as UHPFRCs. The Japan Concrete Institute standard, JCI-SF4, specifies a method of measuring the flexural strength and flexural toughness of unnotched beam specimens, which can be applied for UHPFRCs.

Research also suggests that UHPC shrinks more than conventional concretes, attributed to the higher binder content in these mixtures, as well as the autogenous effects of very low water-to-binder ratios. It has been mentioned that the initiation of shrinkage in UHPC is affected by their delayed set times, and the majority of the shrinkage occurs in a short time just after the concrete has set (B. A. Graybeal 2006). Restrained shrinkage tests can provide indications of cracking susceptibility of UHPCs and potential means to mitigate those. The

influence of fibers on improving the shrinkage behavior of UHPC also needs to be considered.

Although there are no ASTM or EN standards for testing procedures for fiber pullout in cement matrices to determine bond strength, there is literature that describes the test setup and how loading conditions can strongly affect test results. Single-sided test profiles have been carried out (Grünewald 2004; Markovic 2006; Naaman et al. 1991; Banthia and Nandakumar 2003; Macedo, e Silva, and Martins 2010).

2.2.7. Durability

The serviceability and life expectancy of civil structures depend on the environmental and service conditions they are subjected to. As such, durability of concrete used in infrastructure is one of the key aspects of every construction project. Concrete structures may be subjected to ingress by several aggressive ions present in the environment. These ions may react with aggregates in concrete (alkali-silica reaction) or with the reaction products formed in concrete due to hydration of cement/cementitious materials. As a result, the strength of the structure could be severely compromised and service life drastically reduced. Many commonly advocated methods for durability enhancement of concretes rely on a reduction in the water-to-cement ratio of the mixture and the use of partial cement replacement materials that positively impact hydration. Thus, UHPC mixtures should inherently be more durable than conventional concretes. However, there are several factors that are less understood, which play a significant role in concrete deterioration. The commonly evaluated durability criteria for concrete include the resistance to abrasion, water permeation, freezing and thawing, alkali-silica reaction susceptibility, and ionic penetration.

2.2.7.1. Water Absorption

Water absorption, measured in accordance with ASTM C1585 (ASTM C1585 2013), determines the rate of absorption (sorptivity) of water as a function of time, by determining the increase in the mass of the specimen when only one surface is exposed to water. (Abbas, Soliman, and Nehdi 2015) examined the water absorption of UHPC containing steel fibers. It was found that the fiber length did not have a significant effect on the sorptivity coefficient, however, a slight decrease was apparent in the initial and secondary sorptivity coefficients when the dosage of fibers increased. This points to fewer connected pores and a denser microstructure when steel fibers are used. (Ghafari et al. 2014) showed that as the amount of nano silica in the UHPC was increased, up to 4% by mass of cement, there was a corresponding decrease in water absorption of up to 30%.

2.2.7.2. Freeze Thaw Resistance

Freeze thaw degradation, determined in accordance with ASTM C666 – 15 quantifies the resistance of concrete specimens to rapidly repeating cycles of freezing and thawing. (Benjamin Graybeal and Tanesi 2007) used the Procedure A of ASTM C 666, where UHPC prisms were submerged in a water bath while subjected to freezing and thawing. The lower and upper temperatures in the freezing and thawing environment were -18 and 4.4 °C. After 9 months and over 690 cycles of freezing and thawing, they confirmed that UHPC is highly resistant to deterioration regardless of the curing treatments performed on the specimens prior to testing. They did discover that all specimens exhibited a mass increase throughout testing due to the absorption of water into the concrete, causing the unreacted cement particles to hydrate.

2.2.7.3. Alkali Silica Reaction (ASR)

The susceptibility of alkali-silica reaction can be tested in accordance with ASTM C 1260 – 14 (ASTM C1260 2014). Since their UHPC mixtures contained no coarse aggregates, Graybeal (Benjamin Graybeal and Tanesi 2007) was able to directly use mortar UHPC bars in tests conforming to ASTM C1260. The mortar bars were submerged in a 1 M sodium hydroxide solution maintained at 80°C, for an extended duration of 4 weeks. At 14 and 28 days of testing, expansion of the UHPC mortar bars was an order of magnitude lower than the threshold for deleterious behavior prescribed by the standard. This study concludes that, due to the high reactive silica content that is utilized in the formation of a low Ca/Si ratio C-S-H gel, and low permeability of UHPC, ASR is not likely to occur. After 600 days, (Moser, Pfeifer, and Stark 2009) showed a maximum ASR expansion of 0.02% for UHPC, which is lower than the threshold limit of 0.04%.

2.2.7.4. Chloride Permeability

The resistance to chloride ion penetration is typically determined in accordance with ASTM C 1202 – 12 ("ASTM C1202 - 12. Standard Test Method for Electrical Indication of Concrete's Ability to Resist Chloride Ion Penetration" 2012), which is a rapid test method. This test applies a 60 V electrical potential difference across a concrete specimen 50 mm in thickness and 100 mm in diameter, for a duration of 6 hours. (Benjamin Graybeal and Tanesi 2007) observed that the charge passed through the UHPC specimens cured for 28 or 56 days were negligible when measured according to this standard, thereby indicating very high resistance to chloride penetration. (Abbas, Soliman, and Nehdi 2015) also revealed that

after 28 and 56 days of hydration, UHPC specimens displayed negligible chloride permeation.

2.3. Phase Change Materials

2.3.1. Background

The kinetics of phase change has been studied for years in thermodynamic systems. The concept of latent heat was introduced in 1762 by chemist Joseph Black as he noticed that the application of heat to boiling water does not result in a rise in temperature of a water/steam mixture, but rather an increase in the amount of steam. Today, we understand latent heat as the thermal energy released or absorbed by a body or a thermodynamic system, during a constant temperature process. It can also be understood as the thermal energy supplied to a material to change its state without a change in its temperature. Since all materials undergo change of phase at some thermodynamic conditions, the term 'phase change materials' is a generic term that applies to all materials. However, in modern usage, phase change material refers to a material with a high latent heat storage capacity or high heat of fusion. Phase change materials have emerged as an innovative solution to energy efficient urban systems over the past few years due their increased latent heat thermal storage capacity. The earliest studies on application of PCMs in infrastructure date back about 30 years (Collier and Grimmer 1979; Benson, Christensen, and Burrows 1985; Shapiro et al. 1987; Hariri and Ward 1988; Hawes, Banu, and Feldman 1990), when hydrated salts and hydrocarbons were used as phase change materials. PCMs were demonstrated to be useful as passive solar collectors in wall systems, however the extremely high cost associated with manufacturing PCMs on a large scale as well as unreliable long-term performance of those PCMs served as

roadblocks to a larger adaptation of PCM in the construction community. More recently, the development of different PCMs with improved thermodynamic, kinetic, chemical and economic properties have made PCMs more suitable to be utilized in infrastructure applications. Figure 2-11 shows the broad classification of PCMs available.

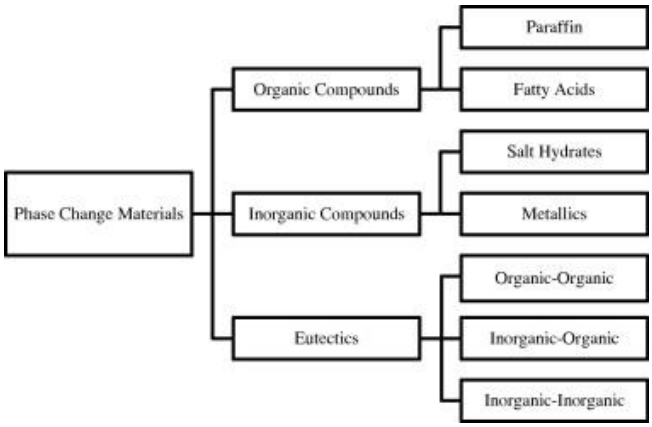

Figure 2-11 Classification of PCMs available (Zhou, Zhao, and Tian 2012)

2.3.2. PCMs in Concrete

The incorporation of PCMs in concrete infrastructure is an optimization problem and the selection criteria for a particular application depends on a number of factors. Abhat (Abhat 1983) in his review paper on low temperature latent heat storage materials listed out the following criteria for the selection of an appropriate PCM (Table 2-2).

Table 2-2 Selection Criteria for PCM (Abhat 1983; Zhou, Zhao, and Tian 2012)

A. Thermodynamic Criteria
(1) Melting temperature in desired range
(2) High latent heat of fusion per unit volume

(3) High thermal conductivity (4) High specific heat and high density (5) Small volume changes on phase transformation and small vapor pressure at operating temperatures to reduce the containment problems (6) Congruent melting
B. Kinetic Criteria (1) High nucleation rate to avoid super cooling (2) High rate of crystal growth to meet demands of heat recovery from the storage system
C. Chemical Criteria (1) Complete reversible freezing/melting cycle (2) Chemical stability (3) No degradation after a large number of freezing/melting cycle (4) No corrosiveness (5) No toxic, no flammable and no explosive material
D. Economic Properties (1) Effective cost (2) Large-scale availabilities

The chemical and kinetic criteria are the most important criteria that need to be satisfied to assess the suitability of any particular PCM for an application. Beyond that, the thermodynamic and economic criteria are the decision-making factors to select the desirable PCM. The melting temperature and enthalpy of commonly available PCMs is shown in Figure 2-12.

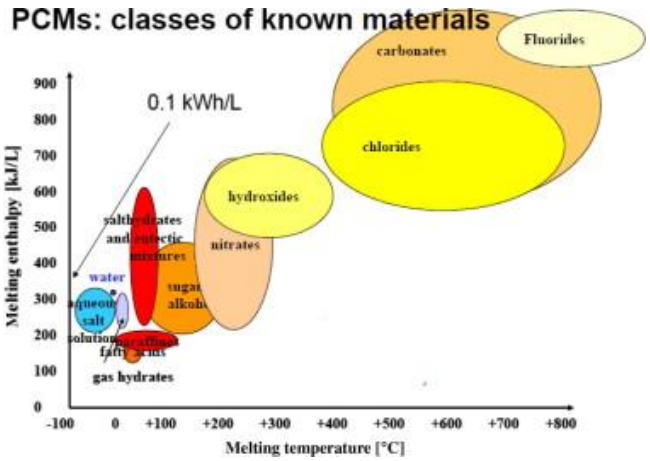

Figure 2-12 Melting temperature and phase change enthalpy of available PCMs (Zhou, Zhao, and Tian 2012)

The transition range of the PCMs for infrastructural applications must be between 0°C and 50°C. The enthalpy of phase change must be high enough to counter the daily temperature variations that a structure might experience. Beyond this, the thermal conductivity of the PCM must be high enough to facilitate internal heat transfer. The addition of the selected PCM in concrete then requires scrutiny about the type of impregnation (Hawes, Feldman, and Banu 1993; Castell et al. 2010) in construction materials (direct incorporation, immersion, macroencapsulation or macroencapsulation) and its effect on the mechanical and durability properties of concrete. Thus, the problem is multi-fold and requires several levels of validation. Experimental investigations have been carried out by several researchers to show the impact of different PCM types on concrete (Ahmad et al. 2006; Fernandes et al. 2014; Aguayo et al. 2016). Since experimental field validation is difficult to carry out with such a variety of PCMs available, researchers have made efforts to simulate the effects of PCM in a concrete environment (Pasupathy et al. 2008; Xu et al. 2005; Šavija and Schlangen

2016). The numerical simulation of PCM in concrete has been dealt with primarily as a heat transfer problem.

The temperature development in a concrete structure subjected to external variations in climate is modeled using the second-order ordinary differential equation known as the heat-diffusion equation (Equation 2-1).

$$\frac{\partial}{\partial x}\left(k\frac{\partial T}{\partial x}\right)+\frac{\partial}{\partial y}\left(k\frac{\partial T}{\partial y}\right)+\frac{\partial}{\partial z}\left(k\frac{\partial T}{\partial z}\right)+q'=\rho c_p\frac{\partial T}{\partial t} \quad \text{(Eq. 2-1)}$$

where k is the material thermal conductivity (W/m/K), T(x,y,z) (°C) is the scalar temperature field, q' (W) is the heat generation term, ϱ (kg/m^3) is the material density, c_p (kJ/kg/°K) is the material specific heat, and t(s) is the time.

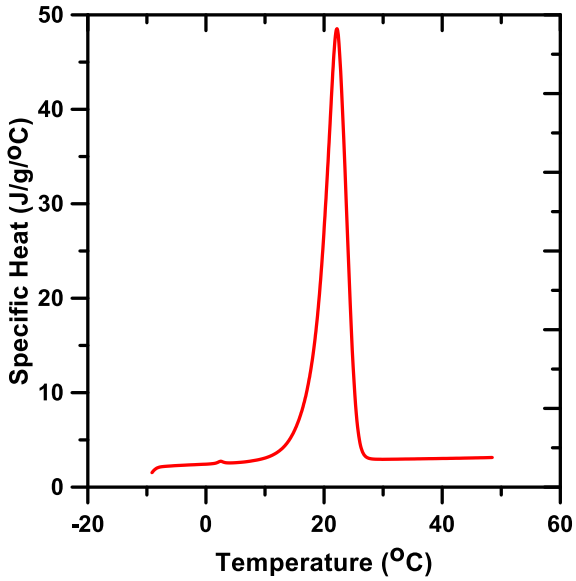

Figure 2-13 Specific heat plot for a phase change material

The boundary conditions involve top and bottom surface temperature values at any time 't' and the initial condition is the temperature profile of the concrete structure at t=0. This equation can be solved analytically or using standard finite element solvers when the values of thermal conductivity, heat generation, specific heat and material density are constants. However, discrete numerical solvers are required when these values are changing with time or are functions of internal variables. In case of PCMs in concrete, the specific heat capacity and thermal conductivity of PCMs vary with the temperature. Figure 2-13 shows a plot of the specific heat capacity of a phase change material. In addition to that, the boundary conditions for a concrete structure vary with time depending on the external climatic conditions. This discussion is presented in detail in Chapters 9-10 of this thesis.

CHAPTER 3

COMPARATIVE INVESTIGATION OF INTERGROUND AND BLENDED LIMESTONE CEMENTS: HYDRATION, PORE STRUCTURE, AND STRENGTH

3.1. INTRODUCTION

The use of limestone as a partial cement replacement material is a topic of great interest in an effort to increase the sustainability of portland cement concrete. As a portion of cement remains unhydrated even at late ages in low water-to-cement concretes, it has been proposed that the replacement of portland cement by limestone may allow for increased sustainability with minimal compressive strength losses (D.P. Bentz 2005; Matschei, Lothenbach, and Glasser 2007c; V. Bonavetti et al. 2003). Several studies have investigated the influence of limestone on portland cement systems, including investigations of hydration and hydration product formation (Vance, Aguayo, et al. 2013; D. Bentz et al. 2009), setting time (Dhir et al. 2007), strength development, rheology (Vance, Kumar, et al. 2013) and durability (D. Bentz et al. 2009). The majority of recent studies have focused on the use of limestone which is finer than the cement it is replacing, as this has been shown to accelerate hydration reactions (Vance, Aguayo, et al. 2013; Darweesh 2004), decrease permeability through increased particle packing, and minimize the strength loss associated with limestone (Vance, Aguayo, et al. 2013). However, use of fine limestone as cement replacement makes it difficult to distinguish filler effects resultant from inclusion of a fine filler from chemical effects resultant from limestone inclusion in these systems.

Two methodologies are commonly used for limestone replacement: (i) intergrinding the limestone with the portland cement clinker, and (ii) blending the ground portland cement

with limestone powder. Intergrinding of portland cement clinker with limestone results in a finer limestone phase in the composite system due to the fact that limestone is a softer material then the clinker. Blending, on the other hand, would result in a limestone distribution that is controlled more directly by the cement producer. Intergrinding of limestone with the clinker has been shown to have comparable mechanical properties at replacement ratios of up to 10% (Tsivilis et al. 1999).

The current study aims to disconnect the physical influences of packing and surface area differences from the actual physicochemical influence of limestone inclusion in these systems, by blending limestone in cements with particle size distributions which match that of the parent cement (or comparative interground PLC). This allows for a thorough exploration of potential benefits of limestone inclusions on strength, pore structure, and hydration product formation. Further, comparing size-matched blended systems to interground systems will enable further exploration of the differences of these two systems from the perspectives of hydration, strength, and pore structure.

3.2. EXPERIMENTAL PROGRAM

3.2.1 Materials

The materials used include: a commercially available Type I/II ordinary portland cement (OPC) conforming to ASTM C150 ("ASTM C150 / C150M - 12. Standard Specification for Portland Cement" 2012), and a nominally pure limestone powder (purity > 95% $CaCO_3$, by mass) of four different median particle sizes denoted as 0.7 μm, 3 μm, 10μm and 15 μm, conforming to ASTM C568 ("ASTM C568 / C568M - 10. Standard Specification for Limestone Dimension Stone" 2012), as well as two different interground PLCs conforming

to ASTM C595 ("ASTM C305-13 Standard Practice for Mechanical Mixing of Hydraulic Cement Pastes and Mortars of Plastic Consistency" 2013) and ASTM C1157 ("ASTM C1157/C1157M-11 Standard Performance Specification for Hydraulic Cement" 2013) respectively. Figure 3-1 shows the particle size distribution of these raw materials, and Table 3-1 presents their respective chemical compositions. It is noted that the C1157 interground cement is finer than OPC (denoted C150), while the C595 interground cement has a roughly comparable particle size distribution

.

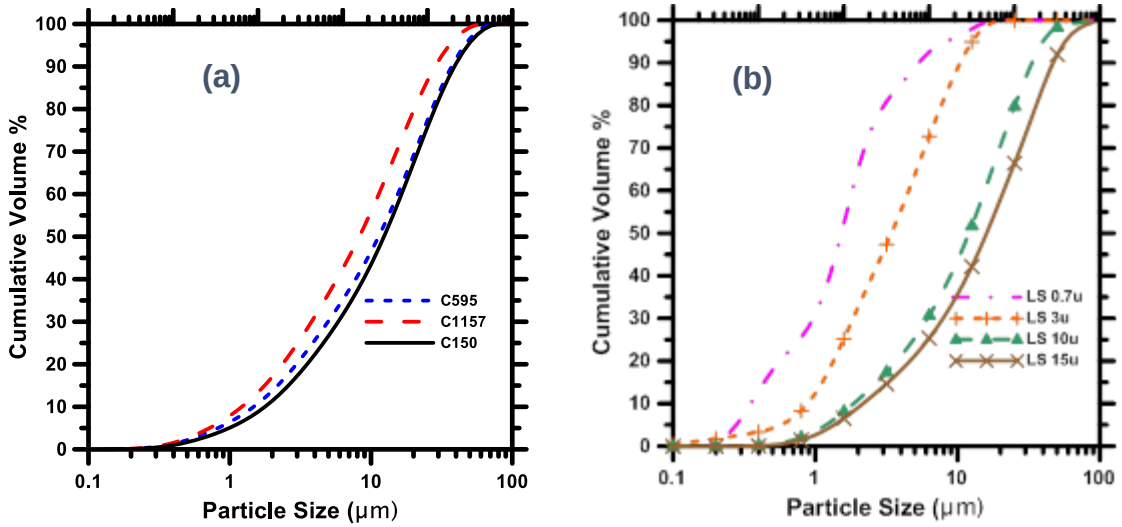

Figure 3-1: Particle size distributions of raw materials used in this study.

Table 3-1: Chemical Compositions of parent cements used in the study

Material	SiO_2	Al_2O_3	Fe_2O_3	CaO	MgO	SO_3	LOI	LS
C150	19.6	4.09	3.39	63.21	3.37	3.17	3.17	-
C595	16.51	3.38	2.66	56.80	2.61	2.80	4.17	11.07

C1157	16.51	3.41	2.77	56.55	3.01	2.87	3.81	11.07

Table 3-2: Median sizes of parent cements used in the study

Material	**C150**	**C595**	**C1157**
Median Size (μm)	11.20	10.03	7.53

In all, six different mixes were considered for the study. Mixture proportions per 100g of sample are shown in Table 3-3. It is noted for reference that the two interground PLCs (C1157 and C595) are already interground with limestone, thus the quantity of limestone for mixture proportioning is shown as zero. A volumetric water to powder ratio of 1.26 was used for all samples, corresponding to a mass-based water-to-powder ratio of 0.40 for the OPC mix. Limestone replaced OPC at a level of 12.68% by volume for all blended and interground cements. Three particle size distribution (PSD) matched portland cement-limestone blends were prepared, one each to match C150, C1157, and C595. The PSD matching was performed by blending the available sizes of limestone to minimize the square error in particle size distribution between the blend and the interground or plain cement powder. Particle size matching these mixtures enables a more in depth look at the true behavior of limestone in portland cement systems by disconnecting the influence of particle packing and surface area. Figure 3-2 shows the final particle size distribution of the blended versus the interground or plain cement after matching their particle size distributions. It is noted from this figure that the blend corresponding to C1157, the finest interground PLC, does not match the particle size distribution of the interground cement as well as the other two blends and the interground

cement is notably finer. The available sizes of limestone for this study could not be mixed in order to achieve a better particle size distribution match than the one provided in this study.

Table 3-3: Proportion of materials (in g) per 100g of sample

Mix ID	C595	C1157	OPC	Total LS	0.7µm LS	3µm LS	10µm LS	15µm LS	Water
C150	-	-	71.43	-	-	-	-	-	28.57
C595	71.05	-	-	-	-	-	-	-	28.95
C1157	-	71.05	-	-	-	-	-	-	28.95
C150 + LS = C595	-	-	63.23	7.87	2.44	0.66	4.10	0.67	28.90
C150 + LS = C1157	-	-	63.23	7.87	0.00	7.87	0.00	0.00	28.90
C150 + LS = C150	-	-	63.23	7.87	0.00	0.49	3.80	3.58	28.90

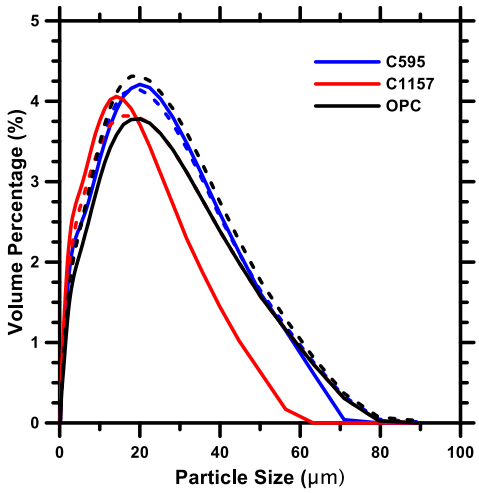

Figure 3-2 – Particle size distribution of OPC and interground limestone-cements (solid lines) as compared to blended mixes (dashed lines).

3.2.2 Experimental Parameters

3.2.2.1. Isothermal Calorimetry

The heat evolution of cement hydration was determined using isothermal calorimetry (TAM Air microcalorimeter 2700 Series) at constant temperature of 25 °C for 72 h. Samples were proportioned, and powders dry blended prior to adding water. To ensure accurate early age measurement and minimize the time to isothermal conditions, the blended powders and water were conditioned in an oven for 12 hours at 25°C. The pastes were then mixed using a kitchen mixer in accordance with ASTM C305 ("ASTM C305-13 Standard Practice for Mechanical Mixing of Hydraulic Cement Pastes and Mortars of Plastic Consistency" 2013, 305). Approximately 10g of sample was extracted immediately, placed in a sealed sample vial to minimize evaporation and placed in the isothermal calorimeter. The heat flow response, determined in watts per gram cement was extracted using the TA Instruments TAM Assistant software package.

3.2.2.2. Thermal Analysis (DTA/TGA)

Simultaneous thermal analysis (STA) simultaneously measures the mass loss and heat flow associated with heating a sample over a defined temperature range. Powders were dry blended prior to adding water, and then samples were mixed in accordance with ASTM C305. Sample sizes of approximately 100g were prepared and cured under sealed conditions at a temperature of 23±1 °C until the desired testing age. Samples were tested at ages of 1, 3, 7, 14, and 28 days. At the desired testing age, the sample was ground to a powder and approximately 80 mg of sample was placed in the instrument for analysis. Thermal analysis was completed using a Perkin Elmer STA 6000. Tests were carried out in a nitrogen

environment, at a gas flow rate of approximately 20 ml/s. Samples were heated from ambient to 995°C at a heating rate of 15°C/min. Heat flow curves resultant from thermal analysis of cementitious samples over this temperature range typically illustrate three distinct peaks: (i) loss of chemically bound water in C-S-H and ettringite, as well as decomposition of monocarbonate species, (ii) the deyhdroxylization of calcium hydroxide, and (iii) the decarbonation of calcium carbonate. Calcium hydroxide and calcium carbonate contents are determined using the stoichiometric relationships associated with their respective decomposition reactions combined with the mass loss associated with their representative heat flow peaks. The quantity of chemically bound water (w_n), a measure of the degree of hydration of the portland cement, is determined by subtracting the mass loss associated with calcium carbonate from the loss on ignition of a dried sample (the mass at 110 °C), normalized by the initial sample mass as presented in Equation 3-1:

$$w_n = \frac{LOI - m_{CaCO_3}}{(1 - w_{LS}) m_d} \qquad \text{(Eq. 3-1)}$$

Where LOI is the total mass loss of a dried sample, m_d is the initial mass of the dried sample, and m_{CaCO3} is the mass of calcium carbonate determined from the mass loss associated with decarbonation, and w_{LS} is the limestone mass fraction in the dried sample.

The consumed carbonate content is the percentage of carbonates consumed during the hydration process relative to the amount of carbonates initially present as determined from mixture proportioning, the loss on ignition of the portland cement powder as listed in Table 3-1 is assumed to be attributed primarily to pre-hydration and is thus neglected. It is calculated by the following relation:

$$(cCO_3)_t = \frac{(CaCO_3)_i - (CaCO_3)_t - (OPC)_t}{(CaCO_3)_i} \quad \text{(Eq. 3-2)}$$

Here $(CaCO_3)_i$ is the initial mass fraction of calcium carbonate present in the mix as determined from mixture proportions shown in Table 3-3, $(CaCO_3)_t$ is the carbonate content present in the sample at time t, calculated using the mass loss attributed to carbonate decomposition in the TGA sample and $(OPC)_t$ is the weight fraction of carbonates present in a sample at time t due to the carbonation of portland cement in the sample. This as determined from the carbonate peak in a plain OPC sample at time t and the equivalent weight fraction of carbonates is taken using the mixture proportions in Table 3-3.

3.2.2.3. Compressive Strength Testing

Compressive strength tests were carried out in accordance with ASTM C109 ("ASTM C109 / C109M - 12 Standard Test Method for Compressive Strength of Hydraulic Cement Mortars (Using 2-in. or [50-Mm] Cube Specimens)" 2012) on 50mm mortar cubes cured in a humid environment at >95% relative humidity and a temperature of 23±2°C. Mortar cubes were prepared with a volume fraction of sand of 50%, and mixed in accordance with ASTM C109. Cubes were cured for the first 24 hours covered to prevent ponding, after which the cubes were demolded and stored until the desired testing age in the environmental chamber. Cubes were tested at ages of 1, 3, 7, 28 and 56 days. A loading rate of approximately 900 N/s was applied up to the point of failure.

3.2.2.4. Mercury Intrusion Porosimetry

Samples were prepared by dry blending powders prior to adding water and then mixed using a handheld mixer for approximately two minutes. Samples of approximately 100g were cured

for 3 and 28 days under sealed conditions at a constant temperature of 23±1 °C. At the desired age of testing, the samples were crushed to an approximate size of 2mm, and then dried in an oven for 2 hours at 60 °C, as this method was found to produce consistent results in a previous study (Vance, Kirk 2014). Approximately 1g of material was selected and weighed using a high precision scale accurate to 0.1 mg. Testing was completed using a 0.5 cc cell in a Quantachrome Instruments PoreMaster mercury intrusion porosimeter to a maximum testing pressure of approximately 410 MPa. Mercury intrusion values were extracted from the Quantachrome Instruments PoreMaster software package and used for analysis. The relationship between pore diameter and intrusion pressure was determined internally in the Quantachrome software package using the Washburn equation (Washburn 1921a) (Equation 3-3), where d is the apparent diameter, P is the applied pressure, and γ is the surface tension of mercury and φ is the mercury contact angle which are assumed to be 0.480 N/m and 117° respectively during intrusion. The contact angle of 117° is typically used in oven dried cementitious specimens for the intrusion phase (Winslow and Diamond 1970; Bager and Sellevold 1975; R. Kumar and Bhattacharjee 2003a), and thus was selected for this study.

$$d = \frac{-4\gamma \cos\varphi}{p} \qquad \text{(Eq. 3-3)}$$

Recent studies have noted potential inaccuracies in the determination of the pore size distribution via mercury intrusion (Diamond 2000; Moro and Böhni 2002a). To investigate the pore structure of these materials, several additional parameters have been determined using the intruded volume data. The critical, or percolation, pore diameter is the pore

diameter corresponding to the highest rate of volume intrusion into the specimen, indicated by the first, largest peak on a plot of differential volume intruded versus pore diameter as calculated using the Eq. 3-3 (Cook and Hover 1999; Winslow and Diamond 1970). This term indicates the threshold pore size at which mercury percolates through surface pores into the sample and is thus thought to be a more direct indication of the permeability of a sample. The porosity of the sample was determined by dividing the total volume intruded by the determined sample volume.

Finally, the mercury volume retained after extrusion was determined using the methodology presented in (Zeng et al. 2012). In a cementitious specimen, the intrusion and subsequent extrusion of mercury results in a hysteresis, where the extrusion curve lies above the intrusion curve, indicating mercury is retained in the sample.

3.3. CEMHYD3D SIMULATION OF HYDRATION

The hydration of pastes was studied using CEMHYD3D 3.0 (D. P. Bentz 2005) in addition to the experiments performed. OPC was modeled using the available particle size distribution for C150, whereas interground cements were modeled as 2-phase materials with contribution from both OPC and Limestone. However, only the composite particle size distributions were available for the interground cements and the details of the intergrinding process were unknown. There have been attempts at determining the individual PSD's of components from the composite distribution experimentally [insert citations], however the accuracy of those methods is questionable. For the current study, it was found suitable to deduce the particle size distribution of limestone in C595 by making the assumption that cement in the composite distribution is the same as C150, which is not exactly true since

cement being harder than limestone should be ground coarser in the intergrinding process. However, considering that there is only 12.68 % of limestone in the interground cement and the median sizes of C150 and C595 are not that dissimilar, this occurs as a reasonable approximation. The limestone particle size distribution in C595 was then determined by calculating the median size of limestone using the rule of mixtures and constructing a normal distribution about the median size. This concept cannot be applied to C1157 where the median particle size is very different as compared to C150. It is expected that limestone will be ground much finer in case of C1157 with a median size much lower compared to C150. An interesting observation made in this regard was that the percentage difference between the finer portion of the differential curve for the particle size distribution of C1157 and C150 was the same as the percentage of limestone in the composite distribution of C1157. This difference was normalized to get the individual PSD for limestone and rest of it was accounted as distribution for the cement component. Getting the exact particle size distribution of limestone from the composite interground distribution theoretically is something to be thought of in future research.

After obtaining individual PSD's of limestone and cement, the distributions were discretized to get the number of particles in a representative volume element of size 100μ using a packing fraction calculated from the water-cement ratio of 1.26 by volume. Bogue's calculations were used to get the volume fraction of individual phases in the parent cement. The hydration was simulated for 100 hours under isothermal conditions in a sealed environment. The cycles to time conversion factor of 0.0035 hours/cycles^2 was used to obtain results in real time.

The results for heat of hydration, degree of hydration and porosity are presented later in Section 3.4. CEMHYD3D was modified to calculate the mean spacing between nearest neighbors to better understand the interactions among the cement and the limestone particles. We define nearest neighbor as the particle with Table 3-4 presents a summary of the results obtained.

Table 3-4: Contact percentage between nearest neighbors. C-C indicates cement-cement interaction, L-L is the % contact between limestone particles and C-L is the % contact between cement-limestone particles in the mixtures.

Mix ID	Average Centroidal Distance (in μm)	C-C	L-L	C-L
C150	6.507 / 5.594	93.02	-	-
C595	5.895/5.609	23.49	23.25	48.37
C1157	6.473/5.567	10.93	38.98	46.44
C150 + LS = C150	6.437/5.711	67.18	1.85	22.35
C150 + LS = C595	6.318/6.748	58.20	4.14	32.22
C150 + LS = C1157	6.299/6.732	48.88	6.55	36.42

The contact percentage between nearest neighbors is useful to get a perspective on the degree of reaction and the rate of hydration of the mixture. Since limestone is known to accelerate hydration of cement, the cement-limestone interaction is vital to understanding

the nucleation process in cement hydration. This is highly dependent on the particle size distribution of both limestone and cement in the mixture. It is noted from Table 3-4 that the cement-limestone and limestone-limestone interactions increase as the median particle size of the mix decreases. The proximity between cement and limestone particles leads to increased hydration rates, since limestone is known to accelerate the hydration of cement. The findings from Table 3-4 here are substantiated in detail in section 3.4.1.

Figure 3-3 shows the initial microstructure of C150 at 100 cycles of hydration created using CEMHYD3D and Figure 3-4 shows three sectioned images of the center slice of C150 after 100, 300 and 1000 cycles of hydration. The size of the microstructure is 100μm. The sectioned images show the evolution of hydration process as a function of time. The black area refers to the voids and the grey part refers to the products being formed as a result of the hydration process. The cement phases C_3S, C_2S, C_3A and C_4AF are indicated in white, maroon, purple and turquoise respectively, whereas blue and violet colors indicate gypsum content in form of hemihydrate and di-hydrate in the cement.

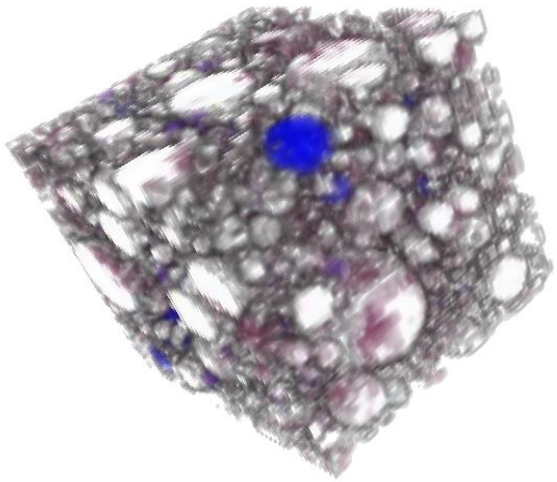

Figure 3-3: 3D microstructure of C150 at 100 cycles of hydration created using CEMHYD3D module.

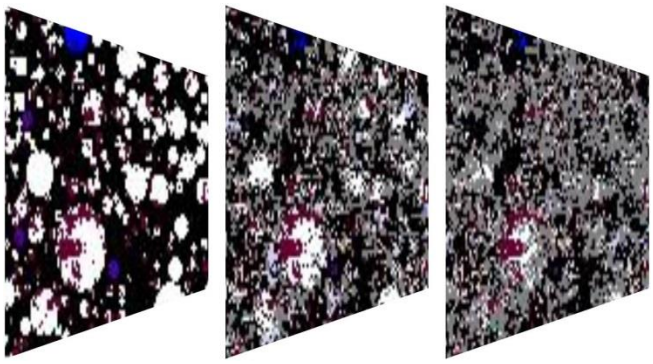

Figure 3-4: Evolution of hydration in C150 cement as a function of number of cycles. From the left, images correspond to 100, 300 and 1000 cycles of hydration respectively.

3.4. RESULTS AND DISCUSSIONS

3.4.1 Influence of limestone addition on early age hydration

The early age hydration kinetics was measured using isothermal calorimetry at 25°C using procedures discussed previously. The heat flow and the cumulative heat curves obtained from calorimetry are shown in Figures 3-5 and 3-6 respectively. The peaks in the heat flow curves correspond to the formation of hydration products. A typical heat flow curve can be characterized into four main phases. The first phase is the dissolution phase related to the dissolution of portland cement grains characterized by the initial peak and which occurs in the first few minutes after addition of water. The second phase is the induction period with low rate of heat evolution. This period occurs in the first few hours after mixing. The third period is characterized by the rapid chemical reaction of C_3S to form C-S-H and CH which

leads to high rate of heat evolution and final setting of cement. This period forms the main hydration peak and is called the acceleration stage. A secondary peak or shoulder on the main hydration is often visible after the C_3S peak and is attributed to C_3A hydration. The fourth period is the diffusion-controlled deceleration stage.

From Figures 3-5 and 3-6, it is immediately evident that all limestone replacement cements resulted in an acceleration effect, as illustrated by a steeper acceleration phase and a higher main hydration peak. In the limestone blended system which is PSD matched to OPC (Figure 3-5(a)), the influence of limestone in portland cement systems on heat evolution can be discerned. The height of the main hydration peak and the slope of the acceleration phase is increased. As limestone replaces portland cement, the quantity of OPC in the system is effectively diluted, which in turn provides an increased surface area per unit of reactive portland cement. Further, calcium carbonate chemically reacts with the C_3A phase in cement to form monocarboaluminates (V. L. Bonavetti, Rahhal, and Irassar 2001). These effects result in an acceleration of portland cement hydration.

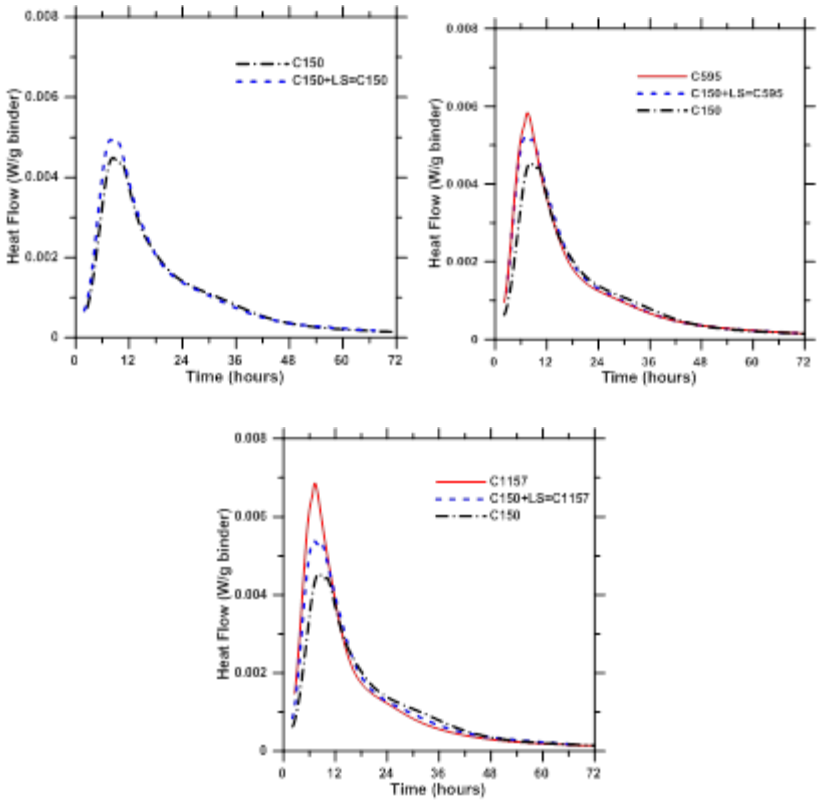

Figure 3-5 – Heat evolution of blended and interground Portland limestone cements, plotted as W/g binder.

It is additionally noted from Figure 3-5 that the acceleration effect is more pronounced in interground versus blended cements, most significantly for the finest interground mix, C1157. It has been noted in the literature, that there is a significant influence of fineness on the heat of hydration of both cement and portland limestone cements. Increased fineness of portland cement results in acceleration of hydration primarily due to the increased surface area of cement particles (Dale P. Bentz, Sant, and Weiss 2008). The influence of limestone on cement hydration has similarly been shown to be dependent on the limestone fineness. Fine limestone increases the surface area and seed locations available for hydration product

nucleation, and as coarseness of the limestone is increased to that of OPC, the surface area effects are minimal, resulting in negligible change in hydration kinetics (Vance, Aguayo, et al. 2013; Soroka and Setter 1977; Thomas, Jennings, and Chen 2009). Further, fine limestone has been shown to be more reactive, while coarser limestone is less reactive and acts more as a filler material (Vance, Aguayo, et al. 2013). When limestone is interground with portland cement clinker, the softer limestone phase is ground more readily than the harder portland cement clinker, resulting in a finer limestone phase. The increased reactivity in interground PLCs as compared to blended PLCs and OPC can thus be explained as follows. The increased quantity of limestone fines significantly increases both the reactivity of the limestone and the surface area available for hydration product nucleation. In particular, increased limestone fines enhance the interactions with the C_3A phase significantly sharpening the main hydration peak, while also decreasing the thickness of the initial hydration product shell forming on particles, enhancing C_3S reactivity (Thomas, Jennings, and Chen 2009). The interaction with C_3A can be confirmed by considering the steeper main hydration peak as compared to the blended mixes or OPC. The enhanced C_3A activity can be confirmed by noting the sharper main hydration peak, as C_3A hydration has been shown to have a significantly steeper acceleration and deceleration phases (Minard et al. 2007).

It is also noted from Figure 3-5 that the shape of the main hydration peak is different when the limestone is interground versus when it has been blended. Blended limestone mixes result in a more traditional heat evolution curve, with a first initial peak corresponding to C_3S hydration, and a second peak or shoulder corresponding to aluminate phase acceleration after depletion of sulfates resulting in secondary ettringite formation (Bullard et al. 2011;

Gallucci, Mathur, and Scrivener 2010). Whereas interground samples show a single sharp vertical peak which most likely corresponds to the C_3A phase. Upon closer examination, it is noted that there is a shoulder on the left side of the main hydration peak in the interground samples. This shoulder is likely the main silicate peak. The presence of an enhanced C_3A peak can be further verified by considering the fact that a well sulfated C_3A phase is known to have a distinctly sharp peak. As the blended cements use the same portland cement as the parent cement as the interground cements, the enhanced C_3A peak can only be attributed to the presence of limestone. The limestone phase resultant from intergrinding is likely to have enhanced fines, which results in enhanced early age hydration, perhaps more quickly depleting the gypsum present in the portland cement, enhancing the C_3A peak. The reactivity of limestone in these systems will be further explored in the proceeding section.

Comparing the blended samples, it is noted that the OPC matched blend has the lowest main hydration peak and the C1157 matched blend had the highest main hydration peak. All blended samples show two distinctive peaks on the main hydration peak. As noted in Table 3-3, the fineness of the limestone replacing cement matches this trend. The C1157 PSD matched blend has the largest quantity of limestone finer than the median particle size of portland cement (0.7 and 3 μm) while the C150 matched mix had the lowest quantity of these fines. As discussed previously, the presence of limestone fines accelerates the hydration reaction by providing nucleation sites for hydration products, resulting in accelerated hydration.

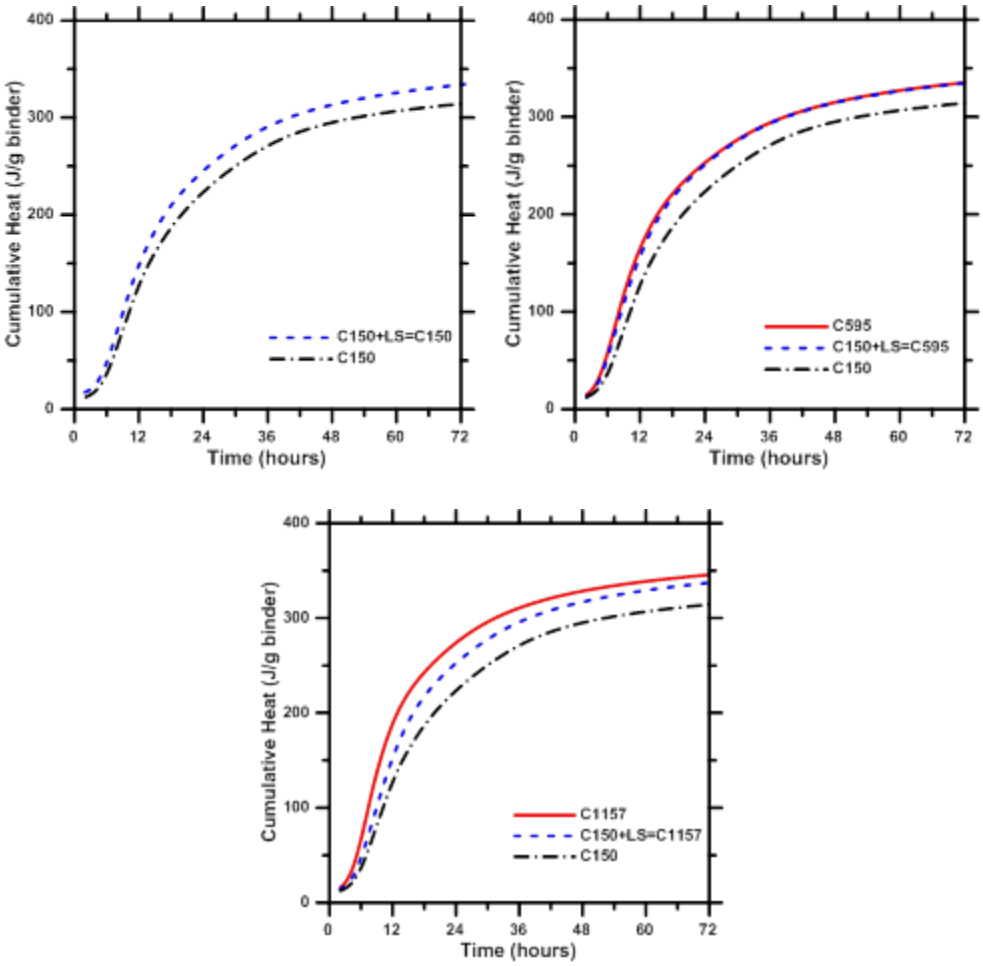

Figure 3-6 – Cumulative heat curves for blended and interground portland limestone cements, plotted in W/g cement.

Cumulative heat curves per gram of binder are presented in Figure 3-6 with OPC provided for comparison. It is evident from all the plots that OPC has the lowest cumulative heat of evolution per gram of binder among all the mixes considered up to 72 hours. It is also noted that blended cements have higher evolution of heat per gram of binder as compared to OPC, and the interground cements are further higher than the blends. As mentioned earlier,

this is due to the finer limestone content present in the size matched blends and the interground cements which accelerate the early hydration process. In case of C595 and its size matched blend, although there is a distinct difference in the heat flow peak in Figure 4, the cumulative heat plots look similar, which is because the peak is much sharper for C595 and broader for its size matched blend. Cumulative heat flow indicates the degree of hydration of the mixes. The higher cumulative heat values of the interground cements as compared to their corresponding size-matched blends are indicative of the fact that at early ages interground cements have a higher degree of hydration as compared to their blended counterparts at early ages, however at later ages it is likely that the degree of hydration of all limestone replacement systems investigated here would be equivalent.

Figure 3-7 illustrates the comparison of cumulative heat flow curves between experimental data obtained from the calorimetric measurements and those predicted by the CEMHYD3D hydration model. The subscript 'b' in Figure 3-7 (b) refers to the blended mix corresponding to the parent mix.

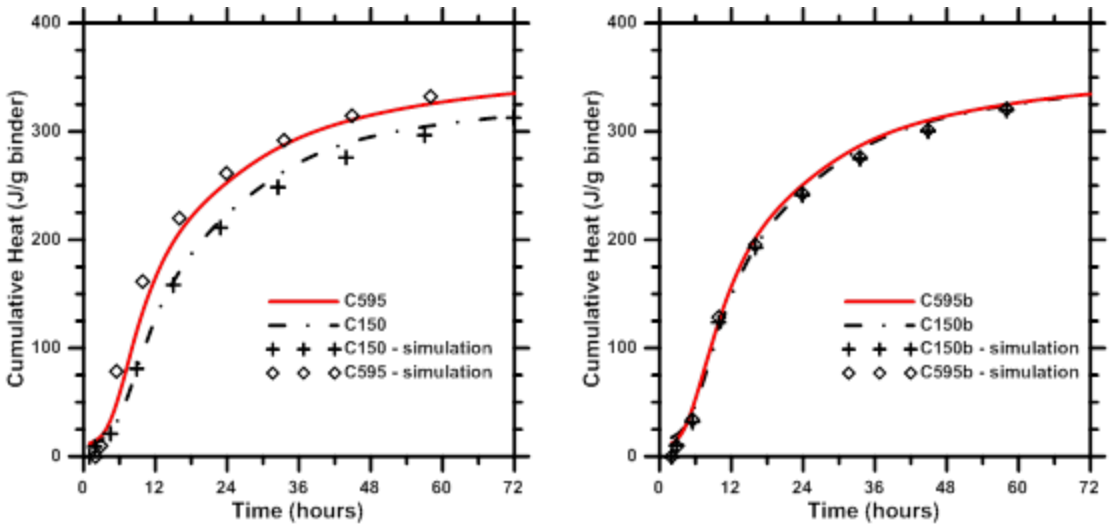

Figure 3-7: Comparison of cumulative heat flow curves between experimental data and CEMHYD3D simulation data for a) Interground cements and OPC, and b) Blended mixes.

It can be observed from figure 3-7 that the experimental values of cumulative heat flow are in good agreement with the predicted values from the hydration model for both the interground and the blended mixes. This reaffirms the reliability of CEMHYD3D hydration model in reference to the incorporation of limestone in the cement mixes. It also confirms our initial assumption about the distribution of cement and limestone as stated in section 3.3.

3.4.2 Analysis of hydration product formation through thermal analysis

The progress of the hydration reaction was investigated using thermal analysis techniques as described in Section 3.2. The resultant mass fraction remaining, and heat flow curves are presented in Figures 3-8 and 3-9. The mass fraction remaining was normalized by the dry mass, as defined in this study as the mass of the sample at 110°C. There are several distinctions that can be noted from these curves: (i) all samples show pronounced peaks at about 130 °C and 450 °C, heat flow peaks corresponding to evaporable water, C-S-H, and ettringite and the dehydroxylization of calcium hydroxide and (ii) all limestone blended samples show a peak at approximately 750 °C corresponding to the decarbonation of calcium carbonate.

At three days (Figure 3-8), it is noted that the mass loss curves associated with C-S-H, ettringite, and evaporable water are equivalent for both the OPC and interground mixes. This indicates that despite the lower quantity of portland cement present in the interground

mixes, an equivalent quantity of hydration products is forming, confirming the analysis of the heat evolution curves above with respect to acceleration of the hydration reactions. The blended samples show a more significant diversion from the OPC mixture at early age, likely attributed to the more limited reactivity of these samples as discussed previously.

At later ages (Figure 3-9) a more significant divergence of early age weight loss is noted in the interground limestone mixes. This is likely attributed to the fact that the early age hydration acceleration associated with the fine limestone presence is mitigated by the sample age. Additionally, it is noted that all blends show very similar mass loss profiles at the later ages.

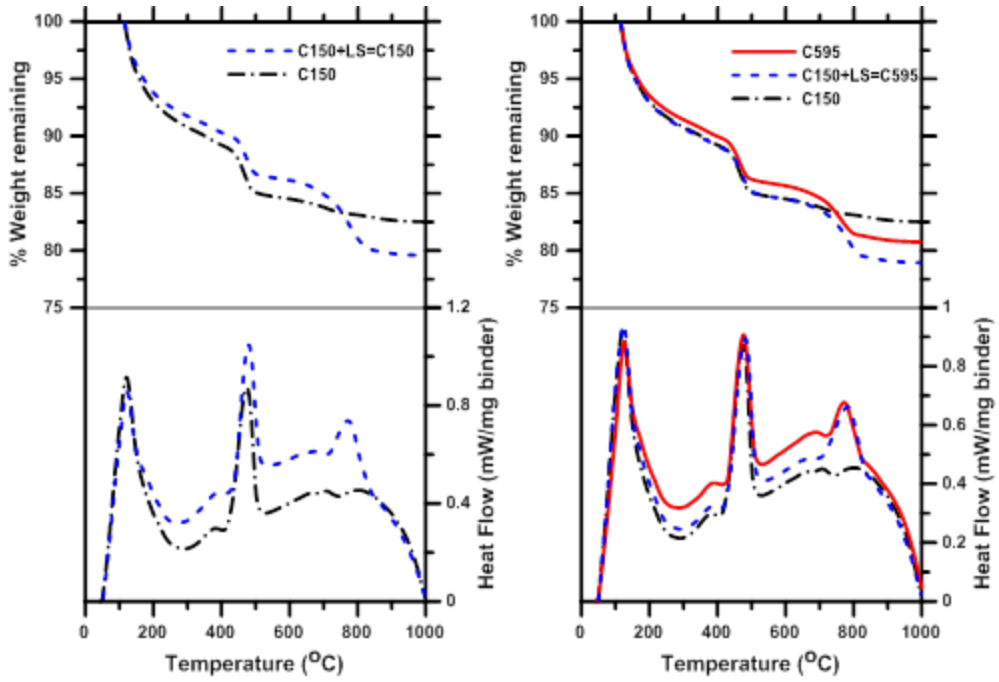

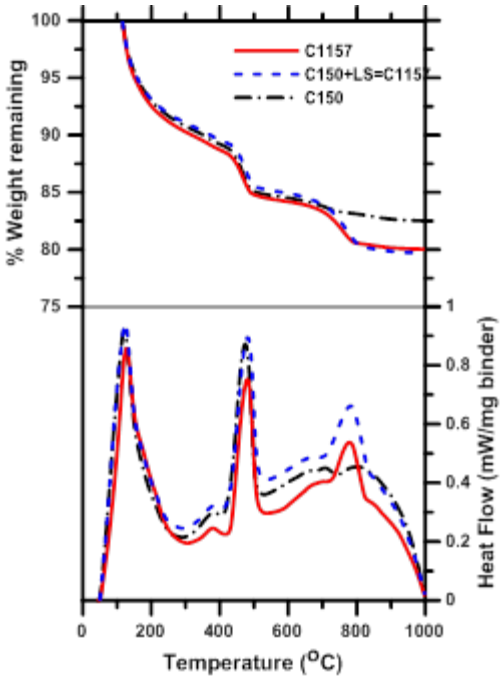

Figure 3-8: Results of thermal analysis of samples at 3 days, mass % remaining and heat flow.

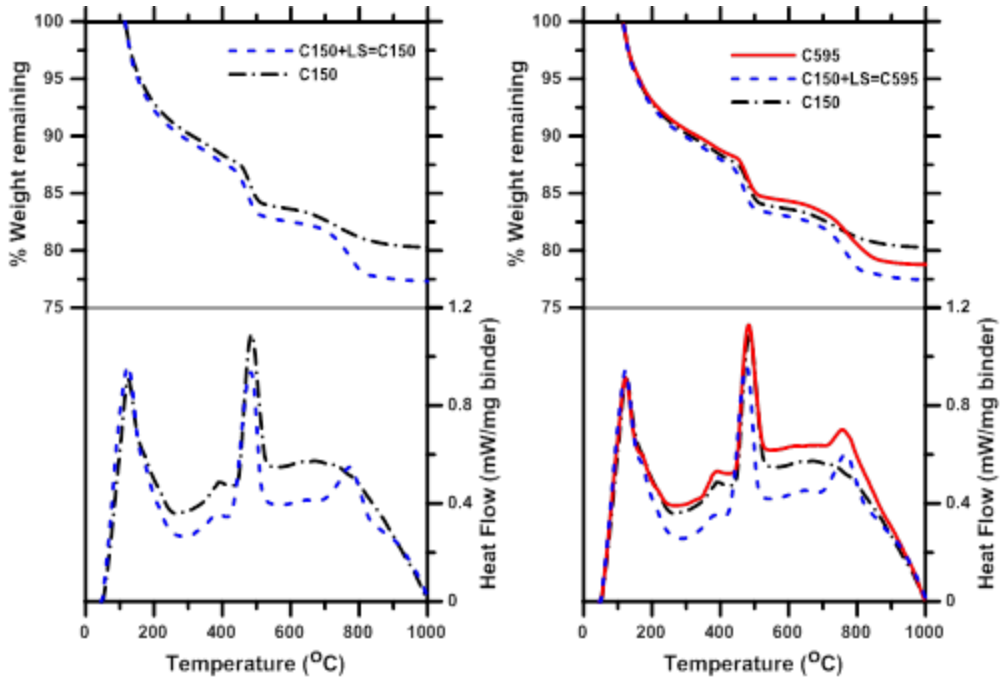

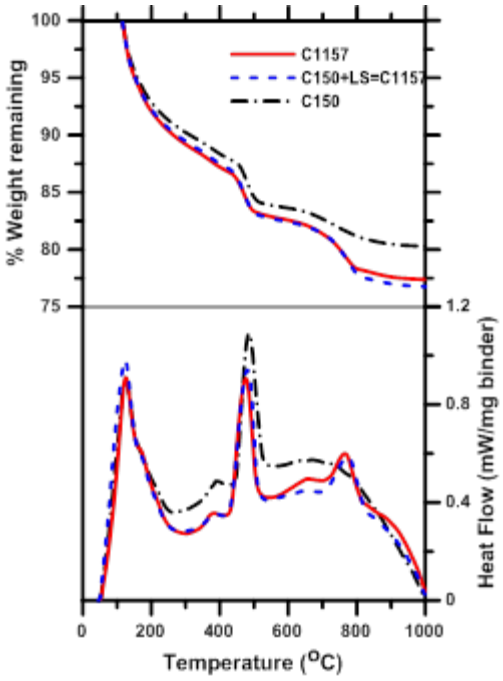

Figure 3-9: Results of thermal analysis of samples at 28 days, mass remaining and heat flow.

Figure 3-10 illustrates the non-evaporable water content and calcium hydroxide content at 1, 7 and 28 days, and the consumed calcium carbonate content at 7 and 28 days. The non-evaporable water content is a measure of the degree of hydration of the sample, determined as presented in Section 3.2. The calcium hydroxide and calcium carbonate contents were calculated based on the mass losses associated with the heat flow peaks as presented in Figures 3-8 and 3-9 and determined as discussed in Section 3.2.

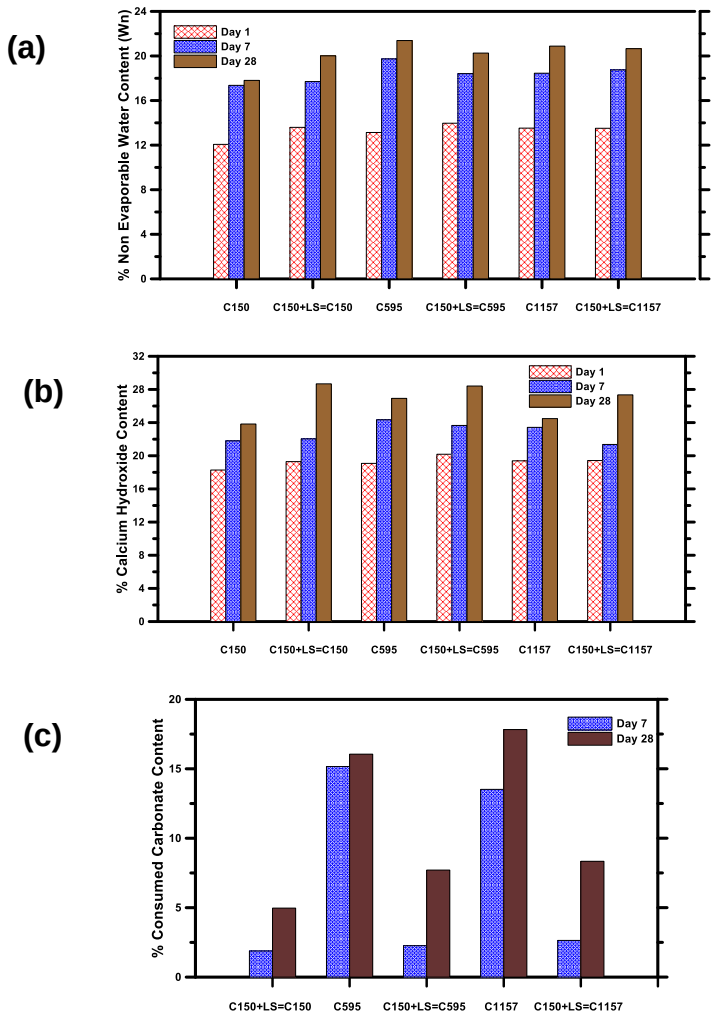

Figure 3-10 – Relative comparison of a) non-evaporable water content, b) calcium hydroxide content, and c) consumed calcium carbonate content at 1, 7 and 28 days.

For all mixes, the bound water and CH content increases with time, as would be expected as the hydration reaction progresses in the diffusion-controlled regime. The consumed $CaCO_3$ content shows a steady increase, indicating that calcium carbonate continues to participate to some extent in the hydration reactions. The bound water content is higher in the interground cements than all others tested as part of this study. This indicates an enhanced

degree of hydration in the interground cements. At early ages, this is attributed to fine limestone providing a nucleation site for hydration products, which accelerates the hydration. Further, the presence of limestone as a nucleation site in hydration decreases the thickness of the hydration shell forming on the portland cement grains, allowing for easier diffusion of water through the hydration shell further enhancing the degree of hydration. However, at later ages, the increase in the bound water content and consequently increase in the degree of hydration is a result of the higher effective water-to-cement ratio due to limestone replacement.

In case of CH content, at one day, the calcium hydroxide contents are roughly equivalent, however between one and 7 days the interground samples are seen to have a more significant increase in CH as compared to the other mixes, with the opposite effect noted between 7 and 28 days. This is likely attributed to the occurrence of two competing effects, firstly dilution due to the presence of limestone which leads to decrease in the amount of OPC present for hydration and secondly, the increase in effective water cement ratio in the mixes due to the consumption of calcium carbonate in the hydration reaction, which enhances the overall consumption of the cement phase thereby increasing the CH content. Inclusion of limestone enhances reactivity but also dilutes the OPC quantity. Further interground limestone mixes have a coarser phase of OPC as compared to the blends, thus the diffusion-controlled phase of hydration is slower for those than the blended cements. It is clearly evident from Figure 3-10(c) that the consumed carbonate content is highest among the interground cements, and is significantly higher than the size matched blends. This is due to the higher amount of limestone fines present in the interground cements due

to the grinding process with portland cement clinker. The increased consumption of limestone in the interground cements also results in higher strengths at all ages as compared to their blended counterparts. It is found that among the blends, the trend of carbonate consumption follows the distribution of limestone added to establish the size matching in these blends. The C1157 blend corresponding to the addition of the finest limestone content among all the size matched blends shows the maximum consumption of carbonates, whereas C150 blend having the largest fraction of coarse limestone shows the least consumption of carbonates relative to the other two blends. These results further confirm the discussions of limestone reactivity presented in Section 3.4.1.

3.4.3 Compressive Strength Development

Compressive strengths of 50mm mortar cubes at ages of 1, 3, 7, 28 and 56 days were determined as presented in Section 3.2.2. Figure 3-11 shows the development of compressive strength over these ages for comparing interground cements to their limestone blended counterparts.

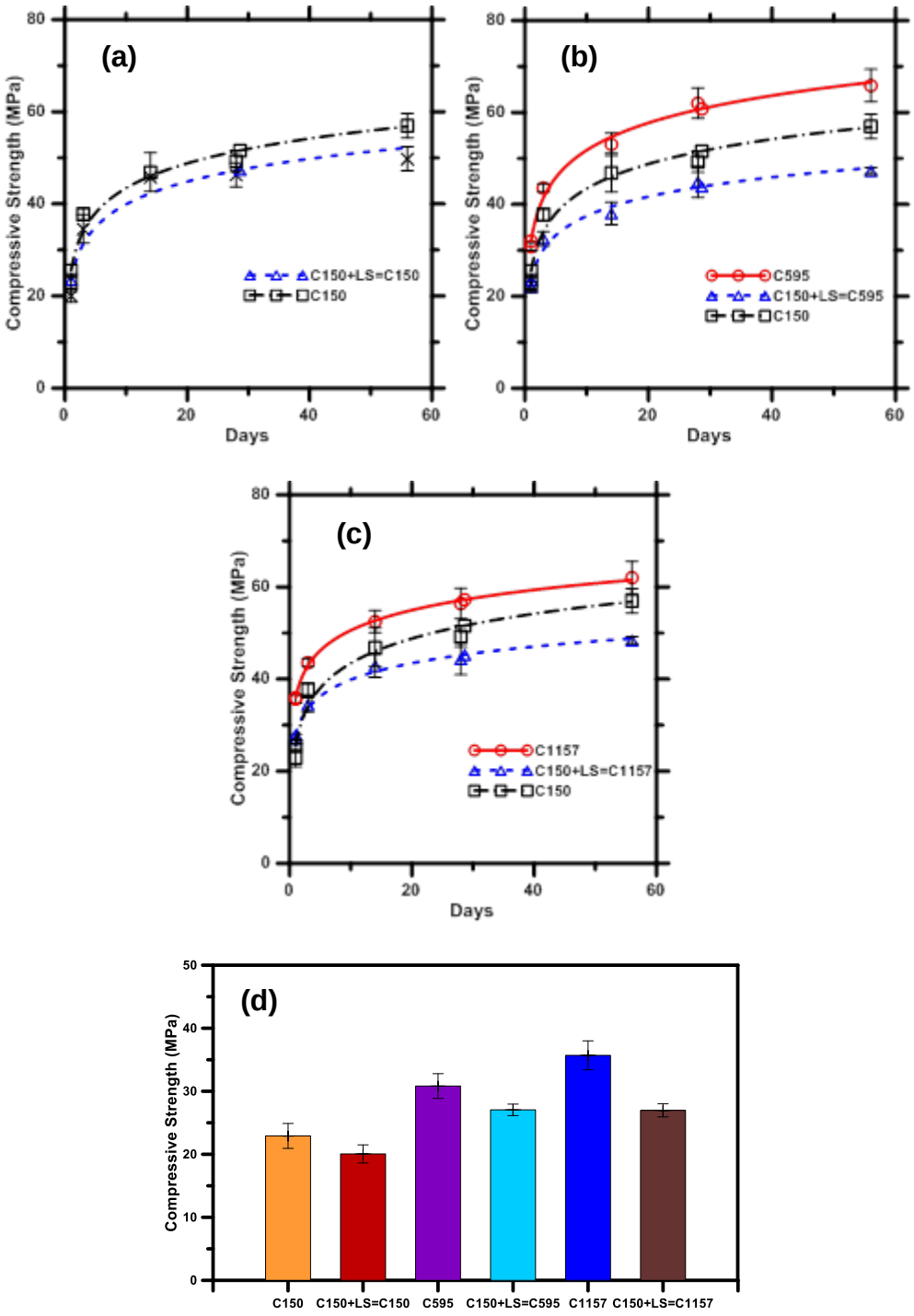

Figure 3-11 – (a-c) Compressive strength development of mortar specimens tested, and (d) compressive strengths at 1 day.

Immediately noted from Figure 3-11 is the fact that OPC has greater strengths at later ages than its PSD matched limestone blended counterpart. This result is consistent with what has been presented in the literature (Vance, Kumar, et al. 2013), where the inclusion of the generally non-reactive softer limestone phase results in an increased effective water-to-powder ratio, decreases the quantity of hydration products, increases porosity, and decreases strength. On the other hand, it is noted that the interground limestone mixes result in higher strengths at all ages than the both the PSD matched blended mixes and the OPC mix. This shift in behavior even with the same quantity of limestone present in the mixtures is likely attributed to the fineness effect of the interground limestone, where the limestone present in the interground system is likely to be finer than that which has been included in the blended system. It has been shown that the limestone with increased fineness results in enhanced mechanical properties due to the increased packing associated with the fine limestone and enhanced reactivity (Kirk Vance, Neithalath, and Sant 2013).

At early ages (Figure 3-11(d)), all PLC mixtures except the OPC particle size distribution matched mixture are shown to have increased strengths as compared to the OPC mixture. These results are consistent with the heat evolution data presented in Figures 4 and 5. The interground mixtures show the highest early age strength of all mixtures, with the finest interground mix, C1157 having the highest strength overall. This effect can be understood due to increased participation of finer limestone content in reactions with C_3A and acting as nucleation site for the formation of hydration products. Upon examination of the cumulative heat curves, the trend in heat evolution at 24 hours coincides with the

compressive strength data at early ages. The interground limestone cements show significantly accelerated strength development as compared to the limestone blends or OPC, leading to higher early age strengths. The accelerated hydration reaction results in more significant formation of hydration products. The blended cements generated to PSD match the C1157 and C595 interground PLCs similarly have an enhanced early age hydration, leading to higher early age strengths as compared to OPC. The diminished strength at early ages for the PSD matched OPC limestone blend despite accelerated hydration as indicated in Figure 3-10 is likely due to the coarseness of the limestone replacing the OPC combined with the dilution of OPC due to limestone replacement. Though hydration is accelerated, the presence of a soft filler which is not participating extensively in the hydration reactions would lead to a strength reduction at all ages.

3.4.4 Influence of limestone addition on pore structure

The influence of limestone on the pore structure in these systems was determined using mercury intrusion porosimetry and the methodology presented in Section 3.2.2.4. The resultant intrusion curves at 3 and 28 days are presented in Figure 3-12. As previously noted, pore size distribution curves determined using mercury intrusion porosimetry have been shown to be prone to error due to the assumptions required in the Washburn equation, thus these figures are presented primarily for reference. However, it is noted that the pore structure development is generally as would be expected. At the later age investigation, the pore volume intruded decreases, and the pore structure becomes more refined. This is due to the progress of the hydration reaction, as more hydration products are incorporated into the paste and the degree of hydration increases, the pore volume decreases, and the pore

structure becomes more refined. Further, from Figure 3-12(a), it is noted that OPC has a lower intruded volume than the size matched limestone replacement cement at both ages tested. This is likely due to the decrease in volume of material which participates in the hydration reactions as well as an increase in effective water-to-cement ratio. The increase in the effective water-to-cement ratio would increase the pore solution as well as decrease the relative quantity of hydration products, resulting in an increase in porosity. From Figures 3-12(b) and (c) it is noted that the blended limestone sample has a higher intruded volume at all ages and diameters than the interground limestone. It was previously noted that limestone is a softer material than portland cement clinker (R. Kumar and Bhattacharjee 2003a), thus as limestone is interground with cement the limestone will achieve a finer particle size distribution than the clinker. Thus, though the replacement volume is the same for both interground and blended limestone cements, the finer limestone present in the interground PLCs accelerate the hydration reaction more effectively (Kirk Vance, Neithalath, and Sant 2013) in increase the particle packing in the system, leading to a decrease in porosity as compared to the blended system where the limestone particle size distribution matches that of portland cement.

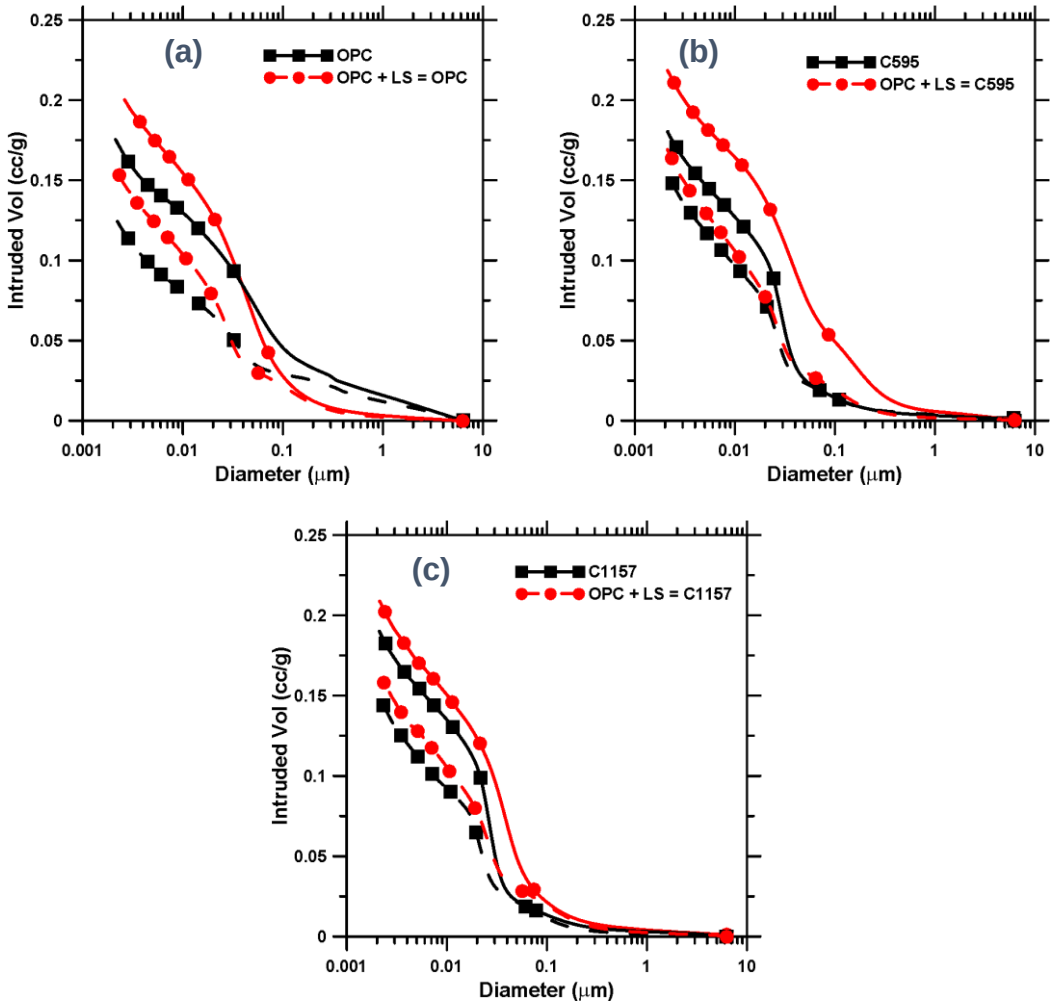

Figure 3-12 – Intrusion curves comparing interground to blended PLCs, solid lines are 3 days, dashed are 28 days for: (a) OPC, (b) C595, and (c) C1157

To explore the influences of limestone on the pore structure of these systems, the porosity and critical pore diameters were determined as presented in Section 3.2.2.4. The results of this analysis are presented in Figure 3-13. Several key aspects of these samples are noted from the upper panel of this figure: (i) the OPC mixture has a lower porosity than all other mixtures at all ages, (ii) the interground mixes have lower porosities than their blended

counterpart at all ages, and (iii) all mixes show approximately equivalent reduction in porosity between 3 and 28 days of about 25%. The overall lower porosity for OPC compared to any of the PLC mixtures is attributed to the effects described above, the limestone filler raises the effective water-to-cement ratio resulting in a greater porosity within the cement paste. The lower porosity for interground samples as compared to blends is similarly attributed to the same effects as above. This analysis is supported by the bound water quantities as shown in Figure 3-10. The interground samples are noted to have higher bound water contents than the size matched blended samples, indicating an increase in reaction product formation, which would decrease the porosity of the sample.

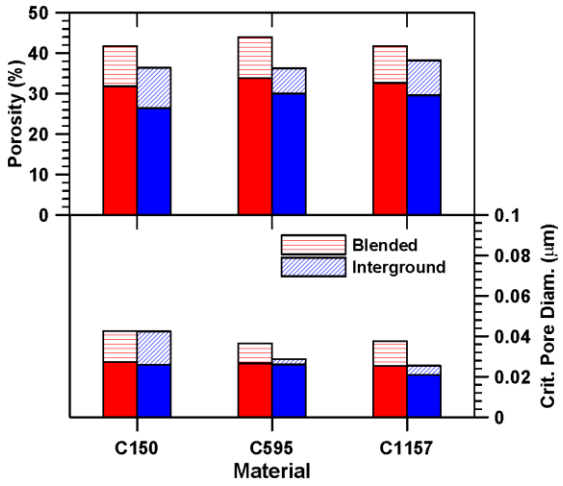

Figure 3-13 – Comparison of porosity and critical pore diameter for PLCs investigated, patterned fill is at 3 days, solid is at 28 days.

From the lower panel in Figure 3-13, it is noted that the critical pore diameter is highest for the OPC and size matched limestone OPC blend samples at all ages, and lowest for the finer interground sample (C1157). It can also be seen from the lower panel in Figure 3-13 that the

inclusion of size matched limestone has little influence on the critical pore diameter in the OPC system at early ages and results in only a slight increase at later ages. Further it is noted that the interground samples have a significantly lower critical pore diameter as compared to the blended samples at early ages, however at later ages the difference is seen to be much less significant. As noted previously, the critical pore diameter is the diameter at which the intrusion rate of mercury into the sample is the highest, represented the threshold diameter when mercury percolates through the sample. Thus, it is thought to be representative of the permeability of the sample, where a lower critical pore diameter would indicate a lower permeability, a factor that is critical to the durability of concrete due to ion permeability and the resultant corrosion. The lower critical pore diameter in interground samples as compared to their blended counterpart is likely due to the relative fineness of the limestone in the sample. The increased fineness in interground samples accelerates hydration and more effectively acts as a nucleation site for hydration products (Thomas, Jennings, and Chen 2009). These two factors result in a more refined pore structure, particularly at early ages, resulting in a decrease in the critical pore diameter. At later ages, the effect of limestone fineness is diminished as hydration proceeds, and the critical pore diameter becomes equivalent for all samples except the interground C1157 sample. This discrepancy is likely due to the difference in fineness between the size matched blended sample and interground sample as noted in Figure 3-2, where the interground sample is noted to have an increased fineness as compared to the blended sample. This increased fineness results in a comparatively more reactive sample, as again illustrated by the bound water contents in Figure 3-10, resulting in a more refined pore structure at both early and later ages.

Studies have noted a strong relationship between the strength and porosity of cementitious samples, a similar relationship is noted in this study and is presented in Figure 3-14. A reduction in porosity is seen to result in a corresponding increase in strength. The increased scatter noted in this figure as opposed to that typically presented in strength-porosity relationships is likely due to the inclusion of soft limestone in the sample, a majority of which remains unreacted in the sample even at later ages as noted in Figure 3-10 and (Vance, Aguayo, et al. 2013). Further, it is noted that the sample with the lowest porosity, OPC, has lower strength than the interground blends at both early and later ages, despite the fact that they have a higher porosity. This effect is likely due to the interground blends having a greater pore volume, but a pore structure that is more refined due to the inclusion of a limestone that is finer than OPC as discussed above, enhancing hydration product nucleation and accelerating the hydration reactions, refining the pore structure while the effective water-to-powder ratio concurrently increases porosity.

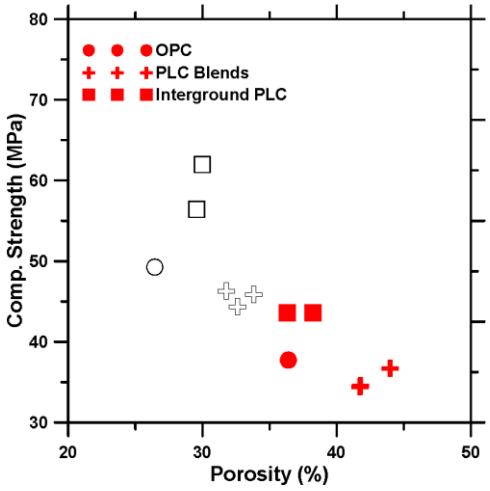

Figure 3-14 – Strength versus porosity relationships at 3 days (solid fill) and 28 days (no fill).

3.5. CONCLUSIONS

This chapter explores the differences in hydration, reaction product formation, and microstructural features in interground and blended portland limestone cements. The results of this study indicate several key features of these systems.

- The influence of limestone is explored using PSD-matched limestone to replace portland cement, enhanced early age hydration, decreased compressive strength, and increased porosity is noted as limestone replaces portland cement.
- The size distribution of limestone replacing portland cement is shown to significantly influence reaction kinetics, pore structure, strength, and carbonate reactivity. The finer limestone phase present in interground cements thereby more significantly increase reaction kinetics than size match blended PLCs. This in turn indicates more beneficial effects with respect to hydration product formation, carbonate reactivity, and compressive strength.
- Interground limestone is seen to have a more refined pore structure than a size match blended limestone, as indicated by a relatively lower porosity, decrease in critical pore diameter, and decrease in volume intruded in mercury intrusion measurements.
- Development of blended PLC systems with comparable properties to interground PLCs will require the use of limestone significantly finer than the parent OPC.

CHAPTER 4[3]

A METHODOLOGY TO EXTRACT THE COMPONENT SIZE DISTRIBUTIONS IN INTERGROUND COMPOSITE (LIMESTONE) CEMENTS

4.1. INTRODUCTION

The use of fine limestone as partial cement replacement is a topic of great interest since it improves the sustainability of portland cement-based concrete and provides comparable properties to that of conventional OPC concrete (Matschei, Lothenbach, and Glasser 2007c; V. Bonavetti et al. 2003). Two methodologies are commonly used to incorporate fine limestone in cementitious systems: (i) intergrinding the limestone with the portland cement clinker to produce portland-limestone cements (PLCs), or (ii) blending OPC with limestone powder in the concrete production process. Intergrinding of portland cement clinker with limestone results in a finer limestone phase in the composite system due to the fact that limestone is a softer material than the clinker. Blending, on the other hand, would result in a limestone size distribution that can be controlled more directly by the cement or concrete producer. ASTM C595 cements, along with cements conforming to CSA A 3000 (Canada), AASHTO M 240 and EN 197-1 (Europe) among others are permitted to contain 5-15% (by mass) of fine limestone. In the U.S., cements conforming to ASTM C1157 (a performance based cement specification, as compared to ASTM C595 and C150 which prescribe limits on chemical composition) have also been manufactured with 5-15% of limestone.

---

[3] This chapter is derived from the publication: Arora, A., Vance, K., Sant, G., & Neithalath, N. (2016). A methodology to extract the component size distributions in interground composite (limestone) cements. Construction and Building Materials, 121, 328-337 (A. Arora et al. 2016).

Several studies have investigated the influence of fine limestone as a partial cement replacement material, blended or interground with OPC (Menéndez, Bonavetti, and Irassar 2003; Ingram and Daugherty 1991). Limestone has also been used in conjunction with other cement replacement materials such as fly ash, slag, or metakaolin (Aashay Arora, Sant, and Neithalath 2016; Tsivilis et al. 2000; Vance, Aguayo, et al. 2013; De Weerdt, Kjellsen, et al. 2011; Zelić, Jozić, and Krpan-Lisica 2009). The early age hydration response, reaction product formation, rheology, strength development, and durability of the binary and ternary systems containing limestone have been reported in detail. A number of studies have focused on the use of limestone which is finer than the cement it replaces, as this has been shown to accelerate hydration reactions (Vance, Aguayo, et al. 2013; Darweesh 2004), increase the packing of particles (Hawkins, Tennis, and Detwiler, n.d.), and minimize the strength loss associated with limestone (Vance, Aguayo, et al. 2013). The formation of carboaluminates in limestone bearing systems that reduces the overall pore volume has been reported in (Matschei, Lothenbach, and Glasser 2007c; De Weerdt, Haha, et al. 2011). A number of studies on the properties of interground limestone cements have also been reported (Sezera, Çopuroglu, and Ramyar 2010; Irassar et al. 2011; Barcelo et al. 2013).

It is well known that the particle size distribution (PSD) of the cement (OPC or PLC) influences the early-age hydration, reaction product formation and consequently the performance (Dale P. Bentz et al. 1999; A. Wang, Zhang, and Zhang 1997). This chapter evaluates whether property equivalence between interground PLCs and OPC-limestone blends can be attained provided the blend is designed to have a similar solids surface area as that of the PLC and is constituted using the same OPC clinker that made up the PLC. This

is of significance for limestone suppliers interested in blending limestone with the cements they use because it is the ASTM C150 or equivalent cement that generally is available to them. Furthermore, a methodology to extract the PSDs of cement and limestone in an interground PLC is proposed, which will help to choose the parent OPC and limestone particle sizes that permit property equivalence. This methodology is generic enough so as to be implemented to extract the size classes of different particles in a wide array of powder mixtures such as in pharmaceutical, chemical, and food industries.

4.2. EXPERIMENTAL PROGRAM

4.2.1 Materials

The materials used in this study are a commercially available Type I/II ordinary portland cement (OPC) conforming to ASTM C150 ("ASTM C150 / C150M - 12. Standard Specification for Portland Cement" 2012), nominally pure limestone powders (> 95% $CaCO_3$, by mass) of four different median particle sizes (0.7 μm, 3 μm, 10μm, and 15 μm), and two different commercially available interground PLCs conforming to ASTM C595 ("ASTM C595 / C595M - 16 Standard Specification for Blended Hydraulic Cements" n.d.) and ASTM C1157 ("ASTM C1157/C1157M-11 Standard Performance Specification for Hydraulic Cement" 2013). Figure 4-1 shows the particle size distribution of these raw materials, and Table 4-1 presents their respective chemical compositions and Blaine fineness. Both the interground cements are finer than the parent OPC (denoted as C150), with the C1157 cement being markedly finer. It is noted that the major difference between these C595 and C1157 cements is in their fineness alone since they are constituted from the same clinker used for the parent C150 cement.

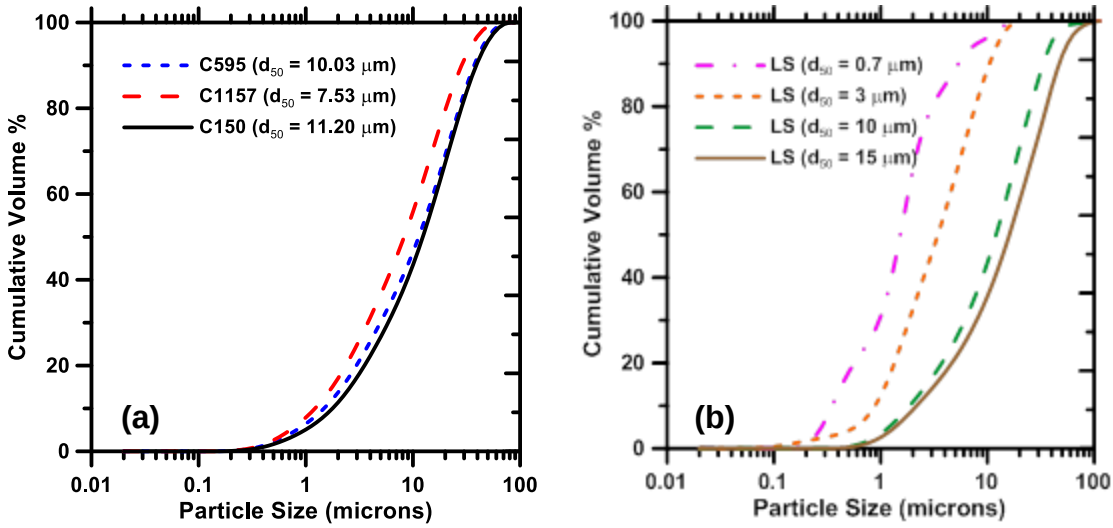

Figure 4-1: Particle size distributions of: (a) three different cements, and (b) the limestone powders used in this study.

Table 4-1: Chemical composition and fineness of the parent cements used in this study

Cement type (ASTM)	Chemical composition (% by mass)								Blaine Fineness (m^2/kg)
	SiO_2	Al_2O_3	Fe_2O_3	CaO	MgO	SO_3	Loss on ignition	Limestone	
C150 Type	19.60	4.09	3.39	63.21	3.37	3.17	3.17	-	452
C595 Type IL	16.51	3.38	2.66	56.80	2.61	2.80	4.17	11.07	497
C1157 Type	16.51	3.41	2.77	56.55	3.01	2.87	3.81	10.51	594

4.2.2 Experiments

4.2.2.1 Compressive strength

Compressive strength tests were carried out in accordance with ASTM C109 ("ASTM C109 / C109M - 12 Standard Test Method for Compressive Strength of Hydraulic Cement Mortars (Using 2-in. or [50-Mm] Cube Specimens)" 2012). The mortar cubes were prepared with a sand volume fraction of 50%. The testing was carried out at ages of 1, 3, 7, 28 and 56 days.

4.2.2.2 Isothermal calorimetry

The heat evolution from the hydration of cement was determined using isothermal calorimetry (TAM Air microcalorimeter™ 2700 Series) at a constant temperature of 25°C for 72 h. The powders were dry blended prior to adding water. To ensure accurate early age measurements and minimize the time required to attain isothermal conditions, the blended powders and water were conditioned in an oven for 12 hours at 25°C. The pastes were then mixed in accordance with ASTM C305 ("ASTM C305-13 Standard Practice for Mechanical Mixing of Hydraulic Cement Pastes and Mortars of Plastic Consistency" 2013, 305). Approximately 10 g of sample was extracted immediately, placed in a sealed sample vial to minimize evaporation and placed in the calorimeter. Three samples per mixture were tested and average values are reported.

4.2.2.3 Mercury Intrusion Porosimetry

Paste samples of approximately 100 g were cured for 3 and 28 days under sealed conditions at a constant temperature of 23±1°C. At the desired age of testing, the samples were crushed to an approximate size of 2 mm, and then pre-treated in an oven for 2 hours at 60°C, as this method was found to produce consistent results in a previous study (Vance, Kirk 2014). Approximately 1 g of material was selected and weighed using a high precision scale. Testing

was completed using a 0.5 cc cell in a Quantachrome Instruments PoreMaster™ mercury intrusion porosimeter to a maximum testing pressure of approximately 410 MPa. The porosity of the sample was determined by dividing the total volume intruded by the determined sample volume. The relationship between pore diameter and intrusion pressure was determined using the Washburn equation. The surface tension of mercury and the mercury contact angle were assumed to be 0.480 N/m and 117° respectively during intrusion (Cook and Hover 1993; R. Kumar and Bhattacharjee 2003a). The potential inaccuracies in the determination of the pore size distribution through mercury intrusion have been detailed in (Diamond 2000; Moro and Böhni 2002a). Thus, to provide indications of the pore structure, the critical (percolating) pore diameter, which is the pore diameter corresponding to the highest rate of volume intrusion into the specimen alone is used (Cook and Hover 1999; Winslow and Diamond 1970).

4.3. RESULTS AND DISCUSSIONS

4.3.1 Comparing the Properties of Interground PLCs (C595 and C1157) and Equivalent Size-Matched Blends

OPC-limestone blends were prepared using the four different limestone PSDs (Figure 4-1(b)) so that the overall PSD of the blend is similar to the PSD of the C595 or C1157 cements. The mass fraction of limestone in the blend is also maintained at the same level (11%) as that in the PLCs. The individual fraction of limestone of each median size required in the blend was calculated using an iterative solver to minimize the mean square error of the final PSD of the blended and the interground mixtures. Size-matching in such a way ensures that the total solids surface area available for the reaction is similar for the corresponding

blended and interground mixtures. However, since OPC is used in the blended mixtures, this does not ensure that the clinker and limestone surface areas in the PLCs and the blends are similar, which likely results in differing reaction rates. The size-matched blends are identified with the letter 'b' after the corresponding parent cement designation (C595 or C1157) in the remainder of this chapter. For instance, C595b indicates a blend of C150 and 11% size-matched limestone such that the final PSD is the same as that of C595 cement.

Figure 4-2 shows the PSDs of the PLCs and the size-matched blended mixtures. As can be noticed from the figure, the PSD of the blend corresponding to C1157 PLC could not be accurately matched to that of its parent cement using the four available limestone sizes. This is predominantly because of the higher fineness of this cement as noted from Table 4-1. Thus, the blend that provided the closest approximation is used in this chapter. This blend is deficient in particles smaller than 20 μm and rich in particles larger than this size, as compared to C1157 PLC.

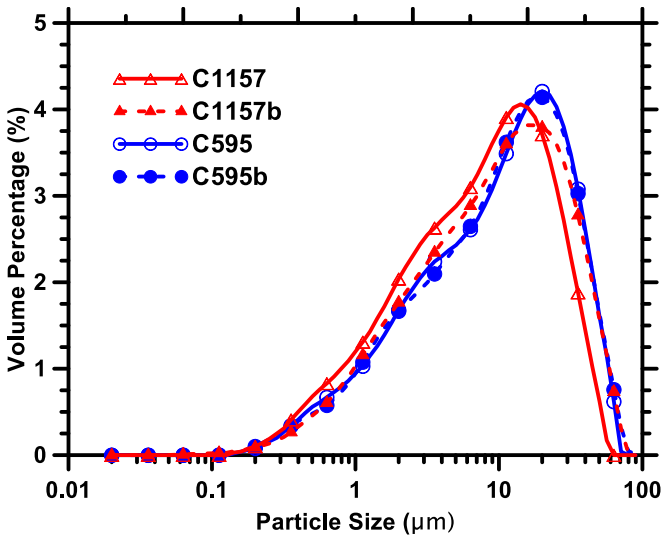

Figure 4-2: Particle size distribution of the PLCs ('C595' and 'C1157') and their equivalent size-matched blends ('C595b' and 'C1157b', respectively).

The open and closed circles correspond to C595 PLC and the corresponding blend whereas the triangles correspond to C1157 PLC and the corresponding blend. Note that the use of four different limestone sizes along with the chosen OPC is unable to accurately replicate the PSD of C1157 PLC.

In an attempt to compare and contrast the properties of the PLCs and the corresponding size-matched blends, the early age hydration, pore structure and compressive strength of these systems are investigated here. It should be noted that when OPC is blended with limestone of different particle sizes to simulate the PSD of PLCs, it is implicitly assumed that the PSD of the clinker fraction in the PLCs and that of the OPC in the blends are the same. The limestone sizes for the blended mixtures are then chosen to match the PSD of the PLCs. In reality, limestone is ground finer in the intergrinding process due to its softness, and the ground clinker fraction might be finer or coarser than that of OPC, depending on the grinding process and the desired composite cement fineness. This results in differences in properties between the interground and size-matched blended mixtures as will be explained in this section, even though the attempt is to provide similar equivalent solid surface areas.

Figure 4-3 shows the isothermal calorimetric response of the parent cements (Figure 4-3(a)) and the corresponding blends (Figure 4-3(b)). From Figure 4-3(a), it can be noticed that the acceleration stage in the heat flow plots occur at earlier times, the acceleration phase is steeper, and the maximum heat released is higher for the PLCs, the effects being more prominent for the C1157 PLC. This can be attributed to the higher fineness of the PLCs as

compared to OPC and the chemical effects of limestone (Vance, Aguayo, et al. 2013). When limestone is interground with portland cement clinker, the softer limestone phase is ground more readily than the harder portland cement clinker, resulting in a finer limestone phase (Hawkins, Tennis, and Detwiler, n.d.). The clinker phase could also be ground finer in the composite cements depending on the desired ultimate fineness of the cement. Fine limestone increases the surface area and seed locations available for hydration product nucleation. In addition, an increase in the amount of limestone fines also enhances the interactions with the C_3A phase, thus significantly sharpening the main hydration peak, while also decreasing the thickness of the initial hydration product shell that forms on particles thereby enhancing C_3S reactivity (Thomas, Jennings, and Chen 2009).

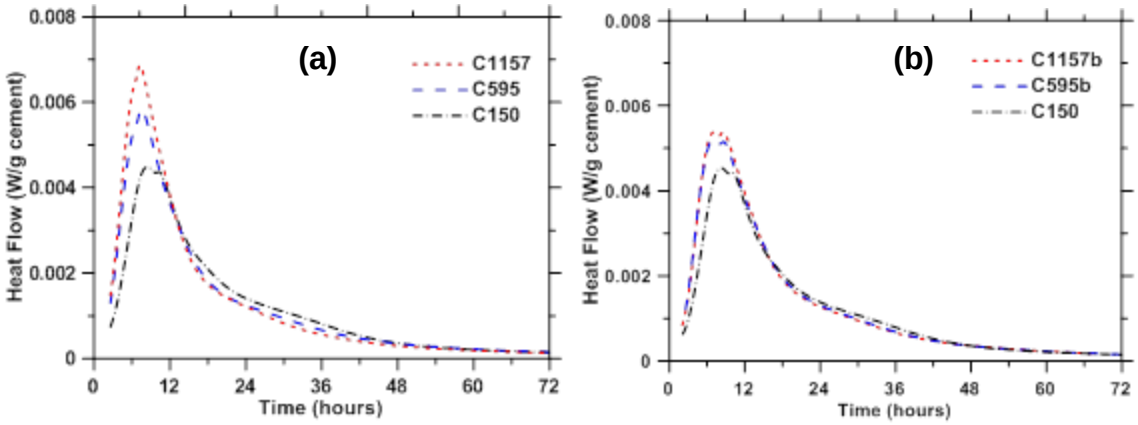

Figure 4-3: Isothermal calorimetric response of: (a) parent cement pastes (OPC and PLCs), and (b) the corresponding size-matched blends.

For the size-matched blends, the calorimetric response is more in line with that of a conventional OPC paste. The heat evolution peak and the total heat released for the blended C595 system is almost comparable to that of the corresponding PLC (333.8 J/g for C595

cement and 331.7 J/g for C595b), except for the fact that the peak is sharper in the PLC paste. This is likely because of the enhanced aluminate reaction owing to the presence of much finer limestone particles in the PLC, as will be shown later. An increase in the slope of the acceleration phase attributable to the presence of fine limestone, as described in detail in (Vance, Aguayo, et al. 2013), is observed for the blended pastes as well. The discrepancy between the heat release peaks of the blended and interground systems corresponding to C1157 can be attributed mainly to the inadequacy of size-matching. Note that the blend designed to match C1157 PLC was deficient in the finer fraction as depicted in Figure 4-2. Figure 4-4 shows the porosities and critical pore diameters of interground and size-matched blended systems after 3 and 28 days of hydration. At 28 days, as expected, the intruded pore volume decreases for all the pastes, and the pore structure becomes more refined as compared to 3 days. OPC has the lowest 28-day porosity among all the pastes while the blended and interground limestone containing pastes show slightly higher porosities because of the reduced clinker fraction in these pastes. Further, it is noted that the interground samples have lower porosities than the corresponding blended samples. This is a likely result of increase in the particle packing of these systems due to pore filling by the finer limestone particles. When the critical pore diameters are compared, the interground limestone paste (C1157) demonstrates the lowest pore size. This is because the limestone in this cement is much finer, along with a higher overall composite Blaine fineness of this cement (Table 4-1) that enables better particle packing and increased reactivity. Even though the total reaction product volume is slightly lower in this case than that of the OPC paste since limestone is not as reactive as that of the OPC, the finer particles result in pore size refinement. The

blended pastes are noted to have a larger critical pore size than the PLC pastes, and comparable to that of the OPC paste.

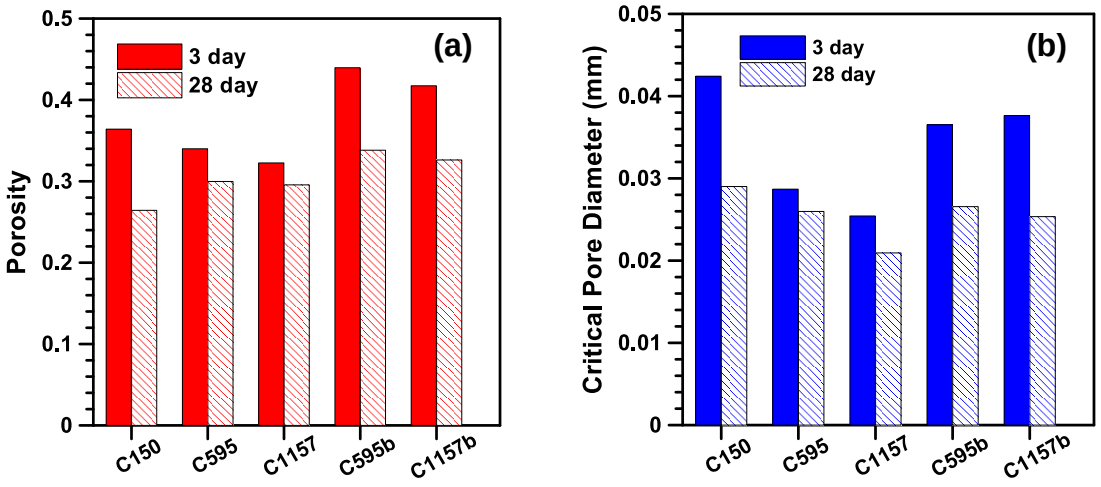

Figure 4-4: Comparison of: (a) porosity and (b) critical pore diameter for the interground and size-matched blended cement pastes at 3 and 28 days.

Figure 4-5 shows the compressive strengths of the PLC mortars (Figure 4-5(a)) and the corresponding blended mixtures (Figure 4-5(b)) as a function of time. It is noted that the PLC mortars result in higher strengths at all ages than the OPC and the size-matched blended mortars. This can be attributed to the higher fineness of the PLCs and the consequent increased packing and enhanced reactivity (Kirk Vance, Neithalath, and Sant 2013). Comparing the early age strengths, it is seen that the finer PLC (C1157) shows the highest strength. This is because of the increased participation of the fine limestone in reactions with C_3A and acting as nucleation site for the formation of hydration products. The compressive strength results are in line with the trends in porosity described above.

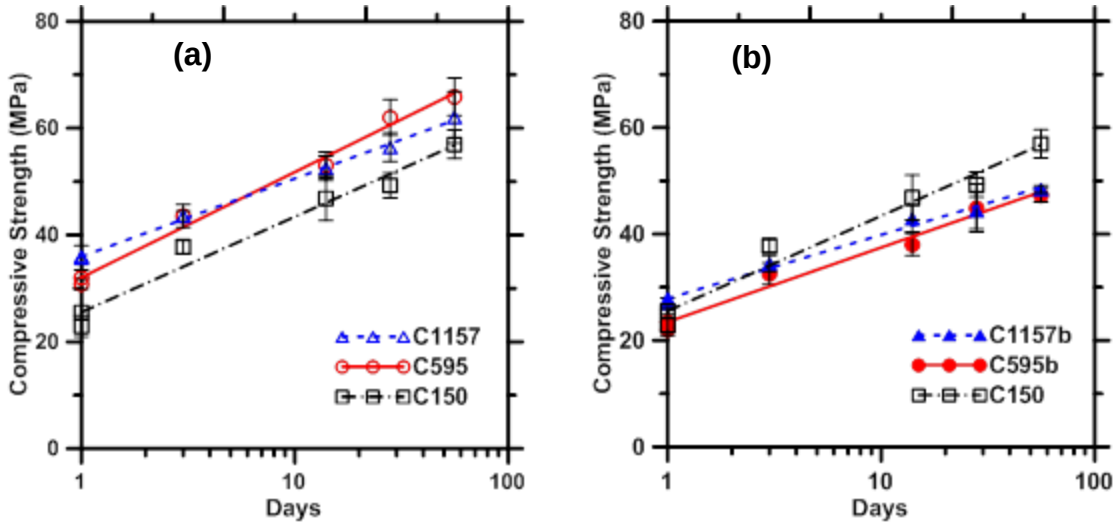

Figure 4-5: Compressive strength development with time for: (a) PLC mortars, and (b) size-matched blended mortars. OPC is shown for comparison.

To proportion blended systems that are performance-equivalent to PLCs, it is necessary to understand the size distribution of the components (clinker and limestone) in the PLCs. The need to understand the size distribution of components that constitute the final product exists in several critical industries such as pharmaceuticals, food processing, and chemical synthesis where the size distribution influences rates of heat and mass transfer or chemical reaction. The forthcoming section sheds more light on this aspect by developing an analysis method to separate the sizes of the component solids. The method is generic and versatile, though it has been implemented in this chapter only to separate the PSDs of clinker and limestone fractions in PLCs.

4.3.2 Extracting the Component Size Distributions in Interground Systems

As noted above, the disparity in the pore structure and properties between the PLCs and the corresponding blended mixtures is indicative of the fact that the OPC and limestone size

distributions in the blended systems are not true representations of the ground clinker and limestone PSD in the interground PLCs. The inherent assumption that the PSD of the ground clinker fraction of the PLCs is the same as that of C150 is incorrect (to varying degrees based on whether the comparison is with C595 or C1157 cement).

An understanding of size distribution of components in multi-particle blends is important for several applications (Pötschke et al. 1999; Pedersen 1994). There have been attempts at determining the individual PSDs of components from the composite particle size distributions experimentally (Chiara F Ferraris 2011). Laser diffraction has been employed to obtain the PSDs of gypsum and cement based on the difference in the refractive indices of the two materials (Chiara F., Bullard, and Hackley, n.d.). For particulate blends with comparable refractive indices such as cement and limestone, this method is inapplicable. A sedimentation method using Andreasson apparatus has been used to obtain the independent PSD of two or more blended solid species (Farmer and Beckman 1984). This method, based on the steady-state settling of spherical particles according to Stoke's law, employs periodic determination of concentration of solids at a given depth in a vertical settling tube. While useful for mixtures containing larger particles, the sedimentation technique is extremely tedious for determining PSDs with size fractions finer than 1 μm. This is because the quadratic relationship between settling time and particle diameter in Stokes' equation makes the intervals between samples extremely long for sampling smaller (~1 μm) particles. Back-scattered electron microscopy and thin section image analysis have also been used to identify the distributions of particle classes in a powder mixture (Nauman and Cavanaugh 1998). This method is rather tedious and demands adequate optical or microscopic contrast

between the particles imaged, which is not always achieved. In order to overcome these limitations, a novel optimization technique is discussed in this work, which has the potential to deconvolute the PSDs of the clinker fraction and limestone from that of the composite cement.

4.3.2.1 The optimized Rosin-Rammler distribution-based PSD deconvolution technique

Rosin-Rammler (R-R) distribution (which essentially is a Weibull distribution but called R-R because it was first applied by Rosin and Rammler to describe PSDs (Rosin and Rammler 1933)), is widely accepted as a method to describe the PSDs of materials processed by grinding, milling, crushing, or comminution operations, such as in the cement manufacturing process (DELAGRAMMATIKAS and TSIMAS 2004; Voglis et al. 2005). R-R distribution is defined by the characteristic diameter and the shape parameter. The characteristic diameter (d_0) represents the cumulative volume fraction that is finer than 63.2%, which makes it a measure of the fineness of the distribution, whereas the shape parameter (n) is a measure of spread of the distribution. The R-R cumulative distribution function, Q(d), where d is the particle size, is defined, as shown in Equation 4-1, as a function of d_0 and n. The parameters of the R-R distribution can be obtained by re-factoring the distribution function to the form shown in Equation 4-2. For the three parent cements used in this chapter (C150, C595, and C1157), the R-R parameters obtained are shown in Table 4-2.

$$Q(d) = 1 - e^{-\left(\frac{d}{d_0}\right)^n} \quad \text{(Eq. 4-1)}$$

$$\ln\left(\ln\left(\frac{1}{1-Q(d)}\right)\right) = \mathrm{n}(\ln(d) - \ln(d_0)) \quad \text{(Eq. 4-2)}$$

An optimization procedure was employed to obtain the values of the characteristic diameter (d_0) and the shape parameter (n) of the clinker and limestone present in interground cements, from which their individual PSDs can be deduced. The constraint used in the optimization procedure was the equivalence of specific surface areas from the PSDs of the actual interground cements and their PSDs obtained using the R-R parameters of both clinker and limestone fractions. Specific surface area (SSA) can be calculated from the PSD using Equation 4-3 (Taylor 1997), where F_s is a constant that accounts for the shape of particles (considered as 1.0 assuming spherical particles), f_d is the mass fraction of particles with size 'd' μm and ϱ is the density of material.

$$SSA = 6 \times 10^3 \times F_s \times \sum \frac{f_d}{d \times \rho} \quad \left(\frac{m^2}{kg}\right) \qquad \text{(Eq. 4-3)}$$

Table 4-2: Rosin-Rammler parameters and SSA of the parent cements used in the study.

Cement type	**R-R parameters**		**SSA (m^2/kg)**	
	d_0 (μm)	n	Predicted SSA using Eq. 3	Experimental Blaine fineness
C150	17.95	1.32	492.4	451.6
C595	16.99	1.28	508.1	496.9
C1157	12.48	1.32	604.1	593.9

The optimization function is defined as the summation of the absolute relative errors in the values of d_0, n and SSA of the actual interground cement and the predicted distribution from the R-R parameters, as shown in Equation 4-4.

$$Z = \left|\frac{\Delta d_0}{d_0}\right| + \left|\frac{\Delta n}{n}\right| + \left|\frac{\Delta SSA}{SSA}\right| \quad \text{(Eq. 4-4)}$$

A rigorous search was carried out to obtain the d_0 and n values associated with each of the individual components in the composite material; in this case, the clinker and limestone. Multiple iterations were carried out using trial d_0 and n values for clinker and limestone fractions selected from a pre-specified range and step interval. These trial combinations were used to calculate the respective PSDs using Equation 4-1. The composite distribution was then calculated knowing that these PLCs contain 12.7% of limestone by volume. Subsequently, d_0 and n values of the composite distribution were determined using Equation 4-2 and SSA was calculated using Equation 4-3. Finally, these values were used in Equation 4-4 to calculate the optimization function. The optimization function was found to converge to a minimum for certain combinations of d_0 and n for the clinker and limestone phases. The region of convergence was used to redefine the range for d_0 and n values for the next iteration cycle. The step interval was reduced in order to explore the region of convergence in search of a better solution. The tolerance value for the optimization function was also subsequently refined so as to finally reach the value of ~ 0.5%. The values of d_0 and n at the minima at an acceptable level of tolerance (~ 0.5% in this case) were taken as the optimized values. A flowchart describing this approach, which has been developed into a computer program, is shown in Figure 4-6. The optimized R-R parameters for the clinker and

limestone phases present in the PLCs are shown in Table 4-3. The median size (and d_0) of the clinker particles in the C595 PLC is higher than that of OPC whereas for the C1157 PLC, it is lower than that of OPC. The spread of the distribution of the clinker particles are rather invariant between the three parent cements. As expected, limestone is ground finer in the C1157 PLC than in the C595 PLC. Figure 4-7 shows the comparison between the actual PSDs of the C595 and C1157 cements and the composite distribution predicted using the optimization scheme that extracted the individual PSDs of clinker and limestone. The adequacy of the proposed optimization approach is evident from this figure.

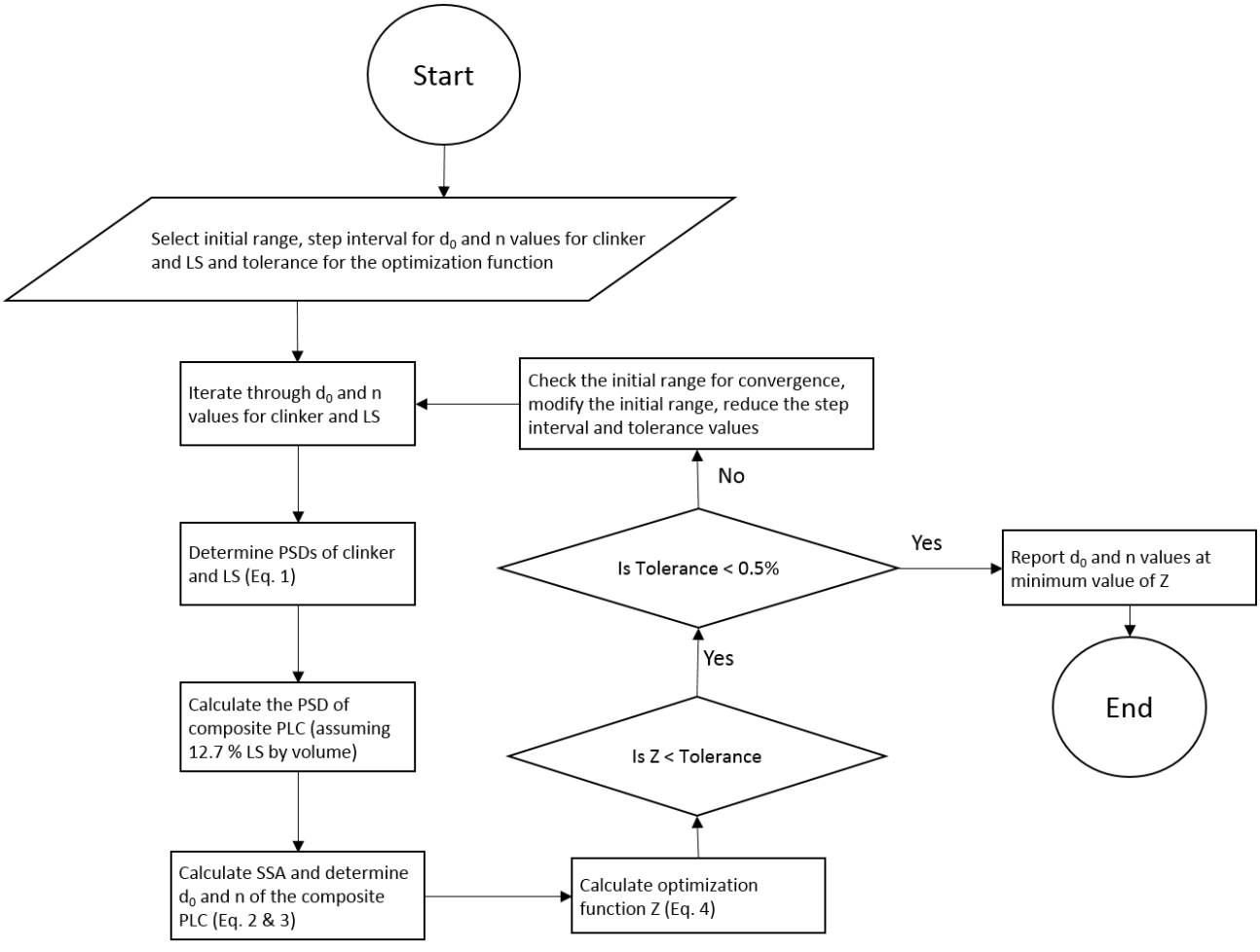

Figure 4-6: Flowchart to demonstrate the steps for the optimized R-R method

Table 4-3: Summary of the parameters of Rosin-Rammler distribution for clinker and limestone in the OPC and PLCs obtained using the optimization approach. d_{50} values are also shown for comparison

Cement type	**Clinker fraction**			**Limestone**			**Error**
	d_0 (μm)	n	d_{50} (μm)	d_0 (μm)	n	d_{50} (μm)	
C 150	17.95	1.32	11.20	--	--	--	--
C595	19.00	1.28	14.26	2.20	1.90	1.82	0.51%
C1157	13.90	1.35	10.61	1.93	1.80	1.57	0.53%

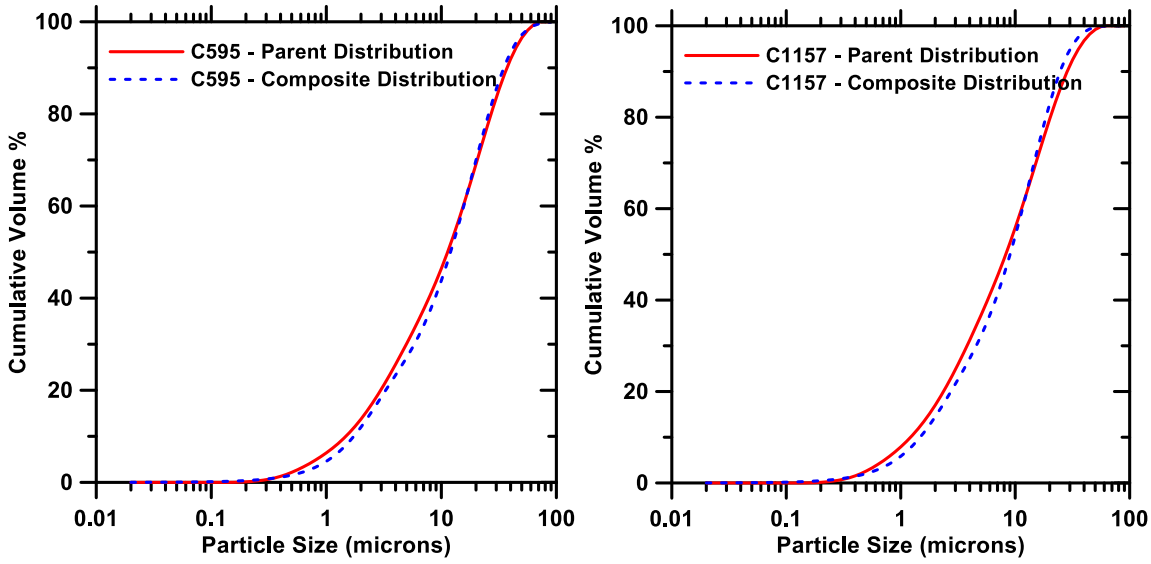

Figure 4-7: Comparison of the actual PSDs of: (a) C595 PLC and (b) C1157 PLC with those obtained from the R-R parameters.

4.3.3 Validation of the Proposed Model through Virtual Microstructure-and-Hydration Modeling

While Figure 4-7 established the correspondence between the PSDs of the interground cement and those extracted from individual clinker and limestone PSDs, it is onerous to experimentally generate blended mixtures of these PSDs separately for validation studies. Thus, virtual microstructures and a cement hydration model is used in this chapter to evaluate the efficiency of the PSD extraction approach. The individual PSDs of the clinker and limestone phases obtained using the R-R optimization approach were used to calculate the composite distributions as shown in Figure 4-7, which were used as inputs in microstructural modeling. The composite PSDs were discretized to get the number of particles of the different components in a representative volume element of side length 300 μm. The packing fraction corresponded to a water-solids ratio of 1.26 by volume (approximately 0.4 by mass). Figure 4-8 shows representative slices from the initial digitized microstructures of the blended mixtures (where OPC and four limestone sizes are used to match the PSD of the PLCs – Figure 4-2) and the composite mixtures after extraction of PSDs of individual components. An observation of these virtual microstructures indicates the drawbacks of the PSD-matching approach adopted in the first part of the study. While the clinker fraction particle sizes are taken to be similar for the blended mixtures (Figures 4-8(a) and (c)) because of the use of parent OPC in the blends, simulation of the optimized

PSDs in Figures 4-8(b) and (d) show that the clinker fraction is much finer for the C1157 cement. Similar, but subtler variations exist for the C595 cement also, which are elucidated in more detail using microstructural quantifiers described below.

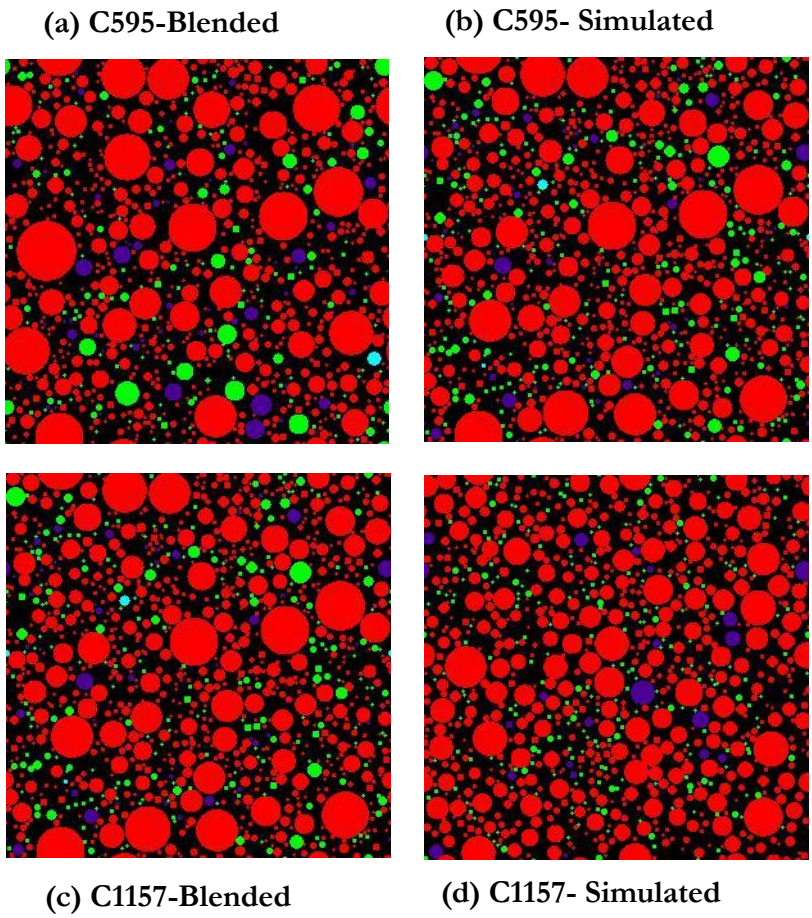

Figure 4-8: Comparison of virtual microstructures (in the unhydrated state) for the PSD-matched blends corresponding to Figure 4-2 (Figure 4-8(a) and (c)) and the simulated PSDs based on R-R method and optimization (Figures 4-8(b) and (d)). Clinker fraction is indicated in red, gypsum in violet and limestone in green. Note the large discrepancy in particle sizes of both clinker fraction and limestone between the blended and simulated PSDs for the C1157 cement.

The interactions between the nearest neighbors in the random multi-component microstructure can be extracted from microstructural simulations such as the ones shown in Figure 4-8. Quantification of the interactions through contact fractions is useful to obtain a perspective on the reaction rates in the mixtures. The particle contact fraction is calculated as the fraction of nearest neighbor pairs in the microstructure. For instance, the cement-limestone contact fraction is calculated as the ratio of the total number of contacts between cement and limestone to the total number of contacts in the system (which includes cement-cement, limestone-limestone, and cement-limestone contacts). Since limestone is known to contribute both physically and chemically to the hydration of cement, albeit to a minor extent, the interaction between cement and limestone particles is vital towards understanding the nucleation process. As is well known, this is highly dependent on the PSDs of both limestone and cement in the mixture. Figure 4-9 shows the like and unlike particle contact fractions in the interground PLCs and the corresponding blended mixtures. The blended mixtures exhibit higher cement-cement interaction than the interground PLCs, indicating that the limestone particles are larger in this case (and thus more separated, given the same volume fraction). This results in the cement-limestone interactions being lower also. The proximity between the cement and limestone particles, coupled with the increased fineness of limestone leads to increased hydration rates since limestone is known to accelerate the hydration of cement. This aspect is evident when the C1157 and C595 PLCs are compared.

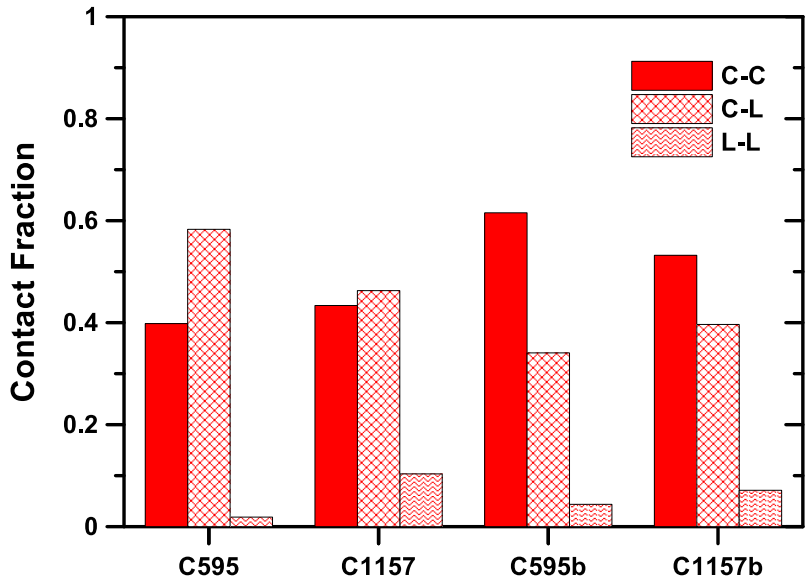

Figure 4-9: Percentages of contact between like and unlike particles obtained from the microstructure model. C-C indicates the % contact between cement particles, L-L between limestone particles and C-L cement and limestone particles.

Cement hydration was modeled using the hydration and microstructure modeling tool CEMHYD3D (D. P. Bentz 2005). The process of hydration of a cement with known particle size distribution is simulated using a set of cellular automata rules. The model has been validated for a number of different types of portland cements as well as portland cements containing limestone (Dale P. Bentz et al. 1999; D. P. Bentz 2006). After the construction of virtual microstructures (Figure 4-8), the volume fractions of individual phases in the parent cements were obtained from Bogue's calculations. The hydration was simulated for 72 hours under isothermal conditions in a sealed environment (D. P. Bentz 2005). A cycles-to-time conversion factor of 0.00035 hours/cycles^2 was used to represent the hydration results as a function of time (D. P. Bentz 2005). Figure 4-10 shows the

simulated cumulative heat release curves based on the PSD-matched blends of OPC and limestone (labelled C595b-Sim or C1157b-Sim in the figures) as well as those based on the individual PSDs extracted from R-R optimization method (labelled C595-Sim or C1157-Sim in the figures). It is noted that the simulations based on the extracted PSDs match very well with the experimental data for both the PLCs. Since the PSD matching was rather satisfactory for the C595 PLC (Figure 4-2), the heat release responses are not very different. However, the adequacy of the PSD extraction process described earlier can be noticed from Figure 4-9(b) where the C1157 cement is simulated.

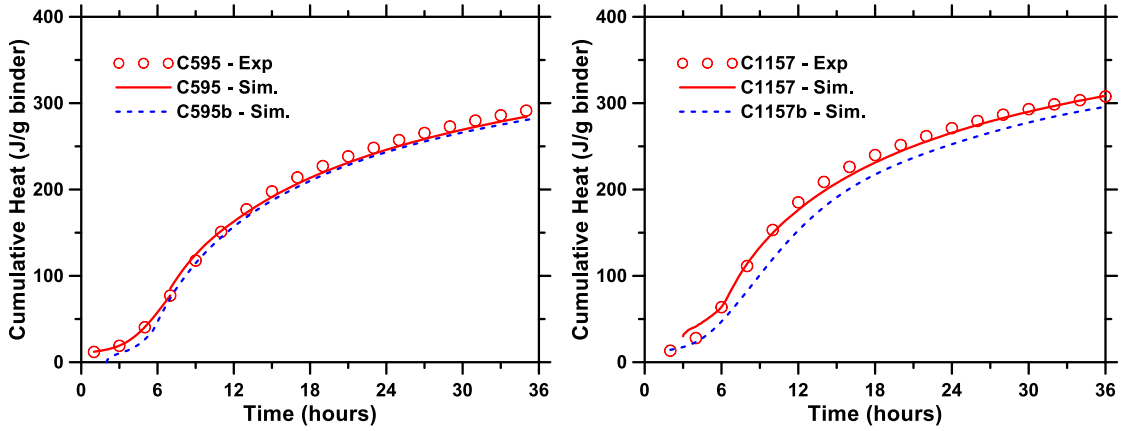

Figure 4-10: Cumulative heat flow curves for the PSD-matched blends (C595b and C1157b) and the PLCs from hydration simulation and their comparison with experiments. Simulation data shown as continuous and dashed lines; experimental data shown as discrete symbols.

Figure 4-11 shows the comparison between the porosities calculated at 3 days using the hydration model and the experimental porosity values obtained using MIP. The porosities calculated by the hydration model for the interground PLCs using the composite

distributions in Figure 4-7 are comparable to the experimental values obtained using MIP, whereas the simulated porosities for the blended mixtures are much higher in comparison. This further validates the composite PSDs calculated using the R-R optimization approach.

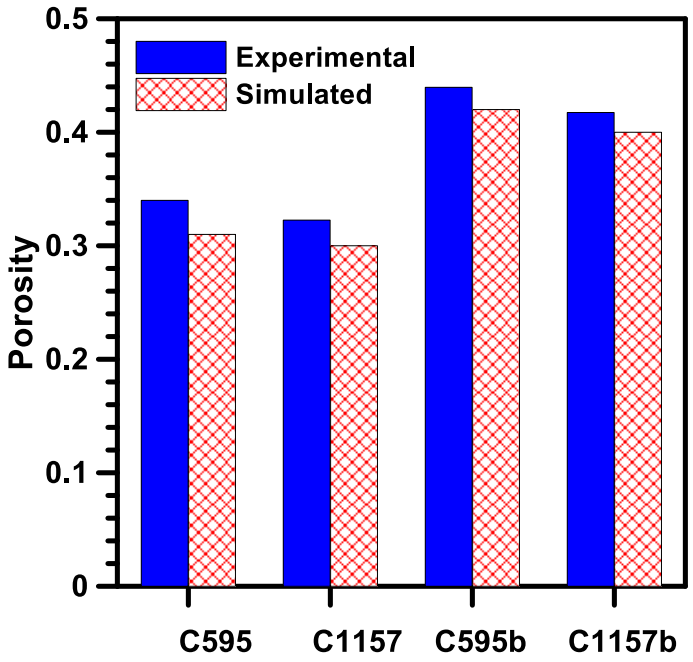

Figure 4-11: Comparison of experimental and simulated porosities at after 72h of hydration

4.4. CONCLUSIONS

This chapter has compared the hydration response, pore structure, and strength of cementitious systems proportioned using two interground portland-limestone cements (conforming to ASTM C595 and C1157) to those of corresponding particle size-matched blends. The PSD-matched blends were proportioned using limestone powders of four different median sizes. The inability of blended systems to match the properties of interground PLCs even with similar or comparable overall solids surface area is brought out

in this chapter. This behavior is based on the difference in the relative size distribution of clinker and limestone in the interground PLCs as compared to the size-matched blends. In order to determine the unknown PSDs of clinker and limestone in the interground PLCs, a novel method was proposed which can aid in better design of blended mixtures to achieve performance equivalence to the PLCs. The approach uses Rosin-Rammler distributions for the clinker and limestone fractions in the interground PLCs and determines the corresponding characteristic diameter (d_0) and shape parameter (n) using an optimization procedure. Such an approach will be of interest to other areas of particle and powder technology such as food processing, pharmaceuticals etc. The validation of the technique was carried out using CEMHYD3D based modeling of cement hydration and microstructure.

CHAPTER 5[4]

TERNARY BLENDS CONTAINING SLAG AND INTERGROUND/BLENDED LIMESTONE: HYDRATION, STRENGTH, AND PORE STRUCTURE

5.1. INTRODUCTION

The environmental impact, particularly the significant emission of greenhouse gases associated with the manufacture of ordinary portland cement (OPC) (Worrell et al. 2001), has catalyzed studies on the use of several environmentally benign alternate materials as partial OPC replacements. Fine limestone powder is one such material that has shown to be a viable partial OPC replacement material. Limestone can be interground with OPC clinker in the cement manufacturing process or blended with the cement during the concrete batching process. Improved particle packing, fine limestone acting as nucleation sites for reaction product formation, and consequently better properties are obtained with interground portland limestone cements (PLC) as well as blended systems where fine limestone is used (A. Kumar, Oey, Kim, et al. 2013; Vance et al. 2015; Vance 2014). Binary and ternary cementitious blends containing fly ash, slag, metakaolin or silica fume are being commonly used to produce sustainable high-performance concretes (Frohnsdorff 1986; Osborne 1999; Vance, Aguayo, et al. 2013). Recently, significant work has been carried out on developing ternary blends based on the idea that limestone is capable of chemically combining with the aluminate phases in the cementitious materials to form carboaluminates

[4] This chapter is derived from the publication: Arora, A., Sant, G., & Neithalath, N. (2016). Ternary blends containing slag and interground/blended limestone: Hydration, strength, and pore structure. Construction and Building Materials, 102, 113-124.

that further densify the microstructure and consequently improve the properties (Guillermo Puerta-Falla et al. 2015; Matschei, Lothenbach, and Glasser 2007b; Oey et al. 2013). Synergistic effects of limestone and fly ash or metakaolin have been elucidated in these studies. This has provided a methodology to realize increased OPC replacement without compromising the performance.

In this chapter, a combination of limestone and slag is utilized as OPC replacement in order to develop binders that contain higher levels of cement replacement, yet result in performance-equivalent concretes. In addition to the alumina content in slag (which is higher than that in OPC but significantly lower than those in fly ash or metakaolin) that facilitates limestone-aluminate synergistic reactions, slag demonstrates cementitious (albeit slow) and pozzolanic reactivity (Lothenbach, Scrivener, and Hooton 2011). Due to the latent hydraulicity of slag, slag-based cements show reduced early age strengths but they have been shown to attain significant compressive strengths at later ages (Bágel 1998; Hwang and Lin 1986). The presence of fine limestone is expected to accelerate the early-age hydration in slag containing blends. The synergistic effects of limestone and slag are explored in detail with respect to their contributions to the formation of hydration products and the development of strength and pore structure. Limestone powders of different size distributions are blended with OPC and slag to obtain similar particle size distribution (PSD) as the corresponding PLC-based mixture, which ensures that the total surface area available for the reaction is similar for all the mixtures. Up to 50% (by volume) of total OPC replacement is studied.

5.2. EXPERIMENTAL PROGRAM

5.2.1 Materials and Mixtures

Commercially available Type I/II ordinary portland cement (OPC) conforming to ASTM C 150 and portland limestone cement (PLC) conforming to ASTM C 595 were the used in this chapter. The PLC has a limestone content of 11.07% by mass (12.68% by volume). A nominally pure limestone powder (purity > 95% $CaCO_3$, by mass) of four different median particle sizes - 0.7 μm, 3 μm, 10 μm and 15 μm, conforming to ASTM C 568, and a ground granulated blast furnace slag (GGBFS, referred to in the remainder of this chapter as slag) conforming to ASTM C 989 were used as partial cement replacement materials. Figure 5-1 shows the particle size distribution of these materials. The median particle sizes are shown in these figures. Table 5-1 presents their respective chemical compositions.

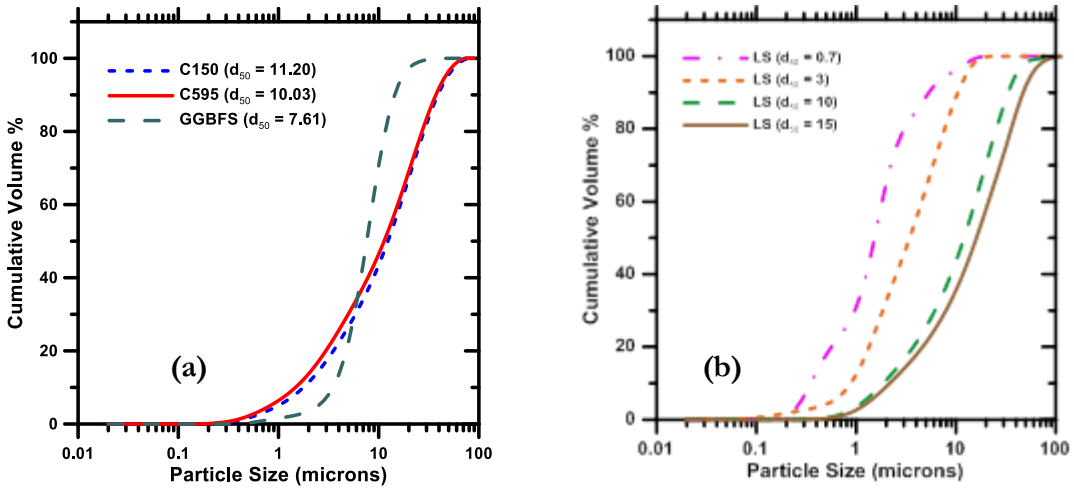

Figure 5-1: Particle size distributions of: (a) parent OPC and PLC, and slag, and (b) limestone powders used in this chapter. The d_{50} values (in μm) are shown in the figure legends.

Table 5-1: Chemical Compositions of materials (% by mass) used

Material	**SiO_2**	**Al_2O_3**	**Fe_2O_3**	**CaO**	**MgO**	**SO_3**	**LOI**	**LS**	**SSA (m^2/kg)**
OPC - C150	19.60	4.09	3.39	63.21	3.37	3.17	2.54	2.90	452
PLC – C 595	16.51	3.38	2.66	56.80	2.61	2.80	4.17	11.07	497
GGBFS – C 989	39.41	8.49	0.37	35.53	12.05	2.83	1.31	-	487

The raw materials were proportioned by volume to obtain eleven different mixtures. Apart from the plain OPC paste, three mixtures were proportioned where 20, 40, or 50% of OPC by volume was replaced by slag. Similarly, PLC (with a limestone content of ~13% by volume) was used as the base material in pastes where 20, 40, or 50% of the clinker fraction in PLC was replaced using a combination of slag and limestone. For example, a mixture with a 40% replacement includes 31.29% of slag (externally added) and 8.71% of limestone (intrinsic to the PLC). In the next set of mixtures, 20, 40, or 50% of OPC was replaced by blending slag and limestone powder of four different sizes so as to match the PSD of the corresponding PLC-based binders. It should be noted that PLC has a limestone content of 12.68% by volume (11.07% by mass), which is interground with the cement clinker during the manufacturing process. In this series, the limestone content was maintained at 12.68% by volume, which is the same as that of the PLC. The sample nomenclature and the amounts of the constituents in the mixture are shown in Table 5-2. These mixtures are indicated as OPC-x, INT-x and BLD-x respectively, where x represents the total replacement (by volume) of the cement clinker in the mixtures. A volume-based water-to-powder ratio

$(w/p)_v$ of 1.26, which is approximately equivalent to a water-to-powder ratio of 0.40 by mass for the plain OPC system, was used.

Table 5-2: Volumetric percentages of the binder components for the mixtures considered

Sample ID	OPC (C150)	PLC (C595)	GGBFS	Limestone (Total)	LS 0.7µm	LS 3µm	LS 10µm	LS 15µm
OPC-0	100.00	0.00	0.00	0.00	-	-	-	-
OPC-20	80.00	0.00	20.00	0.00	-	-	-	-
OPC-40	60.00	0.00	40.00	0.00	-	-	-	-
OPC-50	50.00	0.00	50.00	0.00	-	-	-	-
BLD-20	80.00	0.00	7.32	12.68	3.63	1.05	6.57	1.43
BLD-40	60.00	0.00	27.32	12.68	2.81	1.04	6.44	2.39
BLD-50	50.00	0.00	37.32	12.68	2.40	1.03	6.38	2.87
INT-13	0.00	100	0.00	12.68	-	-	-	-
INT-20	0.00	91.62	8.38	11.62	-	-	-	-
INT-40	0.00	68.71	31.29	8.71	-	-	-	-
INT-50	0.00	57.26	42.74	7.26	-	-	-	-

In the mixtures where limestone was blended, four available limestone size distributions as shown in Figure 5-1 (b) were used such that the overall PSD of the blend is similar to the PSD of the PLC-based mixture at the same level of total replacement. The individual fraction of each limestone size was calculated using an iterative solver to minimize the mean square error of the final PSD of the blended and the interground mixtures. Size-matching in

such a way ensures that the total surface area available for the reaction is similar for the corresponding blended and interground mixtures. However, intergrinding of portland cement clinker with limestone results in a finer limestone phase in the composite system due to the fact that limestone is softer than the clinker.

The volume percentages of different limestone sizes as obtained by matching of the PSDs of the blended mixtures are also shown in Table 5-2. It should be noted that the size distribution available for PLC is a composite distribution of cement and limestone and that the volume percentages of OPC and limestone for PLC mixtures is expressed in terms of their relative contribution to the amount of PLC in the corresponding mixtures. Figures 5-2(a), (b) and (c) show the cumulative PSDs of the blended and interground limestone cement mixtures containing slag, after particle size matching.

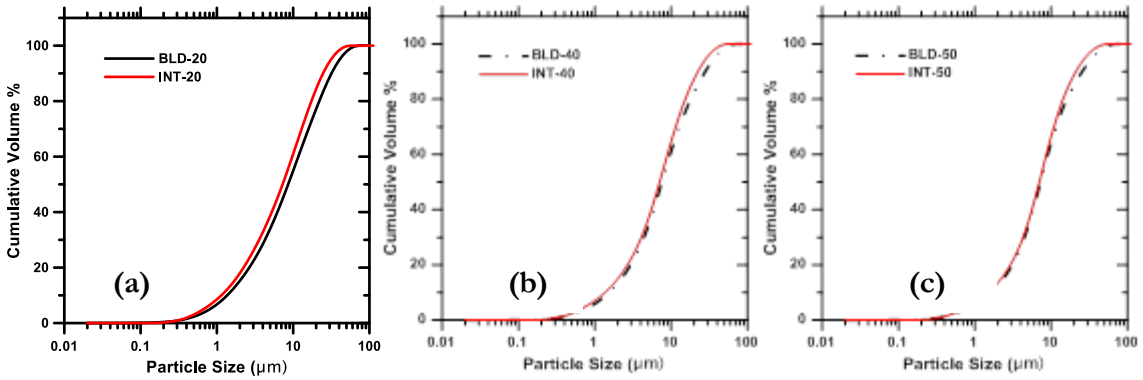

Figure 5-2: Comparison of particle size distributions (PSDs) for the interground and blended mixtures with cement replacement by volume of: (a) 20%, (b) 40% and (c) 50%

5.2.2 Experiments

5.2.2.1. Isothermal Calorimetry

The heat evolution during hydration was determined using isothermal calorimetry (TAM Air micro calorimeter 2700 Series) at a constant temperature of 25°C for 72 hours. To ensure accurate early age measurement and minimize the time to isothermal conditions, the blended powders and water were conditioned in an oven for 12 hours at 25°C. The pastes were then mixed using a laboratory mixer in accordance with ASTM C 305 ("ASTM C305-13 Standard Practice for Mechanical Mixing of Hydraulic Cement Pastes and Mortars of Plastic Consistency. ASTM International, West Conshohocken, PA; 2013.," n.d., 305) . Approximately 10 g of sample was extracted immediately, placed in a sealed sample vial to minimize evaporation and placed in the isothermal calorimeter to determine the heat release response.

5.2.2.2. Compressive Strength Testing

Compressive strength tests were carried out in accordance with ASTM C 109 ("ASTM C109 / C109M - 12 Standard Test Method for Compressive Strength of Hydraulic Cement Mortars (Using 2-in. or [50-Mm] Cube Specimens). ASTM International, West Conshohocken, PA; 2012.," n.d., 109) on 50 mm size mortar cubes cured in a moist environment (>95% RH) and a temperature of 23±2°C. Mortar cubes were prepared with a sand volume fraction of 50%. The cubes were stored in the molds for 24 hours in covered conditions, after which they were demolded and stored until the desired testing age (1, 3, 14, 28, 56 and 90 days) in the moist-curing chamber.

5.2.2.3. Thermal Analysis

Simultaneous thermal analysis (STA) simultaneously measures the mass loss and heat flow associated with heating a sample over a defined temperature range. In this chapter, STA was

carried out at ages of 1, 3, 7, 14, and 28 days. Powders were dry-blended prior to adding water, and the samples were mixed in accordance with ASTM C 305. Paste samples were cured under sealed conditions at a temperature of 23±1°C until the desired testing age. Thermal analysis was completed using a Perkin Elmer STA 6000. Tests were carried out in a nitrogen environment, at a gas flow rate of 20 ml/s. Samples were heated from ambient temperature to 995°C at a heating rate of 15°C/min. Heat flow curves from thermal analysis over this temperature range typically illustrate three distinct peaks - (i) loss of evaporable water and chemically bound water in C-S-H and ettringite, (ii) the dehydroxylization of calcium hydroxide, and (iii) the decarbonation of calcium carbonate. A minor peak corresponding to the decomposition of mono/hemi-carboaluminate species was also observed. Calcium hydroxide and residual calcium carbonate contents were determined using the stoichiometric relationships associated with their respective decomposition reactions and the mass loss associated with their decomposition temperatures. The chemically bound water (w_n) is a measure of the degree of hydration of the portland cement and is determined by subtracting the mass loss associated with calcium carbonate from the loss on ignition of a dried sample (the mass at 110°C), normalized by the mass of the dried sample. The consumed carbonate content is the percentage of carbonates consumed during the hydration process relative to the amount of carbonates initially present as determined from the mixture proportions.

5.2.2.4. Mercury Intrusion **Porosimetry (MIP)**

Paste samples were cured for 28 days under sealed conditions at a constant temperature of 23±1 °C. The samples were crushed to an approximate size of 2 mm, and then dried in an

oven for 2 hours at 60 °C. This pre-treatment method was found to produce consistent results in a previous study (Vance 2014). A mercury intrusion porosimeter capable of exerting a maximum testing pressure of 414 MPa was used. The relationship between pore diameter and intrusion pressure was determined using the Washburn equation (Washburn 1921b) (Equation 5-1), where 'd' is the apparent diameter and 'P' is the applied pressure. 'γ' is the surface tension of mercury and 'φ' is the mercury contact angle which are assumed to be 0.480 N/m and 117° respectively during intrusion. The contact angle of 117° is typically used for the intrusion phase in oven dried cementitious materials (Windslow and Diamond 1969; Bager and Sellevold 1975; R. Kumar and Bhattacharjee 2003b), and thus was selected for this chapter.

$$d = \frac{-4\gamma \cos\varphi}{p} \quad \text{(Eq. 5-1)}$$

Studies have identified potential inaccuracies in the determination of the pore size distribution using MIP (Moro and Böhni 2002b; Diamond 2000). However, the determinations of the total volume of mercury intruded and the critical (percolating) pore diameter which corresponds to the highest rate of volume intrusion into the specimen, have been suggested to be reliable (Cook and Hover 1999; Windslow and Diamond 1969).

5.3. RESULTS AND DISCUSSIONS

5.3.1 Influence of Replacement Levels on Packing Characteristics in Simulated Microstructures

The effect of particle packing on the properties of cement pastes and mortars has been well documented. Several studies have focused on optimizing particle packing arrangements to

obtain high performance mixtures (Lange, Mörtel, and Rudert 1997; Kwan and Fung 2009; Vance 2014). In the present study, the PSD of the component materials are used to determine packing characteristics, which can then be related to the early age hydration and strength development in cement-limestone-slag systems. In order to accomplish this, a microstructural stochastic packing model with periodic boundary conditions was implemented (D. P. Bentz 2005). The algorithm packs spherical particles in a 3D REV (representative element volume, chosen here as 300 x 300 x 300 μm^3). The input volume fractions were determined based on the chosen $(w/p)_v$ and the number of particles of each class based on the respective particle size distributions. The key microstructural features such as the average number of nearest neighbors and the particle contact fractions were extracted from the microstructures for analysis. For any particle, the nearest neighbor is defined as a particle that lies either wholly or partially in the radial field of that particle, defined as a field with a radius of (r+5) μm, where 'r' is the radius of the particle. The particle contact fraction is calculated as the fraction of nearest neighbor pairs in the microstructure. For instance, the slag-limestone contact fraction is calculated as the ratio of the total number of contacts between slag and limestone to the total number of contacts in the system (which includes cement-cement, limestone-limestone, slag-slag, and the three unlike particle contacts). Figure 5-3 shows representative 2D slices from 3D microstructures for the mixtures where OPC is replaced at a level of 50% by volume by slag and/or limestone.

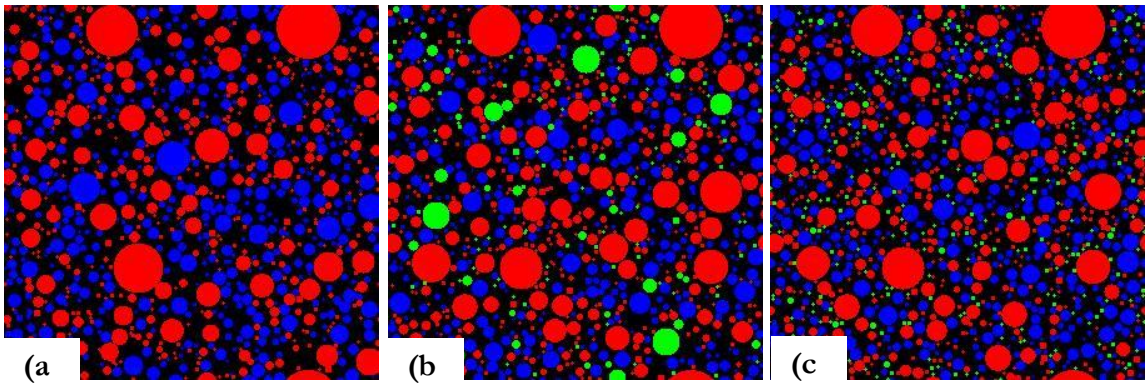

Figure 5-3: 2D slices captured from 3D RVEs generated using the particle packing model for mixtures where 50% of OPC by volume is replaced by slag and/or limestone: (a) OPC-50, (b) BLD-50 and (c) INT-50. The edge length of the RVE is 300μm and w/p ratio by volume is 1.26. Cement is represented in red, slag in blue, and limestone in green.

OPC was modeled using the available particle size distribution for C 150 cement, whereas the PLC was modeled as a two-phase material with contribution from both cement and limestone. However, only the composite particle size distribution was available for PLC and the details of the intergrinding process were not readily available. For the current study, the PSD of limestone in the PLC was determined by assuming that cement in the composite distribution has the same PSD as OPC (this is strictly not true since cement being harder than limestone, will be ground coarser in the intergrinding process; however, this is a necessary assumption). Considering that there is only 12.68 % of limestone in PLC and the median sizes of the OPC and PLC are not very different (11.2 and 10.03 μm), this can be considered to be a reasonable approximation. The limestone PSD in the PLC was then determined by calculating the median size of limestone using rule of mixtures and constructing a normal distribution about the median size. After obtaining individual PSDs of limestone and cement, the distributions were discretized to get the number of particles in a

RVE of size 300 μm using a packing fraction calculated from $(w/p)_v = 1.26$. The results from the particle packing study are presented in Figure 5-4.

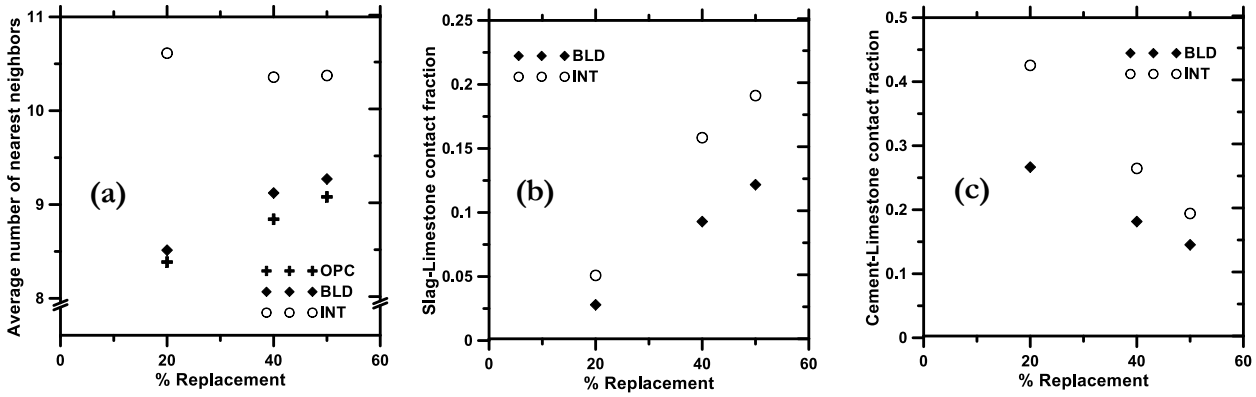

Figure 5-4: Key features extracted from microstructural packing models as a function of clinker replacement level: (a) average number of nearest neighbors, (b) fraction of particle contact between slag and limestone, and (c) fraction of particle contact between cement and limestone.

Figure 5-4 (a) shows the average number of nearest neighbors for a particle in the microstructure. This is an important factor that characterizes the proximity of the reacting species in the RVE which is useful to understand the early age hydration behavior. Replacing OPC with slag or slag and limestone increases the average number of nearest neighbors, and the increase is linear with the replacement level. For the PLC mixture, a slight reduction in the number of nearest neighbors is observed with increasing replacement levels because of the proportional decrease in the amount of finer limestone content. Figures 5-4(b) and 5-4(c) show the contact fraction between slag and limestone, and cement and limestone respectively in the blended and interground systems. Since limestone acts as a heterogeneous

nucleation site as well as participates in the formation of carboaluminates in alumina-rich systems, the proximity of cement and alumina-bearing slag to limestone particles is an important microstructural parameter.

From Figure 5-4(b), it is noticed that the particle contact fraction between slag and limestone increases with increasing clinker replacement level. The particle contact fraction is noted to be much higher in the interground mixtures containing slag compared to the blended ones containing slag. The difference between the particle contact fractions of the interground and blended mixtures increases with the clinker replacement level, even though the fraction of limestone in the blended mixtures is constant at 12.68% and the fraction of limestone in the PLC-slag mixtures decreases in proportion to the clinker content. This is firstly because the limestone in the interground mixtures is much finer compared to the limestone in the blended mixtures and secondly, higher amount of relatively fine slag (d_{50} = 7.61 μm) replaces the cement in the interground mixtures (Table 5-2). This difference in the particle contact fractions is a possible reason for higher initial reactivity of the interground mixtures and the greater synergy between limestone and slag in the interground mixtures, as will be shown later. From Figure 5-4(c), it is observed that the cement-limestone contact fraction decreases with increasing clinker replacement level, as expected. However, the cement-limestone contact fraction in interground mixtures always remains higher than those in the blended mixtures. With increasing replacement level, the difference in particle contact fraction between the blended and interground mixtures reduces. This is because, in both cases, the dominant replacement material (slag) is finer than both the parent cements which are being replaced.

5.3.2 Early Age Hydration Kinetics

The early age hydration kinetics was determined using isothermal calorimetry at a temperature of 25°C as described earlier. The heat flow plots normalized per gram of cement (i.e., the clinker fraction) obtained from isothermal calorimetry are shown in Figures 5-5(a)-(c) for the mixtures shown in Table 5-2. The parent cements in each category of mixtures are represented using solid lines and the samples with partial replacements are represented using dashed lines. Two major peaks, corresponding to the hydration of the silicate and aluminate phases are found in all the calorimetric signatures, as expected. Figure 5-5(a) shows the isothermal calorimetric response of binary OPC-slag mixtures. It is observed that with increasing level of slag replacement, the secondary peak corresponding to the hydration of the aluminate phase becomes more dominant in comparison to the primary peak. This change in the trends is most likely due to the enhanced rate of formation of AFm/AFmc phases (Guillermo Puerta-Falla et al. 2015) and is clearly noticeable in Figures 5-5 (a) – (c) as we go from the parent cement paste to the paste with 50% overall replacement. In the case of binary OPC-slag mixtures in Figure 5-5(a), the reaction follows a more conventional pathway as that of OPC and leads to the formation of AFm phase from the reaction of ettringite with the aluminates. The additional reactive alumina from slag results in a steeper slope of the acceleration curve, and the slope increases with increasing slag content in the paste. Figure 5-5(b) shows the heat evolution for the pastes containing size-matched limestone and slag as OPC replacement. It should be noted that all mixtures in Figure 5-5(b) have the same amount of blended limestone. Therefore, the increase in the slope of the acceleration phase (which is higher than those in binary OPC-slag pastes)

indicates the synergistic effect of slag and limestone (note the increasing slag-limestone particle contacts in Figure 5-4(b)), where the formation of a monocarbonate (AFmc) phase is preferred due to an increase in the overall alumina content in the mixture. Studies have indicated that the formation of AFmc phase is favored over the formation of AFm phase for limestone containing mixtures (Matschei, Lothenbach, and Glasser 2007a). From Figures 5-5(a) and (b), it can also be observed that the primary heat flow peak is higher than the secondary peak for OPC, while for mixtures containing slag and/or limestone, the opposite trend is observed. This is due to the enhanced aluminate hydration in the pastes containing a combination of limestone and slag. The peak also shifts towards earlier times with increasing cement replacement level in both OPC and the limestone blended mixtures, as is noticed in the heat flow plots.

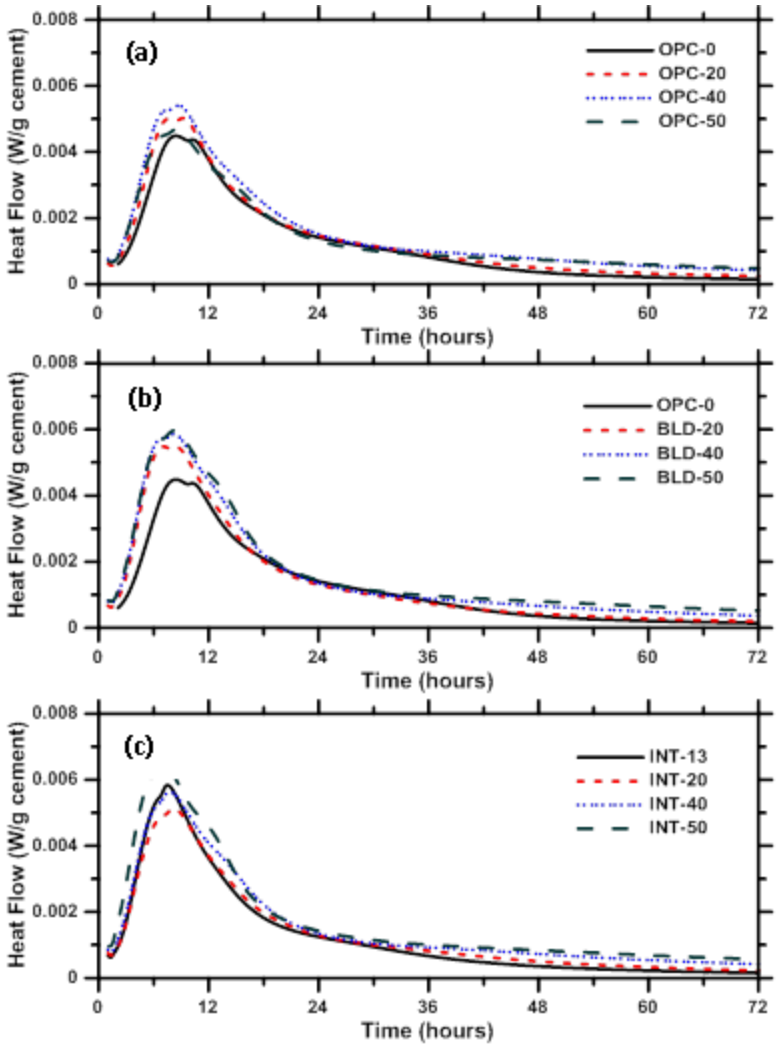

Figure 5-5: Heat flow plotted as W/g cement for: (a) Slag replaced OPC mixtures, (b) Slag and blended limestone replaced OPC mixtures, and (c) Slag-replaced interground mixtures.

Figure 5-5(c) depicts the heat flow response of the parent PLC paste and PLC-slag mixtures. It is noticed that the plain PLC paste and the PLC-slag blends show higher heat flow peaks as compared to other pastes at the same overall replacement level shown in Figures 5-5(a) and (b). Of particular importance among these samples is the parent PLC, which has ~13%

limestone by volume interground with cement clinker. This paste shows a steeper acceleration curve and a higher heat flow peak value as compared to the plain OPC paste. When limestone is interground with portland cement clinker, the softer limestone phase is ground more readily than the harder portland cement clinker, resulting in a finer limestone phase. The increased quantity of limestone fines significantly increases both the reactivity of the limestone and the surface area available for hydration product nucleation (Vuk et al. 2001; A. Kumar, Oey, Falla, et al. 2013), which is observed in the enhanced hydration rates. In the samples where PLC has been partially replaced with slag, beyond a 20% replacement level, it is noted that the rate of the heat flow as well as the peak heat flow increases, in relation to the plain PLC paste. Although the limestone content in the pastes proportionally decreases with increase in the replacement, the increasing slope of the acceleration phase leads to discern that there is an increase in reactivity of limestone in the presence of slag. This synergistic effect of slag and limestone is attributed to the presence of reactive alumina in slag which along with the more reactive PLC, increases the consumption of limestone by the formation of AFmc phase as will be shown later.

It is observed from Figure 5-5 that in the deceleration phase and beyond, the heat flow rate is higher for the mixtures containing slag as compared to plain OPC and PLC pastes. It is also noted that the difference in heat flow response in this phase between the parent cements and the ones containing slag increases with increasing replacement level. This is attributed to the hydration of slag which takes place at a slower pace than cement. The hydration of slag is a slow process and the activity of slag in blended cement systems is predominantly pozzolanic in nature, controlled by the amount of alkali (calcium hydroxide)

produced from cement hydration (Pal, Mukherjee, and Pathak 2003; Odler 2003). Thus, as the cement hydration progresses, it initiates the pozzolanic activity of slag which is noticeable from the deceleration phase in the heat flow rate plots.

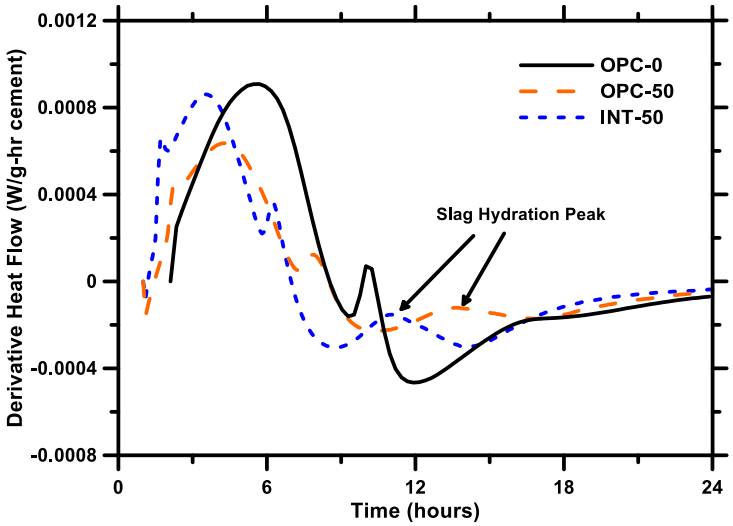

Figure 5-6: The derivative of the heat flow response of OPC and blended/interground mixtures to demonstrate the tertiary peak corresponding to the hydration of slag and accelerated hydration of slag in the presence of limestone.

The characteristic nature of the heat flow curves for all binary and ternary mixtures remains generally similar to that of their parent cement pastes except for a tertiary peak in the slag-containing mixtures, corresponding to slag hydration at about 14 hours (X. Wu, Roy, and Langton 1983; Xuequan Wu, Jiang, and Roy 1990; Lothenbach, Scrivener, and Hooton 2011). This peak, demonstrated as a hump in the deceleration portion of the heat flow curves, can also be identified on close observation of the heat flow plots in Figures 5-5(a – c). This is readily shown in the derivative of the heat flow peak shown in Figure 5-6 for the mixtures containing 50% slag. Similar results are obtained for other replacement levels (not

shown in the figure) as well. The earlier appearance of this peak in the heat flow response of the interground mixture containing limestone and slag as compared with the binary OPC-slag mixture indicates an acceleration in the hydration of slag in the presence of limestone. This could be due to the finer limestone acting as nucleation sites for the hydration of slag.

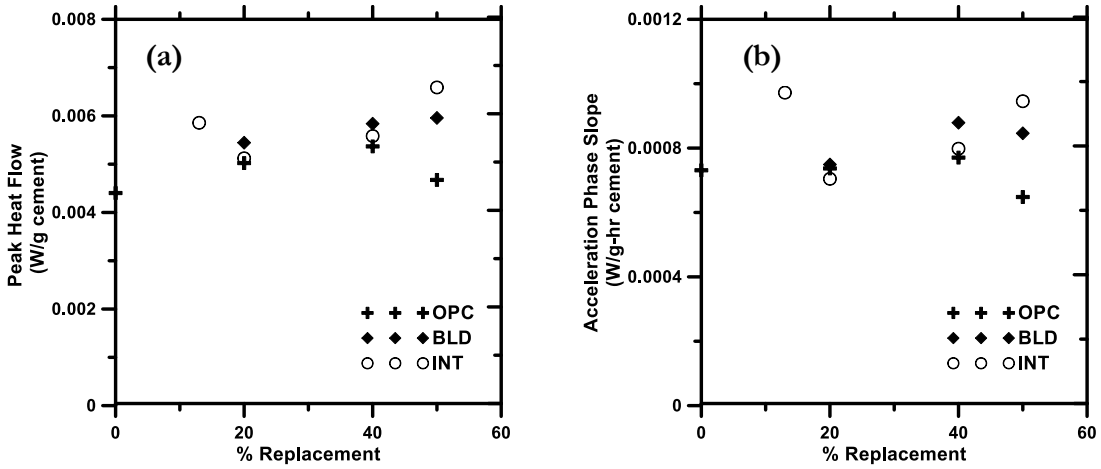

Figure 5-7: (a) Maximum heat flow, and (b) slope of acceleration phase for blended OPC-slag and OPC-limestone-slag pastes, and PLC-slag pastes as a function of clinker replacement level.

To better characterize the hydration behavior and the slag-limestone interaction in these systems, the heat flow peaks for the aluminate phase and the slope of the acceleration phase of the heat of hydration plots are shown in Figure 5-7 as a function of clinker replacement level. The heat flow peak values and the slopes of the acceleration phase generally increase as OPC is replaced by slag in OPC-slag systems until a replacement level of 40%, indicating the influence of a finer (than OPC) replacement material on early age hydration. Beyond that, the dilution effect dominates. At 50% total replacement level, the heat flow peak value as

well as the slope of the acceleration phase are highest for the PLC containing pastes, followed by the blended mixture. This is attributed to the increase in the reaction rates due to the reactive alumina from slag and the finer limestone from the PLC. The rate of heat flow in the acceleration phase as well as the peak heat flow value is positively influenced by acceleration due to the fine filler effect in the presence of limestone and the slag-limestone interaction, and negatively influenced by dilution effect due to the presence of limestone and slag fillers. The latter is better understood from the cumulative heat flow plots plotted per gram of binder (cement + slag) in Figure 5-8.

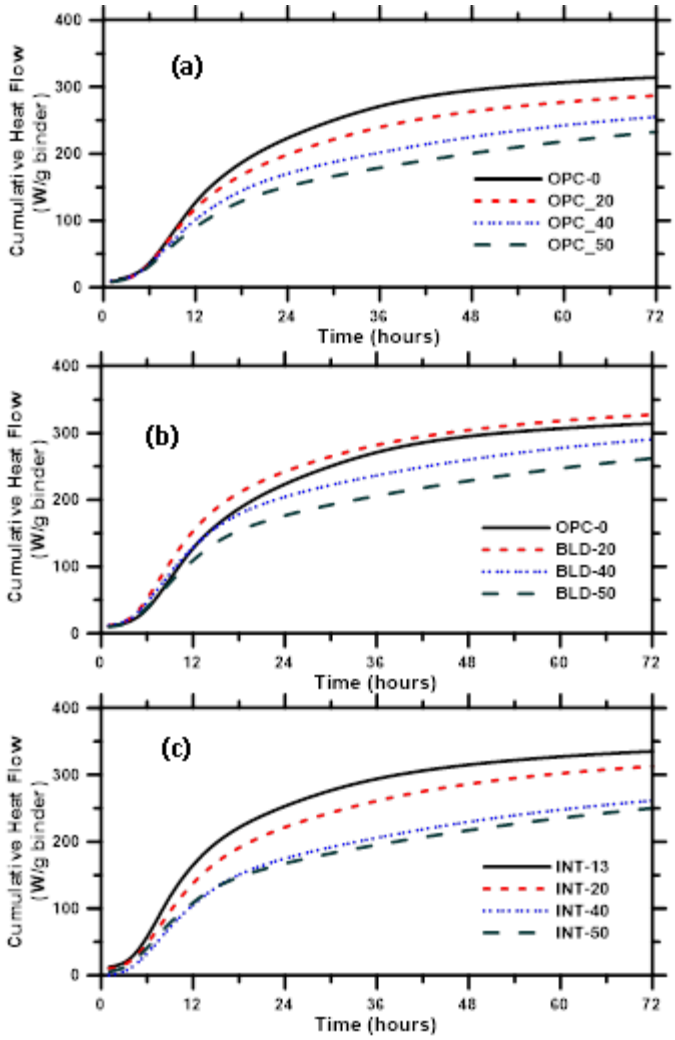

Figure 5-8: Cumulative heat of hydration in W/g of binder (cement + slag) for: (a) volumetric replacement of OPC by slag, (b) OPC replaced by limestone-slag blends, and (c) interground portland limestone cement (PLC) replaced by slag

The cumulative heat content is an indication of the degree of hydration of the overall binder. A combination of cement and slag is considered as the binder. It is observed from Figure 5-8 that the cumulative heat released for all the mixtures is generally lower than that of the OPC paste at all times. This has important implications in early age thermal cracking of

concretes. The cumulative heats are, though, not proportional to the cement content in the mixtures, which is due to the enhanced formation of the AFmc phase resulting in the consumption of limestone, and the hydration of slag. However, the contribution from the latter is not quite significant at 72 hours due to the latent hydraulicity of slag. On closer observation, it is found that the cumulative heat flow values for the blended limestone mixtures containing slag are higher than those of the OPC pastes containing slag alone at the same total replacement levels. This once again is an indication of the increased limestone reactivity in the presence of slag.

5.3.3 Compressive Strength Development

Compressive strengths of 50 mm mortar cubes at ages of 1, 3, 7, 28, 56 and 90 days were determined as described in Section 2.2.2. Figure 5-9 shows the evolution of compressive strength over these ages for the mixtures considered in this chapter.

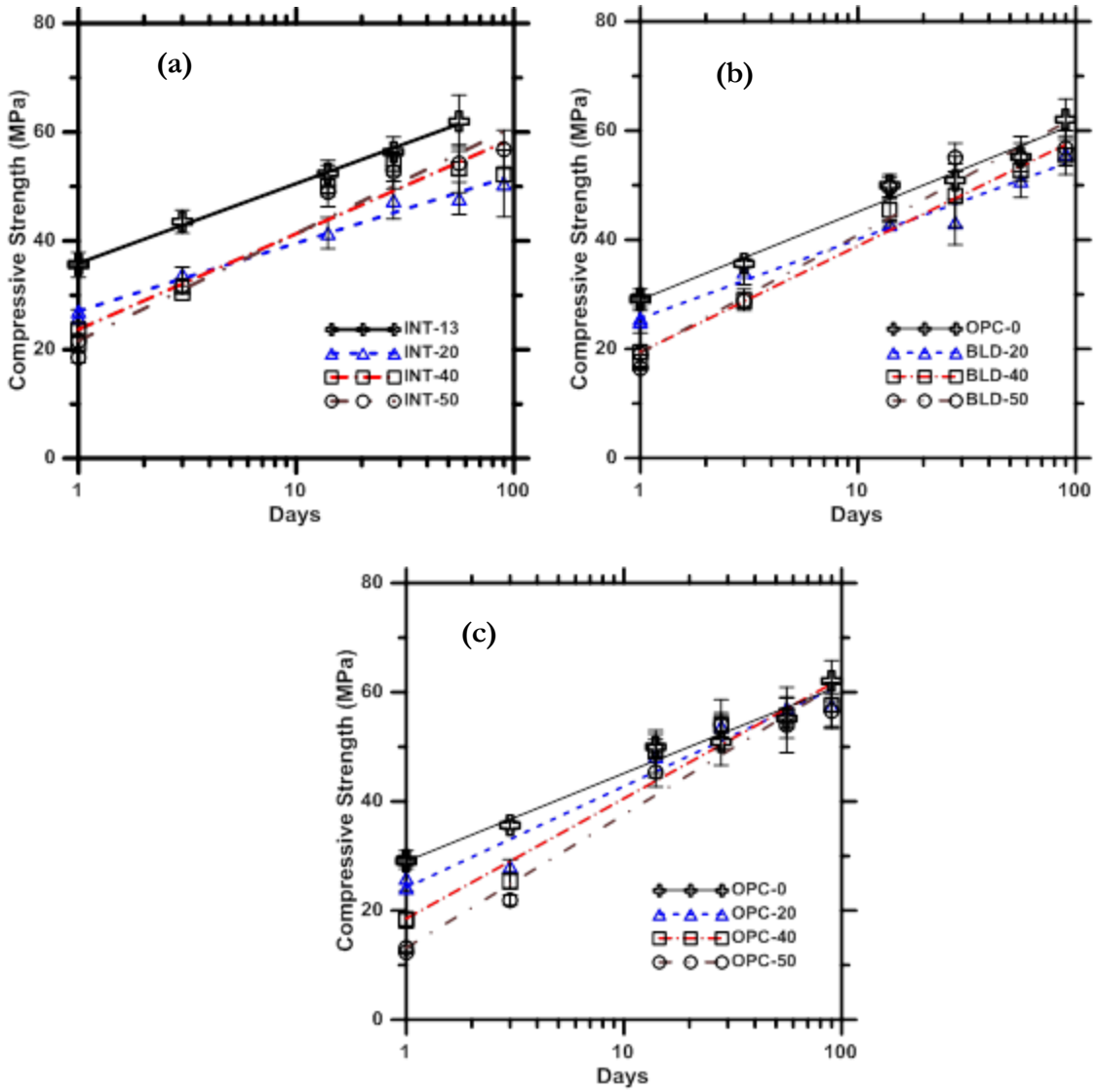

Figure 5-9: Compressive strength development of mortars with time: (a) volumetric replacement of OPC by slag, (b) OPC replaced by limestone-slag blends, and (c) interground portland limestone cement (PLC) replaced by slag

With respect to early age strengths, it can be immediately observed from all plots in Figure 5-9 that increasing cement (OPC or PLC) replacement levels decrease the compressive strengths as expected. This is attributed to the higher volume of hydration products

produced in the mixtures with lower overall cement replacement at early ages. It is also observed from Figure 5-9(a) that the 1 and 3-day strengths are rather proportional to the OPC content in the mixtures, indicating the effect of dilution in the early stages of hydration even though some slag hydration has been noticed in the isothermal calorimetry curves. It is well known that the hydration of slag is minimal at early ages (Beushausen, Alexander, and Ballim 2012; Menéndez, Bonavetti, and Irassar 2003). However, in mixtures containing blended limestone (Figure 5-9(b)), the compressive strength values at early ages are slightly higher than when dilution is dominant as in the case of OPC-slag blends. This is because of the presence of fine limestone particles which act as nucleation surfaces and enhance the hydration process, and the increase in the activity of limestone in the presence of slag which was explained earlier. It should be noted that the silicate and aluminate components of slag have different rates of reaction, and the aluminate phase reacts more rapidly as compared to the silicate phase (24). For the slag-PLC blends in Figure 5-9(c), the 3-day strengths are independent of the replacement levels. This is likely attributed to the dilution effect being compensated by the hydration of slag and the increased reactivity of cement in the presence of finer limestone. The hydration of slag occurs earlier in the PLC-slag blends, more particularly in the mixtures containing 40% or 50% as discussed in the previous section. The compressive strength values increase rapidly between 3 and 14 days of hydration. This is due to the formation of secondary C-S-H as a result of hydration and pozzolanic reaction of slag during this period. The extent of increase is more evident in the mixtures with higher replacement levels. From Figures 5-9 (a-c), it can be clearly seen that the rate of increase in strength for mixtures with 40% and 50% replacement levels is much higher as compared to

the mixtures with 20% replacement. This is because of the pozzolanic activity of slag in these mixtures. The pozzolanic behavior is due to the reaction of the glassy phase which corresponds to the silicates present in the slag, whereas the increase in the reactivity of limestone at early ages is attributed to the presence of aluminates. Comparing between the OPC-limestone-slag blended mixtures in Figure 5-9(b) and the PLC-slag mixtures in Figure 5-9(c), it can be noticed that the difference in strengths for the parent cement paste and the blended mixtures containing slag are higher for the PLC-slag system. This can be attributed to the much higher early age strength of the parent PLC mortar owing to its increased fineness.

For the OPC-slag blends, the later age strengths (56 days and beyond) are comparable to that of the parent OPC mixture. The hydration of slag and its pozzolanicity is responsible for this behavior as will be shown using thermal analysis results later. A similar observation is noted for the OPC-limestone-slag blends. For the PLC-slag blends, the strengths are slightly lower than that of the plain PLC mortar, attributed to the increased fineness and reactivity of the PLC. Comparing Figures 5-9(a-c), it is observed that the mixtures with 40% or 50% replacement levels obtain later-age strengths higher than those of the mixtures with 20% replacement level at different times depending on the mixture constitution. For the OPC-slag mixtures, this happens between 56 and 90 days whereas for the OPC-limestone-slag blends, this occurs between 10 and 14 days. For the PLC-slag mixtures, this occurs before 7 days, suggesting increased synergistic performance between limestone and slag. Since limestone is ground much finer in PLC, its reactivity with aluminates from slag is expected to be higher, which is represented in increased carbonate consumption for these

systems as shown later. In most cases, the later age strengths at 56 days and 90 days for all the mixtures approach the strength of mixtures made solely using their parent cements – OPC or PLC.

The lower rate of strength gain in the binary OPC-slag mixtures as compared to the ternary mixtures containing limestone can be explained using the difference in reactivity of slag in the two systems. It is known from previous studies (W. Chen 2007, 2; Kolani et al. 2012) that the hydration of slag in slag-blended systems is proportional to the amount of alkalis (CH). The production of CH, which is a result of the hydration of OPC, is lower in the case of the OPC-slag mixtures as compared to the mixtures containing limestone. Vance et al. (Vance, Aguayo, et al. 2013) showed that hydration kinetics of OPC is positively influenced in the presence of fine limestone and therefore, in absence of fine limestone, lower relative quantities of CH have a detrimental effect on the reaction of slag in the binary OPC-slag mixtures.

To obtain a better understanding of the influence of limestone and slag on the early and later age strengths, the compressive strengths at 3 and 56 days are represented as a function of the clinker factors in Figures 5-10(a) and (b) respectively. Clinker factor is defined as the ratio of the volume of cement (OPC) in the dry mixture to the total volume of the powder. It is therefore an effective criterion which indicates the sustainability of the mixture. From Figure 5-10 (a), it is noted that the 3-day compressive strengths of both the blended and interground mixtures containing limestone are higher than those of the OPC-slag blends at all clinker factors, signifying the influence of limestone in the early-age strength development process. Even at such an early age, below a clinker factor of 0.6, there is no strength

reduction for both the blended and interground systems containing limestone, which is attributable to the limestone-slag interaction as well as the particle packing in these systems, as discussed in an earlier section. It is noted that the slag-limestone interaction increases (Figure 5-4(b)) as the total level of replacement increases in these systems, which leads to increased slag reaction, with limestone acting as a heterogeneous nucleation site. The average number of nearest neighbors also increases as shown in Figure 5-4(a), which leads to increase in the probability of formation of reaction products and therefore increases the degree of reaction. The two factors mentioned above play an important part in counteracting the effect of dilution at early ages and lead to increase in strength at higher level of replacement. At later ages, as observed from Figure 5-10(b), the compressive strengths remain rather unchanged irrespective of the clinker factor for all the mixtures.

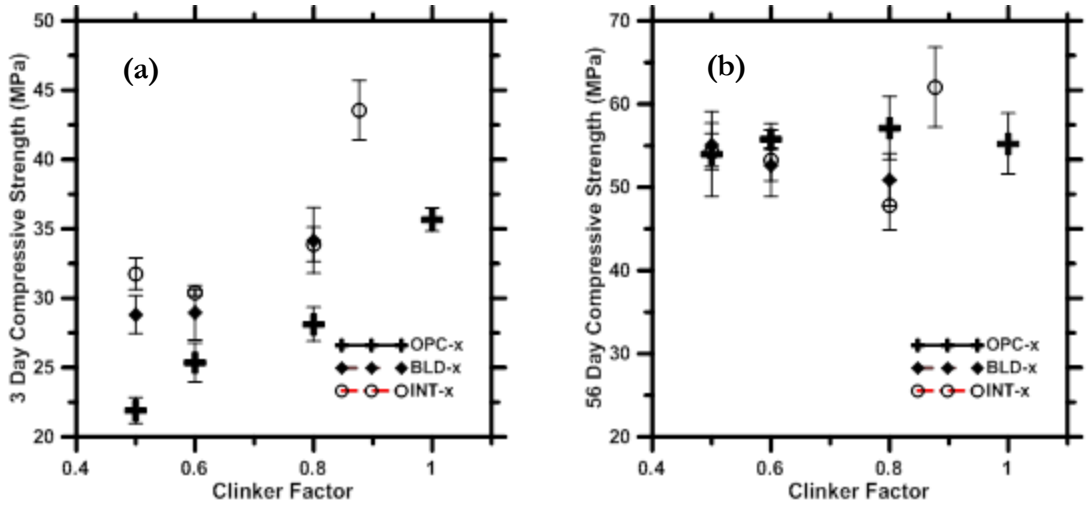

Figure 5-10: Compressive strength of all the binder systems studied as a function of clinker factor at: (a) 3-days and (b) 56-days

5.3.4 Hydration Products

The progress of the hydration reaction was investigated using thermal analysis techniques. Representative differential thermogravimetric (DTG) curves are shown in Figure 5-11. These curves show several distinguishable features: (i) all pastes show pronounced peaks at about 130°C and 450°C, corresponding to the decomposition of C-S-H and ettringite, and the dehydroxylization of calcium hydroxide respectively, (ii) all pastes containing limestone show peaks at about 180°C corresponding to decomposition of hemi/mono-carboaluminates (Damidot et al. 2011) and at approximately 750°C corresponding to the decarbonation of calcium carbonate.

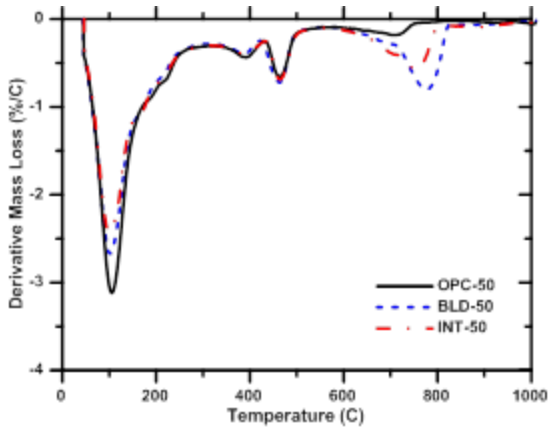

Figure 5-11: 28-day representative DTG profiles of pastes

5.3.4.1. Non-evaporable water contents

Figures 5-12 illustrates the evolution of non-evaporable water (w_n) content for all the pastes after 3 and 28 days of hydration. Non-evaporable water content is considered to be one of the key indicators of the progress of the hydration reaction process in hydraulic cements.

An increase in w_n with time is noticeable between 3 and 28 days. In case of pastes containing slag, especially after 28 days, w_n denotes the contribution of the cement and the slag fractions in the paste. Here, the progress of hydration in all the blended and interground mixtures studied is evaluated as a function of the overall clinker replacement level, the amounts of limestone and slag, and the process of intermixing (intergrinding vs. blending).

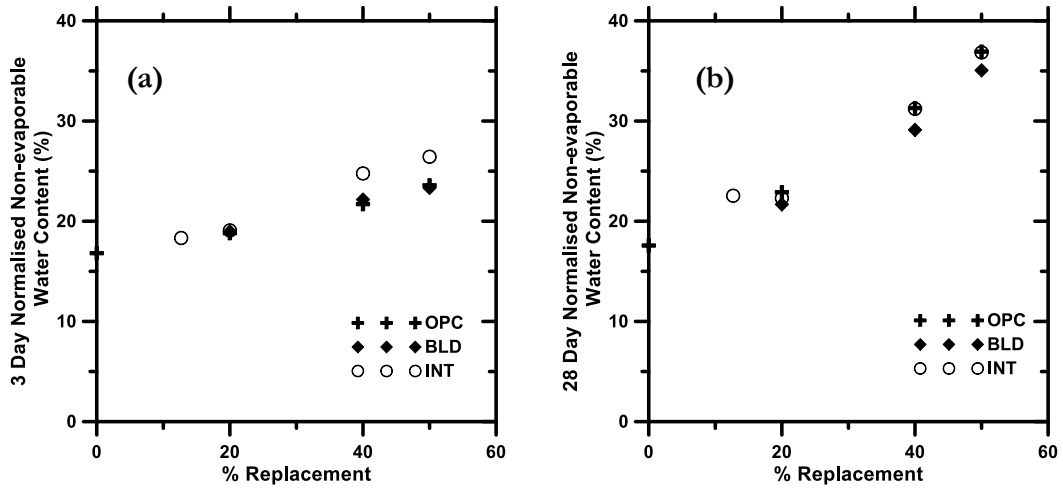

Figure 5-12: Non-evaporable water content normalized with respect to clinker factor as a function of the clinker replacement level at: (a) 3 Days and (b) 28 Days

As the slag content in the OPC-slag mixture increases, the normalized w_n also increases at early ages (Figure 5-12(a)). However, this increase is not proportional to the clinker content in the mixes. This can be explained based on the fact that slag has slower reaction kinetics than cement, and it behaves mostly as inert filler at early ages. It may be argued that the filler effect of slag should lead to a higher cement hydration at higher replacement values; however, that is compensated by the dilution effect. It is also noted that the 3-day values for

w_n are higher for the PLC-slag mixtures in comparison to the OPC-slag and OPC-slag-limestone blended mixtures. This is attributed to the enhanced hydration at early ages in the interground mixtures due to the presence of finer limestone particles acting as nucleation sites, as also suggested from the particle packing model with respect to the increased cement-limestone interaction (Figure 5-4(c)). At later ages, the hydration of cement continues to produce increased quantities of CH, which enhances the hydration of slag (Kolani et al. 2012). Thus, when the 28-day w_n values are considered, they increase more significantly with increasing slag content as can be noticed in Figure 5-12(b). Here, it is also noticed that the w_n values at a particular replacement level are relatively invariant of the type of intermixing or the presence/absence of limestone.

5.3.4.2. CH contents

Figure 5-13 presents the CH contents normalized by the clinker fraction for all the pastes. A cursory look at the figures will result in the deduction that the actual CH contents (non-normalized) reduce with increase in replacement level as expected, primarily attributed : (i) at early ages to the reduced clinker fraction in the mixture, and (ii) at later ages to their consumption by slag to produce secondary C-S-H. Between 3 and 28 days, the normalized CH contents do not change appreciably, showing that the additional CH produced by the cement hydration during this period is consumed by the pozzolanic reaction of slag to produce additional C-S-H gel. This is apparent in the increase in w_n values ranging between 15% and 50% between 3 and 28 days, depending on the replacement level.

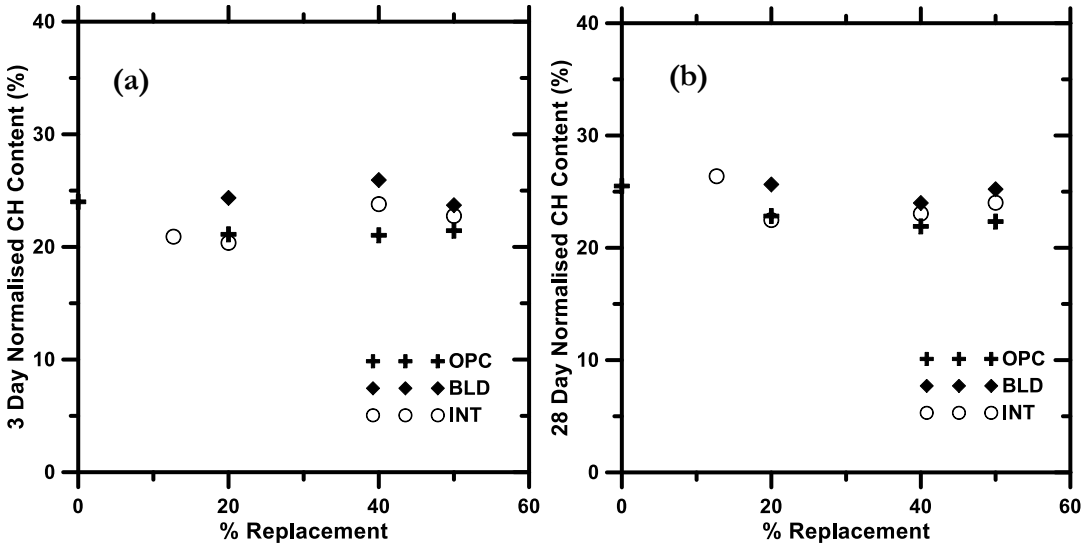

Figure 5-13 – CH content normalized with respect to clinker factor plotted as a function of the clinker replacement level at: (a) 3 Days and (b) 28 Days

5.3.4.3. Carbonate consumption

A quantification of the consumption of carbonate is essential to establish the reactivity of limestone in the cementitious systems and identify conditions under which this can be maximized to produce performance-equivalent low cement content concretes. Figures 5-14(a) and (b) respectively show the carbonates consumed after 3 and 28 days of reaction in the blended and interground systems containing slag. From Figure 5-14 (a), it is observed that more than 10% of the carbonates are consumed in the PLC-slag mixtures within the first 3 days while for the blended OPC-slag-limestone mixtures, the consumption is around 5%. This is mostly attributed to the finer limestone present in the interground (PLC-based) mixtures. However, for both the cases, the consumption of carbonates at 28 days is similar which indicates an increased rate of consumption of limestone in the blended systems at

later ages, possibly due to the slower reactivity of coarser limestone in the blended pastes with the available aluminates. It is also noticed from Figure 5-14 (b) that the consumption of carbonate increases with the clinker replacement level, which is due to the formation of AFmc phase as will be quantified below.

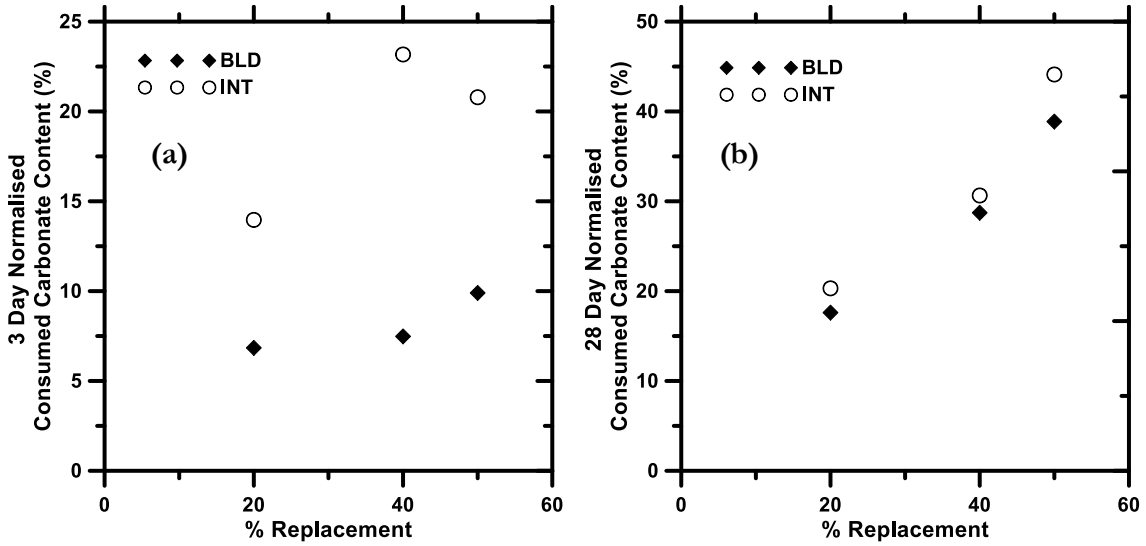

Figure 5-14: Consumed carbonate content normalized with respect to clinker factor plotted as a function of the clinker replacement level at: (a) 3 Days and (b) 28 Days

The higher reactive alumina content present in slag (8.68%) alters the reaction pathway and leads to the formation of carboaluminates instead of monosulfoaluminates. As a result of this, all mixtures containing limestone and slag show an accelerated secondary peak in the isothermal calorimetry plots in the initial hydration phase corresponding to the formation of carboaluminates. To quantify the synergistic effect of slag and limestone, the amounts of AFmc phase were determined from the TGA plots in the temperature range between 150 ºC

and 200 ºC (Damidot et al. 2011). Figure 5-15 shows the relationship between consumed carbonate content and the AFmc phase content in these mixtures after 3 and 28 days of hydration. An increasing amount of AFmc phase corresponds rather linearly to an increase in carbonate consumption (or reduction in carbonates detected by thermogravimetry), which is explained by the fact that the carbonate reacts with the alumina present in cement and slag to form mono/hemi carboaluminates. However it should also be noted that not all alumina present in slag reacts with the carbonate to form the AFmc phase and is also bound in the denser pozzolanic C-S-H phase formed by the hydration of slag (Lothenbach, Scrivener, and Hooton 2011).

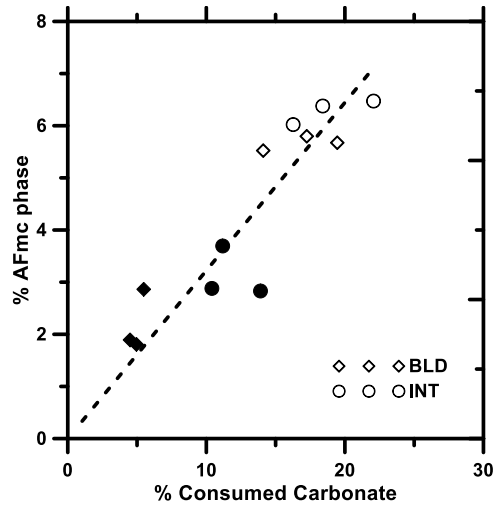

Figure 5-15: Plot showing positive correlation between the fraction of consumed calcium carbonate and AFmc phase in interground and blended mixtures. The solid symbols correspond to 3-day values and the empty symbols correspond to 28-day values.

The blended limestone in the OPC-slag-limestone mixtures and the interground limestone in the PLC mixtures are the only major source of carbonate in the respective pastes. There is a

small amount of limestone in the OPC, and the residual carbonate contents in the blended pastes are adjusted with the amount of residual carbonate content of OPC at the same hydration age. It has been noted in previous studies that limestone participates to a limited extent in the cement hydration process by providing nucleation sites for the formation of hydration products and forming carboaluminates and hemi-carboaluminates by reacting with alumina phases present in the mixture and thereby stabilizing ettringite (Kim et al. 2013). In alumina-bearing pozzolanic material incorporated cement systems, the effect of limestone in stabilizing ettringite is much more obvious, which is noticeable in the results shown in Figure 5-15.

5.3.5 Pore Structure

The pore structure of the pastes was determined using MIP. Even though the pore size distribution determined using MIP have been shown to be prone to error (Diamond 2000; Moro and Böhni 2002b), they are useful for relative comparison.

To explore the influences of the addition of slag and limestone on the pore structure of these systems, the porosity and critical pore diameters are presented in Figure 5-16. Several key aspects are noted from Figure 5-16 (a). The OPC paste has a lower porosity than all the other mixtures. The PLC-slag mixtures have comparable or slightly lower porosities than their blended counterparts at the same total level of replacement. This is likely due to the enhanced nucleation effect of finer limestone from the interground cement, which accelerates the cement hydration as well as slag hydration process as was explained in the previous sections. The slag-OPC binary blends have the least porosity as compared to all mixtures at the same clinker replacement level. In other words, from a total pore volume

standpoint, the absence of limestone results in lower porosities because both the cement and slag are capable of hydrating and producing reaction products. However, as the overall replacement level increases, it is noted that the porosity increases for all the pastes, with the highest value noted for the pastes with 50% overall replacement level in each of the categories. This is due to the reduction in the cement content of the paste. Thus, although the total binder content remains the same, the decrease in the cement content decreases the total volume of hydration products, since slag does not achieve the same degree of hydration as compared to cement after 28 days of hydration (Escalante et al. 2001). On the other hand, it should also be noted that the increase in porosity is not substantial in relation to the cement replacement level. This is because the decrease in cement content is balanced to an extent by the pozzolanic activity of slag (Kolani et al. 2012; Richardson and Groves 1992) and the limited participation of limestone in the reactions.

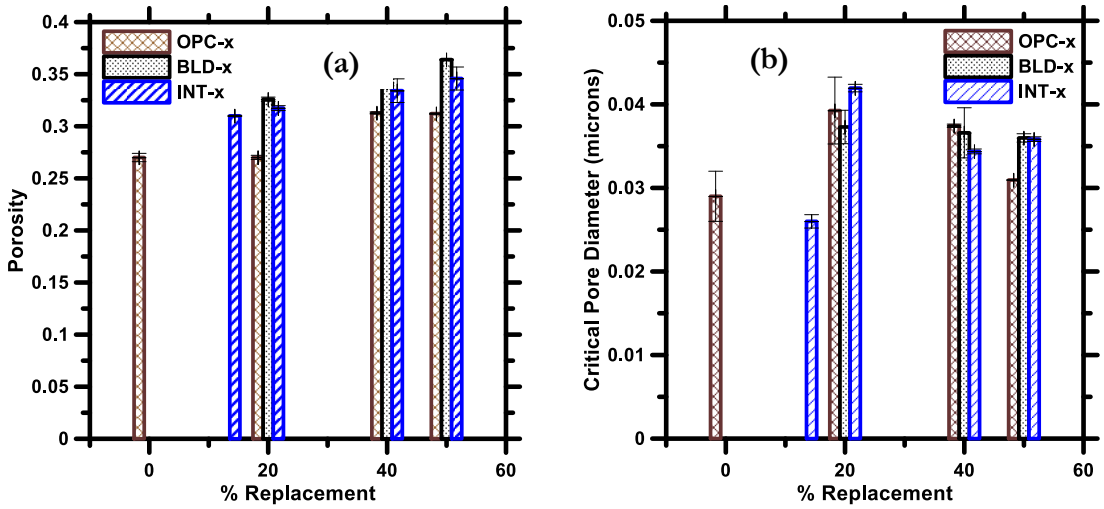

Figure 5-16 – (a) Porosity and (b) critical pore diameter for blended OPC-slag and OPC-limestone-slag pastes, and PLC-slag pastes at 28 days as a function of clinker replacement level.

Figure 5-16 (b) shows the critical pore diameter in all the mixtures. The critical pore diameter is representative of the permeability of the sample, which is critical to the durability of concrete. It is noted that the critical pore diameter decreases with increasing level of replacement, indicating pore size refinement which is commonly reported with the use of pozzolanic materials (Courard and Michel 2014). For the PLC-slag mixtures and the OPC-limestone-slag blended pastes, the critical pore diameters at higher replacement levels are similar to or lower than those of companion mixtures at a lower cement replacement level even when the corresponding porosities are higher. In addition, for all the pastes, the critical pore diameter varies within a small range (between 0.025 and 0.04 μm) demonstrating that the reduction in clinker factor does not adversely influence the transport-controlling pore sizes in systems containing limestone and slag.

5.4. CONCLUSIONS

The development of high volume cement replacement using a combination of slag and limestone was discussed in this chapter. The influence of blending limestone and slag with OPC or using slag along with PLC where limestone is interground during the manufacturing process, was evaluated in detail. The overall clinker replacement levels varied from 20% to 50% by volume. A particle packing model was utilized to quantify the changes in the number of nearest neighbors and particle contacts, which have a bearing on the hydration and reaction product formation in these systems. The heat flow peak values and the slope of the

acceleration phase from isothermal calorimetry were found to be highest for the interground limestone-slag systems, followed by the blended ternary systems, indicating the synergistic effect of limestone and slag in these mixtures. The slag hydration was also noted to be accelerated in the presence of limestone, with the finer limestone in interground systems providing increased acceleration than the blended ones.

The compressive strengths were found to be lower for the binary and ternary systems at early ages than their parent OPC or PLC counterparts because of the dilution effect. However, the presence of limestone resulted in an increased strength than the OPC-slag blends, in both the blended and interground states. The later age strengths, even at 50% total replacement were similar for the blended limestone-slag, and OPC-slag mixtures. The strength gain between 3 and 28 days was found to be the highest in PLC-slag mixtures, followed by the OPC-limestone-slag blends, and it was the lowest for the OPC-slag binary mixtures. This further indicates the influence of limestone in these systems. As a function of the clinker factor in the mixtures, the later age compressive strengths remained invariant of the limestone and slag addition or method of addition. The synergistic effect of slag and limestone was also confirmed by the linear correlation between the consumption of carbonates and the formation of AFmc phase in the pastes. The presence of finer limestone in the PLC containing pastes led to increased carbonate consumption and thereby increase in the formation of carboaluminates. Although the total porosity in the pastes at later ages increased with cement replacement levels due to the incomplete reaction of slag, the critical pore diameters decreased, indicating pore size refinement in the presence of slag and limestone.

CHAPTER 6[5]

MICROSTRUCTURAL PACKING- AND RHEOLOGY-BASED BINDER SELECTION AND CHARACTERIZATION FOR ULTRA-HIGH PERFORMANCE CONCRETE (UHPC)

6.1. INTRODUCTION

Ultra-high performance concrete (UHPC) belongs to a special class of cementitious materials that shows very high mechanical properties and enhanced durability. Compressive strengths in excess of 120-150 MPa are generally reported for UHPC mixtures (Yoo and Banthia 2016; B. Graybeal 2011). When reinforced with high volumes of steel fibers (in the order of 2-3% by volume), these composites exhibit high tensile strengths and strain hardening (Gesoglu et al. 2016), making them useful for many high-end structural applications. For example, the U.S Federal Highway Administration and several state Departments of Transportation have been investigating the use of UHPC for deck-level connections between modular precast components that are heavily stressed in service (Saleem et al. 2011; B. A. Graybeal 2011). Use of UHPC for blast protection has also been reported (Yi et al. 2012). While immense efforts have focused on the use of UHPC for such special applications, the downside is the high cost of these mixtures. Thus it is critical to develop cost-effective UHPC using commonly available materials and conventional concrete

[5] This chapter is derived from the publication: Arora, A., Aguayo, M., Hansen, H., Castro, C., Federspiel, E., Mobasher, B., & Neithalath, N. (2018). Microstructural packing-and rheology-based binder selection and characterization for Ultra-high Performance Concrete (UHPC). Cement and Concrete Research, 103, 179-190.

production methods (C. Wang et al. 2012; Kay Wille, Naaman, and Parra-Montesinos 2011; Kay Wille and Boisvert-Cotulio 2015).

Several studies in the recent past have elucidated the mixture design of UHPC, to achieve high mechanical properties and high durability. This is generally accomplished through a combination of a high cement content, low water-to-binder ratio (w/b), high admixture dosage (water reducing and viscosity modifying admixtures), elimination of coarse aggregates, and incorporation of high volumes of steel fibers (C. Wang et al. 2012; Bakhshi, Barsby, and Mobasher 2014; Yang et al. 2009; Yoo and Yoon 2015). However, the very high cement content poses durability- and sustainability-related challenges (Randl et al. 2014; Aldahdooh, Muhamad Bunnori, and Megat Johari 2013). This has led to the use of a variety of cement replacement materials in UHPC, including commonly used materials such as fly ash, slag, silica fume, and metakaolin (Yu, Spiesz, and Brouwers 2014a, 2015; Sobuz et al. 2016; Alsalman, Dang, and Micah Hale 2017; Tafraoui, Escadeillas, and Vidal 2016; W. Huang et al. 2017a). However, contrary to high performance concretes (HPC) that generally limit silica fume or metakaolin contents to less than 10% by mass of the cementing materials, UHPCs can contain much higher proportions of these materials for enhanced mechanical performance. This increases both the material and processing cost of UHPC. Moreover, the presence of large amounts of fine materials enhances chemical and autogenous shrinkage, resulting in increased early-age cracking (Schachinger et al. 2002). The use of fine limestone powder as a cement replacement/filler material in UHPC has also been investigated (W. Huang et al. 2017b). The use of an inert filler like limestone is a particularly attractive strategy since the very low w/b used in UHPC results in only a fraction of the cement

getting hydrated. Other less common cement replacement materials and additives such as nanosilica (Yu, Spiesz, and Brouwers 2014a; W. Li et al. 2015), nano metakaolin (Muhd Norhasri et al. 2016), rice husk ash (Van Tuan et al. 2011), glass powder (N. A. Soliman and Tagnit-Hamou 2016), and graphite and carbon nanofibers (Meng and Khayat 2016) have also been incorporated in the formulation of UHPC.

Along with the selection of raw materials, it is also important to ensure adequate packing of particles (both fine and coarse) to achieve a dense microstructure, which is crucial towards mechanical and durability properties. Several analytical packing tools have been used in the formulation of UHPC (de Larrard and Sedran 1994a). In this chapter, binders for UHPC are selected based on microstructural packing-based and rheology-based criteria. Packing is a function of particle sizes and their distribution, while sizes and distribution along with particle surface characteristics influence the rheology. A microstructural packing algorithm is used to determine parameters relevant to particle packing. Yield stress, plastic viscosity, and mini-slump spread are used as the rheological parameters. Mixture selection is based on either individual considerations of the microstructural and rheological parameters, or on combinations of the parameters. The proposed method relies on the premise that, for low w/b concretes where only a fraction of the cement hydrates,: (i) improved packing through the use of cement replacement materials and fine fillers is a better means of strength enhancement than increasing cement content, and (ii) better rheology helps better dispersion of the grains, aiding in mixture placement as well as hydration in the presence of low amounts of water, and consequently better mechanical properties. The hydration product

formation, pore structure, and the strength of the selected binders are investigated in detail to establish their applicability to UHPCs.

6.2. EXPERIMENTAL PROGRAM

6.2.1 Materials and Mixtures

The materials used in this chapter include a Type I/II ordinary portland cement (OPC) conforming to ASTM C 150, Class F fly ash and metakaolin conforming to ASTM C 618, slag conforming to ASTM C 989, limestone powder conforming to ASTM C 568, and micro silica (silica fume) conforming to ASTM C 1240. Limestone powders with two different median particle sizes (1.5 μm and 3.0 μm) were used to ensure improved particle packing. The particle size distribution (PSD) curves of these materials are shown in Figure 6-1. The chemical compositions and physical characteristics of these materials are shown in Table 6-1.

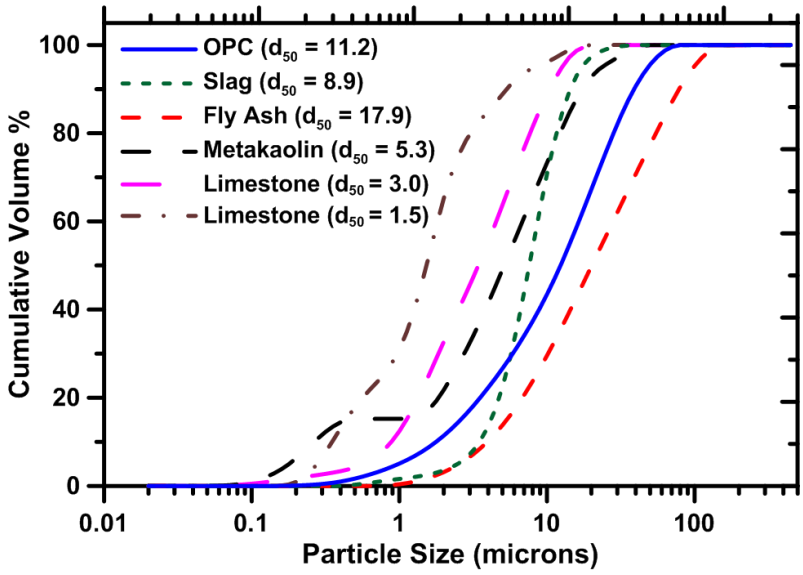

Figure 6-1: Particle size distribution curves for cement, fly ash, slag, metakaolin, and limestone powders. The median size in microns is shown in parentheses.

Table 6-1: Chemical composition of the materials used.

Components of the binder	Chemical composition (% by mass)						
	SiO_2	Al_2O_3	Fe_2O_3	CaO	MgO	SO_3	LOI
OPC	19.60	4.09	3.39	63.21	3.37	3.17	2.54
Slag (S)	39.41	8.49	0.37	35.53	12.05	2.83	1.31
Fly Ash (F)	58.40	23.80	4.19	7.32	1.11	3.04	2.13
Metakaolin (K)	51.70	43.20	0.50	-	-	-	0.16
Micro silica (M)	> 90.0	-	-	< 1.0	-	-	-

Binary, ternary and quaternary blends were proportioned by mixing different amounts of these replacement materials with OPC. The total cement replacement level generally varied between 20 and 30% by mass of OPC. Binary mixtures consisted of commonly employed cement replacement materials including fly ash, slag, micro silica or metakaolin. In the ternary and quaternary blends, the replacement levels of fly ash or slag were varied between 10 and 25%, while those of silica fume or metakaolin were varied between 7.5 and 10%. Fly ash or slag were considered to be the primary cement replacement materials in ternary and quaternary blends because of their abundance and the larger OPC replacement levels that can be accomplished. Limits to the amounts of micro silica and metakaolin were necessary to ensure adequate dispersion of these materials within the paste. Limestone powders of two different median sizes, either individually, or in equal parts, were used to supplement the binary and ternary mixtures with even finer sizes that they were deficient in, to enhance particle packing. The limestone content varied between 5 and 10%. Table 6-2 shows the proportions of all the 33 different mixtures (one UHP-control, one HP-control, and 31 UHP

pastes) evaluated in the initial phase of this work. All the ultra-high performance (UHP) pastes were proportioned using a volumetric water-to-powder ratio, $(w/p)_v$, of 0.63 (corresponding to a mass-based $(w/p)_m$ of 0.20; 0.22 when the water in the HRWR is also added). In addition to the control UHP paste ($(w/p)_m$ of 0.20), a high performance OPC paste with a $(w/p)_m$ of 0.32 was also proportioned. A commercially available high range water reducer (HRWR) (Master Glenium 7500, manufactured by BASF[6]) was used at 5% by mass of the powder to improve the workability of the UHP pastes. In Table 6-2, UHP-control refers to the control mixture made using OPC alone and a $(w/c)_m$ of 0.20, and HP-control refers to the mixture made using a $(w/c)_m$ of 0.32.The HRWR dosage for the HP-control mixture was 2% by mass of the powder. Fly ash is represented as F, Slag as S, limestone as L, micro silica as M, and metakaolin as K.

Table 6-2: Mixture proportions for pastes evaluated in this study. All the pastes except HP-Control were proportioned using a $(w/p)_m$ of 0.20.

Mixture composition	Replacement material (% by mass of cement)			
	Fly Ash (F)/ Slag (S)	Metakaolin (K)	Microsilica (M)	Limestone (L); d_{50} of 1.5 or 3 μm[#]
UHP-control	0	0	0	0
HP-control	0	0	0	0
OPC + F/S	20, 30	0	0	0
OPC + M	0	0	10, 20	0

[6] Certain commercial products are identified in this paper. However such references do not indicate endorsement of the product, nor does it imply that there are no other commercial products that can satisfy these requirements.

OPC + K	0	10	0	0
OPC + F/S + M	10, 20	0	10	0
OPC + F/S + K	10, 20	10	0	0
OPC + F/S + L	20	0	0	10a, 10b
OPC + F/S + L	25	0	0	5a, 5b
OPC + F/S + M + L	17.5	0	7.5	5b,5c
OPC + F/S + K + L	17.5	7.5	0	5b,5c

[#]The subscripts 'a', 'b' and 'c' along with the dosage of limestone powder indicate the type of limestone used in the mixture: 'a' – 1.5 μm limestone, 'b' – 3 μm limestone and 'c' – 50% 1.5 μm + 50% 3 μm limestone.

6.2.2 Experimental Methods

All dry powders were thoroughly mixed prior to wet mixing. Paste mixing was performed in accordance with ASTM C 1738 using a M7000 high speed shear mixer. The following mixing sequence was used: (i) all water and HRWR was added to the mixer, (ii) the blended dry powders were then added as the mixer was run at 4000 rpm for approximately 30 s, (iii) the mixer was then run at 12,000 rpm for 30 s, (iv) the paste was allowed to rest for two minutes, and (v) final mixing of the paste was carried out at 12,000 rpm for 90 s.

6.2.2.1. Rheological studies

The rheological characteristics of all the pastes were determined using TA instruments AR 2000EX rotational rheometer with a vane in cup geometry. This geometry eliminates issues with slip in rheological measurements. All experiments were carried out with the set up maintained at a temperature of 25 ± 0.1 °C. Approximately 40 mL of paste is placed in the

rheometer geometry using a disposable syringe. The amount of time between the addition of mixing water and beginning the rheological experiment was approximately 5 min.

Two different rheological experiments were conducted. First, a shear rate ramp study (strain-controlled) was used to evaluate the yield stress and plastic viscosity of all the pastes. The rheological procedure consisted of a ramp-up pre-shear phase from 10-to-100/s lasting around 75 s to homogenize the paste, followed immediately by a ramp-down to 0.005/s. This phase is followed by a ramp-up phase from 0.005-to-100/s, and a ramp-down phase from 100-to-0.005/s. Figure 6-2(a) graphically represents this procedure. Excluding the pre-shear phase, data is acquired every second until three consecutive torque measurements are within 8% of each other, at which time the experiment advances to the next shear rate.

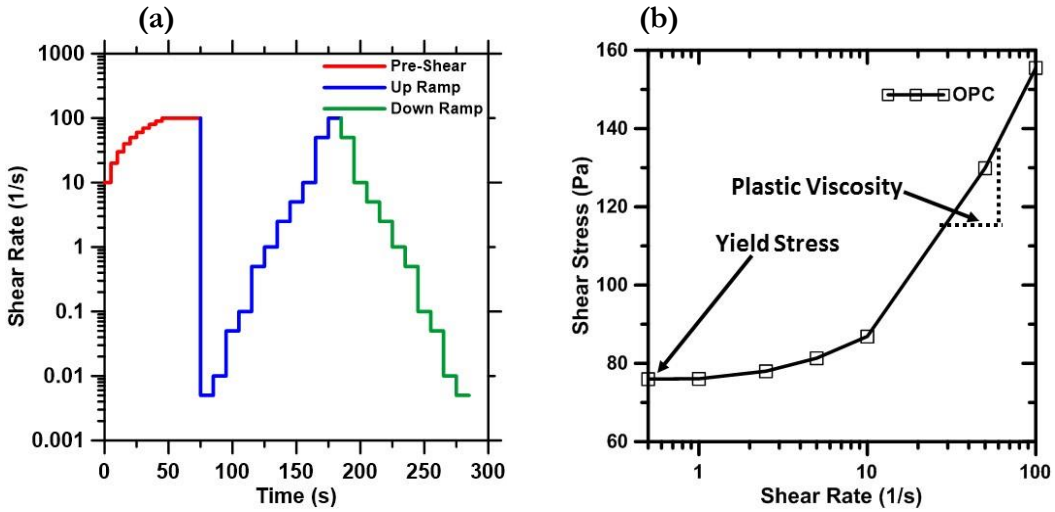

Figure 6-2: (a) Representation of the strain-controlled rheological procedure and (b) representative flow curves to illustrate model-less estimation of yield stress.

The wide shear rate range (0.005-to-100/s) is used to enable extraction of yield stress without the use of models (e.g. Bingham model). The inconsistencies in the extracted yield

stress when such models are used have been elucidated in detail in (Vance, Sant, and Neithalath 2015). When a wide shear rate range is used, a stress plateau which corresponds to the yield stress is obtained, as shown in Figure 6-2(b). This method was shown to be more consistent than using any of the commonly used rheological models (such as Bingham or Herschel-Buckley) for cementitious suspensions. The slope of the rising portion of the curve is the plastic viscosity of the paste, which is independent of the shear rate range (Vance, Sant, and Neithalath 2015). Replicate measurements on at least two separately mixed pastes were carried out for each mixture.

Second, small amplitude oscillatory shear study (stress controlled) was used to determine the storage and loss moduli of selected UHP pastes. An oscillatory stress was applied from 0.5 Pa to 100 Pa at a frequency of 10 Hz. This stress range was found to capture the linear viscoelastic regime in cementitious suspensions. The experiment duration was minimized in order to limit the effects of hydration.

In addition to rheometry, a simple method to estimate the flow properties of different pastes using a mini-slump was also carried out (Choi et al. 2016; Roussel, Stefani, and Leroy 2005). Paste was filled in the mini-slump cone (Figure 6-3) resting on a polymeric sheet. The cone is slowly lifted directly upwards to allow the paste to spread as shown in Figure 6-3. Multiple measurements of flow diameter are taken and the corresponding areas of spread averaged.

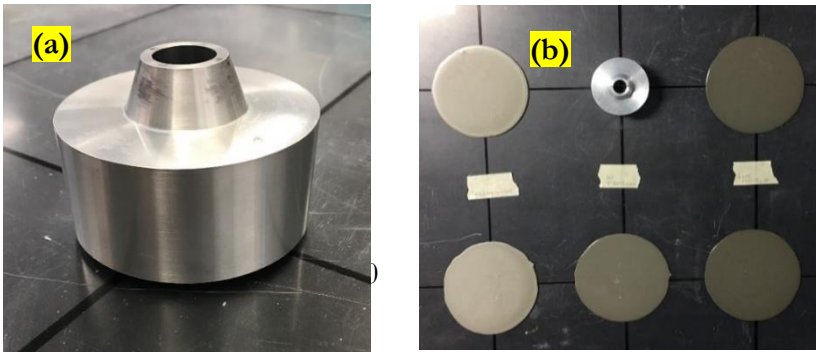

Figure 6-3: (a) Mini-slump cone, and (b) mini-slump flow of different pastes.

6.2.2.2. Thermal analysis

Isothermal calorimetry was carried out in accordance with ASTM C 1702 using a TAM Air micro calorimeter 2700 Series for a duration of 72 hours on pastes maintained at 25°C. To ensure accurate early age measurement and minimize the time to isothermal conditions, the powders and water were conditioned in an oven for 12 hours at 25°C. The pastes were then mixed using a laboratory mixer in accordance with ASTM C 305.

Simultaneous thermal analysis was performed on hardened cement pastes after 1, 3, 7, 14, and 28 days of hydration to determine the non-evaporable water (w_n) and calcium hydroxide (CH) contents. The tests were performed in an inert N_2 environment at a gas flow rate of 20 ml/s. The samples were heated from ambient temperature to 800°C at a heating rate of 15°C/min. The non-evaporable water contents (w_n) were determined as the difference in mass when the sample was heated from 105°C to 800°C, normalized by the mass at 800°C. CH contents at different ages were determined based on the change in mass over the temperature range of decomposition of CH (400°C to 450°C) (Pane and Hansen 2005).

6.2.2.3. Pore structure

The pore volume fractions and the critical pore diameters of the paste samples were determined using mercury intrusion porosimetry (MIP) after 28 days of hydration. Small

samples, approximately 2-3 mm in size were pre-treated in an oven at 60°C for 2 hours. This methodology provides consistent results for cementitious samples (Vance 2014). The test was performed in two steps – a low pressure step that evacuates vapors, fills the sample holder with mercury, and carries out pressurization up to 345 kPa, and a high pressure step which achieves pressures of up to 414 MPa. The relationship between pore diameter and intrusion pressure given by the Washburn equation (Washburn 1921b) was used to determine the pore sizes. The contact angle and surface tension values used were 117° and 0.485 N/m respectively, as these values are reported to be typical for oven dried samples (Shi and Winslow 1985; Liabastre and Orr 1978). The critical (percolation) pore size is defined as the size at which the maximum rate of mercury intrusion occurs, given by the first peak in the plot of derivative of volume intruded vs. diameter curve. While the shortcomings of MIP are well reported, this method enables determination of the total volume of mercury intruded and the critical (percolating) pore diameter.

6.2.2.4. Compressive strength

Compressive strength at desired ages were determined in accordance with ASTM C 109 on 50 mm mortar cubes cured in a moist environment (>98% RH) and a temperature of 23±2°C. Two different fine aggregates, one with a d_{50} of 0.5 mm and another with d_{50} of 0.6 mm were blended in equal proportions to constitute the fine aggregate for the mortar since such a combination was found to achieve higher strengths. The paste volume fraction was maintained at 65%.

6.3. METHODS OF BINDER SELECTION

From a large matrix of paste mixtures (Table 6-2), a smaller sub-set needs to be chosen for detailed studies. In this chapter, a comprehensive method of binder selection is adopted, which relies on a combination of computational microstructural packing and experimental paste rheology, along with considerations for maximizing OPC replacement. This methodology eliminates the traditional trial-and-error method of mixture design for UHP binders and provides a rational process to select candidate mixtures from a large set of potential raw materials.

6.3.1 Microstructural Packing

Microstructural models were created for all the paste mixtures, based on the particle size distribution and proportion of the component powders, to analyze different aspects of particle packing that are important in influencing both the flow of the pastes as well as their mechanical properties. A microstructural stochastic packing model with periodic boundary conditions was developed in MATLAB® to create virtual 3D microstructures. The algorithm digitally packs spherical particles in a 3D RVE (representative volume element, chosen here as 300 x 300 x 300 μm^3). The total volume of particles in the RVE is determined based on the $(w/p)_v$. The cumulative particle size distributions of the component powders (Figure 6-1) were discretized to obtain the number of particles of the individual components required to satisfy the desired solid volume fraction. Figure 6-4(a) shows a representative virtual 3D microstructure and Figures 6-4(b-d) show the 2D slices corresponding to binary, ternary, and quaternary mixtures respectively.

The digital microstructures allow the extraction of several features that are influential in early- and later age paste response. The mean centroidal distance (MCD), coordination

number (CN), and the number density (N_d) are the key parameters that are chosen in this chapter. The mean centroidal distance is a measure of the packing density of the microstructure. It is calculated as the average distance to the center of a particle from the centroid of the microstructure. The coordination number is defined as the average number of nearest neighbor pairs in the microstructure. For any particle, the nearest neighbor is defined as a particle that lies either wholly or partially in the radial field of that particle, defined as a field with a radius of (r+5) μm, where 'r' is the radius of the particle. By virtue of this, the coordination number represents the inter-particle contacts. The number density is defined as the number of particles in a unit volume. It is directly related to the overall fineness of the powders in the paste. Other parameters, similar in nature to those represented here (e.g., particle contact fraction, which is similar to CN) have been used in the past to define the microstructure (Aashay Arora, Sant, and Neithalath 2016; Vance et al. 2015).

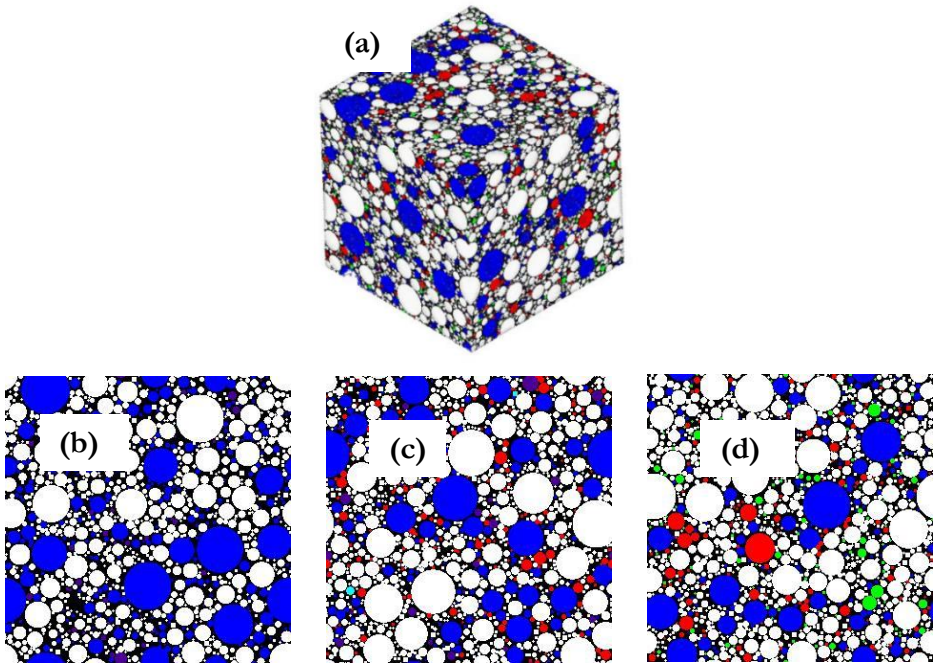

Figure 6-4: (a) Representative volume element (RVE) for a quaternary OPC-fly ash-metakaolin-limestone system. 2-D slices from the simulated 3D microstructures of: (b) binary OPC-fly ash system, (c) ternary OPC-fly ash-metakaolin system, and (d) quaternary OPC-fly ash-metakaolin-limestone system.

OPC is indicated in white, fly ash in blue, metakaolin in red, and limestone in green.

Figure 6-5 shows the relationships between the microstructural parameters of the UHP pastes. As the number density increases, the mean centroidal spacing between the particles decreases and the coordination number increases. The coordination number as well as the number density indicates the interparticle contacts in the microstructure and thus can be related to the yield stress of the paste and its degree of hydration at early ages. Moreover, plastic viscosity has been stated to be dependent heavily on the solid volume fraction (and thus the surface contacts) in the paste, thereby relating to the above-mentioned parameters. These microstructural parameters can therefore be considered to influence both the rheology and hydration in cementitious materials. The influence of improved particle packing of the paste on the mechanical and durability properties of cementitious mixtures, as well as their role in economizing concrete mixtures is well documented (de Larrard and Sedran 1994a; Lange, Mörtel, and Rudert 1997).

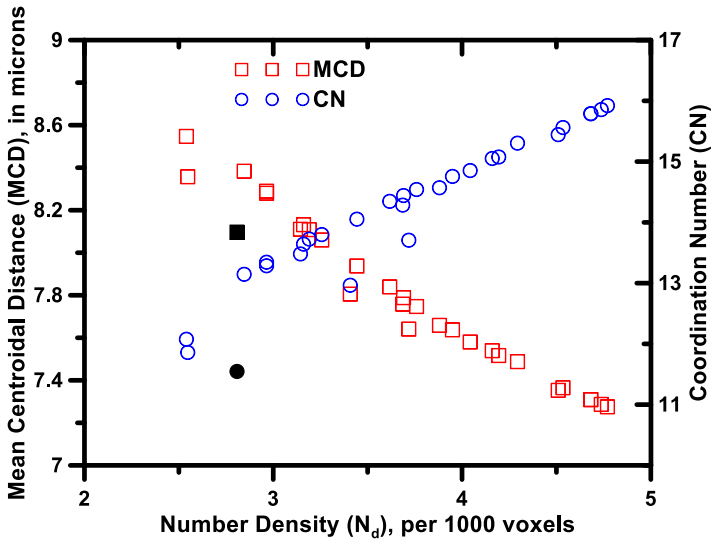

Figure 6-5: Relationships between the number density, mean centroidal distance and coordination number for the UHP pastes. The values for the UHP-control paste are shown using filled symbols.

6.3.2 Rheological Parameters

Rheological evaluation of cementitious suspensions helps in understanding the flow characteristics and early-age structure development in pastes. Cement pastes are yield stress fluids, where the yield stress (τ_y) is a consequence of interparticle forces. The interparticle forces are influenced by the particle-scale properties and the packing of particles. The yield stress is generally defined as the non-zero (finite) stress at a "zero" strain rate, and depends on time and previous shear history. The plastic viscosity (μ_p) of particulate suspensions is considered to be primarily influenced by inter-particle friction and surface contacts, wherein decreasing the inter-particle (friction) forces by increasing the particle spacing (or by decreasing surface contacts) results in a decrease in plastic viscosity. Attempts have been made to relate the rheological and microstructural packing parameters (Vance et al. 2015; Flatt and Bowen 2006, 2007; Olhero and Ferreira 2004). A simpler way to characterize the

flowability of cementitious suspensions is the mini-slump test which measures the radius (or area) of spread of the fresh paste, as described earlier. The radius of spread of the paste has been related to the yield stress using the volume of the sample and a constant related to the liquid-vapor interfacial energy and wetting angle of the material on the horizontal base plate (Roussel, Stefani, and Leroy 2005).

Figures 6-6(a) and (b) show the yield stress, plastic viscosity, and the normalized mini-slump spread area (A_{ms}) for all the pastes in which fly ash and slag respectively are the dominant cement replacement materials. The areas of the mini-slump spread are shown by normalizing them with respect to the spread area for the UHP-control paste. The numbers as subscripts in the mixture labels indicate the OPC replacement level with that material. Note that all the mixtures shown here contain 5% of HRWR by mass of the powder.

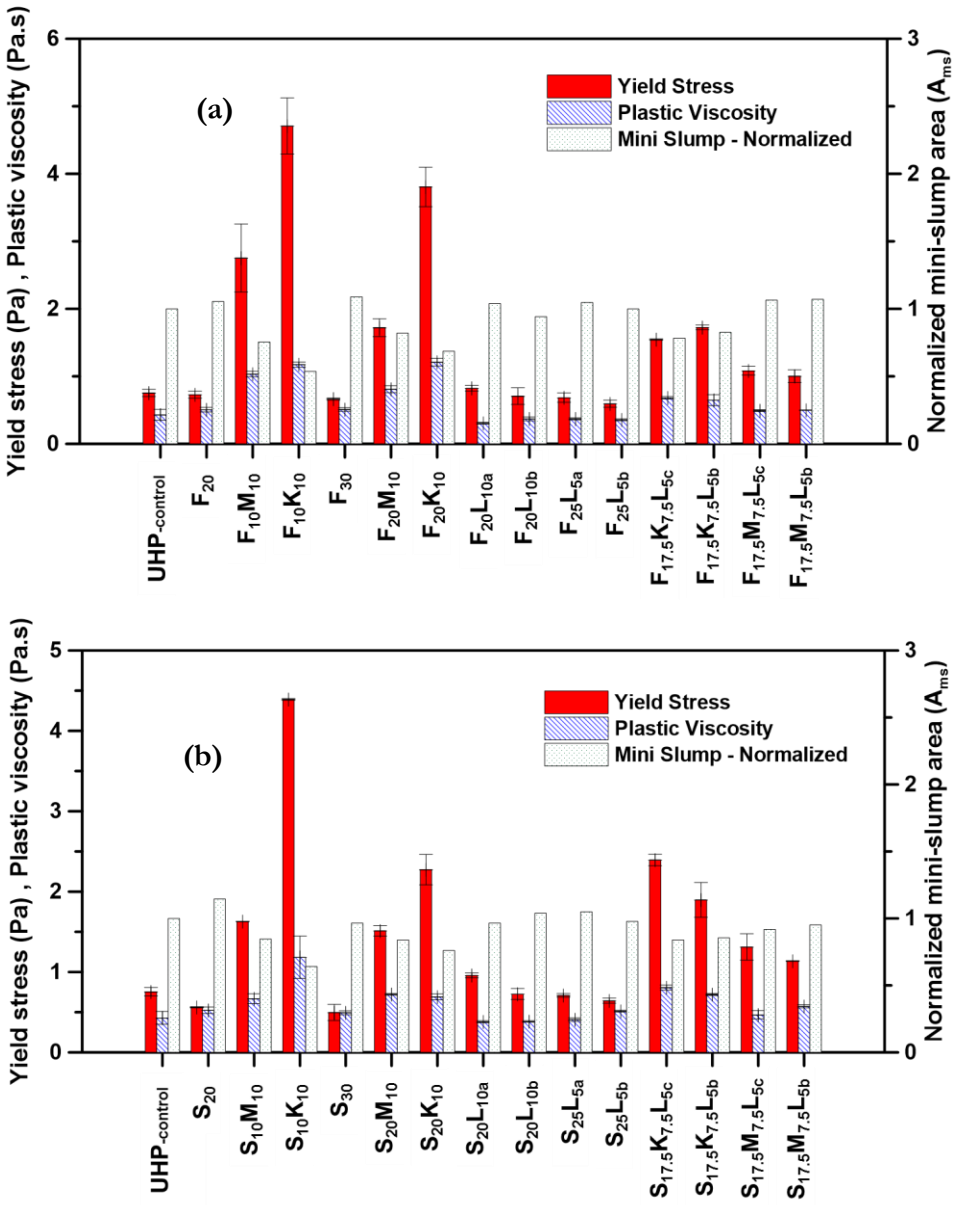

Figure 6-6: Yield stress, plastic viscosity and normalized mini slump values for pastes containing: (a) fly ash as the primary cement replacement material, and (b) slag as the primary cement replacement material. The subscript numbers represent the % by mass of the corresponding material replacing cement.

From Figure 6-6, it can be noted that, in general, the yield stress and plastic viscosity values are directly related, with an increase in one causing the other also to increase, even if not proportionally. The mini-slump spread is inversely related to the yield stress and plastic viscosity. It can also be noticed that the binary pastes containing fly ash or slag demonstrate relatively lower yield stress and plastic viscosity values as compared to the UHP-control paste. This is due to the lower inter-particle frictional forces in these pastes; a result of particle sizes and surface characteristics. It is also seen that the ternary mixes containing metakaolin show high yield stress values; however, incorporation of fine limestone reduces the yield stress in quaternary mixtures. The presence of fine limestone improves the overall packing and reduces the inter-particle friction (Vikan and Justnes 2007; Vance, Aguayo, et al. 2013) in the quaternary mixtures thus lowering the yield stress and plastic viscosity, thereby leading to increased flowability of these mixtures.

6.3.3 Strategies to Select Potential UHP Pastes

The primary goal of this work is to determine paste compositions with the optimum rheological parameters and a densely packed microstructure, such that they aid in the formulation of economical and sustainable UHPC. The microstructural packing and rheological studies described above provide preliminary indicators as to the applicability of these paste systems for UHPC. Packing influences rheology and mechanical/durability properties, while rheology influences placeability and early-age structure development, which in turn influences the later age properties. In a composite binder consisting of particles of different size distributions and surface characteristics, along with admixtures to control the rheological features, well-defined strategies are needed to select optimal and sustainable (e.g.

low cement content) compositions for beneficial properties. Two such strategies are presented, based on the 31 UHP paste mixtures considered for preliminary evaluation (Table 6-2).

6.3.3.1. Selection based on independent consideration of microstructural and rheological parameters

This straightforward approach directly uses results from the microstructural packing (Section 3.1) and rheology (Section 3.2) studies to select paste mixtures that satisfy the criteria with respect to both packing and rheology. From Section 3.1, it is obvious that that a lower mean centroidal distance, a higher coordination number, and a higher number density will lead to a densely packed microstructure. The control UHP paste is used as the baseline case, since the intention of using several cement replacement materials is not just to reduce the cement content, but to result in a paste that demonstrates improved properties than the control mixture. Hence, the potential UHPC binders should satisfy all the three following packing-based criteria:

$$Criteria\ based\ on\ Packing: \begin{cases} MCD_i \leq MCD_{UHP-control} \\ CN_i \geq CN_{UHP-control} \\ N_{d-i} \geq N_{d-UHP-control} \end{cases} \quad \text{(Eq. 6-1)}$$

For better workability, a lower yield stress and plastic viscosity and a higher mini-slump spread are desired. However, an examination of Figure 6-6 suggests that the yield strengths and plastic viscosities of the UHP control paste are already quite low due to the use of high amounts of HRWR; thus enforcing a criterion that requires τ_y and μ_p of the pastes to be lower than that of the UHP control paste would result in few to no pastes being selected.

Considering that even 2-to-3 times higher yield stress and/or plastic viscosity than that of the UHP-control would not detrimentally influence the workability, a subjective rheology-based selection criterion as shown below is imposed. This criterion can be modified based on the rheological parameters that the user is comfortable with, since the requirements of workability vary between different applications. Here also, the potential mixture should satisfy all the three criteria. Absolute values of the rheological parameters, as opposed to those relative to UHP control paste, can also be used if the user decides so.

$$\textit{Criteria based on Rheology:} \begin{cases} \tau_{y-i} \leq 3 \times \tau_{y-UHP-control} \\ \mu_{p-i} \leq 3 \times \mu_{p-UHP-control} \\ A_{ms-i} \geq 0.75 * A_{ms-UHP-control} \end{cases} \quad \text{(Eq. 6-2)}$$

Figures 6-7(a) and (b) show the Venn diagrams depicting the number of mixtures that satisfy the microstructural packing and rheology criteria respectively. From Figure 6-7(a), it can be seen that 30 mixtures satisfy the CN and N_d criteria while 24 satisfy the MCD criterion. 22 of the 31 UHP mixtures satisfied all the three packing criteria, and 23 of the 31 mixtures satisfied all the rheology criteria. Figure 6-7(c) shows that 17 mixtures satisfied both the packing- and rheology-based criteria. These criteria can be modified to further refine the mixture selection, as mentioned earlier. Figure 6-8 shows the matrix of 31 mixtures among which the selected ones are highlighted.

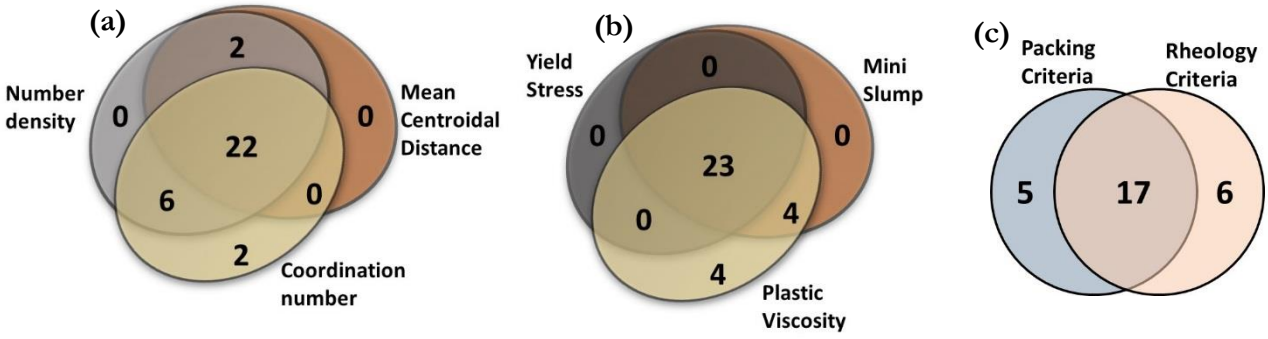

Figure 6-7: Venn diagrams showing the number of mixtures selected based on: (a) microstructural criteria, (b) rheology criteria, and (c) the intersection of both the criteria. Note that Venn diagrams could not be drawn to scale because of the presence of zeros.

K_{10}	M_{10}	M_{20}	F_{20}	F_{30}	S_{20}	S_{30}	
$F_{10}K_{10}$	$F_{20}K_{10}$	$S_{10}K_{10}$	$S_{20}K_{10}$	$F_{10}M_{10}$	$F_{20}M_{10}$	$S_{10}M_{10}$	$S_{20}M_{10}$
$F_{20}L_{10a}$	$F_{20}L_{10b}$	$F_{25}L_{5a}$	$F_{25}L_{5c}$	$S_{20}L_{10a}$	$S_{20}L_{10b}$	$S_{25}L_{5a}$	$S_{25}L_{5b}$
$F_{17.5}K_{7.5}L_{5b}$	$F_{17.5}K_{7.5}L_{5c}$	$F_{17.5}M_{7.5}L_{5b}$	$F_{17.5}M_{7.5}L_{5c}$	$S_{17.5}K_{7.5}L_{5b}$	$S_{17.5}K_{7.5}L_{5c}$	$S_{17.5}M_{7.5}L_{5b}$	$S_{17.5}M_{7.5}L_{5c}$

Figure 6-8: Matrix of mixtures with the highlighted cells showing the mixtures selected based on independent consideration of microstructural and rheological parameters. The subscript numbers represent the % by mass of the corresponding material replacing cement.

6.3.3.2. Selection based on packing and flow coefficients

In this model, rather than considering the individual microstructural and rheological parameters as in the previous case, they are combined into a packing coefficient (γ) and flow coefficient (κ) respectively, as defined in Equations 6.3 and 6.4.

$$Packing\ Coefficient\ (\gamma) = \frac{CN\ X\ N_d}{MCD}\ [m^{-4}] \quad \text{(Eq. 6-3)}$$

$$Flow\ Coefficient\ (\kappa) = \sqrt{\frac{A_{ms}}{\tau_y\ X\ \mu_p}}\ [m.Pa^{-1}.s^{-1/2}] \quad \text{(Eq. 6-4)}$$

A higher value for γ indicates better packing whereas a higher value for κ indicates better workability for the UHP paste. The subjective criteria adopted for mixture selection are:

$$\gamma_i \geq 1.0 * \gamma_{UHP-control} \quad \text{(Eq. 6-5)}$$

$$\kappa_i \geq 0.25 * \kappa_{UHP-control} \quad \text{(Eq. 6-6)}$$

As in the previous model, the user can change the multiplicative constants for selection based on desired applications. Here, constants of 1.0 and 0.25 are adopted for packing and flow criteria respectively. It is desirable to have a packing that is better than that of the control UHP paste, which justifies the presence of the multiplier 1.0. Higher values will be needed for requirements that are more stringent. A constant of 0.25 is chosen for the flow coefficient based on the experience that even when the flow coefficient as defined in Equation 6-4 was four times lower than that of the control UHP paste, the considered paste demonstrated adequate workability. Out of the 31 UHP mixtures, 23 satisfied Equation 6-5, and 28 satisfied Equation 6-6. 22 mixtures satisfied both the criteria and are highlighted in Figure 6-9.

K_{10}	M_{10}	M_{20}	F_{20}	F_{30}	S_{20}	S_{30}	
$F_{10}K_{10}$	$F_{20}K_{10}$	$S_{10}K_{10}$	$S_{20}K_{10}$	$F_{10}M_{10}$	$F_{20}M_{10}$	$S_{10}M_{10}$	$S_{20}M_{10}$
$F_{20}L_{10a}$	$F_{20}L_{10b}$	$F_{25}L_{5a}$	$F_{25}L_{5c}$	$S_{20}L_{10a}$	$S_{20}L_{10b}$	$S_{25}L_{5a}$	$S_{25}L_{5b}$
$F_{17.5}K_{7.5}L_{5b}$	$F_{17.5}K_{7.5}L_{5c}$	$F_{17.5}M_{7.5}L_{5b}$	$F_{17.5}M_{7.5}L_{5c}$	$S_{17.5}K_{7.5}L_{5b}$	$S_{17.5}K_{7.5}L_{5c}$	$S_{17.5}M_{7.5}L_{5b}$	$S_{17.5}M_{7.5}L_{5c}$

Figure 6-9: Matrix of mixtures with the highlighted cells showing the mixtures selected based on packing and flow coefficients. Mixtures in the dark shaded cells were chosen for detailed studies

As can be noted from Figure 6-9, the chosen packing and flow coefficients yield a large number of mixtures. The selection criteria could be made more rigorous to eliminate further mixtures to make the final selection manageable. However, this study favors implementing additional constraints based on multiple considerations: (i) only ternary and quaternary mixtures are considered in view of their better packing, with limestone included only in the quaternary mixtures, (ii) a total cement replacement level of 30% is used to ensure sustainable UHP binders, (iii) limestone is considered only in mixtures containing metakaolin or microsilica since its size range is in between those of fly ash/slag and microsilica/metakaolin, and its low reactivity (Vance, Aguayo, et al. 2013) limits the dosage to 5% (even though a recent study has shown increasing strengths with increasing limestone content in UHPC (W. Huang et al. 2017b)), and (iv) when limestone is used, equal proportions of those with d_{50} values of 1.5 μm and 3 μm are preferred for improved packing. This resulted in final eight mixtures which are shown in the dark shaded cells in Figure 6-9. Either of the two methods presented here can be employed along with user-defined constraints to select optimal pastes for UHP mixtures. The methodologies reported here are flexible enough to also allow weighting of the packing or rheology criteria as per the users' demands.

6.4. CHARACTERIZATION OF SELECTED BINDERS

6.4.1 Oscillatory Rheology

Yield stress and plastic viscosity, the fundamental rheological properties of suspensions, have been used in the past for binder selection, mixture qualification, and quality control. In this section, results of small amplitude oscillatory stress growth experiments to determine the storage modulus (G') and loss modulus (G") are reported. The oscillatory shear response enables the identification of solid-like behavior at stresses lower than the yield stress. The changes in dynamic moduli can be observed without disturbing the microstructure. Oscillatory rheology was performed on the eight selected ternary and quaternary UHPC mixes along with the control mixtures. As a function of applied stress within a viscoelastic material, the storage and loss moduli represent the elastic and viscous response respectively. The stress-moduli relationships typically shows a horizontal modulus plateau at lower stresses, followed by a reduction in modulus as the stress increases, indicating structural breakdown (Wallevik 2009). A low modulus plateau at higher stress levels follows. The dynamic modulus is dependent on the water-to-powder ratio, type of mixing (i.e., hand mixed or high shear mixing), and amount of HRWR in the paste.

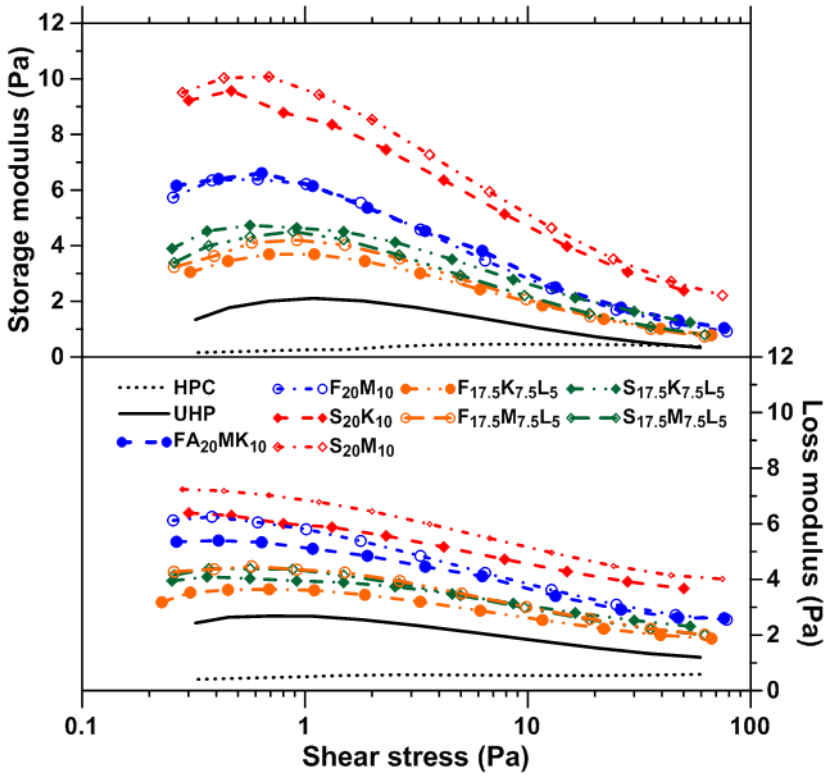

Figure 6-10: Relationship between shear stress and storage or loss moduli for the control and UHP pastes

Figure 6-10 shows the relationship between the shear stress and storage or loss moduli for the ternary and quaternary UHP pastes and the UHP and HP control pastes (w/c of 0.20 and 0.32 respectively, with admixture dosages of 5% and 2% respectively). The plateau region for most pastes is generally limited to shear stresses smaller than 1 Pa, which is typical for pastes containing HRWR. The corresponding stresses for a conventional OPC paste at a higher w/c (of 0.40) was found to be 3 to 5 Pa (Vance et al. 2015). The storage and loss moduli for all the UHP pastes examined in this study ($(w/p)_m$=0.20; HRWR = 5% by mass of powder) are lower than 10 Pa, which is about three orders of magnitude lower than those

of conventional OPC pastes (w/c=0.40; no HRWR) (Vance et al. 2015). This is not surprising since the interparticle attraction that gives rise to solid-like response (yield stress, storage modulus) is almost neutralized by the high concentration of dispersing admixtures such as HRWR. The HP-control paste ($(w/p)_m$=0.32; HRWR = 2% by mass of powder) shows much lower moduli as compared to the UHP-control paste. Although the UHP-control paste contains twice the amount of HRWRA than the HP-control paste, the higher fraction of cement in the UHP pastes leads to reduced interparticle spacing and increased particle-to-particle contacts, thereby increasing the moduli. The slag-based ternary blends containing metakaolin or microsilica shows the highest moduli, attributable to the higher number density in these mixtures. The fly ash-based ternary blends, even with similar amounts of metakaolin or microsilica show reduced moduli than those of slag-based binders because of the spherical nature of fly ash particles. This effect is also amplified by the slightly larger particle sizes in fly ash (Figure 6-1) which enhances the separation between particles. When limestone is added to produce quaternary mixtures, the moduli reduces as compared to those of corresponding ternary mixtures without limestone. The interparticle attractive forces between limestone and cement are shown to be lower than those between the cement grains (Vance et al. 2015). More limestone-cement contacts and the consequent reduction in interparticle forces help reduce the moduli.

6.4.2 Early Age Hydration Kinetics

Isothermal calorimetry was carried out on the selected binders at a temperature of 25ºC. The heat flow curves normalized by the mass of cement are plotted in Figure 6-11. Figures 6-11(a) and (b) show the heat flow curves for the mixtures with fly ash and slag respectively as

the dominant cement replacement materials. The heat flow curves for the UHP-control and HP-control mixtures are also shown for comparison. It is noticed that the HP-control mixture (w/c of 0.32) has the highest heat release rate among all the mixtures studied, attributable to the higher water content in this mixture as well as a lower HRWR content than the other UHP mixtures. The higher HRWR content in the UHP pastes slows down the acceleration phase for these mixtures. Most of the UHP mixtures demonstrate heat release rates that are comparable to that of the control UHP paste. The ternary UHP mixtures containing fly ash show slightly high peak heat flows as compared to the corresponding quaternary mixtures, while the peak heat flow in quaternary mixtures is slightly depressed (Figure 6-11(a)). The combination of limestone and fly ash results in an increase in heat flow per unit mass of cement for conventional cement pastes (Vance, Aguayo, et al. 2013). The lack of sufficient amount of water for chemical reactions in very high surface area mixtures might be a contributing factor. For the mixtures containing slag, the heat flow responses are similar to those containing fly ash as can be observed from Figure 6-11(b). However, the quaternary slag-metakaolin-limestone paste has a higher peak heat flow, which likely is attributable to the early reactivity of limestone in the presence of higher amounts of reactive alumina from slag and metakaolin (Aashay Arora, Sant, and Neithalath 2016; Menéndez, Bonavetti, and Irassar 2003). The synergy between limestone and slag is also evident from the fact that the quaternary slag-microsilica-limestone paste also shows a similar peak heat flow as compared to the corresponding ternary blend. The quaternary mixtures, in general, demonstrate a broader heat flow peak, which is indicative of the enhanced aluminate phase reactivity in the presence of limestone.

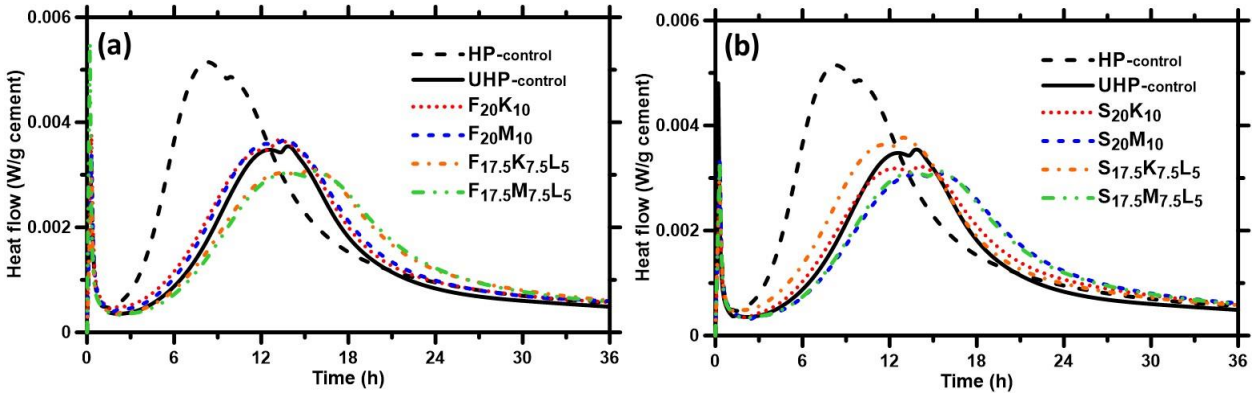

Figure 6-11: Heat flow for UHP pastes containing: (a) fly ash as the primary cement replacement material, and (b) slag as the primary cement replacement material.

6.4.3 Hydration Products

Thermo-gravimetric analysis was carried out to quantify the reaction products in the selected UHP pastes. Representative mass loss and differential thermogravimetric (DTG) curves are used for reaction product identification and quantification. The DTG curves show several distinguishable peaks attributable to the decomposition of: (i) C-S-H and ettringite around 120-130ºC, (ii) CH around 450ºC, and (iii) calcium carbonate around 750ºC. In the presence of limestone and reactive alumina (as in the case of quaternary mixtures), carboaluminates are formed in place of monosulfoaluminates, which decomposes in the temperature range of 150-200ºC. To keep the discussions succinct, the evolution of non-evaporable water contents (w_n) and CH contents in the selected mixtures are only reported.

Figures 6-12 (a) and (b) show the w_n and CH contents after 1, 3, and 28 days of hydration. Figure 6-12(a) shows the highest amount of non-evaporable water content for the HP-control paste at all ages, because of the higher w/c that enhances cement hydration. Among

the UHP pastes, the control mixture shows the highest w_n at 1 day, because of the higher cement content in this mixture. Considering that complete hydration results in a w_n of 0.23 (Molina 1992), the degree of hydration of the HP-control paste at 28 days is calculated as 0.61. For the UHP-control paste, the 28-day degree of hydration is 0.46. As expected for a very low w/c paste, the cement grains stay partly hydrated, justifying the use of cement replacement materials and fine fillers to improve particle packing and thus enhance the properties. Even with an overall cement replacement level of 30%, all the other UHP mixtures show comparable 28-day w_n values as that of the UHP-control paste. It is also important to note that, between 3 and 28 days, the increase in w_n of UHP-control paste is much lower as compared to the ternary and quaternary blend pastes. The benefits of reactivity of cement replacement materials is evident here. From Figure 6-12 (b), it can be noted that the CH contents increase from 1 to 28 days for the UHP-control and HP-control mixtures, similar to the w_n contents. However, between 3 and 28 days, CH contents do not increase at the same rate as w_n for the ternary and quaternary UHP pastes. This is attributable to the consumption of CH by the replacement materials to form secondary C-S-H. The hydration product quantification of UHP pastes shows that it is indeed beneficial to incorporate significant amounts of cement replacement materials in low w/c systems since a considerable part of cement remains unhydrated.

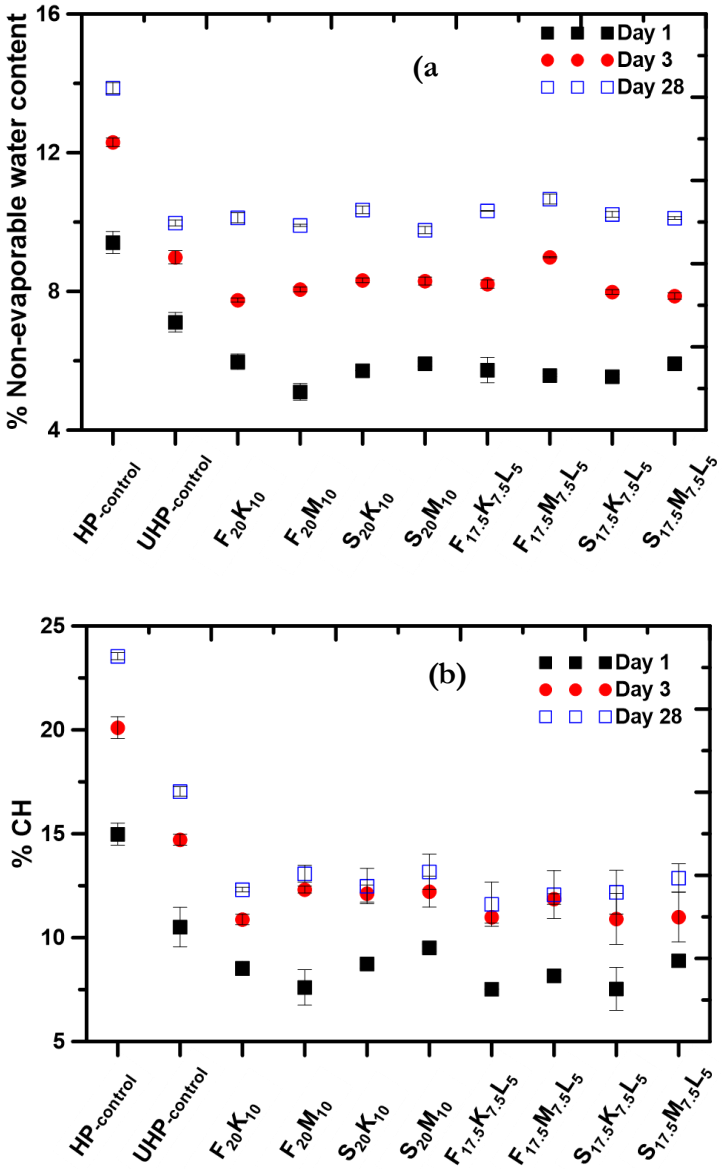

Figure 6-12: (a) Non-evaporable water, and (b) CH contents of the UHP pastes at different ages. Error bars indicate one standard deviation from the average of duplicate specimens

6.4.4 Porosity and Pore Sizes

The pore structure of the UHP pastes was investigated using mercury intrusion porosimetry (MIP). Figure 613(a) shows the porosity and critical pore diameters of the selected UHP pastes. The HP-control paste made using a w/c of 0.32 has the highest porosity (0.21) and the largest critical pore size (0.031 μm) among the mixtures presented owing to the higher w/p used. Porosity and critical pore size of the 0.20 w/c UHP-control paste (0.16 and 0.02 μm) are much lower than that of the HP-control, and significantly lower than that of a conventional OPC paste of w/c 0.40 (0.28 and 0.036 μm) (Aashay Arora, Sant, and Neithalath 2016). The ternary blends show overall porosities that are similar to that of UHP-control mixture, while the quaternary blends show slightly higher porosities than the ternary blends. However, segmentation of total pore volume into three size ranges as per IUPAC recommendations: 0.0036-to-0.05 μm, 0.05-to-0.2 μm, and > 0.2 μm (Rouquerol et al. 1994) shown in Figure 6-13(b) reveals that, for the quaternary mixtures, there is a higher proportion of pores present in the 0.0036-to-0.05 μm range. This corresponds to the pores in the hydration products (i.e., gel pores), which indicates increased formation of reaction products, which is also corroborated by the non-evaporable water content measurements. The reaction of fine limestone with aluminates result in the formation of carboaluminates that occupy space and reduce the porosity (Aashay Arora, Sant, and Neithalath 2016; Puerta-Falla et al. 2015; V. L. Bonavetti, Rahhal, and Irassar 2001). The synergistic use of small amounts of limestone with aluminate bearing cement replacement materials thus is a beneficial strategy both from performance and sustainability viewpoints.

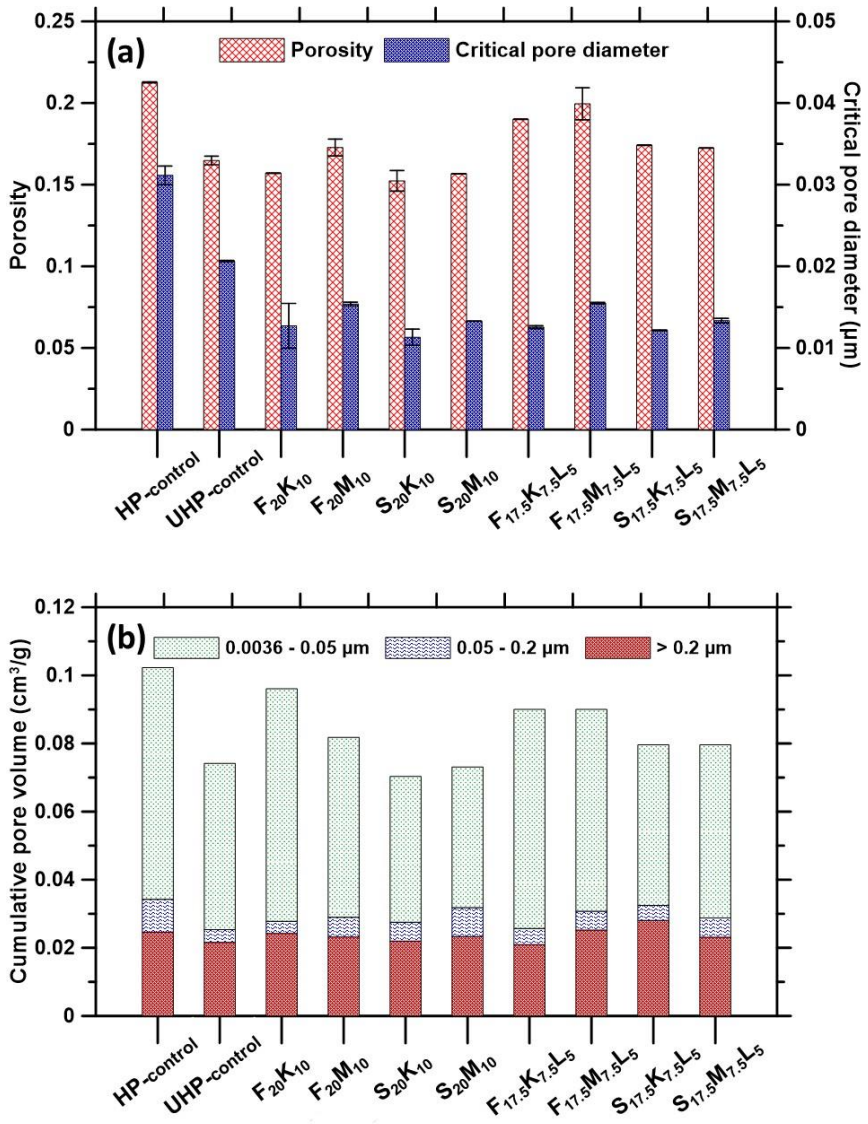

Figure 6-13: (a) Porosities and critical pore sizes of UHP pastes after 28 days of hydration, and (b) segmentation of total pore volume after 28 days of hydration into three size ranges. Error bars indicate one standard deviation from the average of duplicate specimens

The critical pore diameter is an important determinant of the durability of concrete. As can be noticed from Figure 6-13(a), the critical pore diameter is similar for both the ternary and

quaternary mixtures, and lower than the UHP-control paste. The pore size refinement is once again a result of the reactivity of the cement replacement materials. The blends containing slag show slightly reduced porosities and pore sizes as compared to those containing fly ash, by virtue of their better early reactivity.

6.4.5 Compressive Strength

Figure 6-14 shows the compressive strengths of mortars made using the selected UHP pastes after 14 and 28 days of moist curing. Note that (fine) aggregate gradation optimization was not carried out for the mortar. Even with a clinker factor reduction of 30%, most of the UHP mortars, especially the quaternary blends demonstrate 28 day strengths that are comparable to, or higher than that of the control UHP mortar. This is consistent with the pore structure features for those mixtures. The mixtures containing slag demonstrate higher strengths than those containing fly ash at 28 days, but it is conceivable that the pozzolanic reaction of fly ash and its later synergy with the other replacement materials could improve the strength with further curing. It is important to note that strengths in excess of 90 MPa have been obtained through the use of standard cement replacement materials and effective packing to enhance the reactivity of the paste phase (Figure 6-14). When combined with densely packed strong aggregates, and an insignificant fraction of metallic fibers (2-2.5% by volume), compressive strength of 150 MPa has been achieved, which is in line with those reported for similar UHPC mixtures (Yu, Spiesz, and Brouwers 2014a, 2014b). The development of ultra-high performance blends as

demonstrated in this chapter will result in economical and durable UHPCs, as indicated by the improvements in reaction products and the pore structure.

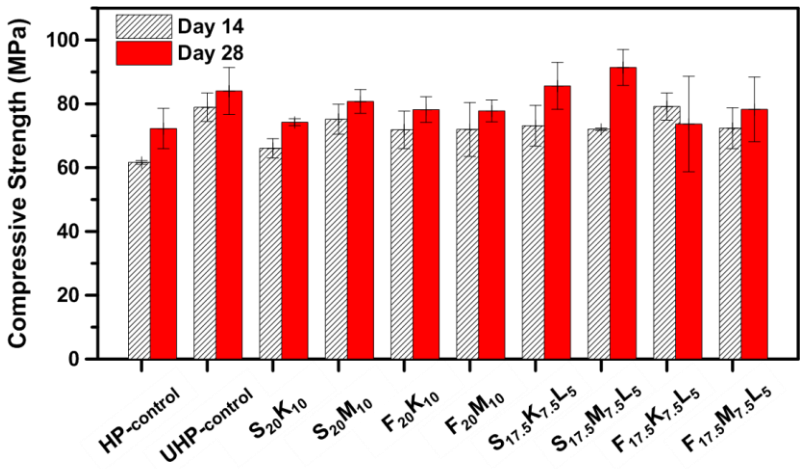

Figure 6-14: 14-day and 28-day compressive strengths of selected UHP mortars. Error bars indicate one standard deviation from the average of at least three replicate specimens

6.5. SUMMARY AND CONCLUSIONS

This chapter has described rational methodologies for selection of the paste phase in UHPCs using fundamental microstructural and flow characteristics of the paste that are influenced by the component materials. Commonly available cement replacement and fine filler materials were used. A microstructural packing algorithm was used to extract the mean centroidal spacing, number density, and the coordination number for binary, ternary, and quaternary blends of potential UHP pastes. The rheological parameters extracted include yield stress, plastic viscosity, and the mini-slump spread. Better packing allows improved utilization of cement replacement and filler materials, while better rheology facilitates better dispersion of particles and consequently improved mechanical properties. The

microstructural and rheological parameters were utilized to create two different selection criteria. The first one was based on the individual microstructural or rheological parameters, and the second through the definition of packing and flow coefficients that expressed the combined effect of the chosen microstructural and rheological parameters. No relative weights were assigned for the microstructural and rheological parameters here, though it can be applied if needed. The proposed methodology allows the user to select mixtures based on acceptable ranges of microstructural packing and rheological parameters demanded by the application. For instance, a UHP mixture used for closure pours in a bridge deck connection would require very high workability and high strength, whereas a UHP used for a precast application would not require such high degree of flowability. In this chapter, emphasis was also given to clinker factor reduction; hence paste formulations containing more than 70% of cement by mass of the powder were not chosen.

The selected UHP paste formulations were thoroughly characterized. The selected UHP pastes showed non-evaporable water contents that were comparable to or higher than that of the UHP-control paste after 28 days, even with a 30% reduction in clinker factor. The ternary and quaternary blended UHP pastes demonstrated significantly lower pore sizes as compared to the UHP-control paste. The efficient microstructural packing in these mixtures coupled with reaction product formation resulted in this outcome, which is known to translate into better long-term durability. 28-day compressive strengths in excess of 90 MPa were obtained for some mortars while all the mixtures showed strengths of more than 80 MPa at 28 days. The inclusion of fibers and maximum density packing of strong aggregates

in these selected mixture designs allow 28-day compressive strengths in excess of 150 MPa, while still maintaining the workability of the concrete at acceptable levels.

CHAPTER 7[7]

MATERIAL DESIGN OF ECONOMICAL ULTRA-HIGH PERFORMANCE CONCRETE (UHPC) AND EVALUATION OF THEIR PROPERTIES

7.1. INTRODUCTION

Ultra-high performance concrete (UHPC) is an emerging cement-based material with high compressive and tensile strengths, ductility, and long-term durability (B. Graybeal 2011; Russell and Graybeal 2013; C. Wang et al. 2012; Kay Wille and Boisvert-Cotulio 2015). Some of the applications for which UHPC is well suited for are bridge piers, decks and deck-level connections between modular precast components, blast protection elements, and high ductility designs (B. A. Graybeal 2012; Maya and Graybeal 2017; Tazarv and Saiidi 2015; Vítek, Coufal, and Čítek 2013). Compressive strengths in the range of 150 MPa are generally reported for UHPCs, aided by careful selection of cementitious materials considering their particle sizes and reactivity, and a low water-to-powder ratio, w/p ($0.15 < w/b < 0.23$) to ensure a dense microstructure (Reda, Shrive, and Gillott 1999). The use of non-standard cement replacement materials such as quartz (silica) flour, rice husk ash, and nanoparticles (nano-silica, nano-metakaolin) to achieve high strengths, in additional to common high-performance replacement materials such as silica fume and metakaolin, has been reported (Muhd Norhasri et al. 2016; Ghafari et al. 2015; Z. Li, Venkata, and Rangaraju 2015; Shafieifar, Farzad, and Azizinamini 2017; H. Huang et al. 2017; Ghafari et al. 2014; Van

[7] This chapter is derived from the following publication under review: Arora, A., Almujaddidi, A., Kianmofrad, F., Mobasher, B., & Neithalath, N. (2018). Material Design of Economical Ultra-High Performance Concrete (UHPC) and Evaluation of their Properties.

Tuan et al. 2011). Limestone powder has also been used in several UHPC formulations (W. Huang et al. 2017b; W. Li et al. 2015; Burroughs et al. 2017; Aashay Arora et al. 2018). Recently, the use of calcium aluminate cement for UHPC has been explored, with a focus on high temperature applications (Lee et al. 2017). Higher strength and durability are direct consequences of microstructure densification, while the use of discontinuous steel fibers (generally greater than 3% by volume) provides sustained post-cracking strengths and ductility (Le Hoang and Fehling 2017).

The material design of UHPC binders need to be governed by an efficient particle packing process since the low w/p in these mixtures will result in sub-optimal levels of hydration of cement. High material and processing costs and energy implications of UHPC can partly be attributed to the use of large amounts of cement that acts as an expensive filler. Thus, improved packing of the binder phase through the use of cement replacement materials and fine fillers is a better means of strength enhancement than increasing cement content. A recent work by the authors (Arora et al. 2018) has explained a methodology to design economical and efficient UHP binders that incorporate only conventional cement replacement materials (at an overall replacement level upwards of 30%), that achieves a high degree of microstructural packing and desirable rheology for flowable concrete. Similarly, the importance of aggregate packing to ensure desirable concrete properties has also been well documented. A well-designed aggregate component in mixtures such as UHPC also helps to lower the cost and improve volumetric stability, in addition to providing enhanced performance. Aggregate packing strategies to design UHPC mixtures have been reported (de

Larrard and Sedran 1994b; Nancy A. Soliman and Tagnit-Hamou 2017; Yu, Spiesz, and Brouwers 2014a; Chan and Kwan 2014).

This chapter describes an aggregate (size and amounts) selection method based on the compressible packing model (De Larrard 1999; Roquier 2016), that is implemented alongside the binder selection method based on microstructural packing and rheology described in (Arora et al. 2018), to develop strong and economical UHPC mixtures. The binder component is designed to be sustainable and economical, with 30% to 50% replacement of portland cement (mass-based) by commonly available fine materials including fly ash, silica fume, metakaolin, and limestone powder. Contrary to many UHPC mixtures that contain only fine aggregates, the material design reported in this chapter considers coarse aggregates (passing 9.5 mm sieve) also. The effect of fibers on aggregate packing is also accounted for. The mechanical (compressive and flexural strengths) and durability (moisture and ion transport resistance) performance of the designed UHPC mixtures are also reported, along with the material cost of these mixtures. The methodology is designed in such a manner for implementation in a computer program to optimize the UHPC mixtures from both the performance and cost perspectives.

7.2. MATERIALS AND TEST METHODS

7.2.1 Materials

The components of the binder phase of UHPC mixtures studied here include a Type I/II ordinary portland cement (OPC) conforming to ASTM C 150, Class F fly ash and metakaolin conforming to ASTM C 618, ground granulated blast furnace slag (GGBFS) conforming to ASTM C 989, limestone powder conforming to ASTM C 568, and micro

silica (silica fume) conforming to ASTM C 1240. Limestone powders with two different median particle sizes (1.5 μm and 3.0 μm) are used to ensure improved particle packing. The particle size distribution (PSD) curves of the powders are shown in Figure 7-1, while their chemical compositions and physical characteristics are shown in Table 7-1. The water-to-powder ratios (w/p) varied between 0.165 and 0.20 depending on the starting materials used. A polycarboxylate ether (PCE)-based superplasticizer was used, with a solids content of 43%. The ratio of solids content of the superplasticizer to the binder content was maintained between 1% and 2%.

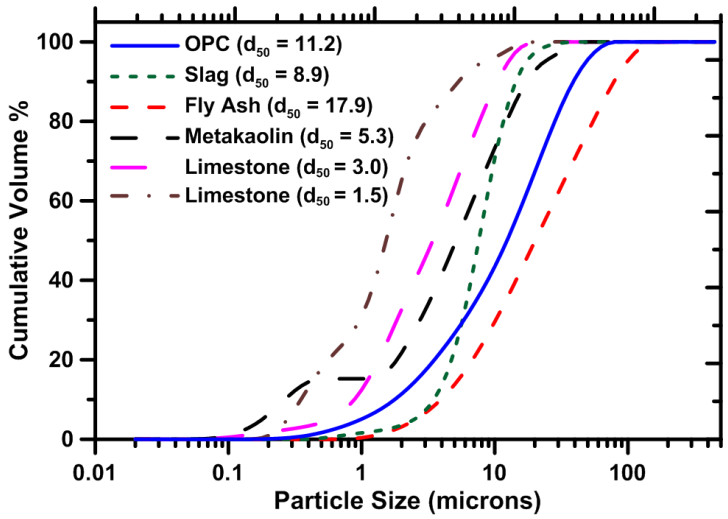

Figure 7-1: Particle size distribution curves for cement, fly ash, slag, metakaolin, and limestone powders. The median size in microns is shown in parentheses.

Table 7-1: Chemical composition and physical properties of the starting materials used for the binders

Components of the binder	Chemical composition (% by mass)							BET Specific surface area
	SiO_2	Al_2O_3	Fe_2O_3	CaO	MgO	SO_3	LOI	
OPC	19.60	4.09	3.39	63.21	3.37	3.17	2.54	1318
Slag (S)	39.41	8.49	0.37	35.53	12.05	2.83	1.31	1282
Fly Ash (F)	58.40	23.80	4.19	7.32	1.11	3.04	2.13	3021
Metakaolin (K)	51.70	43.20	0.50	-	-	-	0.16	14915
Micro silica (M)	>	-	-	< 1.0	-	-	-	18253
Limestone (L), 1.5	> 97% $CaCO_3$							7518
Limestone (L), 3 μm								1860

Fine and coarse aggregates conforming to ASTM C 33 were used. Smaller coarse aggregates are required to proportion UHPC mixtures, and thus only those passing a 3/8" sieve (9.5 mm) was used. The aggregates were then classified into three nominal maximum sizes: ¼" (6.25 mm), #4 (4.75 mm), and #8 (2.36 mm). Due to the relatively high proportion of 6.25 mm particles in the sourced aggregates, they were crushed using a laboratory pulverizer to obtain the requisite amounts of 4.75 mm and 2.36 mm size particles. The aggregates were washed and dried to remove impurities on the surface that might interfere with water demand and strength. Their bulk specific gravity and absorption were determined as 2.65 g/cc and 0.94% respectively. Coarse and fine silica sands with median sizes of 0.6 mm and 0.2 mm respectively were used as fine aggregates. The mortar mixtures had both sand types

[8] BET is a direct and more appropriate method to determine specific surface area since it does not make any assumptions on particle shapes. BET method measures a monolayer of N_2 molecules covering the surface area. BET is also able to interrogate the small pores in the particles, which makes the specific surface areas of materials like fly ash very different from the Blaine's measurements. The BET specific surface areas of the source materials reported here are in line with generally reported values for such materials.

in equal amounts. The mortar cubes and the cylindrical concrete specimens were proportioned using a paste volume fraction of 65%. The fiber reinforced UHPCs employed straight high-strength steel microfibers having a length of 13 mm and a diameter of 0.5 mm. The aggregates and fibers used are shown in Figure 7-2.

The aggregates were washed and dried to remove impurities on the surface that might interfere with water demand and strength. Their bulk specific gravity and absorption were determined as 2.65 g/cc and 0.94% respectively. Coarse and fine silica sands with median sizes of 0.6 mm and 0.2 mm respectively were used as fine aggregates. The mortar mixtures had both sand types in equal amounts. The mortar cubes and the cylindrical concrete specimens were proportioned using a paste volume fraction of 65%. The fiber reinforced UHPCs employed straight high-strength steel microfibers having a length of 13 mm and a diameter of 0.5 mm. The aggregates and fibers used are shown in Figure 7-2.

Figure 7-2 – Coarse aggregates (6.25mm, 4.75mm and 2.36mm), fine aggregates (coarse sand, fine sand) and steel fibers used in the study.

7.2.2 Mixing and Curing Procedure

Two different mixing methods were adopted in this chapter, one for small volumes, and another for a larger volume. For smaller volumes, a mixing bucket made of HDPE was used. A 12.5 mm Dewalt™ spade drill attached to a spiral drill bit was used as the mixing tool for better shearing of particles. This is required to disperse the finer components of the binder – micro-silica and metakaolin in particular. Coarse and fine aggregates were initially blended together. If the aggregates were dry, mixing water corresponding to their absorption values was added. The aggregates were then blended with micro-silica for 5 minutes. This allowed for shearing between the hard quartz particles and micro-silica to de-agglomerate the micro-silica particles and disperse them adequately. Next, limestone powder was added and mixed until it was uniformly dispersed in the mixture. Fly ash or slag and OPC were subsequently added and mixed for a minimum of 3 minutes until the mixture became homogenous. After all the dry powders and fine aggregate were mixed, half the amounts of desired mixing water and superplasticizer were added and mixed for another 5 minutes. Care was taken to ensure that the mixture did not adhere to the sides of the mixer. The remaining water and superplasticizer were added and mixing was continued for an additional 5 minutes. The final stage of mixing lasted between 5-10 minutes (depending on the type of the mixture) until the mixture became very fluid and cohesive. In the case of fiber reinforced UHPC, fibers were slowly added during the final stage of mixing.

To evaluate the effects of scaling the size of the mixture and to evaluate if proper mixing can be accomplished under field conditions, one selected UHPC mixture was mixed in a Croker RP100XD Rotating Pan Mixer with a capacity of 0.14 m^3 (5 ft^3). The mixer consists of two shearing paddles which are held-in-place while the pan containing the concrete rotates at a pre-defined speed of 74 rpm. This mixing arrangement simulates more closely, the mixing of concrete in a truck. A fixed scraper blade attached to the assembly helps remove any paste sheared to the sides and provides a uniform mixing environment. A 0.06 m^3 (2 ft^3) UHPC mixture was mixed in the large mixer following the same mixing sequence, and mixing-and-rest times described earlier. Figure 7-3 shows the self-consolidating UHPC mixture thus obtained. The slump flow was measured on a non-absorbent polycarbonate plate in accordance with ASTM C 1611 ("ASTM C1611/C1611M-14 Standard Test Method for Slump Flow of Self-Consolidating Concrete" 2014). A slump flow of 355 mm was obtained, which is comparable to those of conventional self-consolidating concretes (Khayat 1999; Su, Hsu, and Chai 2001).

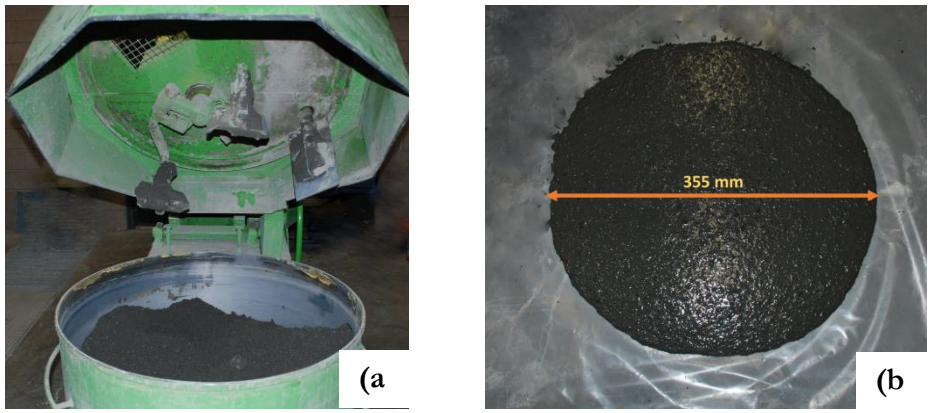

Figure 7-3 – (a) Image showing the self-consolidating UHPC mixture in the Croker RP100XD rotating pan mixer, and (b) slump flow test conducted on fresh UHPC, showing no segregation

Immediately after mixing, the mixture was poured into the cube, beam and cylinder molds resting on a vibrating table. The molds were filled, rodded, and then vibrated (~0.5-2 minutes). Care was taken while vibrating so that any entrained air is removed, and segregation prevented. Once the molds were filled, they were tightly covered with a plastic wrap, and then loosely covered with a plastic sheet for 24 hours, after which they were demolded and stored in a moist chamber (>95% RH) maintained at a constant temperature of 23 ± 2 ºC until the desired age of testing.

7.2.3 Determination of Compressive and Flexural Strengths

The compressive strength of 50 mm mortar cubes was determined in accordance with ASTM C 109 and that of the 75 mm x 150 mm cylindrical concrete specimens in accordance with ASTM C 39. The flexural response of the specimens after 28 days of curing was evaluated using four-point bending tests in accordance with ASTM C 1609 in a closed-loop, servo-controlled testing system. Prismatic concrete beam specimens (50 mm x 65 mm x 380 mm) were tested in flexure. Six beams were tested for each mixture.

7.2.4 Determination of Moisture and Ionic Transport Properties

The moisture transport tests were carried out in this chapter after 28 days of curing, in accordance with ASTM C 1585. 50 mm thick discs cut from 200 mm long and 100 mm diameter cylindrical specimens were used for these tests after conditioning them in KBr solution first, and then in a sealed container to equilibrate the internal humidity. The

specimens were then completely sealed on their sides and bottom, leaving only the top surface exposed. The exposed surface of the specimen was placed face down on plastic supports inside the pan containing water filled up to 3 mm above the top of the supporting device. The mass of the specimens was measured at regular intervals in accordance with the specification and the initial and final sorptivities calculated.

The resistance of UHPC to chloride ion penetration was measured using the Rapid Chloride Permeability test (RCPT, ASTM C 1202) and Non-Steady State Migration test (NSSM, NT Build 492). Both tests are carried out on 100 mm diameter and 50 mm long concrete discs that are cut from 200 mm long cylinders. RCPT provides an indication of the resistance of the concrete to chloride ion penetration under an externally applied potential of 60 V. The test records the total charge passed through the specimen during the 6 hour testing duration. NSSM test facilitates the determination of the ionic migration coefficient typically under lower applied potentials (based on the initial value of the current when a 30 V potential is applied; for highly resistive samples, a higher potential might be required). Each specimen was enclosed in a test cell containing 2 N NaCl in the catholyte chamber and 0.3 N NaOH in the anolyte chamber. After the specified test duration (generally, 24 hours), the specimen was axially split and a 0.1 N silver nitrate solution sprayed on the split surfaces to determine the chloride penetration depth. Five to seven measurements of penetration depth were made on each split surface. The NSSM coefficients, (D_{nssm}) were calculated using the average values of the penetration depths (x_d) and Equations 7-1 and 7-2.

$$D_{nssm} = \frac{RT}{zFE} \cdot \frac{x_d - \alpha\sqrt{x_d}}{t} \qquad \text{(Eq. 7-1)}$$

$$E = \frac{U-2}{L}$$

(Eq. 7-2)

Here, R is the molar gas constant (8.314 J/(K·mol)), Z is the absolute value of ion valence, (1, for chloride ions), F is the Faraday's constant (9.648×10^4 J/(V·mol)), U is the absolute value of the applied voltage, T is the average value of the initial and final temperatures in the anolyte solution (K), L is the thickness of the specimen (m), t is the test duration (s), C_d is the chloride concentration at which white silver chloride precipitates, and C_0 is the chloride concentration in the catholyte solution ($C_0 \approx$ 2N).

7.3. BINDER SELECTION FOR UHPC

The cementitious paste is a major component of UHPCs, ranging in volume from 50% to 75% (Park et al. 2008; Kay Wille et al. 2011; Russell and Graybeal 2013). Thus, developing economical and efficient UHPC mixture design involves optimal design of the paste phase. Using commonly available binding materials (fly ash, slag, silica fume, metakaolin and limestone), several carefully designed combinations with cement replacement levels (mass-based) ranging from 20% to 50% were evaluated for microstructural packing and paste rheology. The mass-based w/p for the paste studies was around 0.20. A regular high-performance plain cement paste (w/c = 0.32) was also formulated for comparison. The microstructural packing was evaluated using a stochastic packing model with periodic boundary conditions, developed in MATLAB®. The algorithm digitally packs spherical particles in a 3D representative volume element (RVE), chosen here as 300 x 300 x 300 μm^3. Microstructural models were created for the paste mixtures based on the particle size distribution and relative proportions of the component powders. The packing parameters

extracted from the microstructural models were the coordination number (CN) and mean centroidal distance (MCD) of particles, and the number density of the microstructure (N_d) while the rheological parameters included yield stress (τ_y), plastic viscosity (μ_p) and mini-slump flow area (A_{ms}). The microstructural and rheological parameters individually, or their combinations to define packing and flow coefficients, were used in binder selection as shown in Figure 7-4. The preset values for packing and flow coefficients were arrived at based on detailed analysis of microstructural packing and rheological parameters, and their comparison with similar values for control mixtures. This algorithm for binder selection based on both the microstructural packing and rheological parameters has been described in detail in (Arora et al. 2018).

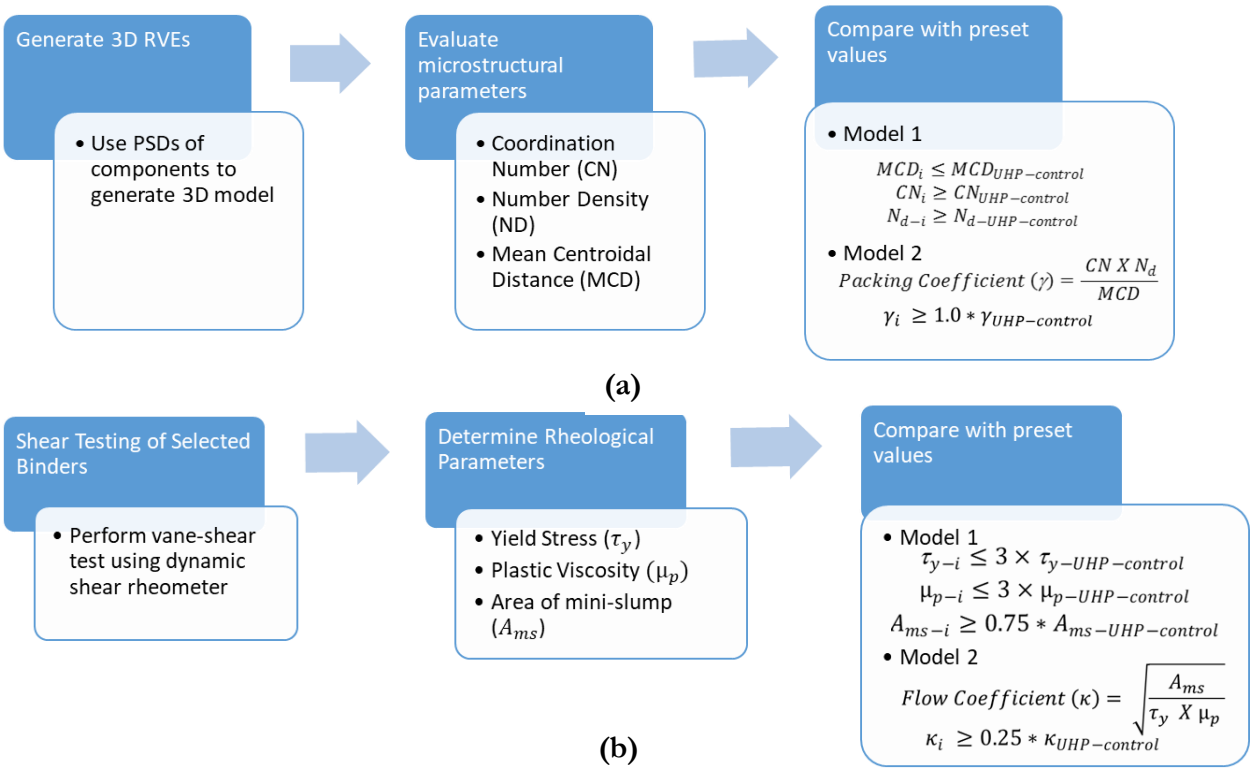

Figure 7-4 – Binder selection strategy based on: (a) microstructural parameters (coordination number, number density and mean centroidal distance) from virtual RVEs, and (b) rheological parameters (yield stress, plastic viscosity and area of mini slump)

Based on the algorithms shown in Figure 7-4 and the 28-day compressive strength results, a smaller sub-set of binders were selected for the second stage study. Consideration was also given to the clinker factor of the binders, so that sustainable UHPC mixtures can be formulated. Thus, three different binder combinations are chosen as matrices for economical UHPCs in this chapter, and are shown in Table 7-2. Two of the binders are quaternary blends of cement, silica fume, limestone, and fly ash/slag with an overall cement replacement of 30% by mass, and the third is a ternary blend of cement, silica fume, and limestone with an overall cement replacement of 50% by mass. The mixtures were initially composed of a low w/p, and then incremental amounts of water and superplasticizer were added in stages to achieve the desired workability. Hence the w/p and superplasticizer dosage are different for the three mixtures detailed in Table 7-2. Owing to the spherical nature of its particles, the mixture containing fly ash as the dominant cement replacement material required the least amount of water and superplasticizer for desired workability. The higher water demand for metakaolin and microsilica-bearing mixtures are attributed to the high surface area of these particles.

Table 7-2 – Selected binders and their compositions

Mixture composition	Mixture ID*	Replacement material (% by mass of cement)				w/p	Superplasticizer content (%
		Fly Ash	Metakaolin	Microsilica	Limeston		

		(F)/ Slag (S)	(K)	(M)	e (L)**		solids content by mass of the binder)
OPC + S + M + L	$S_{17.5}M_{7.5}L_5$	17.5	0	7.5	5	0.194	1.5
OPC + F + M + L	$F_{17.5}M_{7.5}L_5$	17.5	7.5	0	5	0.166	1.2
OPC + M + L	$M_{20}L_{30}$	0	0	20	30	0.188	1.4

*The mixtures containing fibers are labeled in the graphs with '-f' after the mixture ID specified in this table.
**Equal amounts of limestone powder with d_{50} of 3 μm and 1.5 μm are used in these mixtures.

Mortars were cast using the mixture proportions reported in Table 7-2. As mentioned earlier, the fine aggregate used was an equal mixture of coarse sand (d_{50} = 0.6 mm) and fine sand (d_{50} = 0.2 mm) since this combination was found to provide higher strengths for several trial mixtures. The volumetric ratio of paste-to-aggregate was selected to be 0.65:0.35, again based on improved strength results that were obtained for this combination as opposed to a 0.50:0.50 paste-to-aggregate ratio that was employed in several trial mixtures. The mixing procedure as specified in Section 2.2 was followed to cast 75 mm x 150 mm cylinders. Figure 7-5 shows the compressive strengths of these mortars as a function of the age determined in accordance with ASTM C 109. At 90 days, all the mixtures attained a compressive strength of 150 MPa or higher, with the quaternary fly ash-based mixture showing the highest

strength. Better workability of the mixture, along with a lower w/p contributed to this response. Even with a 50% clinker factor reduction, the ternary silica fume-limestone blend shows a 90-day strength of 150 MPa. This demonstrates the utility of a proper binder design procedure based on microstructural packing and rheology in obtaining high compressive strengths without resorting to trial-and-error based mixture proportioning strategies. It is thus shown that UHPC can be proportioned using commonly available starting materials without having to resort to specially processed materials or nanoparticles that significantly increase the material and processing cost associated with UHPC.

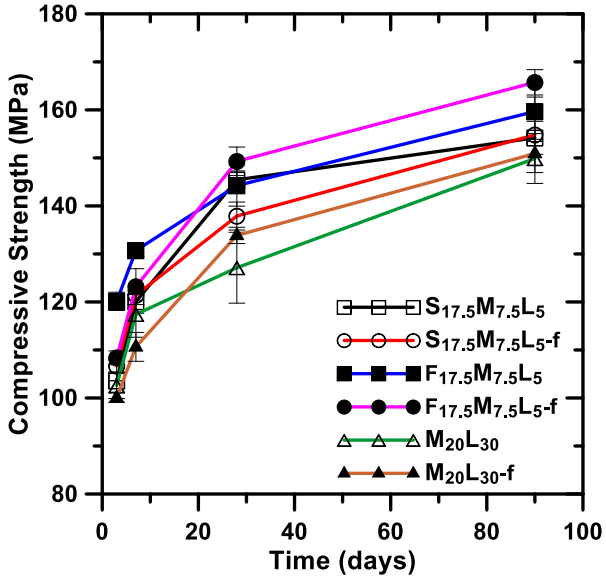

Figure 7-5 – Compressive strength of UHP mortar samples as a function of age.

7.4. PARTICLE PACKING-BASED DESIGN OF UHPC

7.4.1 Packing of Aggregates: An Overview of the Compressible Packing Model and its Application to UHPC

Adequate particle packing is extremely important in economical design of UHPCs because of the extreme performance requirements. Existing methods account for desirable packing either using packing parameters of some components (generally the coarse aggregates), or by approximating an 'ideal' grading curve that is expected to lead to maximum solid volume in a unit volume. The mixture proportioning approach for UHPC must ensure appropriate selection of the paste and the aggregate phases. The methodology for the selection of paste phase, governed by paste rheology and microstructural packing of powders has been described in detail in (Arora et al. 2018), and summarized earlier in this chapter for clarity. The selection of aggregates is governed by aggregate packing at the meso-scale since average aggregate sizes are about 100 times larger than the average sizes of the powders in the pastes. The use of a proper size distribution of aggregate particles can help increase the overall packing density of the concrete mixture in combination with the use of a properly chosen paste phase.

Virtual packing density, in a random packing model (Fu and Dekelbab 2003; Stroeven and Stroeven 1999) is defined as the maximum packing density which can be achieved by placing each particle one by one in appropriate positions in a representative volume. Yu et.al (Yu, Spiesz, and Brouwers 2014a) employed the Andreasen and Andreasen particle-packing model to produce a dense UHPC with a binder content of about 650 kg/m^3. Stovall and de Larrard (Stovall, de Larrard, and Buil 1986) modified the suspension viscosity model by Mooney (Mooney 1951) to derive the linear packing density model, which considers the packing of solids as a suspension of infinite viscosity. The Funk and Dinger packing theory was used by Le (Le et al. 2015) in order to determine the grading of aggregates for self-

compacting high performance concrete. Several other related particle packing models that can be used for concrete mixture proportioning are reported (Toufar, Born, and Klose 1976; Dewar 2002; Goltermann, Johansen, and Palbøl 1997). This chapter employs a compressible packing model (Stovall, de Larrard, and Buil 1986) to select appropriate combinations of aggregate sizes and amounts in order to maximize the packing density of a poly-disperse mixture. The compressible packing model for multi-sized grains expresses the packing density as a function of the fractional solid volume of each grain size present in the mixture. It is assumed that there is at least one dominant component (that has the highest packing density) among the various grain sizes present in the mixture. By sequentially considering each class of particles as dominant, a series of packing density functions are obtained. The minimum packing density obtained by considering each of the aggregate sizes as the dominant size, can conservatively considered as the packing density of the mixture (De Larrard 1999; Lecomte 2006b).

For the UHPCs in this study, only three separate size ranges of coarse aggregates with nominal maximum sizes of 6.25 mm, 4.75 mm and 2.36 mm were considered. Two size ranges of fine aggregates – with d_{50} of 0.6 mm and 0.2 mm, were also chosen. In order to select the proportions of particles of different sizes, several combinations were considered and the particle packing density for each combination was obtained using the compressible packing model. A scalar index, termed the compaction index, 'K', is defined as shown in Equation 7-3, to define the physical effort involved in packing these particles. A higher compaction index implies a lower amount of voids and a higher packing fraction of

aggregates. A 'K' value of 9 can be used when the particles are extremely well packed (De Larrard 1999). The packing density φ of the mixture is related to the compaction index K as:

$$K = \sum_{i=1}^{n} \frac{y_i/\beta_i}{1/\phi - 1/\gamma_i} \quad \text{(Eq. 7-3)}$$

Here, y_i represent the individual packing fractions of the aggregates in the mixture. The residual packing density β_i represents the packing density of a mixture containing only the aggregate class 'i'. The values for residual packing density can be determined experimentally using the dry rodded unit weight (DRUW) test. The virtual packing density γ_i is the theoretical value of packing density for the aggregate mixture when aggregate class 'i' is dominant. A dominant aggregate class is the one with the maximum volume fraction amongst all the other aggregate classes. Equation 7-3 can be numerically solved (the Newton-Raphson method was used in this work) to obtain the packing density φ once all the other parameters are determined using Equations 7-4 to 7-6.

$$\gamma_i = \frac{\beta_i}{1 - \sum_{j=1}^{i-1}[1 - \beta_i + b_{ij}\beta_i(1 - 1/\beta_j)]y_j - \sum_{j=i+1}^{n}[1 - a_{ij}\beta_i/\beta_j]y_j} \quad \text{(Eq. 7-4)}$$

Equation 7-4 is a linear formulation for the calculation of virtual packing density, which considers the interactions encountered by aggregate class 'i' due the presence of other aggregate classes in the mixture. These interactions generally manifest in the form of loosening effect a_{ij} and wall effect b_{ij} for aggregate class 'i' due to the influence of aggregate class 'j' (Stovall, De Larrard, and Buil 1986). Loosening and wall effects interfere with the overall packing densities. While calibration of the model can be done by determining the coefficients a_{ij} and b_{ij} using experiments, simplified empirical formulations which are

functions of the diameters d_i and d_j of aggregate classes 'i' and 'j' respectively, are available for these parameters (De Larrard 1999; Lecomte 2006a).

7.4.2 Accommodating Fibers using a Perturbation Model

High fiber volume fractions used in UHPC enhances its post-cracking performance and provides strain hardening response. Fibers are also beneficial in cementitious mixtures to control microcracking and restrain shrinkage cracking. Discrete steel fiber reinforcement included in UHPC allows the concrete to maintain tensile capacity beyond the cracking strain of matrix. However, the inclusion of fibers, which are essentially volumes with one dimension significantly larger than the other two dimensions, increases the fraction of voids in a poly-disperse mixture of aggregates. A perturbed volume approach was proposed by Ben-Aim (Aim and Le Goff 1969) to account for the effect of fibers. The perturbed volume (V_p) encompasses a region where the distance between the wall and each point is less than d/2, where d is the fiber diameter. In this perturbed volume, the mean packing density is reduced to $k_w\alpha$ with $k_w < 1$, whereas α is the packing density in the rest of the container. The mean value of packing density for the whole system φ' is then given by Equation 7-5. Here φ is the packing density determined using Equation 7-1.

$$\acute{\Phi} = \left[1 - (1 - k_w)V_p\right]\Phi \qquad \text{(Eq. 7-5)}$$

7.4.3 Selecting Aggregate Combinations and Amounts for UHPC Mixtures

Several studies on UHPC predominantly consider it as a mixture of paste and fine aggregates with an extremely low w/p (Kay Wille, Naaman, and Parra-Montesinos 2011; Park et al. 2008; Alkaysi et al. 2016). The volumetric ratio of paste-to-aggregate in UHPC is about 1.5:1,

as reported in several studies (Reda, Shrive, and Gillott 1999; Russell and Graybeal 2013; Yu, Spiesz, and Brouwers 2015). This is considerably different from ordinary concrete where the paste-to-aggregate ratio is nearly 0.4:1 and coarse and fine aggregates together make up for about 70% of the total concrete volume. These predominantly fine aggregate-based mixture designs are suitable for small volumes of UHPCs (e.g. bridge connections) or for applications where larger aggregates are a hindrance (grouting and shotcreting). They are also suitable in applications where shrinkage is not a critical issue. However, for UHPC to be used in larger volumes such as in bridge decks and piers, the use of coarser particles need to be considered to minimize volume changes and to reduce cost. Therefore, in this study, coarse aggregates, (smaller than 6.25 mm) are employed in addition to fine aggregates to form a stable backbone for the paste phase. The dimensionally stable aggregate network comprises of size ranges from 0.2 mm (fine sand) to 6.25 mm (larger coarse aggregate). The packing density for any given combination of aggregate classes can be determined by solving Equation 7-3. The optimum fraction of individual aggregate classes required to achieve the maximum packing density was obtained by solving Equation 7-3 for multiple aggregate combinations. The volume fraction of each aggregate class was varied from 0.0 to 1.0 in increments of 0.1. This resulted in a total of 885 different aggregate combinations. A computer program written in MATLAB was developed to automatically choose the aggregate combinations and input them into the algorithm for packing density determination. The methodology for packing density determination accounts for the wall and loosening effects.

The distribution of packing density as a function of the fraction of aggregate classes is shown in Figures 7-6 (a-f). In Figure 7-6 (a), the volume fraction of the coarse aggregate refers to the combined volume fraction of aggregates whose nominal maximum size exceeds 2.36 mm, and includes the 6.25 mm, 4.75 mm and 2.36 mm nominal maximum size aggregates. Similarly, in Figure 7-6 (b), fine aggregate refers to the two sands of median sizes 0.6 mm and 0.2 mm. In Figure 7-6(a), for each value of volume fraction of coarse aggregate on the x-axis, one can notice multiple values of the calculated packing density. These values correspond to the packing densities obtained by using different combinations of the chosen aggregates that result in a net coarse aggregate volume fraction equal to that shown on the x-axis. For instance, a coarse aggregate volume fraction of 0.60 may be achieved using multiple aggregate combinations of coarse aggregates (nominal maximum sizes of 6.25mm, 4.75mm, and 2.36 mm). Similarly, the fine aggregate volume fraction of 0.40 can be composed of different combinations of the two selected sizes of fine aggregates (d_{50} of 0.6 mm and 0.2 mm). As examples, the volume fractions of particles in a combined mixture containing 60% coarse aggregates and 40% fine aggregates, in the order of decreasing sizes, can be listed as (0.2,0.2,0.2,0.2,0.2), (0.4,0.1,0.1,0.2,0.2), (0.4,0.1,0.1,0.3,0.1) etc. Each of these combinations would result in a unique aggregate packing and therefore present a unique value of packing density. It can be observed from Figure 7-6(a) that maximum packing density occurs when the volume fraction of coarse aggregates is 60%. The plot of packing density as a function of aggregate size combinations helps understand the combined effect of coarse and fine aggregates on the packing density of the mixture.

Figures 7-6(c-e) show the packing density determined as a function of the amount of individual coarse aggregate sizes. These plots help discern the effect of aggregate sizes on the total packing density. It is noticed that maximum packing densities occur when the amounts of 6.25 mm, 4.75 mm and 2.36 mm size aggregates in the mixture are 40%, 10% and 10% respectively, thereby providing an overall coarse aggregate content of 60%, which is the same as that obtained from Figure 7-6(a). Figure 7-6(f) compares the packing densities predicted by the model when two different volume fractions of fibers are introduced into the aggregate mixture. The perturbation model described earlier was used to determine the influence of fibers. To keep the figure concise, only the maximum packing density obtained for each volume fraction of coarse aggregate in the total aggregate mixture is plotted. Since fibers disrupt the packing of the mixture due to their elongated shape, an increase in the fiber content is observed to reduce the maximum packing density; however, the locations of the packing density maxima are unchanged irrespective of the fiber content. Thus, the combination of aggregates to achieve the maximum packing density can be considered to be independent of the fiber volume fractions commonly employed in UHPC mixtures.

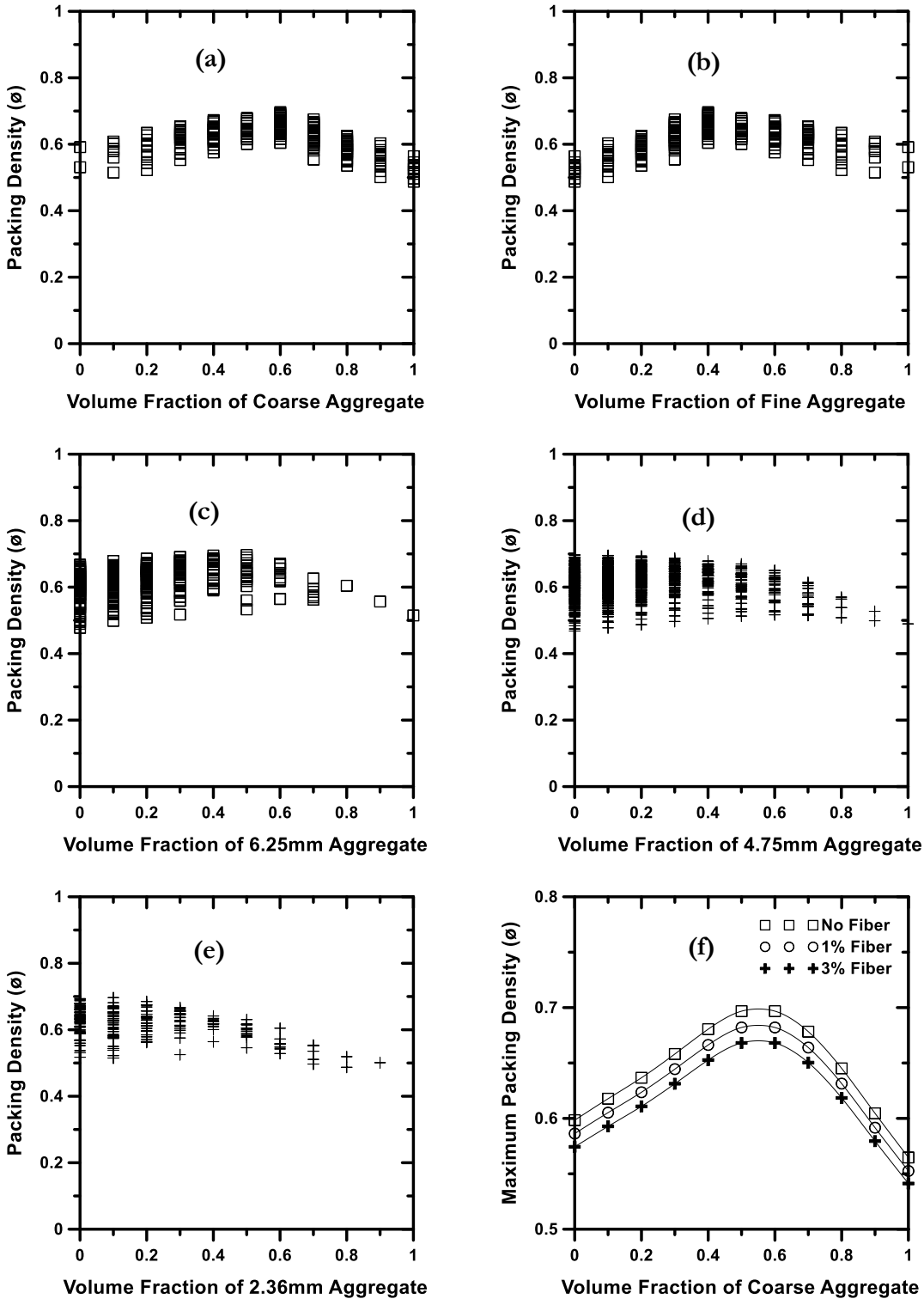
(a)
Packing Density (ø)
Volume Fraction of Coarse Aggregate
(b)
Packing Density (ø)
Volume Fraction of Fine Aggregate
(c)
Packing Density (ø)
Volume Fraction of 6.25mm Aggregate
(d)
Packing Density (ø)
Volume Fraction of 4.75mm Aggregate
(e)
Packing Density (ø)
Volume Fraction of 2.36mm Aggregate
(f)
No Fiber
1% Fiber
3% Fiber
Maximum Packing Density (ø)
Volume Fraction of Coarse Aggregate

Figure 7-6 – Packing density as a function of volume fractions of: (a) coarse aggregate, (b) fine aggregate, (c) 6.25mm aggregate, (d) 4.76mm aggregate and (e) 2.36mm aggregate. (f) Maximum packing fraction as a function of volume fraction of coarse aggregates for different fiber volume fractions.

From the simulation results of 855 combinations of aggregates, the maximum value of packing density of aggregates, ø, was obtained as 0.696 for a mixture with 40% of fine aggregates and 60% coarse aggregates as shown in Figure 7-6(a). The packing density values for a few aggregate proportions solved using CPM are shown in Table 7-3, with the proportion corresponding the maximum packing fraction highlighted. The simulated packing density values were also verified for a few selected blends using the DRUW method and are shown in Figure 7-7.

Table 7-3 – Packing density values for a few aggregate proportions obtained using CPM

#4	**#8**	**#10**	**Concrete Sand**	**Fine Sand**	**Packing Density**
0.4	**0.1**	**0.1**	**0.2**	**0.2**	**0.696**
0.3	0.1	0.2	0.2	0.2	0.685
0.1	0.3	0.1	0.3	0.2	0.675
0.5	0.1	0.1	0.2	0.1	0.671
0.1	0.3	0.2	0.3	0.1	0.657
0.2	0.1	0.4	0.1	0.2	0.634
0.1	0.1	0.1	0.2	0.5	0.599
0	0	0	0.6	0.4	0.591

0.2	0.1	0.5	0.1	0.1	0.587
0.4	0.1	0.5	0	0	0.546
0.1	0.1	0.8	0	0	0.494

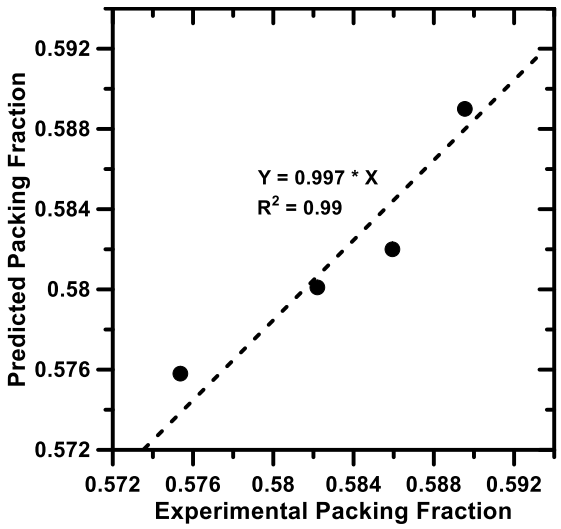

Figure 7-7 – Comparison of experimental packing fractions obtained from DRUW test and predicted packing fractions obtained from CPM

7.4.4 Practical Guidelines for Choosing Aggregates for UHPC

Figure 7-8 shows the PSD for the optimized aggregate gradation obtained and compares it with the PSD of aggregate gradations commonly used in the construction industry in the U.S., and specified in ASTM D 448 for road and bridge construction. The optimized aggregate proportion obtained here is finer than any of the conventional aggregate PSD. Therefore, in order to obtain the optimized aggregate proportion, existing stockpiles must be screened to obtain higher volume proportions of the finer aggregate sizes. An alternative to

this is to blend the available aggregate stockpiles together in different proportions to maximize the fractions of the desired aggregate sizes, and then sieve the resultant aggregate blend. It is observed that aggregate stockpiles #89 is the closest to the optimized packing gradation.

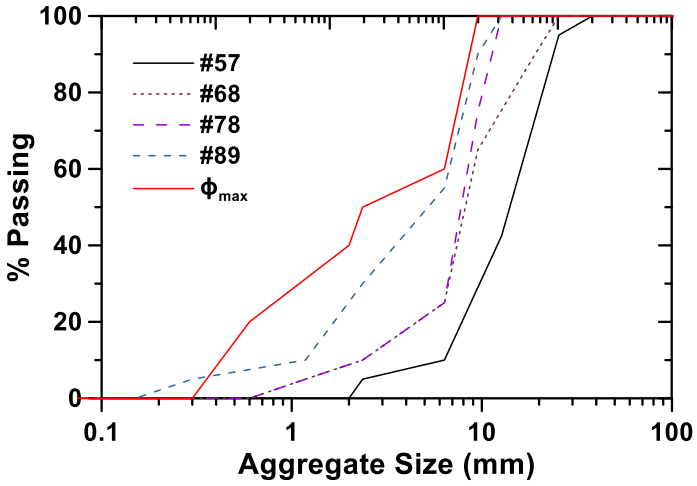

Figure 7-8 – Comparison of PSDs of commercially available aggregate gradations and optimized gradation obtained from this study. Refer to ASTM D 448 for details on sizes (#58, #68, #78, and #89).

The packing density values for the existing aggregate stockpile gradations were also calculated using CPM. The results are presented in Table 7-4. It is observed that since the individual aggregate proportions in the standard stockpile gradations allows a range (see ASTM D 448), the results also show a wide range of packing density values that could be obtained for these stockpiles. In such a case, quality control becomes extremely important to maximize the packing density of such aggregates. It is observed that aggregate stockpile #89 gives the highest packing density, whereas #68 stockpile gives the lowest density.

Table 7-4 – Comparison of packing densities obtained

Aggregate Type	**#57**	**#68**	**#78**	**#89**	φ_{max}
Packing Density	0.55-0.62	0.54-0.63	0.55-0.65	0.56-0.66	0.696

A dense packing obtained from the optimized aggregate gradation as described in this chapter, coupled with an optimized paste phase is expected to lead to a concrete microstructure that has a low porosity and consequently, higher strength and durability. The aggregate combination with the highest packing density was further selected towards the design of UHPC mixtures.

7.5. PROPERTIES OF SELECTED UHPC MIXTURES

7.5.1 Compressive and Flexural Strengths

Since all the three selected binders detailed in Table 7-2 showed comparable mortar compressive strengths as was shown in Figure 7-5, two out of the three mixtures were selected for casting concrete cylinders and beam specimens for further mechanical and durability property evaluation. Two concrete batches were prepared for each binder mixture, one without any steel fiber reinforcement and the other incorporating 1% of steel fiber by volume. While fiber-reinforced UHPC mixtures require 3% (or more) by volume of fibers in order to demonstrate strain-hardening behavior, the fiber content is limited to 1% in this study to obtain economical mixtures that show appreciable post-peak response, if not strain-hardening. The mixture proportions chosen for the concrete mixtures are given in Table 7-5.

Table 7-5 – Mixture proportions for concrete mixtures. All the starting material contents, except the fiber content are relative masses with respect to that of the OPC.

Mixture components	$F_{17.5}M_{7.5}L_5$	$F_{17.5}M_{7.5}L_5$-f	$M_{20}L_{30}$	$M_{20}L_{30}$-f
OPC	1.0	1.0	1.0	1.0
Fly Ash (FA)	0.175	0.175	-	-
Silica Fume (SF)	0.075	0.075	0.20	0.20
Limestone (LS)	0.05	0.05	0.30	0.30
Superplasticizer	0.0125	0.0125	0.0127	0.0127
Steel Fibers (% by volume)	-	1.0	-	1.0
w/b (mass-based)	0.165	0.168	0.180	0.185
Aggregate/Binder	0.7	0.7	0.7	0.7

The compressive strengths of concrete cylinders were determined using a 2670 kN load frame. Three cylinders each were tested after 7, 14 and 28 days of curing in a moist chamber and the average values are reported in Figure 7-9 (a). It was found that the compressive strength of all the specimens exceeded 140 MPa at 28 days. The mixture containing fly ash, silica fume, and limestone, with an overall cement replacement level of 30%, was found to have the highest 28-day strength, of 153 MPa. Based on the mortar strength results shown in Figure 7-5, this mixture can be expected to provide compressive strength in excess of 175 MPa after 56 or 90 days. The mixtures with fibers show comparable strengths as that of the mixtures without fibers, which is expected since 1% by volume of fibers do not contribute significantly to the compressive strength. Moreover, the reduction in overall packing density because of the incorporation of fibers also impacts the compressive strength. The 28-day

flexural strength results shown in Figure 7-9 (b) also reveal similar trends. However, companion load-deflection studies of UHPC beams under closed-loop testing brought out with more clarity, the beneficial post-peak influence of fibers.

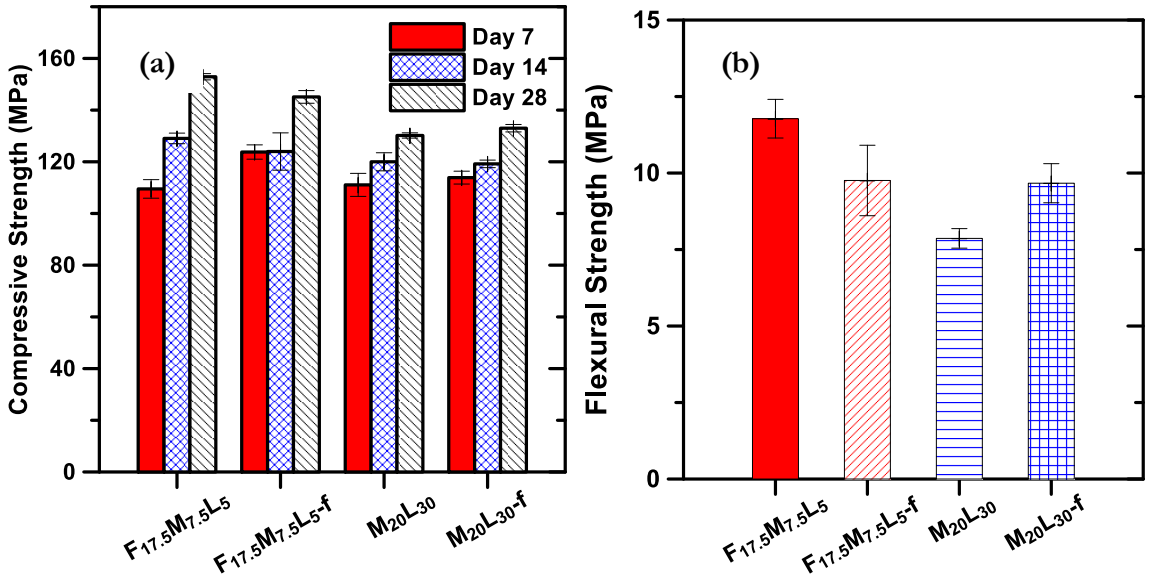

Figure 7-9 – (a) Compressive strength of UHPC mixtures after 7, 14 and 28 days of curing, and (b) 28-day flexural strength of UHPC mixtures

7.5.2 Moisture and Ionic Transport through UHPC

The durability properties of the selected UHPCs were evaluated using moisture and ionic transport tests after 28 days of moist curing in accordance with procedures mentioned in Section 2.4. Figure 7-10(a) shows the absorption, I, as a function of square root of time. The absorption (in units of length) is calculated as the change in mass of the specimen divided by the product of its cross-sectional area and the density of water. It is observed from Figure 7-10(a) that both the UHPC mixtures show a very low value of absorption as compared to the plain OPC concrete. Among the two UHPC mixtures, the ternary silica fume-limestone

mixture (with an overall cement replacement level of 50%) shows a lower value of absorption as compared to the quaternary fly-ash mixture. This is expected because of the high volume of extremely fine silica fume and limestone particles present in the mixture, which helps in pore refinement and reduction of overall porosity. The initial sorptivity is calculated as the slope of the linear fit of the data in Figure 7-10(a) for the first six hours and the secondary sorptivity is the slope of the linear fit of the absorption data from days 1 to 7. Figure 7-10(b) shows the initial and secondary sorptivities of the selected UHPCs and compares those to the sorptivities of a conventional OPC concrete proportioned with a w/c of 0.40. The initial sorptivity has been found to be related to the porosity of the paste phase and the threshold diameter of the pores, and the secondary sorptivity to the critical pore diameter in the paste (Cam and Neithalath 2010). Figure 7-10(b) shows that the initial and final sorptivities for the UHPCs are much lower than those of the conventional OPC concrete, as expected. The secondary sorptivities of UHPCs show a much more dramatic reduction (about 5 times lower), which is not surprising since the critical pore diameter of UHP pastes showed much larger reductions than the porosities when compared to a conventional OPC paste (Arora et al. 2018).

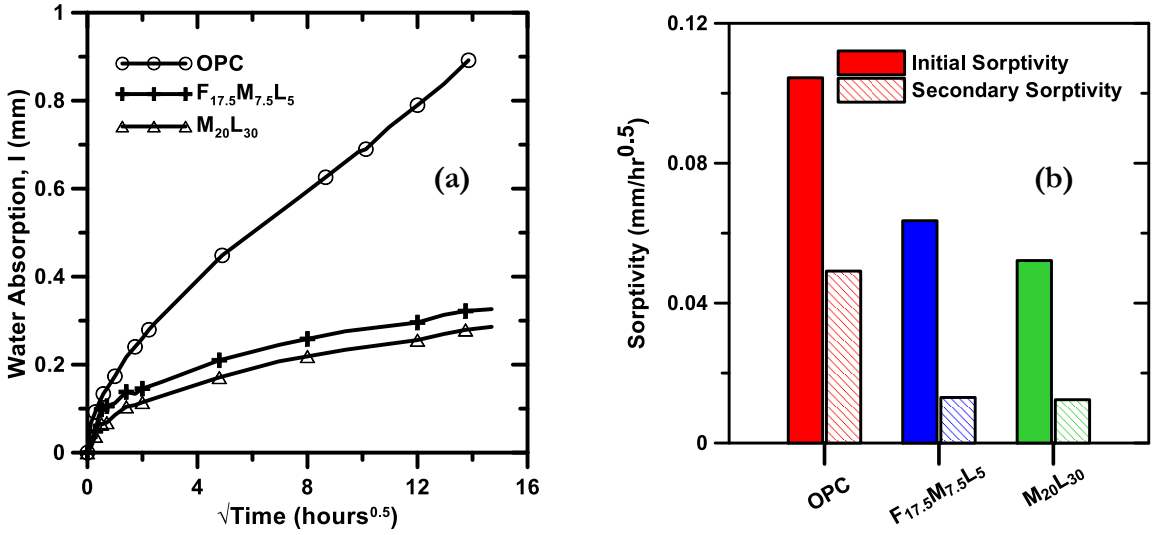

Figure 7-10 – (a) Water absorption as a function of time for UHPCs, and (b) initial and secondary sorptivity values of UHPCs and their comparison to a conventional OPC concrete with w/c of 0.40.

RCP and NSSM tests were used to determine the resistance of the UHP mixtures to chloride ion transport. Since both are electrically accelerated tests, the steel fiber reinforced mixtures were not considered. RCP test is one of the most commonly used chloride transport tests, even though it is not without serious limitations (Neithalath and Jain 2010). In practice, it is generally used to prequalify concrete mixtures or to ascertain the effectiveness of cement replacement materials. Figure 7-11(a) compares the results for total charge passed for the UHPC mixtures during the RCP test with known values for regular OPC concrete (w/c = 0.40) and high-performance concrete (HPC; w/c = 0.32) obtained from previous studies (Poon, Kou, and Lam 2006; Neithalath and Jain 2010). The total charge passed during the RCP test is extremely low for the UHPC mixtures selected, attributable to the refinement of the pore structure through the use of a very low w/p and cement replacement materials, and

the changes in pore solution conductivity primarily brought about by the use of silica fume. This is more evident in the case of the mixture with 20% of silica fume by mass replacing OPC, the reasons for which have been extensively detailed in (Neithalath and Jain 2010). As per ASTM C 1202 classification, both the UHPC mixtures designed here fall under the "very low" rapid chloride permeability category.

The non-steady state migration (NSSM) test overcomes some of the drawbacks of RCP test, and provides a migration coefficient (D_{nssm}) that is more realistically related to chloride ion transport through concrete. A lower D_{nssm} value indicates better chloride ion penetration resistance under electrically accelerated conditions. The non-steady state migration coefficient (D_{nssm}) was calculated based on Equations 7.1 and 7.2 described in Section 2.4. It is important to note that the NSSM test carried out in accordance with NT Build 492 specifies different voltage values to be applied to the specimens based on the initial value of current under an applied voltage of 30 V (potential of 600 V/m). For UHPCs, because of the very dense microstructure, the initial current was very low, and thus a higher applied voltage of 60 V (1200 V/m potential) was needed. The NSSM coefficients for both the UHPC mixtures are shown in Figure 7-11(b) along with the corresponding values for OPC concrete and HPC. Note that the UHPCs demonstrate much lower migration coefficients even under a higher applied voltage that accelerates ionic transport. The selected UHPCs have migration coefficients that are an order of magnitude lower than that of conventional OPC concrete. This has considerable implications in service-life of concrete structures designed using UHPCs.

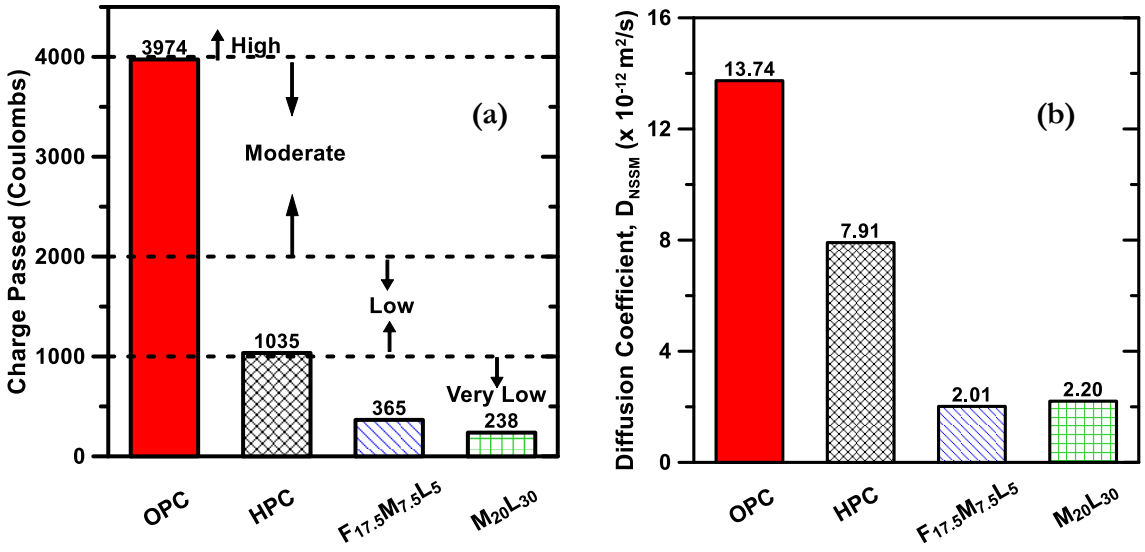

Figure 7-11 – (a) Charge passed during the RCP test, and (b) non-steady state migration coefficients (m^2/s) of the studied mixtures.

7.5.3 Cost and Other Impacts of Selected UHPC Mixtures

The cost per m^3, and the strength-normalized cost (cost normalized by the 28-day compressive strength) of the selected UHPC mixtures are shown in Table 7-6. The material cost is alone considered here, which was obtained from published literature (Kay Wille and Boisvert-Cotulio 2015) as well as from manufacturers/suppliers. Compared to proprietary UHPC mixtures that are reported to cost between $1500 and $3000 per m^3, the UHPC mixtures designed as part of this study can be proportioned at a fraction of the cost, making it a viable alternative for transportation and infrastructural agencies interested in high-strength and high-performance mixtures. From a compressive strength-normalized cost perspective, the fiber-reinforced mixtures appear less attractive, but realistically, they should

be compared based on ductility or post-cracking tensile strength-normalized cost to ensure fair comparisons.

Figure 7-12 (a) shows the cost of raw materials required to proportion the selected UHPC mixtures, with and without fibers, while Figure 7-12 (b) provides the relative cost of each of the mixture constituent as a fraction of the total cost of the mixture[9]. In conjunction with the material design strategy described in this chapter, an understanding of the material costs, their local availability, and energy-and-emission implications can be used to conduct life cycle cost and impact analyses which help decision makers choose the appropriate material combinations for respective UHPC applications. Note that this analysis does not address the capital investment necessary for equipment upgrade to crush, separate, and proportion large volumes of aggregates. These figures clearly demonstrate that, from a cost perspective, superplasticizer and fibers comprise the major portion of the cost of UHPC, followed by OPC. Note that in mixtures where the paste fraction is not optimized, the OPC cost can be further higher. A higher OPC content leads to other environmental impacts associated with such mixtures, reinforcing the importance of a mixture selection strategy as explained in this chapter.

Table 7-6 – Material costs for each mixture considered in study

Mixture ID	**Cost ($) per m^3**	**Cost ($) per MPa per m^3**
Proprietary UHPC	2616	15.85

[9] The cost of water is not accounted for in these calculations

(Berry 2015)		
$M_{20}L_{30}$-f	868	6.53
$M_{20}L_{30}$	618	4.72
$F_{17.5}M_{7.5}L_5$-f	788	5.32
$F_{17.5}M_{7.5}L_5$	545	3.56

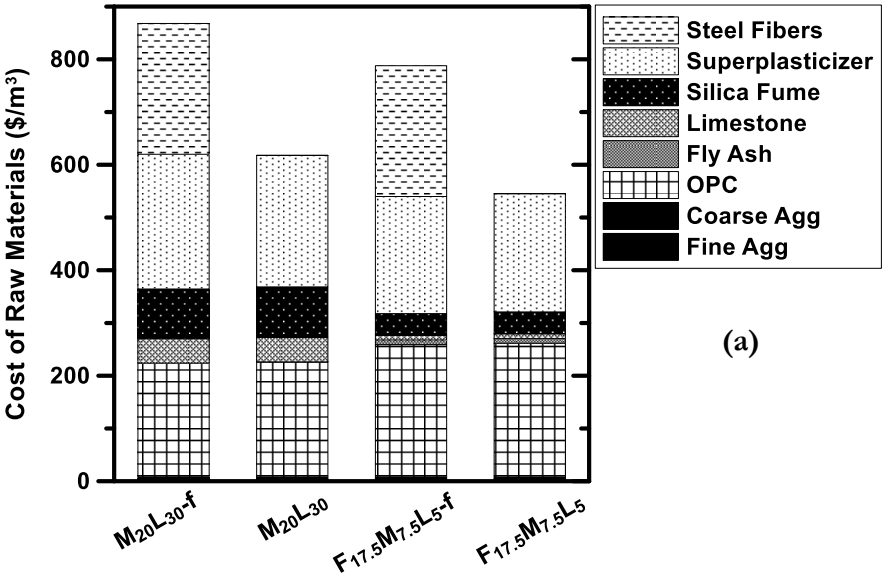

(a)

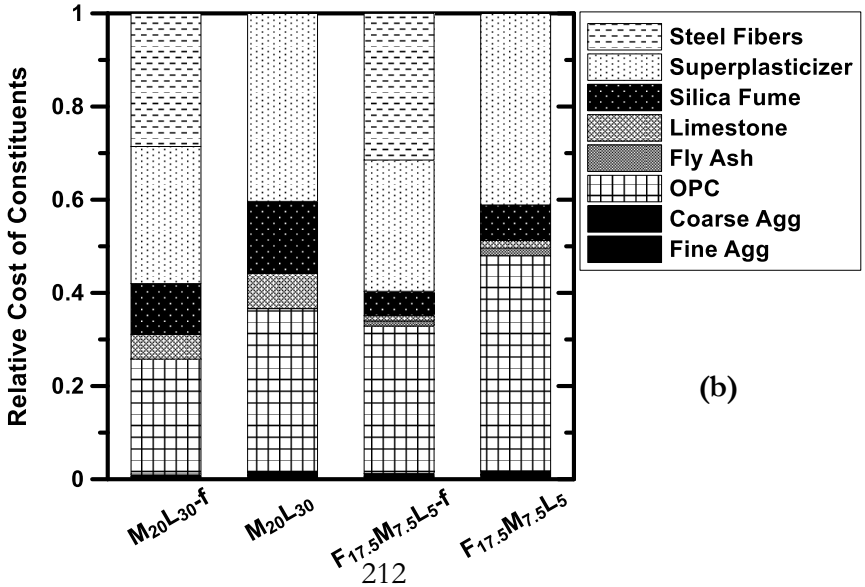

(b)

Figure 7-12 – (a) Cost of raw materials per m^3 of selected UHPC mixtures, and (b) relative cost of the individual components in the UHPC mixtures.

7.6. CONCLUSIONS

This chapter reports a particle-packing based methodology for the design of UHPC mixtures. This approach follows a procedure for the selection and optimization of the binder phase of UHPC using microstructural packing and rheology considerations and scales it to address the proportioning of the aggregates. The focus of the binder selection and optimization process was on the use of commonly available cement replacement materials and fillers (fly ash, silica fume, metakaolin, and limestone) to proportion economic and sustainable UHP binders (~30-50% replacement of OPC, mass-based) without having to resort to special materials (e.g., nanoparticles) that significantly increase the material and processing cost associated with UHPC. From a large family of binders, three systems – two quaternary binders containing fly ash or slag, microsilica, and limestone (for an overall cement replacement level of 30%), and one ternary binder containing microsilica and limestone (for an overall cement replacement level of 50%), were identified for detailed studies on UHPCs. These binders demonstrated 90-day compressive strengths in the range of 145-165 MPa.

While many UHPC studies only consider fine aggregates, this study considered three different sizes of coarse aggregates: nominal maximum size of 6.25 mm, 4.75 mm, and 2.36

mm, in addition to two different median sizes of fine aggregate: 0.6 mm and 0.2 mm. A compressible packing model was used for the packing of coarse and fine aggregates in UHPC. The influence of loosening and wall effects in poly-disperse mixtures were considered, as was the effect of fibers in perturbing the particle packing. A computer program analyzed 885 combinations of the three coarse and two fine aggregate sizes, and arrived at the combination with the densest packing (of 0.696). This combination consisted of 60% of coarse aggregates comprising of 40% of 6.25 mm size and 10% each of 4.75 mm and 2.36 mm aggregates. Highly flowable concretes (slump flow > 350 mm) were proportioned using the chosen aggregate combination and two of the selected binders, with and without 1% of steel fibers by volume. 28-day compressive strengths in excess of 150 MPa and flexural strengths in excess of 10 MPa were obtained. Significantly improved resistance to moisture and ionic transport as compared to conventional or high performance concretes was also observed, validating the material design procedure.

A preliminary cost analysis suggested that these mixtures could be proportioned at a fraction of the cost of proprietary UHPC mixtures. The use of conventional binder and filler materials, and high levels of OPC replacement through microstructural packing and rheology optimization also facilitates reduction in material cost. Moreover, the UHPC mixtures with optimized binder and aggregate combinations are also expected to fare well in a life cycle cost and impact analysis, attributable to the large reduction in OPC content as well as the use of common cement replacement materials rather than ones with larger economic and environmental impacts for production.

CHAPTER 8[10]

FUNDAMENTAL INSIGHTS INTO COMPRESSIVE AND FLEXURAL RESPONSE OF BINDER- AND AGGREGATE-OPTIMIZED ULTRA-HIGH PERFORMANCE CONCRETE

8.1. INTRODUCTION

Ultra-high performance concrete (UHPC) is a multi-scale microstructure-designed material, tailored for very high compressive strength in excess of 150 MPa, high flexural and tensile strengths, and high ductility (Habel et al. 2006; Kay Wille, Naaman, and Parra-Montesinos 2011; Ben Graybeal 2011; Yoo and Yoon 2015). UHPCs use a very low water-to-cementitious materials ratio and a high fraction of fine reactive particles that reduce the pore sizes and volume in the matrix. This ensures that the resistance of UHPCs against common deterioration drivers including moisture and ionic penetration is very high, as has been reported in several studies (El-Dieb 2009; Abbas, Soliman, and Nehdi 2015; Alkaysi et al. 2016a). UHPCs are used in several applications including bridge decks (Ahlborn, Peuse, and Misson 2008; Honarvar et al. 2016), deck-level connections between modular precast bridge components (B. A. Graybeal 2010), blast protection (Yi et al. 2012; Aoude et al. 2015), and repair and rehabilitation of infrastructural components (Brühwiler and Denarié 2013). One of the major impediments to large scale commercial adoption of UHPC in infrastructural applications is its high cost, due to the use of high volumes of conventional and special

[10] This chapter is derived from the following publication under review: Arora, A., Yao, Y., Kianmofrad, F., Al Bannai, K., Mobasher, B., & Neithalath, N. (2018). Fundamental insights into compressive and flexural response of binder- and aggregate-optimized ultra-high performance concrete.

binder materials and fine fillers (including, but not limited to micro- and/or nano-silica, nano-alumina, ground quartz, metakaolin, limestone etc.), specialty admixtures (including high-range water reducers, hydration enhancers, and viscosity modifiers), and specialty fibers comprise additional cost drivers (W. Huang et al. 2017b; Yu, Spiesz, and Brouwers 2014b; Muhd Norhasri et al. 2016; Meng and Khayat 2016).

Consumption of energy-and-CO_2 intensive, and expensive components such as ordinary portland cement (OPC) can be reduced using higher volumes of alternative binding materials having lower energy and CO_2 footprints. The proprietary nature of many competing blends available on the market has prompted a focused development of economical and sustainable UHPCs with locally sourced and waste/by-product materials (C. Wang et al. 2012; Alsalman, Dang, and Micah Hale 2017). In addition, performance specifications for an extended service life by means of a dense microstructure, which in the case of mixtures with very low water content, cannot be fully accomplished by enhancing the degrees of reaction of the constituent particles alone. Efficient physical packing of binder particles in the microstructure is required, which demands careful selection of materials not just from the viewpoints of availability and reactivity but based on synergistic size distributions. Moreover, it is also important that high volumes of fine particles do not contribute to adverse rheological performance. Lack of proper dispersion of the components in the matrix, which detrimentally influences the rheology, also contributes to non-optimal properties in the hardened state.

A methodology to determine the binder constitution for UHPC by considering all these aspects was recently published by the authors (Arora et al. 2018). This binder selection

method employs a few conventional cement replacement materials and fine fillers, and is robust enough to allow customization by the user to satisfy the desired performance requirements. Recently, the authors augmented the UHPC binder selection method with a compressible packing model for coarse and fine aggregates (> 6.3 mm nominal maximum size) to develop UHPCs optimized at multiple length-scales (Arora et al., n.d.).

This chapter examines in detail, the fundamental responses of such optimized UHPCs when tested in compression and flexure. The development of compressive stress in UHPCs as a function of axial and radial strains, along with the calculated volumetric strain are used to extract critical stress states that are of relevance in UHPC performance. The flexural response of UHPCs are examined through a combination of mechanical tests and digital image correlation (DIC). The influence of UHPC matrix type and fiber volume on strain localization and crack propagation is also brought out.

8.2. MATERIALS, OPTIMIZING MIXTURE PROPORTIONS, AND TEST METHODS

8.2.1 Materials

The binder phase of UHPC mixtures was composed primarily of Type I/II Ordinary Portland Cement (OPC) conforming to ASTM C 150. Since UHPC mixtures rely on very low water-to-powder ratios (w/p) (typically < 0.23), the hydration degree of cement is rather low. Thus, better particle packing through a variety of reactive or filler particles is an efficient method of UHPC binder design, as has been illustrated in detail in (Arora et al. 2018). In this study, we employ a Class F fly ash conforming to ASTM C 618, microsilica (silica fume) conforming to ASTM C 1240, and fine limestone powder conforming to ASTM C 568 as

partial cement replacement materials in the UHPC mixtures. Limestone powders with two different median particle sizes (1.5 μm and 3.0 μm) were used to ensure efficient packing. While several studies on UHPC consider the use of finely ground quartz or nanoparticles (Ghafari et al. 2014; W. Li et al. 2015) to enhance the strength of the mixtures, our study uses only commonly available source materials in order to keep the material and processing costs low. The particle size distribution (PSD) curves of the powders are shown in Figure 8-1. The chemical compositions and physical characteristics of the materials used are shown in Table 8-1. A polycarboxylate ether (PCE)-based superplasticizer with a solids content of 43% was used to ensure workability at the very low w/p used (< 0.20 for all the UHPC mixtures in this study).

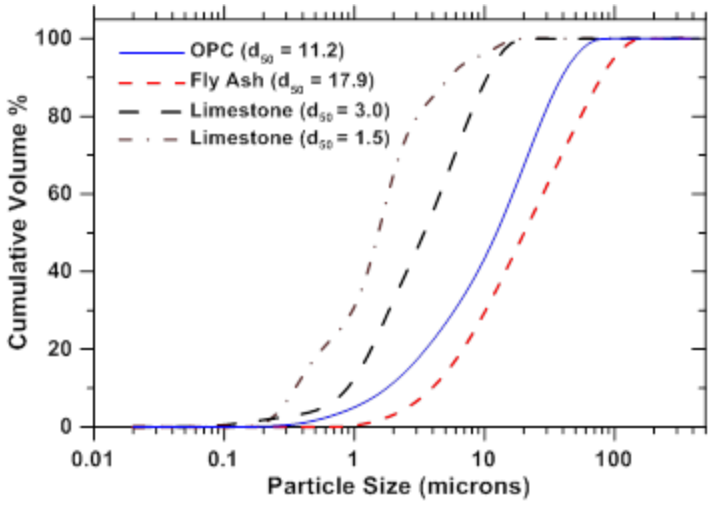

Figure 8-1: Particle size distribution curves for cement, fly ash and limestone powders. The median size in microns is shown in parentheses. The PSD of microsilica is not shown.

Table 8-1: Chemical composition of the materials used in this study.

Components of the binder	Chemical composition (% by mass)							Density (g/cm^3)
	SiO_2	Al_2O_3	Fe_2O_3	CaO	MgO	SO_3	LOI	
OPC	19.60	4.09	3.39	63.21	3.37	3.17	2.54	3.15
Fly Ash (F)	58.40	23.80	4.19	7.32	1.11	3.04	2.13	2.34
Microsilica (M)	> 90.0	-	-	< 1.0	-	-	-	2.20
Limestone (L), 1.5	> 97% $CaCO_3$							2.70
Limestone (L), 3								

The UHPC mixture blends contained coarse aggregates passing 3/8" sieve (9.5 mm). The aggregates were sieved into three nominal maximum size classes: ¼" (6.3 mm), #4 (4.75 mm), and #8 (2.36 mm). The measured bulk specific gravity and absorption of the aggregates were 2.65 g/cm^3 and 0.94% respectively. Coarse and fine silica sands median sizes of 0.6 mm and 0.2 mm respectively were used as fine aggregates. The fiber reinforced UHPCs contained straight high-strength steel microfibers (L=13 mm & dia.=0.5 mm).

8.2.2 Binder and Aggregate Optimization

Achieving economical and sustainable UHPCs demand a first principles-based approach in material selection and proportioning. For the design of the UHPC pastes, an integrated microstructure packing and rheology-based procedure developed earlier was used (Arora et al. 2018). Virtual microstructures of binder systems at a mass-based w/p of 0.20 and containing several combinations of cement replacement materials were developed in consideration to the particle size distribution, a desired microstructural packing coefficient (γ) and relative proportions of the components. The packing coefficient accounted for the mean centroidal distance between the particles, the nearest neighbors number density, and

coordination number of the microstructure (Wolfsdorf, Bender, and Voorhees 1997; A. Kumar, Oey, Kim, et al. 2013). Using experimentally measured yield stress, plastic viscosity, and mini slump area of the pastes, a flow coefficient ($\varkappa$) was developed. These parameters were designed such that high values for both γ and $\varkappa$ would result in a paste with high strength as well as desirable rheological properties for flowable UHPC mixtures.

Using OPC, fly ash, microsilica, and limestone as the source materials, and ensuring at least a 30% replacement (mass-based) of OPC, several feasible UHPC pastes were designed (Arora et al. 2018). Among those pastes, two were chosen for this study based on their superior properties: (i) a quaternary binder containing 17.5% by mass of fly ash, 7.5% silica fume, and 5% limestone (all mass-based) replacing OPC for an overall cement replacement level of 30%, and (ii) a ternary binder containing 20% microsilica and 30% limestone (mass-based) replacing cement, for an overall cement replacement level of 50%. Note that, from a cost standpoint, the binder with a higher microsilica content might be more expensive, even though it has a lower cement content. The limestone in both the mixtures is composed of equal amounts of 1.5 μm and 3 μm median size particles.

Aggregate optimization for UHPC was carried out using a compressible packing model, with the intention of obtaining the aggregate blending proportions that result in maximum packing density. Both coarse and fine aggregates were considered in the optimization scheme. This resulted in five distinct aggregate classes: coarse aggregates with nominal maximum sizes of 6.3 mm, 4.75 mm, and 2.36 mm, and fine aggregates with median sizes of 0.6 mm and 0.2 mm. A custom computer program in MATLAB was used to choose the aggregate combinations and determine their packing density. A total of 855 aggregate blends

were evaluated. The volume fraction of each aggregate class was varied from 0 to 1.0 in increments of 0.10. A coarse aggregate volume fraction of 0.60 and a fine aggregate volume fraction of 0.40 was found to provide the maximum packing density. The volume fractions of individual classes of coarse aggregates in the total (coarse + fine) aggregate blend were 0.40, 0.10, and 0.10 for nominal maximum sizes of 6.3 mm, 4.75 mm, and 2.36 mm respectively. The volume fractions of both the fine aggregate classes in the total aggregate blend were 0.20. More details on the aggregate packing methodology, determination of packing densities, and the algorithms can be found in (Arora et al., n.d.).

UHPC mixtures were proportioned based on the paste and aggregate design described above. Two different binder compositions (one quaternary and one ternary binder) as described above, along with the aggregate sizes and contents as obtained from the compressible packing model, were used to produce the UHPC mixtures. Both the UHPC mixtures were produced with and without 1% of fibers by volume. Furthermore, the UHPC made using quaternary blend binder was also proportioned using 3% of fibers by volume, since many commercial UHPCs use such high volume fractions to obtain higher levels of ductility. Table 8-2 provides the details of the UHPC mixtures for detailed mechanical property evaluations. The mass-based w/p for all the concrete mixtures varied from 0.17 to 0.19. A higher w/p was required for the mixtures with a higher amount of microsilica because of its large surface area. Since fibers disrupt the packing of the microstructure, mixtures containing a higher fiber content required a higher HRWR dosage. Table 8-2 also shows the unit cost of these mixtures, calculated based on the individual material costs

obtained from published literature (K. Wille and Boisvert-Cotulio 2013) as well as from local suppliers/manufacturers.

Table 8-2: Mixture proportions of the UHPCs used in this study

Content of materials (kg/m³)	**$F_{17.5}M_{7.5}L_5$**	**$M_{20}L_{30}$**	**$F_{17.5}M_{7.5}L_5$ – 1f***	**$M_{20}L_{30}$ – 1f***	**$F_{17.5}M_{7.5}L_5$ – 3f***
OPC	946	784	937	777	913
Fly ash (F)	166	0	164	0	160
Microsilica (M)	71	157	70	155	68
Lime stone (L)	47	235	47	233	46
Coarse aggregate (6.3 mm)	344	329	341	326	332
Coarse aggregate (4.75 mm)	86	82	85	82	83
Coarse aggregate (2.36 mm)	86	82	85	82	83
Fine aggregate (0.6 mm)	172	165	170	163	166
Fine aggregate (0.2 mm)	172	165	170	163	166
Water	166	171	164	169	157
Fibers	0	0	75	75	225
Superplasticizer (% solids content by mass of binder)	1.25	1.45	1.30	1.50	1.37
Material cost ($/m³ of concrete)	565	626	808	868	1312

*1f or 3f in the mixture nomenclature denotes either 1% or 3% by volume of fibers

8.2.3 Mixing, Specimen Preparation, and Curing

Successful UHPC mixtures rely heavily on a well-devised mixing plan. The UHPC mixtures were mixed in a Croker RP100XD rotating pan mixer with a capacity of 0.28 m^3 (10 ft^3). The mixer consists of two shearing paddles which are held-in-place, while the pan containing the concrete rotates at a pre-defined speed of 74 rpm. This mixing arrangement simulates the mixing of concrete in a truck mixer. A fixed scraper blade attached to the assembly removes the paste adhering to the sides of the wall and provides a uniform mixing environment. All aggregates were washed and dried to eliminate surface impurities prior to mixing. This treatment enhanced the water demand and compromise the mechanical properties. Aggregates were first mixed with the pre-determined amount of mixing water to a saturated surface-dry condition. Powders were incrementally introduced into the mixture in decreasing order of fineness (microsilica, limestone, cement, and fly ash, in that order). This helps ensure adequate shearing of powders and restricts agglomerations that might occur otherwise. Every successive powder addition was followed by a mixing time of approximately 3-4 minutes. Finally, a mixture of water and superplasticizer was introduced in one-third increments and mixed for 5 minutes after every addition. During the last stage, fibers were added after the other components were uniformly mixed. A further mixing for 3-4 minutes was carried out to ensure that the fiber dispersion is uniform. As evident from this description, the mixing procedure of UHPC is very intense, but is essential to obtaining a flowable and consistent mixture at the low w/p employed. UHPC cylinders (50 mm/75 mm diameter and 100 mm/150 mm long for compressive strength, 100 mm diameter and 200 mm long for moisture and ionic transport tests), and beams (50 mm x 65 mm x 380 mm and 100 mm x 100 mm x 457 mm) were prepared for mechanical property testing and stored in a

moist chamber at >98% RH and 23 ± 2°C until the age of testing, after removal from the molds after 24 hours.

8.2.4 Constitutive Response and Pulse Velocity Determination under Compression

The compressive strengths of the selected UHPC mixtures after 7, 14 and 28 days of moist curing were determined on 75 mm diameter x 150 mm long cylindrical specimens in accordance with ASTM C 39. The stress-strain response of the UHPC specimens in compression was obtained on 50 mm diameter x 100 mm long cylindrical specimens cored from 100 mm diameter x 200 mm long cylinders (Figure 8-2(a)), since the 75 mm diameter cylinders exceeded the load capacity of the available test equipment. The ends of the specimens were ground to a surface roughness of less than 200 μm using successively finer grits to ensure smooth load transfer between the loading head of the test machine and the specimen surface. The stress-strain response of the UHPC specimens was determined using a 450 kN load frame after 28 days of moist curing. Figure 8-2(b) shows the test setup to determine the constitutive response, with the corresponding instrumentation.

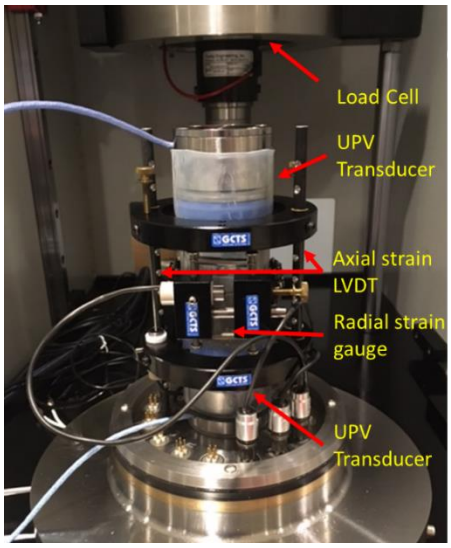

Figure 8-2 – (a) 50 mm diameter cylinders cored from 75 mm diameter specimens, and prepared for compression testing, and (b) test setup to determine compressive stress-strain response of UHPC cylinders. The instrumentation includes LVDT to measure change in length of the specimen, radial strain gage to measure radial deformation, and ultrasonic pulse velocity transducers.

Prior to the testing, the specimen was jacketed in a polymer sleeve to prevent the debris from damaging the instruments (Figure 8-2(a)). The confining pressure applied on the specimens by the sleeve can be considered to be minimal and does not influence the test results. Two axial strain gauges and one circumferential displacement gauge were attached to the sample prior to testing. The axial strain was calculated from the average output of two axial strain gauges. The testing procedure involved three phases: (a) a load controlled mode up to a normal stress of 1 MPa, (b) an axial strain-controlled mode at a rate of 0.025% axial strain/min from a stress of 1 MPa to 30 MPa, and (c) a radial strain-controlled mode at a rate of -0.01% radial strain/min until a radial strain of 1.5% or failure.

I The ultrasonic pulse velocitythrough the sample can be used to determine the damage-dependent elastic modulus and Poisson's ratio during the test. Using an internal transducer assembly inside the loading platens ed of the P-wave (compression wave) and S-wave (shear wave) velocities were measured continuously during the loading Sets of Two transducers were embedded in the top and bottom platens to measure each of the P and S wave velocities. Figure 8-3 shows the typical P-wave and S-wave response of a UHPC specimen under compression.

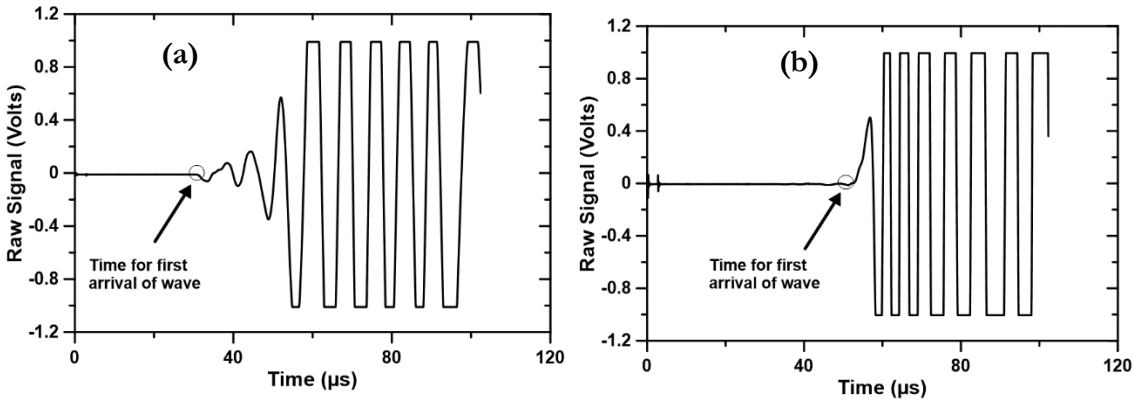

Figure 8-3 – Typical raw voltage signal profile for: (a) P-Wave and (b): S-Wave, for a 50 mm x 100 mm UHPC cylindrical specimen. The time of first arrival of the wave is quantified as the time when the first significant change in the slope of the raw signal is detected.

The raw voltage signal is used to determine the time of flight of the wave, defined as the time taken for the first arrival of the wave from one transducer to the other. This is indicated by a measurable change in the slope of the temporal voltage signal, as shown in Figure 8-3. The wave velocity can be calculated, given the transducer spacing (specimen length) and the signal arrival time. The elastic constants (Poisson's ratio, 'ν' and Elastic modulus, 'E') of the

material are calculated from the P-Wave velocity (V_p) and the S-Wave velocity (V_s) using the following relations (Jones and Fącąoaru 1969; Komlos̆ et al. 1996). Here 'ϱ' corresponds to the density of the specimen.

$$\nu = \frac{\frac{V_p^2}{2} - V_s^2}{V_p^2 - V_s^2} \quad \text{(Eq. 8-1)}$$

$$E = V_p^2 . \rho . \frac{(1+\upsilon)(1-2\upsilon)}{(1-\upsilon)} \quad \text{(Eq. 8-2)}$$

Since the specimen undergoes axial and radial deformation under compressive loading, a dynamic correction factor (F_{CD}) is introduced to account for the change in the distance between the transducers during the test and used to evaluate the wave velocities. F_{CD} is a function of the engineering strain (ε_e) and given in Equation 8-3. The corrected length, shown in Equation 8-4, is used to obtain the wave velocity at different stress or strain levels.

$$F_{CD} = (1 + \varepsilon_e) \quad \text{(Eq. 8-3)}$$

$$L_{corrected} = L_{original} * F_{CD} \quad \text{(Eq. 8-4)}$$

8.2.5 Flexural Response under Four-Point Bending

The flexural response of the fiber-reinforced UHPC specimens after 28 days of moist curing was evaluated using four-point bending tests in accordance with a modified ASTM C 1609 protocol in a closed-loop, servo-controlled testing system as shown in Figure 8-4(a). The modification was based on the size of the beam and the loading span used. Two different beam sizes were tested: 50 mm x 65 mm x 380 mm, and 100 mm x 100 mm x 457 mm. Six

beams were tested for each UHPC mixture. The mid-span deflection was experimentally measured using an LVDT placed in contact with a steel plate glued to the center of the rear of the beam. The test procedure consisted of three phases: (a) an initial load-controlled phase up to a contact load of 134 N, (b) actuator displacement-controlled mode at the rate of 0.5 mm/min up to an actuator displacement of 3.5 mm, which was close to the peak load experienced by the beam, and (c) actuator displacement-controlled mode at the rate of 0.1 mm/min until a displacement of 19 mm or failure. The actuator displacement rates were selected to maintain the rate of mid span deflection in compliance with ASTM C 1609. For the unreinforced specimens, only the peak load at failure was noted.

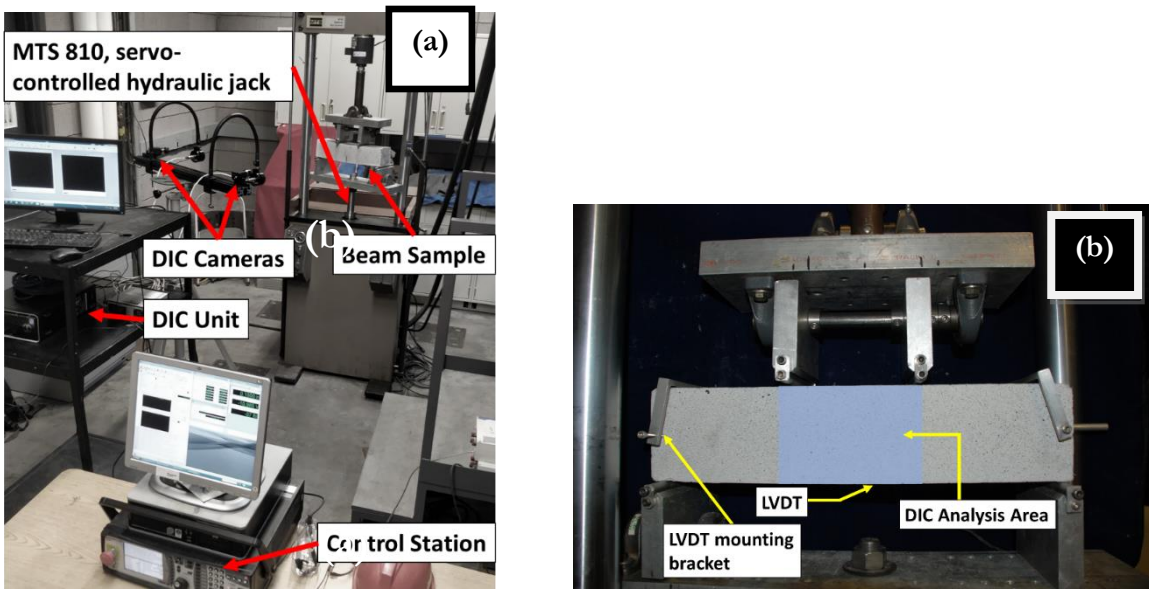

Figure 8-4 – (a) Flexural test setup showing the control station, digital image correlation (DIC) unit and the load frame, and (b) beam specimen (100 mm x 100 mm x 457 mm) under four-point flexural test with LVDT mounted at the rear of the beam to measure mid-span deflection. The area in the center marks the area to be analyzed by the DIC technique.

8.2.6 Digital Image Correlation (DIC) to Analyze Flexural Response of UHPC Beams

Digital image correlation (DIC) is a reliable non-destructive method based on speckle tracking, to analyze the full displacement field on the surface of a specimen using digital images taken at specific intervals during the test (Chu, Ranson, and Sutton 1985; Pan et al. 2009). The beams were painted using a speckle pattern of white and fine random black dots on the side facing the camera, to improve image correlation. Two Charge-Coupled Device (CCD) cameras were used to capture images of the beam every 2 seconds during testing. The cameras captured the rectangular region between the two load points (see Figure 8-4(b)), for further analysis to determine the displacement fields. The DIC technique determines the horizontal and vertical displacement fields in the analysis region by minimizing the correlation coefficient computed between the subset of images in the deformed and the undeformed state (Das et al. 2014). The displacement fields u(x,y) and v(x,y) in the x and y directions are calculated using Equations 8-5 and 8-6, when a point (x,y) in the undeformed state transforms to (x*,y*) in the deformed state. The displacement fields are given as:

$$u(x,y) = x^* - x \tag{Eq. 8-5}$$

$$v(x,y) = y^* - y \tag{Eq. 8-6}$$

The correlation coefficient (C), the minimization of which gives the displacement fields, is given as (Chu, Ranson, and Sutton 1985; Vendroux and Knauss 1998):

$$C = \frac{\sum[G(x,y) - H(x^*,y^*)]^2}{\sum G^2(x,y)}$$

(Eq. 8-7)

Here, G and H are grey scale light intensities corresponding to the point in the subset. Image analysis for DIC was carried out using VIC-2D software™ from Correlated Solutions. The displacement fields were used to derive the Lagrangian strain fields to evaluate the localized cracking zone in the beams. The strain profile along the bottom fiber of the beam was averaged to calculate the flexural strain in the beam. The DIC technique also helps monitor the mid-span deflection of the beam and helps to verify the LVDT measurements. The curvature of the analysis region was evaluated using the VIC-2D software and used to extrapolate the deflection of the end point of the beam. The net mid-point deflection of the beam ($\Delta_{center\text{-}net}$) is calculated using Equation 8-8, where $\Delta_{endpoint\text{-}top}$ represents the upward displacement of the top surface of the beam and $\Delta_{center\text{-}bottom}$ represents the downward displacement of the mid-span of the beam.

$$\Delta_{center-net} = \Delta_{endpoint,top} + \Delta_{center,bottom}$$

(Eq. 8-8)

The load- crack opening displacement (COD) response was evaluated for the major crack in all the UHPC beams studied. Since the beams were unnotched, the precise location of the major crack was identified using the last image captured before ending the test in the post-peak region at a pre-defined axial strain. A virtual extensometer was then placed parallel to the beam length in the undeformed state, along the extreme tension fiber. The time-dependent deformation of the extensometer was determined along the crack opening

direction and denoted as the crack opening displacement, which was then plotted along with the time-stamped load response to obtain the load-COD curve for the beam.

8.2.7 Determination of Micro-Mechanical Properties using Micro-indentation

Micro-indentation was carried out on paste samples of UHPC binders. All dry powders were thoroughly mixed prior to wet mixing. Paste mixing was performed in accordance with ASTM C 1738 using a M7000 high speed shear mixer. The following mixing sequence was used: (i) all water and HRWR was added to the mixer, (ii) the blended dry powders were then added as the mixer was run at 4000 rpm for approximately 30 s, (iii) the mixer was then run at 12,000 rpm for 30 s, (iv) the paste was allowed to rest for two minutes, and (v) final mixing of the paste was carried out at 12,000 rpm for 90 s. Specimens were placed in sealed containers until 28 days. At the age of testing, specimens were removed from the sealed containers and cut into half-inch thick disks using a diamond saw. The disks were polished manually on a Buehler EcoMetTM 250 at a speed of 400 rpm. The polishing protocol began with using coarse alumina pads of grit sizes varying from 240 to 1200. Further polishing was done using fine alumina pads of particle sizes 9, 3 and 1 micron to obtain a smooth and reflective surface suitable for micro-indentation. The samples were ultra-sonicated in iso-propyl alcohol at each stage of polishing to remove any excess debris from the surface. The overall polishing regime took about 2 hours for every sample.

Micro-indentation was carried out on half inch disk samples using an Anton Paar Micro Combi Scratch Tester. Tests were conducted using a Berkovich indenter with a half angle of 65.35° and a tip radius of 20 nm. The load cell in the instrument was set to 30 N. A force controlled loading protocol limited to a max penetration depth (h) of 20 microns was

implemented. Previous studies have shown that the interaction volume for the material response is three to four times the indentation depth for a Berkovich indenter. Therefore, selecting a penetration depth of 20 microns ensures homogeneity of material response within the paste, since all the paste features are expected to be smaller than the size of the interaction volume and satisfies the scale separability condition: (h>>D/10, where D is the size of the largest heterogeneity). A square grid of size 1.26 mm x 1.26 mm [Figure 8-5] was selected on the paste sample to obtain a 10 x 10 grid with a spacing of 140μm between consecutive indents. Thee grid spacing was selected as seven times the maximum penetration depth to avoid any interference between adjacent indents.

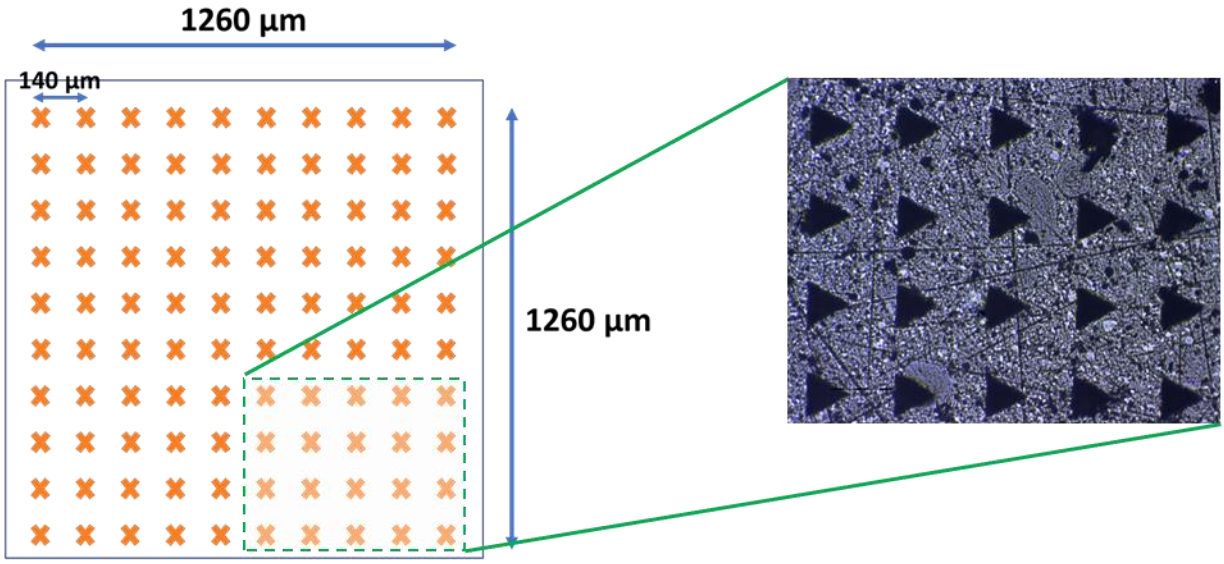

Figure 8-5 – Schematic of indentation grid on the sample

For every indent, the loading and unloading rates were specified to be 7500 nm/min and 10000 nm/min respectively with a dwell time of 3 seconds at the point where max depth was

attained. The pause duration after rapid loading is small enough to avoid any creep effects and at the same time allows the material to stabilize before the unloading stage begins. The force and indenter displacement data were acquired at 15 Hz. The indented sample profile and a typical indentation plot is shown in Figure 8-6.

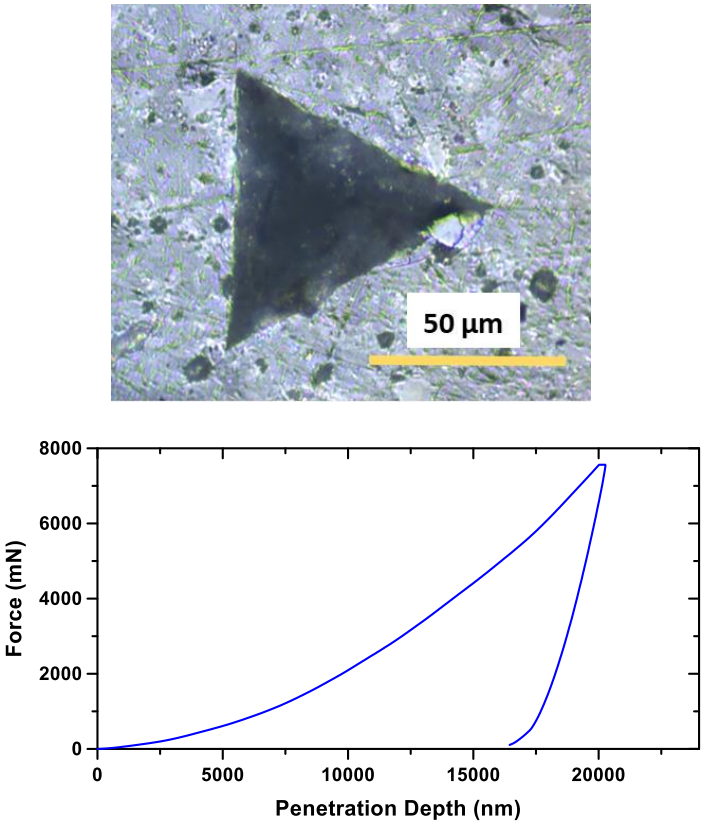

Figure 8-6 – (a) Indent impression on QFA sample, (b) Typical force versus penetration depth plot

The unloading part of the force-displacement plot obtained from each indent is fitted in a power law expression using an in-built software package which is used to determine the unloading stiffness (S) at 98% of the peak load. The indentation parameters, hardness (H)

and indentation modulus (M) or the reduced elastic modulus (E_r) are obtained as shown in equations 8-9 and 8-10.

$$M \equiv E_r = \frac{\sqrt{\pi}}{2}\frac{S}{\sqrt{A_c}} \quad \text{(Eq. 8-9)}$$

$$H = \frac{P_{max}}{A_c} \quad \text{(Eq. 8-10)}$$

Here, S is the measured unloading stiffness, P_{max} is the peak load and A_c is the area shape function, which is a function of the indenter geometry and the penetration depth. For a Berkovich indenter, A_c is given by equation 8-11.

$$A_c = 24.5h_c^2 \quad \text{(Eq. 8-11)}$$

8.3. RESULTS AND DISCUSSIONS

8.3.1 Compressive Strengths of UHPC Mixtures and Constitutive Response in Compression

8.3.1.1. 90-day compressive strengths of selected UHPC mixtures

The compressive strengths of the 75 mm diameter x 150 mm long UHPC specimens with and without 1% fiber volume are shown in Figure 8-7. It is observed that 90-day compressive strengths of at least 150 MPa are obtained for all the UHPC mixtures developed in this study. The material cost (Table 8-2) of these mixtures are among the lowest for UHPC mixtures reported, which demonstrates the beneficial effects of carrying out a first principles-based packing analysis at both the binder and the aggregate level. The

influence of 1% by volume of fibers on the compressive strength is negligible. Though high volumes of fibers provide some confinement effect, thereby increasing the apparent compressive strengths, they also detrimentally interfere with the packing of particles in the mixture as has been quantified in (Arora et al., n.d.). The compressive strength evolution depends to a great extent on the volume of reaction products formed in the microstructure and the packing density of aggregates. The microstructural packing and reactivity of these microstructures were studied in (Arora et al. 2018), and it was found that low w/p and the pozzolanic activity of microsilica and fly ash in these mixtures leads to a densely packed microstructure, even though a significant amount of cement remains unhydrated. Coupled with an optimized aggregate gradation, it leads to an extremely low paste and concrete porosity, and thus high strengths.

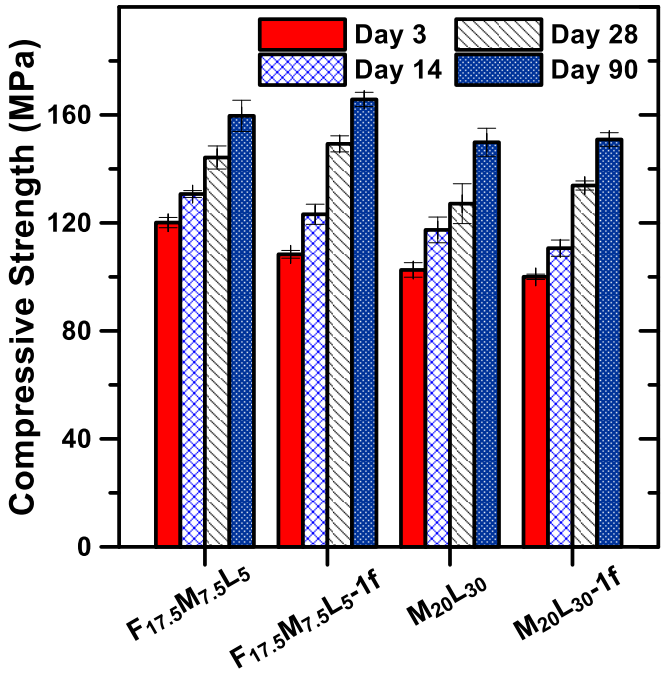

Figure 8-7 – Compressive strength evolution of 75 mm x 150 mm cylindrical UHPC specimens. The error bars correspond to one standard deviation from the mean of three replicate specimens.

8.3.1.2. Compressive stress-strain relationships

Figure 8-8 shows the unconfined compressive stress as a function of axial and radial strains for the 50 mm diameter x 100 mm long UHPC cylinders without fiber reinforcement. The specimens were tested after 40 days of moist curing. The non-fiber reinforced UHPC is very brittle, but the stable radial displacement control allowed for the post peak response to be captured for these specimens as can be seen in Figure 8-8. It is observed that the response of the unreinforced specimens is similar to that reported in (Zohrevand and Mirmiran 2011; Hassan, Jones, and Mahmud 2012). The initial elastic modulus begins to degrade as internal damage increases with the stress approaching the peak stress. Both the unreinforced UHPC specimens are able to withstand as much as 50% of their ultimate capacity at axial strains of around 0.0015. The ultimate axial strains are in the range of 0.0035 to 0.004 for both the UHPC mixtures.

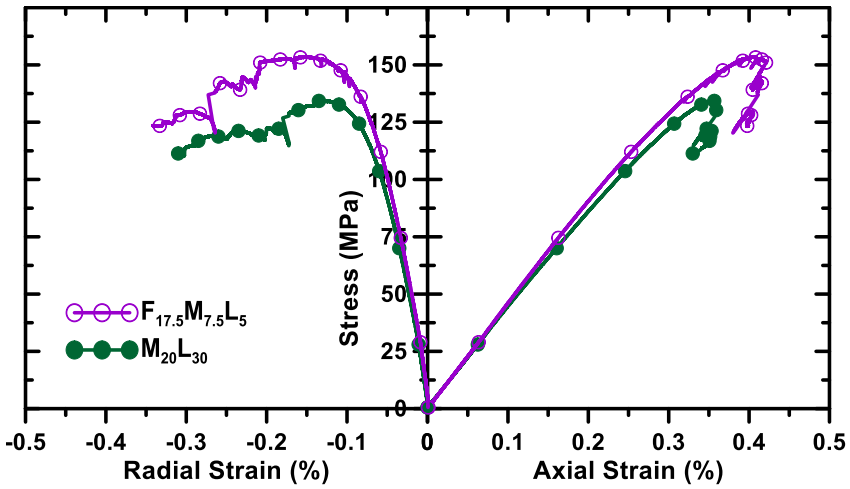

Figure 8-8 – Representative axial and radial stress-strain responses in compression for the 50 mm diameter x 100 mm long unreinforced UHPC cylinders.

Figure 8-9 shows the relationships between compressive stress and axial and radial strains for the UHPC mixtures containing fibers. The difference in post-peak ductility contributed by the higher volume of fibers (1% vs. 3% by volume) can be easily noticed from this figure. The elastic modulus of the fiber reinforced and unreinforced UHPCs are found to be comparable. This is expected since the range of fiber volume fraction considered does not significantly contribute to increase in compressive strength or elastic stiffness. While the peak stress occurs at similar axial and radial strains (~0.35% and 0.2% respectively) for the fiber-reinforced and unreinforced UHPCs, the post peak behavior is significantly enhanced due to the presence of fibers. The fiber-reinforced UHPC mixtures show stable post-peak response and retain almost 50% of their peak strength at 1% radial strain (equivalent to ~0.5% axial strain). For the quaternary blend UHPC, there is more than a 50% increase in axial and radial strain capacities at ~50% of peak stress in the post-peak regime when the fiber volume fraction is increased from 1% to 3%.

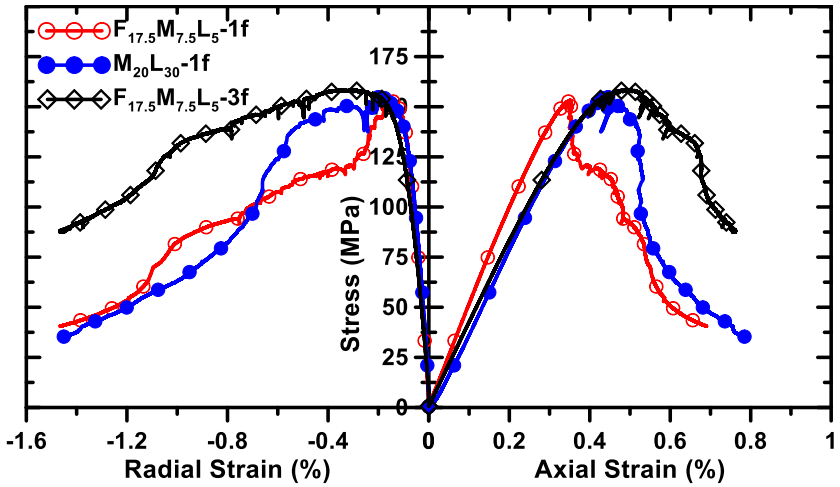

Figure 8-9 – Representative axial and radial stress-strain responses in compression for the 50 mm diameter x 100 mm long fiber-reinforced UHPC cylinders.

8.3.1.3. Critical stress states of UHPC in compression

The representation of axial stress as a function of axial and radial strains provides an opportunity to extract critical stress states in UHPC undergoing uniaxial compression. Previous studies on rocks and brittle materials (Matti Hakala and Heikkilä 1997; Martin and Chandler 1994; Cai et al. 2004; M. Hakala, Kuula, and Hudson 2007) have identified four characteristic phases until the peak load is reached, followed either by a marked post-peak behavior or sudden failure, based on the material constitution. The existence and the duration of the different phases are a function of the material microstructure and the density and orientation of microcracks within the specimen. Figure 8-10 shows the stress-strain response of a typical UHPC specimen and describes the different phases. The initial phase, Phase I, corresponds to the closing of pre-existing microcracks in the sample when a compressive stress is applied, and can be considered to extend to about -0.01% radial strain.

This phase is dependent on the distribution of inherent internal flaws viewed in the context of initial crack density in the material and the crack geometry. Phase II is the elastic region where the material behaves in a linear elastic manner. The elastic parameters, i.e., Young's modulus and Poisson's ratio are evaluated in this region. Traditionally, the elastic parameters are taken based on the secant value from -0.01% radial strain to half of peak strength (Matti Hakala and Heikkilä 1997). The elastic region ends when damage starts accumulating and new cracks are formed in the material. The location of the crack initiation may be attributed to positions where internal stiffness mismatch exists at the interfaces. Such initiations may occur at orientations that are random with respect to the direction of applied stress. This need not exactly correspond to half the peak strength, and thus a crack initiation stress is defined later in this chapter. Cracks begin to grow, and orient parallel to the direction of applied load and this marks the onset of Phase III or the stable crack growth regime. Phase IV corresponds to unstable crack growth. The determination of stress states corresponding to Phases III and IV are explained below.

The beginning of Phase III can be considered to correspond to crack initiation under uniaxial compressive stress. The crack initiation stress (σ_{ci}) is defined as the axial stress when the crack volumetric strain ($\varepsilon_{v,cr}$) starts to deviate from the zero value in the axial-volumetric strain relationship as shown in Figure 8-10. The crack volumetric strain ($\varepsilon_{v,cr}$) is calculated from the measured total volumetric strain (ε_v) and its elastic component ($\varepsilon_{v,e}$) as shown in Equations 8-12 to 8-14. The curve for $\varepsilon_{v,cr}$ is adjusted in Figure 8-10 such that its maximum value is zero for the calculation of σ_{ci} (Matti Hakala and Heikkilä 1997).

$$\varepsilon_v = \varepsilon_{axial} + 2\varepsilon_{radial}$$

(Eq. 8-12)

$$\varepsilon_{v,e} = \frac{1-2\nu}{E}(\sigma_1 - \sigma_3)$$

(Eq. 8-13)

$$\varepsilon_{v,cr} = \varepsilon_v - \varepsilon_{v,e}$$

(Eq. 8-14)

Here, ε_{axial} and ε_{radial} are the axial and radial strains, and ν is the Poisson's ratio. E is the elastic modulus, taken as the slope of the axial stress-strain curve between axial stress values corresponding to -0.01% radial strain and half of the peak stress. The volumetric and crack volumetric strains are also shown in Figure 8-10. Beyond a certain axial stress level, the cracks begin to open up and the volumetric strain (ε_v) reverses from compaction to dilation. This point denotes the crack damage stress (σ_{cd}), which represents the beginning of Phase IV, which is the unstable crack growth phase. The crack density is found to increase significantly (~ 2-7 times) in this phase, as noticed from a rapid increased in the crack volumetric strain in Figure 8-10 (Hallbauer, Wagner, and Cook 1973; Ngab, Slate, and Nilson 1981; Hearn 1999). σ_{cd} can also be considered as the true strength of the material, and any stress value observed beyond that to be a result of temporary strain-hardening, influenced by factors such as the loading rate (Martin and Chandler 1994). The crack initiation and crack damage stresses are referred to as the critical stress states. Phase IV terminates at the maximum load bearing capacity or the peak stress (σ_p), which is the onset of the post-peak response.

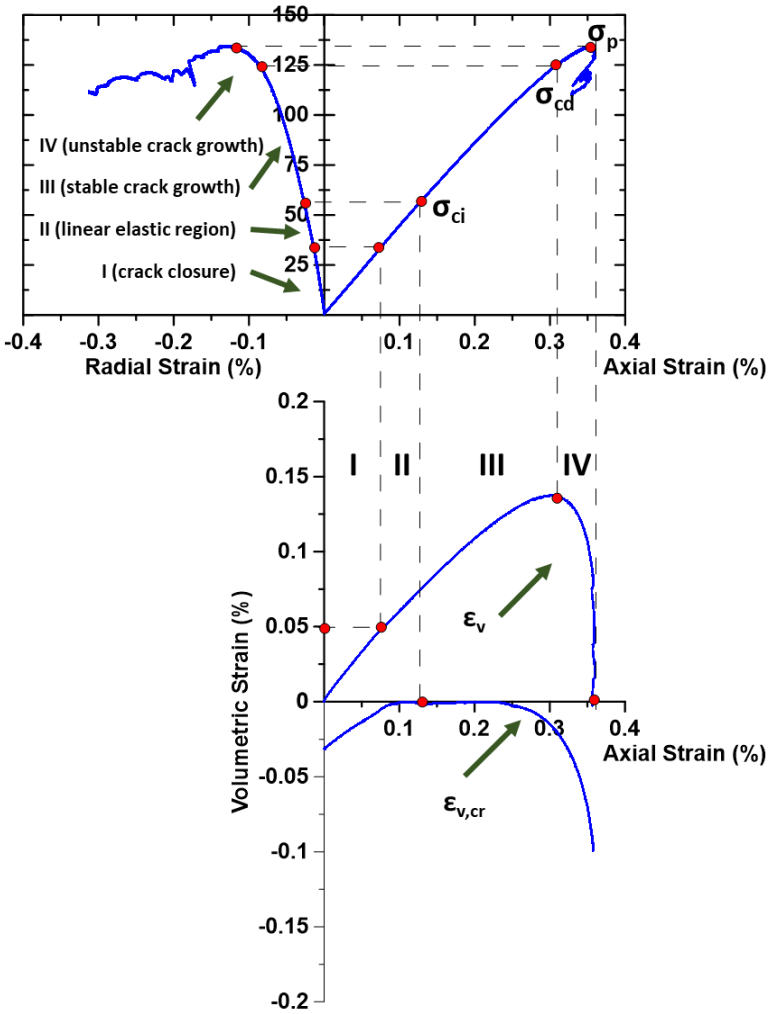

Figure 8-10 – Characteristic phases in the stress-strain response of UHPC and identification of critical stress states

Figures 8-11(a) and (b) show the relationship between axial strain and volumetric strain for the unreinforced and fiber-reinforced UHPC mixtures respectively, used in this study. An increase in volumetric strain with axial strain indicates compaction of the specimen. The volumetric strain in compression increases until the crack damage stress (σ_{cd}) and starts

dropping until it becomes zero at the peak stress. The stress corresponding to the peak in the volumetric strain, after which dilation begins, can realistically be considered as the true strength of the specimen, as described earlier. While the unreinforced beams fail around the peak stress, the fiber-reinforced specimens undergo significant post-peak dilation, as the radial strain increases at a much higher rate as compared to the axial strain. The data in Figure 8-11 is only until the peak load is achieved, to ensure fair comparisons, even though the fiber-reinforced specimens show much higher radial strain post-peak, and thus dilation. The ternary blend UHPC containing microsilica and limestone shows a significantly higher volumetric strain as compared to the quaternary blend, plausibly attributed to the higher amounts of softer limestone in the former mixture. When the mixtures containing 1% and 3% fiber volume fractions are compared, it is found that the overall volumetric strain is higher for the mixture with higher fiber volume, as expected. This is contributed by a more stable pre-peak crack growth in this mixture due to the presence of a large amount of fibers.

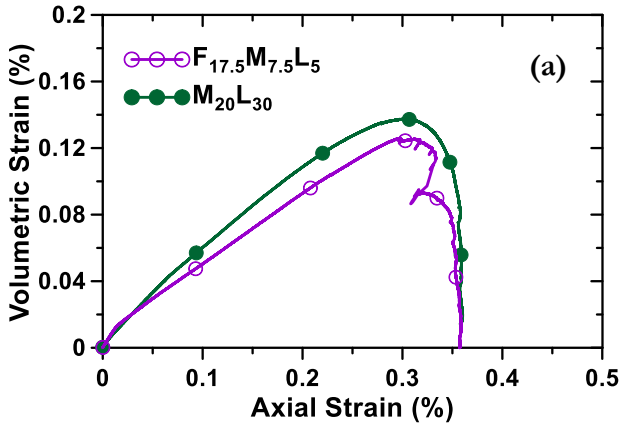

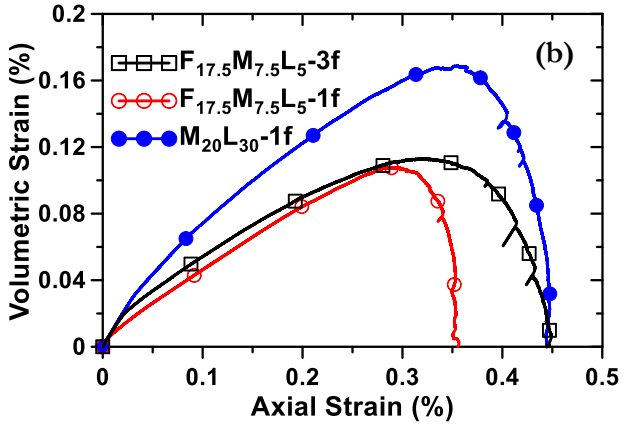

Figure 8-11 – Relationship between axial strain and volumetric strain for: (a) unreinforced, and (b) fiber-reinforced UHPC specimens under compression.

Figure 8-12 shows the different critical stress state parameters obtained for the UHPC mixtures based on the analysis scheme described earlier. It is noticed that the ternary blend UHPC containing microsilica and limestone shows a lower crack initiation stress as compared to the quaternary blend UHPC. This is attributed to the lower amounts of hydration products in this mixture due to the higher OPC replacement level (50% by mass compared to 30% for the quaternary blend) and the higher amounts of low-reactive limestone filler. The ultimate strength of the ternary blend is not significantly lower than the quaternary blend because of the improved particle packing, but the lower matrix strength results in a lower σ_{ci}. The crack initiation stresses lie between 40% and 60% of the peak strength for all the mixtures. The true peak strength, which is the crack damage stress (σ_{cd}), is about 10% lower than the measured peak stress. Specimens deteriorate very quickly beyond the crack damage stress (σ_{cd}) because the crack volumetric strain and crack density significantly increase beyond σ_{cd}. Based on the aforementioned observations, crack damage

stress is suggested as a more conservative design parameter than the ultimate compressive strength for UHPC mixtures.

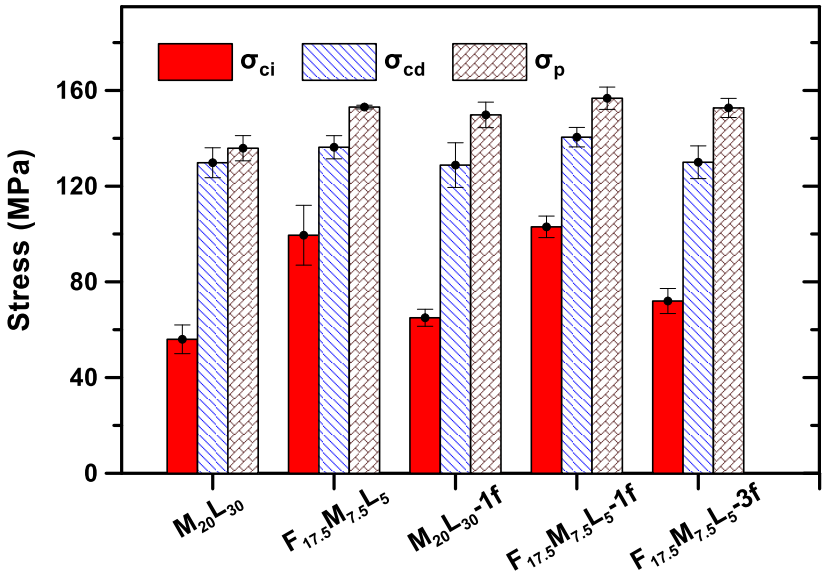

Figure 8-12 – Critical stress state parameters of the UHPC mixtures. The error bars correspond to one standard deviation from the corresponding mean values for three replicate specimens.

8.3.2 Elastic Constants of UHPC mixtures

As mentioned in Section 8.2.4, ultrasonic pulse velocity (UPV) was determined in conjunction with the uniaxial compression tests on the 50 mm diameter x 100 mm long cylindrical UHPC specimens. The P- and S-wave velocities obtained from UPV were analyzed to obtain E and ν at applied stress intervals of 10 MPa, as per Equations 8-3 to 8-6. It was observed that the velocities remain fairly consistent throughout the test until the peak stress is attained, after which the specimen undergoes large deformation in the form of matrix cracking. Beyond the peak stress, a noticeable change in the stiffness was observed,

indicated by a decrease in the P- and S-wave velocities. Table 8-3 shows the E and ν values computed from the wave velocities and from the compression stress-strain plots (Figures 8-8 and 8-9). $E_{\sigma-\varepsilon}$ and $\nu_{\sigma-\varepsilon}$ are calculated from the stress-strain plots, based on the secant values from -0.01% radial strain to 50% of the peak stress (Matti Hakala and Heikkilä 1997). $E_{initial}$ corresponds to the elastic modulus calculated using the P- and S-wave velocities measured at a low axial stress (10 MPa in this case), and $E_{post\text{-}peak}$ corresponds to the elastic modulus computed at the end of the test when the sample fails, or when a maximum radial strain of 0.3% or 1.5% is reached for the unreinforced and fiber-reinforced mixtures respectively. $\nu_{initial}$ and $\nu_{post\text{-}peak}$ are calculated at the same stress/strain levels as $E_{initial}$ and $E_{post\text{-}peak}$. The E values obtained from both methods are generally similar, with those determined from wave velocities slightly higher, the reasons for which have been extensively discussed (Han and Kim 2004; Popovics, Zemajtis, and Shkolnik 2008). The values are comparable to those obtained in literature (Alsalman et al. 2017).The Poisson's ratios of fiber-reinforced UHPC specimens determined from the compressive stress-strain response are higher than those obtained from wave velocities.

Table 8-3 - Elastic constants of UHPC mixtures determined from P- and S-wave velocities, and from quasi-static stress-strain relationships

Elastic constant	$M_{20}L_{30}$	$F_{17.5}M_{7.5}L_5$	$M_{20}L_{30}$-1f	$F_{17.5}M_{7.5}L_5$-1f	$F_{17.5}M_{7.5}L_5$-3f
$E_{\sigma-\varepsilon}$ (GPa)	43.10	47.53	46.26	49.84	42.25
$E_{initial}$ (GPa)	44.56	48.24	44.05	51.55	52.79

$E_{post\text{-}peak}$ (GPa)	43.57	48.16	41.75	47.22	50.87
$\nu_{\sigma\text{-}\varepsilon}$	0.19	0.27	0.32	0.29	0.30
$\nu_{initial}$	0.22	0.26	0.22	0.19	0.19
$\nu_{post\text{-}peak}$	0.23	0.23	0.23	0.24	0.24

8.3.3 Flexural Response of UHPC Mixtures

8.3.3.1. Load-deflection response, flexural strengths, and toughness

Four-point flexural tests on UHPC beams were carried out after 28 days of curing as described in Section 8.2.5. The fiber-reinforced specimens were subjected to the load-deflection tests. Six beams were tested for each UHPC mixture and the representative load-midspan displacement (P-δ) plots are shown in Figures 8-13(a) and (b). Midspan deflections were measured using an LVDT. Figure 8-13(a) shows the P-δ plots for both the ternary and quaternary blend binder UHPC beams 50 mm x 65 mm x 380 mm in size, containing 1% fiber by volume, while Figure 8-13(b) compares the P-δ response for the quaternary blend UHPC beams of size 100 mm x 100 mm x 457 mm, containing 1% or 3% volume fraction of fibers. The LVDT data was not available for the unreinforced mixtures and only the peak loads were recorded. From Figure 8-13(a), it is noted that the P-δ response in the pre-peak region is very similar for the ternary and quaternary blend UHPCs with 1% fiber volume, even though the quaternary blend sustains a slightly higher load, which is in line with their compressive strength results shown in Figure 8-7. The quaternary blend UHPC also shows a higher post-peak load retention capacity. A comparison between the quaternary blend

UHPCs containing 1% or 3% fiber volume shown in Figure 8-13 (b) conveys the expected trend of significantly increased load capacity – a two-fold increase when fiber volume is increased from 1% to 3%. A closer view of the P-δ response at small δ values (in the inset of Figure 8-13(b)) shows that the response is linear until a deflection of ~0.1mm for both the UHPCs. This corresponds to the peak load for the specimen with 1% fiber volume fraction. The specimen containing 3% fiber volume shows a strain hardening-like response between 0.1 mm and 0.5 mm deflection, attributable to the larger volume of fibers that bridge the microcracks generated in the matrix (Mobasher and Cheng Yu Li 1996; Yoo, Lee, and Yoon 2013).

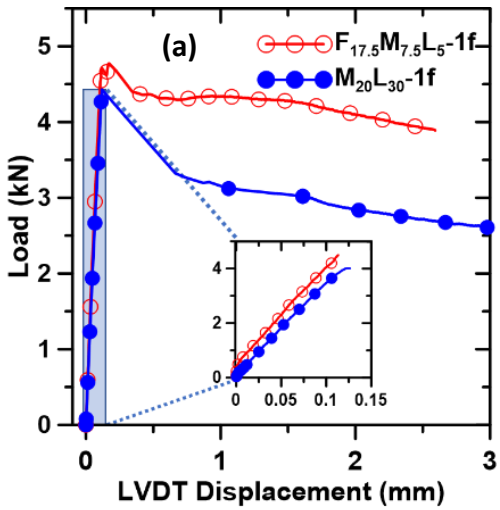

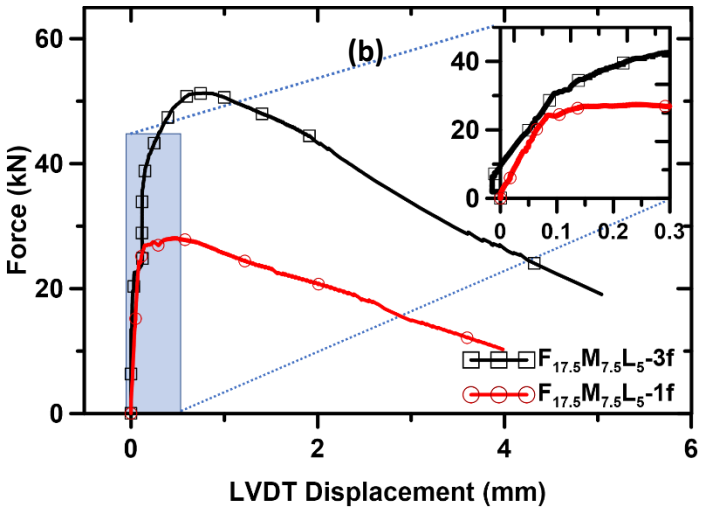

Figure 8-13 – Relationship between force and mid-span deflection for fiber-reinforced UHPC mixtures: (a) ternary and quaternary blend UHPCs containing 1% fiber volume (50mm x 65 mm), and (b) comparison between quaternary blend UHPCs containing 1% and 3% fiber volume (100 mm x 100 mm).

The 28-day flexural strengths of the UHPC mixtures are shown in Figure 8-14. The flexural strengths of the UHPCs with 1% fiber volume are similar to those of the corresponding unreinforced mixtures. It is likely that the particle packing is disturbed by the presence of fibers (Arora et al., n.d.), thereby slightly weakening the overall composite. However, at a higher fiber loading, significantly increased flexural strengths (~22 MPa) are achieved. The higher strength of the high volume fiber reinforced UHPC should be taken into account in conjunction with its higher ductility as observed in Figure 8-13(b), for structural design purposes.

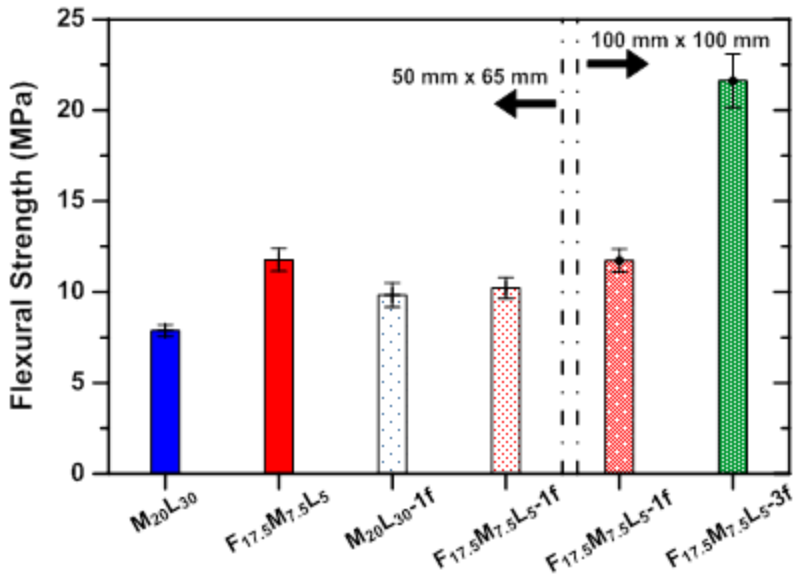

Figure 8-14 – Flexural strengths of UHPC mixtures after 28 days of moist curing. The error bars correspond to one standard deviation from the mean value of six replicate specimens.

The toughness of the UHPC mixtures is determined by numerically integrating the area under the load-deflection plots such as those shown in Figure 8-13. The toughness values are calculated for the peak load (also denoted as resilience), and at mid-span deflections of L/600 and L/150, where L is the effective beam span, and are shown in Figure 8-15. The influence of increase in fiber volume fraction on toughness can be easily observed from these figures.

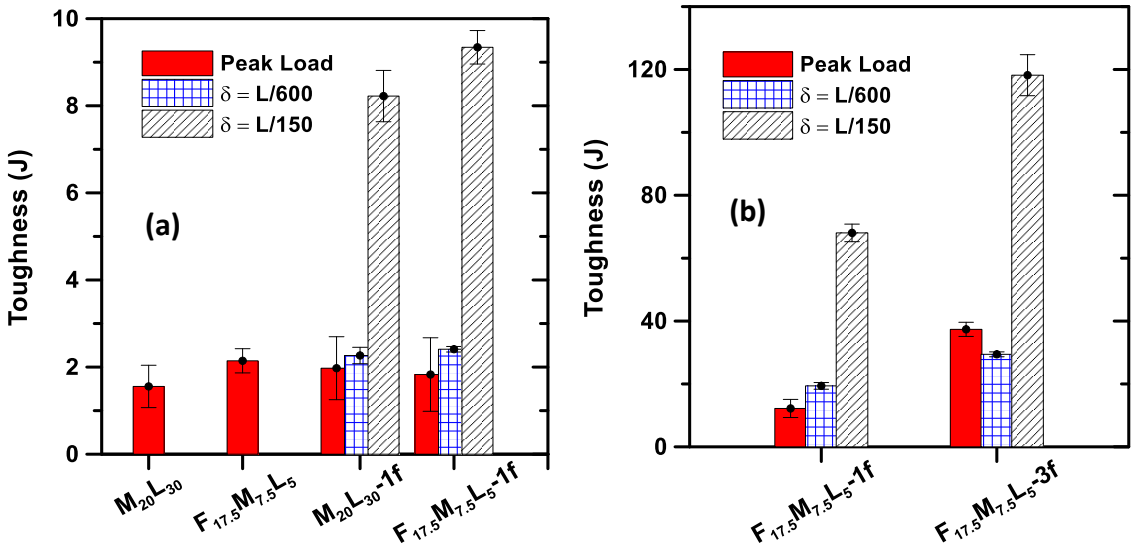

Figure 8-15 –Toughness of UHPC mixtures: (a) 50 mm x 65 mm x 380 mm beams, and (b) 100 x 100 x 457 mm beams. Toughness calculated as the area under the load displacement plot at peak load, and at mid-span deflections of L/600 and L/150. The error bars correspond to one standard deviation from the mean of six replicate specimens.

8.3.3.2. Strain field analysis using DIC

Digital image correlation (DIC) was carried out on beams subjected to flexure, as described in Section 8.2.6. Detailed discussions are limited to the strain fields in fiber-reinforced UHPCs, since the unreinforced specimens fail in a brittle manner, and the crack propagation could not be effectively monitored without a pre-defined crack (notch). However, the strain fields in the unreinforced mixtures just before failure (peak load) show well-dispersed tensile and compressive strains in the bottom and top of the beams respectively, as can be seen in Figure 8-16.

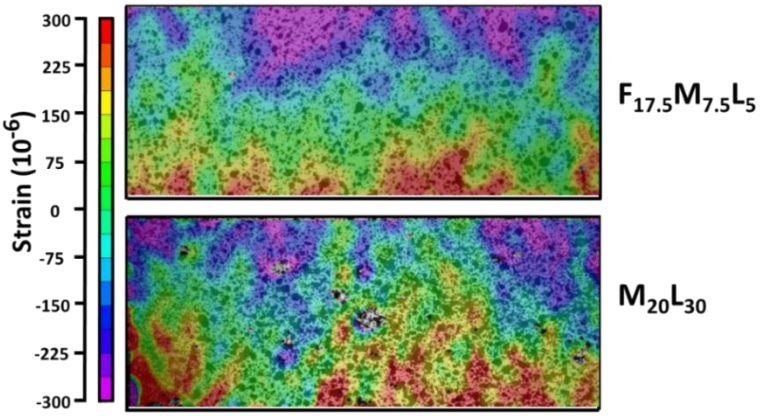

Figure 8-16 – Surface strain fields obtained by DIC for unreinforced beams just before failure

The load- crack opening displacement (COD) response was evaluated for the primary and secondary cracking in the fiber-reinforced UHPC beams studied. For the fiber-reinforced UHPCs, the location of the major crack was identified using the last image prior to stopping the DIC testing, in the post-peak zone. Section 8.2.6 has detailed the methodology to determine the load-COD response. Figure 8-17 (a) shows the load-crack opening displacement (COD) relationship for the fiber-reinforced UHPCs, where the COD was extracted from the DIC data. 50 mm x 65 mm x 380 mm beams were used, with a fiber volume fraction of 1%. As expected, the COD is negligible prior to the peak load for both the UHPC mixtures. The rate of crack opening beyond the peak is lower in the quaternary blend with fly ash than in the ternary blend. Since both of these mixtures contain the same amount of fibers, the increased ductility can likely be attributed to a more ductile matrix in case of the quaternary blend mixture. In fact, higher amounts of microsilica (as is the case in the ternary blend) has been reported to increase the brittleness of the binder (Dubey and

Banthia 1998), and the softening effect of limestone is likely compensated to some extent by this response. Figure 8-17 (b) shows the effect of fiber volume fraction on the load-COD response of 100 mm x 100 mm x 457 mm beams of the quaternary blend UHPC. Unsurprisingly, the flexural strength and ductility enhancements as a function of fiber dosage is brought out in a manner very similar to the load-deflection relationships.

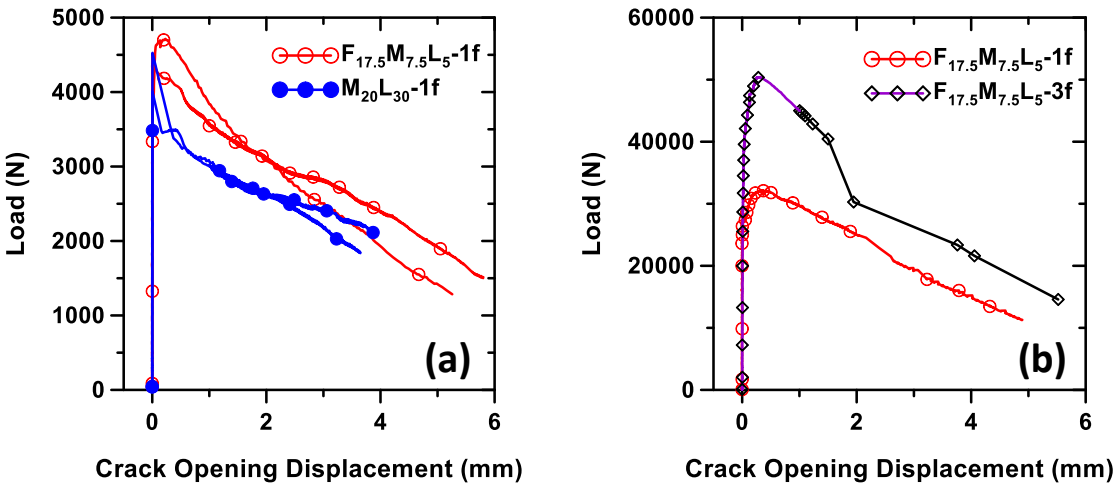

Figure 8-17 – (a) Load-COD response for 1 % fiber reinforced mixtures (50 mm x 65 x 380 mm), and (b) Load-COD response for UHPCs with 1% and 3% fiber volume fraction (100 mm x 100 mm x 457 mm)

The strain field analysis of fiber-reinforced UHPC is shown for five different load values marked from A to E in a typical load-COD relationship shown in Figure 8-18. A and B correspond to 50% and 90% of the peak load in the pre-peak region. C corresponds to the peak load. D and E correspond to 90% and 50% of the peak load in the post-peak region.

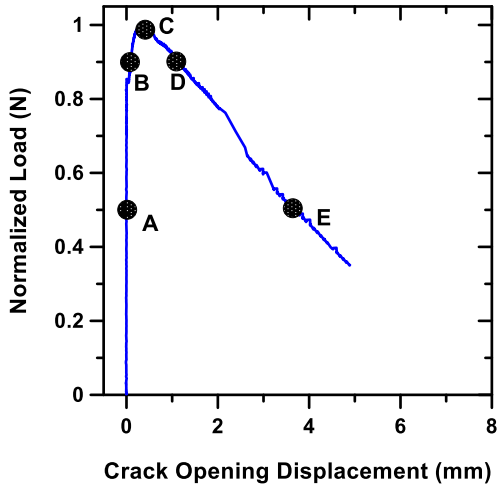

Figure 8-18 – Normalized load-COD response showing the regions A-E used for the DIC strain field analysis

Figure 8-19 shows the Lagrangian strain fields evaluated from the displacement fields calculated by DIC for the specimens containing 1% fiber volume. The images correspond to the points marked in Figure 8-18. It is clearly noticeable that that the beams experience no significant localized strains up to about 50% of the peak load. Strain localization is noticed generally close to the peak load. The quaternary blend UHPC shows multiple regions of localized strains before the peak load, while such a behavior is observed only at or close to the peak load for the ternary blend UHPC. This is indicative of the fundamental differences in the matrix behavior, brought about by the constituent materials (Das et al. 2015). As noted in Figure 8-12, the ternary blend UHPC has a lower crack initiation stress (σ_{ci}) as compared to the quaternary blend UHPC. This leads to a longer crack growth phase for the former, which is reflected in the more intense strain fields that accumulate at or close to the peak load. Surface cracking is not evident until the peak load. The first crack appears in the

ternary blend UHPC beam near the peak load whereas it does not make an appearance until 90% of the peak load in the post-peak regime for the quaternary blend UHPC. In the post-peak region, the strain fields are more dispersed for the quaternary blend UHPC, and the strains continue to grow in other regions of the beam along with strain at the major crack. This ultimately results in a higher value of residual strength and a higher toughness for the quaternary blend UHPC as was shown earlier.

Figure 8-20 shows the representative Lagrangian strain fields for the quaternary blend UHPC beams (100 mm x 100 mm x 457 mm) containing 1% and 3% steel fibers. The presence of higher volume of fibers result in a better dispersion of strains, and multiple cracking as noted in Figure 8-20. The increased amount of fibers help bridge micro-cracks and arrest crack growth in the post-peak region. This response is also related to the higher ductility and higher toughness of the beam containing 3% fiber volume.

Location in P-COD curve	**$M_{20}L_{30}$-1f**	**$F_{17.5}M_{7.5}L_{5}$-1f**
A	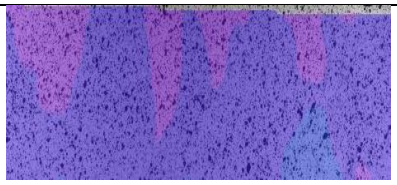	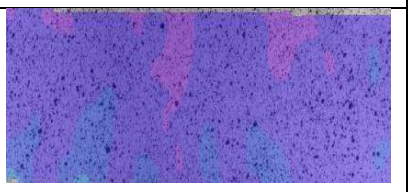
B	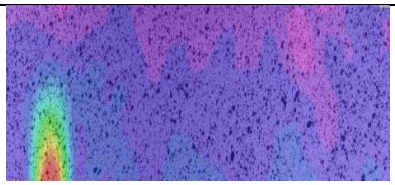	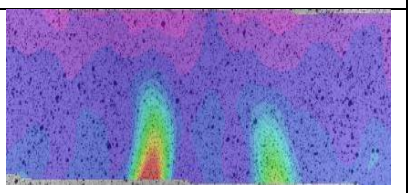

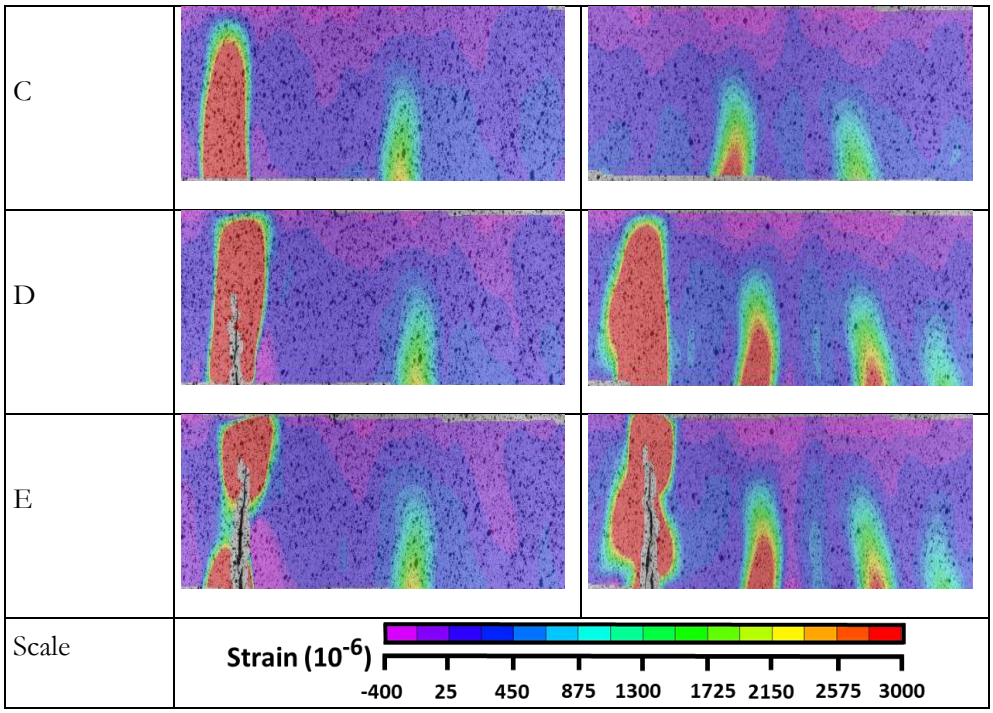

Figure 8-19 – Lagrangian strain fields in the pre-peak and post-peak regions of ternary and quaternary blend UHPC beams (50 mm x 65 mm x 380 mm) with 1% fiber volume

Location in P-COD curve	**$F_{17.5}M_{7.5}L_5$-1f**	**$F_{17.5}M_{7.5}L_5$-3f**
A	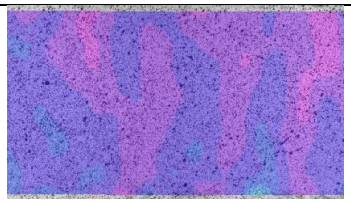	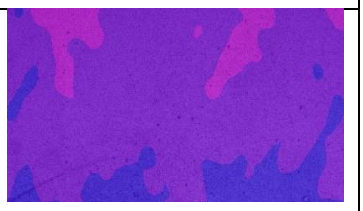
B	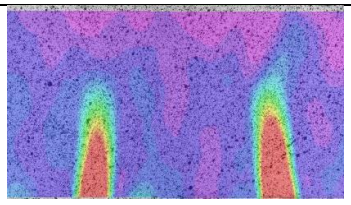	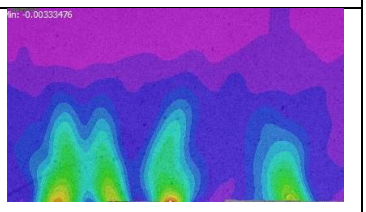

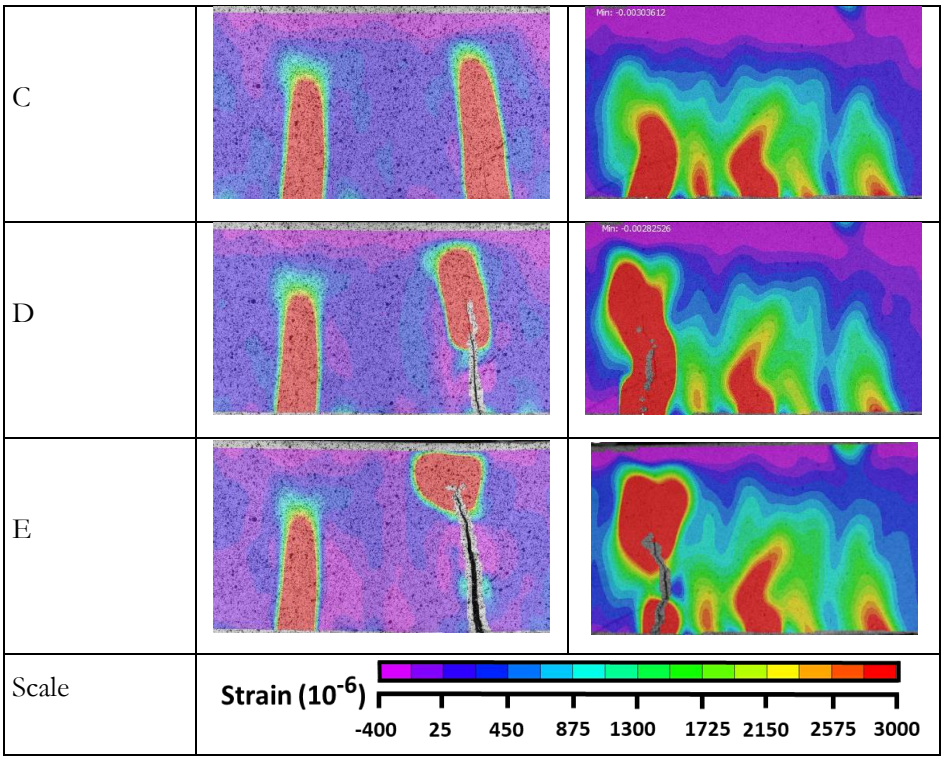

Figure 8-20 - Lagrangian strain fields in the pre-peak and post-peak regions for beams (100 mm x 100 mm x 457 mm) with 1% and 3% fiber volume. The DIC results on the right have more contrast due to a relatively low pixel resolution.

8.3.4 Indentation Response and Inverse Calculation

The indentation response was determined by post-processing the force versus penetration depth data for the 100 indents performed on each of the non-fiber reinforced UHPC samples. Approximately 5% of the plots were discarded from the final analysis of each of the pastes since they exhibited sudden jump during either the unloading or the loading part indicative of micro-cracks or pores at the location of indentation. The results for the indentation modulus (M) and hardness (H) obtained from the indents are shown in Figure 8-21.

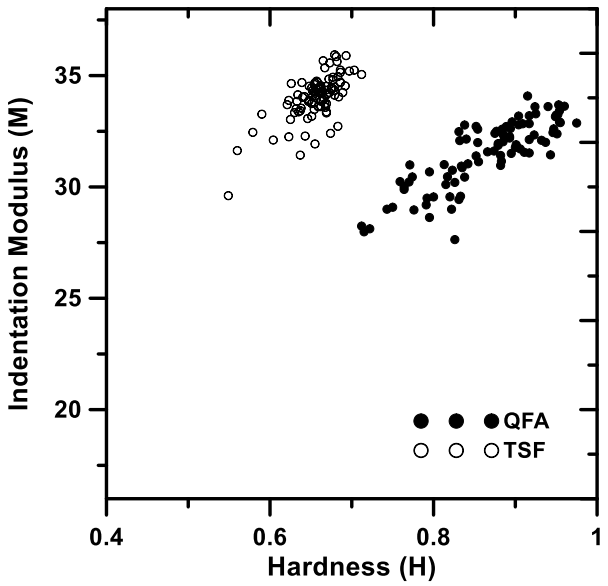

Figure 8-21 – Results of indentation – Indentation Modulus (M) versus Hardness (H)

A summary of the indentation results is given in Table 8-4. It is noted that the standard deviation lies within 10% of the average values of both hardness as well as indentation modulus. This gives a reasonable indication of a homogenized paste response been obtained from the indentation. It is observed that the indentation modulus of the ternary silica fume paste is higher than that of the quaternary fly ash paste. This is likely because of the presence of a large volume fraction of very stiff micro-silica particles ($E_{micro\text{-}silica}$ ~ 50 GPa) present in the mixture. The hardness modulus of quaternary fly ash paste is 30% higher than that of the ternary silica fume mixture, which is a likely result of the increased amount of hydration product formed in the quaternary fly ash system (Vance, Aguayo, et al. 2013; Guillermo Puerta-Falla et al. 2015; Arora et al. 2018).

Table 8-4 -Hardness and modulus results from micro-indentation testing of UHPC paste samples

Sample ID	Hardness (H) [GPa]	Indentation Modulus (M) [GPa]
$F_{17.5}M_{7.5}L_5$	0.865 ± 0.106	32.33 ± 1.504
$M_{20}L_{30}$	0.655 ± 0.027	35.15 ± 0.915

The parameters for the constitutive response of the specimen can be deduced from the statistical analysis of the hardness and indentation modulus data obtained using a simple fitting algorithm formulated by Franz et al. (Sorelli et al. 2008; Cariou, Ulm, and Dormieux 2008; Bobko et al. 2011). The Young's modulus of the material can be calculated using equation 8-15 assuming isotropic material behavior.

$$\frac{1}{E_r} = \frac{1-\nu^2}{E} + \frac{1-\nu_i^2}{E_i} \qquad \text{(Eq. 8-15)}$$

Here, E_r is the indentation modulus (M) determined from the experiment, E is the Young's modulus of the paste, E_i is the Young's modulus of the indenter, ν is the Poisson's ratio of the paste and ν_i is the Poisson's ratio of the indenter. The Poisson's ratio of the UHPC specimens was determined from the compression stress-strain test as 0.20 for QFA and 0.19 for the ternary silica fume sample.

A detailed analysis was carried out by Cheng and Cheng (Cheng and Cheng 2004) and later Cariou (Cariou, Ulm, and Dormieux 2008) using the Buckingham Pi-theorem to derive dimensionless expressions for hardness and indentation modulus for a porous composite. In

their derivation, Cariou et al. assumed that hardness and modulus values obtained as outputs from the indentation curve ('P' vs 'h') are representative of the properties of the porous composite at every point of indentation, which are tied to the properties of the solid phase as well as the pore morphology. Assuming UHPC to be a granular material with a cohesive-frictional solid phase, the solid phase is composed of particles with particle hardness h_s, particle stiffness m_s, friction coefficient α and locally packed with a packing density of η ($\eta = 1 - \varphi$). Equations 8-16 and 8-17 show the relations for the modulus and hardness measured at the n^{th} indent. Here, C^s is the stiffness matrix of the material, and η_0 is the solid percolation threshold and θ is the cone angle of the indenter.

$$H_n = h_s \times \Pi_H(\alpha, \eta_n, \eta_0, \theta) \qquad \text{(Eq. 8-16)}$$

$$M_n = m_s \times \Pi_M\left(\frac{C^s}{m_s}, \eta_n, \eta_0\right) \qquad \text{(Eq. 8-17)}$$

For a Berkovich indenter, θ is known to be 65.35°. Assuming isotropic material behavior, C^s is reduced to E. The percolation threshold η_0 can vary between zero and one depending on the pore-solid morphology of the composite material. The linear self-consistent scheme applicable to granular materials of high packing density provides the value for $\eta_0 = ½$. Applying these known values in equation 8-16, we obtain a simplified equation 8-18.

$$\frac{H}{h_s(c_s, \alpha)} = \Pi_H(\alpha, \eta, \eta_0) \qquad \text{(Eq. 8-18)}$$

The particle hardness (h_s) in the above equation is a function of the cohesion (c_s) and friction angle (α). In other words, h_s is defined as the hardness of an ideal composite with a zero porosity ($h_s = h_s(c_s, \alpha) = \lim_{\eta \to 1} H$). For a Drucker-Prager solid, Cariou et al. (Cariou, Ulm, and Dormieux 2008) and Bobko et al. (Bobko et al. 2011) simulated the indentation response using a Limit Analysis Solver for different packing densities of clay (a cohesive-frictional solid) and obtained a polynomial fitting function to relate material hardness and its cohesion and friction angle (equation 8-19). The value of the fitting parameters (A,B,C and D) of equation 8-19 can be found in (Bobko et al. 2011). Using these constants, the value of particle hardness can be determined given the value of friction and cohesion.

$$h_s = c_s \times A(1 + B\alpha + (C\alpha)^3 + (D\alpha)^{10}) \qquad \text{(Eq. 8-19)}$$

Since the percolation threshold is known ($\eta_0 = 1/2$), the hardness function on the right-hand side of equation 8-18 becomes a function of the friction angle and packing density. It can be written as a summation of two dimensionless functions Π_1 and Π_2 as given in equation 8-20, where the first part is independent of the friction coefficient α.

$$\Pi_H(\alpha, \eta) = \Pi_1(\eta) + \alpha(1 - \eta)\Pi_2(\alpha, \eta) \qquad \text{(Eq. 8-20)}$$

The two functions Π_1 and Π_2 were fitted to the simulation results to obtain polynomial expressions in terms of α and η [Equations 8-21,8-22]. The fitted parameters can be found in (Bobko et al. 2011).

$$\Pi_1(\eta) = \frac{\sqrt{2(2\eta-1)} - (2\eta-1)}{\sqrt{2}-1}(1 + g(1-\eta) + h(1-\eta)^2 + j(1-\eta)^3)$$

(Eq. 8-21)

$$\Pi_2(\alpha,\eta) = \frac{2\eta-1}{2}(k + m(1-\eta) + p(1-\eta)\alpha + q\alpha^3)$$

(Eq. 8-22)

Now, for a linear isotropic material, the indentation modulus assumes the same value as that of the plane stress elastic modulus (Equation 8-23). Here, K and G correspond to the bulk modulus and shear modulus of the indented material.

$$M = \frac{E}{1-\nu^2} = 4G\frac{3K+G}{3K+4G}$$

(Eq. 8-23)

The expressions for K and G are formulated for a porous composite in terms of the solid phase bulk and shear properties and the packing density using microporomechanics theory (Constantinides and Ulm 2007). Finally, the expression for the dimensionless function Π_M in equation 8-24 is derived under the self-consistent scheme ($\eta_0 = 0.5$) as:

$$\Pi_M = 2\eta - 1$$

(Eq. 8-24)

Now, knowing the values for H and M at each of the 'N' number of indents, we have 2N equations to solve for N+4 unknowns (η_i,m_s,c_s,α). An inverse analysis is carried out using a MATLAB program to arrive at the unknown values using a minimization algorithm coupling both H and M values (Bobko et al. 2011). Since the minimization function is not convex, the

algorithm gives several allowable values for the unknown parameters from which the ideal set of values must be derived by applying certain constraints.

In this case, we refer to the work done by Pichler and Hellmich (Pichler and Hellmich 2011), who predicted the evolution of uniaxial compressive strength of cement pastes as a function of the water-cement ratio corresponding to their hydration degree. The maximum attainable degree of hydration for a cement paste sample of a known water-to-cement ratio is given in Equation 8-25.

$$\xi_{max} = \begin{cases} \frac{w/c}{0.42}; & w/c \leq 0.42 \\ 1; & > 0.42 \end{cases}$$

(Eq. 8-25)

This relationship works well in the case of pure cement paste and for a UHPC specimen containing 100% cement at a w/c = 0.20, the maximum degree of hydration, $\xi_{max} = 0.47$.

The UHPC specimens in this study are composed of SCMs, that form secondary hydration products and therefore a measure of the degree of hydration may be obtained by quantification of the reaction product using statistical EBSD experiments. The water-to-cement ratio for the quaternary fly ash sample is 0.26 and for the ternary silica fume sample is 0.3. In both cases, assuming 80% hydration at 90 days, the value for the dimensionless compressive strength is approximately equal to 0.7 (Equation 8-26). f_{cu} is the uniaxial compressive strength of the cement paste, and $\sigma_{hyd,crit}^{dev}$ is the deviatoric hydrate strength which is related to the cohesion of the cement paste using equation 8-27.

$$\frac{f_{cu}}{\sigma_{hyd,crit}^{dev}} = 0.7$$

(Eq. 8-26)

$$c_{hyd} = \sigma_{hyd,crit}^{dev} \frac{\sqrt{3}}{2}$$

(Eq. 8-27)

Solving the above equations, we obtain the relationship between cohesion and the compressive strength of the UHPC paste (Equation 8-28). f_c is the compressive strength of UHPC concrete. Since UHPC mixes are primarily composed of paste (~70%), the factor 1.25 is assumed to be the scaling factor between paste and concrete strength.

$$c_{hyd} = 1.25 * f_{cu} \cong f_c$$

(Eq. 8-28)

Based on the value of cohesion obtained here, we go back to the minimization problem described earlier and determine the solution for the material constants that is nearest to the cohesion value calculated. The results of the analysis are shown in Table 8-5.

Table 8-5 – Material properties obtained from micromechanical analysis

Sample ID	m_s (GPa)	h_s (GPa)	c_s (MPa)	α (°)
$F_{17.5}M_{7.5}L_5$	54.93	2.37	155	24.20
$M_{20}L_{30}$	45.66	1.12	145	11.35

8.4. CONCLUSIONS

This chapter provides fundamental insights into the mechanical response of UHPCs proportioned using optimized binder proportions and aggregate gradation. Two different UHPC mixtures, a quaternary blend binder (OPC, fly ash, limestone and microsilica), and a ternary blend binder (OPC, microsilica and limestone) were proportioned using an optimized aggregate gradation predicted by the compressible packing model and experimentally validated. For some of the mixtures, steel fibers were used at volume fractions of 0.01 or 0.03. All the mixtures demonstrated a 90-day compressive strength of more than 150 MPa, with no significant changes in strength between unreinforced and fiber-reinforced specimens.

The stress-strain response of UHPC mixtures in compression was brought out using radial strain-controlled compression tests on 50 mm x 100 mm cylinders. The influence of fiber reinforcement on the post-peak response in compression were adequately quantified using these tests. The critical stress states under compression were extracted from the relationships between axial stress and axial/radial strain, and axial strain-volumetric strain relationships. Crack initiation stress (σ_{ci}) and crack damage stress (σ_{cd}) are the major parameters of interest extracted from these relationships, which are indicators of change in the internal structure of the material under uniaxial compression. Differences in σ_{ci} and σ_{cd} between the ternary and quaternary blend binders were attributed to differences in composition that influence the matrix strength. Beyond the crack damage stress, unstable cracking was observed to begin, as noticed by a significant increase in the crack volumetric strain. Thus, σ_{cd} is suggested as a more accurate measure of the true unconfined compressive strength of UHPC, which is around 10% lower than the peak stress. The material parameters, E and ν, were extracted

using the compression stress-strain response as well as ultrasonic pulse velocity measurements.

The influence of steel fibers on the UHPC response was brought out using flexural tests on beams of two different sizes under four-point bending. The UHPC mixture with 3% fiber volume showed a significantly higher flexural strength (~22 MPa) than the unreinforced and 1% fiber volume mixtures (~12 MPa). The toughness calculated based on the load-deflection response also showed the beneficial influence of fibers bridging the matrix micro-cracks, especially when calculated at a larger deflection, which included the post-peak response. The Lagrangian surface strain fields under flexure were evaluated from displacement fields mapped using DIC, from which load-crack opening displacement relations were extracted. The influence of matrix characteristics and fiber reinforcement on dispersion and localization of strains, and crack propagation were accurately captured by the DIC measurements. The studies described in the paper have thus elucidated the fundamental response of economical UHPC mixtures in both compression and flexure, concurrently providing insights into the microstructural changes occurring under the respective loading regimes, either through the determination of critical stress states or strain fields.

CHAPTER 9[11]

NUMERICAL SIMULATIONS TO QUANTIFY THE INFLUENCE OF PHASE CHANGE MATERIALS ON EARLY AND LATER-AGE THERMAL RESPONSE OF CONCRETES

9.1. INTRODUCTION

The use of phase change materials (PCMs) as components of building systems has been steadily increasing because of their capacity to store and release energy in the form of heat, thereby facilitating energy efficient envelope systems (Baetens, Jelle, and Gustavsen 2010; Khudhair and Farid 2004; Shilei, Neng, and Guohui 2006; Cabeza et al. 2007; Schossig et al. 2005). PCMs are combined (sensible and latent) thermal energy storage (TES) materials. When subjected to an increase in temperature, PCMs act as sensible energy storage media until their phase transition temperature is reached. When the temperature exceeds their melting temperature, phase transition of PCMs from solid to liquid state occurs, thus allowing them to act as a latent heat storage medium. During the latent heat storage phase, the system temperature is maintained constant. In other words, the energy provided to the system is used in the change of phase of PCMs, by which they provide an auto-adaptive capability to a system like concrete in which they are embedded, to maintain the temperature. In addition to the well-researched avenue of building energy efficiency, this behavior presents a unique opportunity to utilize PCMs as a strategy to mitigate early- and

[11] This chapter is derived from the publication: Arora, A., Sant, G., & Neithalath, N. (2017). Numerical simulations to quantify the influence of phase change materials (PCMs) on the early-and later-age thermal response of concrete pavements. Cement and Concrete Composites, 81, 11-24.

late-age thermal cracking in concrete structures. Solid-liquid PCMs broadly belong to three categories: organic compounds such as paraffins and fatty acids, inorganic compounds such as salt hydrates, and eutectic compounds (Zalba et al. 2003). Paraffins are the most commonly used PCMs in building applications. They are either encapsulated in the form of micro or macro capsules (Schossig et al. 2005; Fernandes et al. 2014; Aguayo et al. 2016), impregnated into porous materials such as lightweight aggregates (Aguayo et al. 2017), or directly added to the host material. The former two methods are more applicable to cement-based materials since paraffins generally interfere with the hydration of cement when added directly.

The heat released during the hydration of cement at early-ages is well understood to be a reason for early-age cracking of restrained concrete elements such as pavements and bridge-decks, while diurnal changes in temperature can cause thermal fatigue and associated cracking in mature concrete at later ages (Springenschmid 1994; Emborg and Bernander 1994). A previous study has experimentally shown that the use of microencapsulated PCMs in concrete effectively reduces the adverse effects of heat of hydration by reducing the peak temperature rise and the rate of heat evolution/release during cement hydration (Fernandes et al. 2014). It has also been shown that small volume fractions (in the range of 5-to-10% by volume of concrete) of such PCMs can be well dispersed in concrete with little influence on the resulting mechanical properties (Aguayo et al. 2016).

In this study, a numerical modeling approach is implemented to evaluate the influence of microencapsulated PCMs in reducing the early-age temperature evolution in concrete pavements, as well as to quantify the benefits in terms of reducing the propensity of the

member to early-age cracking through an analysis of stress development. A finite difference model is used for the hydrating concrete pavement with considerations of mixture proportions, member geometry, and structural and thermal (environmental) boundary conditions. PCMs with two different phase transition temperatures are considered since the effectiveness of the PCMs in reducing temperature gradients is an intrinsic function of the local climate. The influence of PCMs in dictating the long-term response of the pavement with respect to reducing temperature gradients and stresses are elucidated using year-long simulations of virtual pavements located in Phoenix, AZ (hot, dry environment), and San Francisco, CA (cool, humid environment). The numerical simulations shown in this chapter demonstrate the effectiveness of PCMs in reducing the risks of thermal cracking in concrete pavements at both early- and later-ages, and serves as a tool to enable designers/engineers devise strategies for crack-resistant material design of concrete based on the environmental conditions. Note that the analysis presented in this chapter considers only the temperature development and associated thermal stresses. Moisture movement that causes drying and associated shrinkage, which is also a function of early-age temperature development, and creep that consequently reduces the stresses, are not considered here.

9.2. EARLY-AGE RESPONSE MODELING

9.2.1 Model Formulation and Boundary Conditions

A brief overview of the model formulation and boundary conditions is provided here, considering that the latent heat storage/release capacity of PCMs result in perceptible changes in the temperature (and consequently the early-age thermal stress) profiles in hydrating concrete. The simulation methodology detailed below has been programmed using

Matlab© with the capability to read climatic data from a national climate database, allowing the simulations of concrete pavements in any geographic location.

The temperature development in a concrete pavement section subjected to external variations in climatic conditions is generally modeled using the second-order heat-diffusion equation (Reynolds and Perkins 1977; Springenschmid 1994) given as:

$$\nabla.(k\nabla T) + \dot{q} = \rho c_p \frac{\partial T}{\partial t} \quad \text{(Eq. 9-1)}$$

where k is the thermal conductivity of the concrete ($W.m^{-1}K^{-1}$), T(x,y,z) is the scalar temperature field (K), q' corresponds to the heat generated from the cement hydration reactions (W), ϱ is the density of concrete ($kg.m^{-3}$), c_p is the specific heat capacity of concrete ($J.kg^{-1}K^{-1}$), and t is the time (s). For hydrating cementitious systems (i.e., at early ages), the thermal conductivity and specific heat capacity are dependent on the degree of hydration. Equations 9-2 and 9-3 have been used to represent the hydration-dependent thermal conductivity and heat capacity (Reinhardt, Blaauwendraad, and Jongedijk 1982).

$$k(t,T) = k_{uc} * (2 - \alpha) \quad \text{(Eq. 9-2)}$$

$$c_p(t,T) = c_{p-uc} * (1.25 - 0.25 * \alpha) \quad \text{(Eq. 9-3)}$$

where k_{uc} is the ultimate (i.e., at 100% hydration) thermal conductivity of concrete (taken as 0.612 $W.m^{-1}K^{-1}$), $c_{p\text{-}uc}$ is the ultimate heat capacity of concrete (910 $J.kg^{-1}K^{-1}$) (Lamond and Pielert 2006) and α is the degree of hydration of the system. The degree of hydration α is a function of temperature and time, which is expressed as (Pane and Hansen 2002):

$$\alpha(t_e) = \alpha_u * \exp\left(-\left(\frac{\tau}{t_e}\right)^{\beta}\right)$$

(Eq. 9-4)

where $\alpha(t_e)$ is the degree of hydration at equivalent age t_e (given in Equation 9-5), α_u is the ultimate degree of hydration, τ is the hydration time parameter (hours), and β is the slope parameter. These parameters have been shown to be adequately represented as functions of the chemical composition of the binding materials (Anton K. Schindler and Folliard 2005). The equivalent age t_e represents the effect of temperature on the degree of hydration (ASTM 2011; Carino and Lew n.d.). The actual age of concrete 't' was converted to an equivalent age t_e at the reference temperature using Equation 9-5.

$$t_e(T) = \int_0^t \exp\left(\frac{E_a}{R}.\left(\frac{1}{T_r} - \frac{1}{T}\right)\right) dt$$

(Eq. 9-5)

Here, T_r is the reference temperature (298 K), E_a is the activation energy ($J.mol^{-1}$), and R ($J.mol^{-1}K^{-1}$) is the universal gas constant.

When the cementitious mixture contains PCMs, suitable adjustments are needed in the thermal conductivity and heat capacity terms of Equation 9-1. The specific heat capacity of PCM is a function of the temperature as shown in Figure 9-1 (a) for two different microencapsulated PCMs used for the simulations reported in this study, having phase transition temperatures in the neighborhood of 24°C and 35°C. During the phase transition, the PCM stores latent heat energy, helping to maintain a constant system temperature as shown in Figure 9-1(b). The heat capacity and thermal conductivity of PCM-incorporated

concrete depend on the volume fraction of the PCM in concrete, and are calculated using a rule of mixtures approach as shown in Equations 9-6 and 9-7.

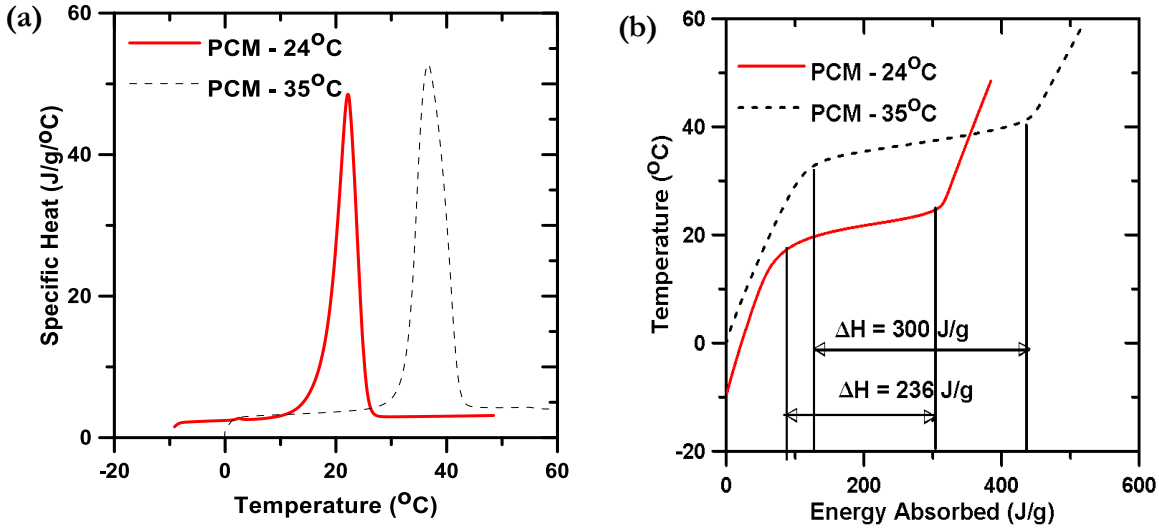

Figure 9-1 – (a) Differential scanning calorimetry (DSC) plot for two different PCMs showing specific heat as a function of the temperature, and (b) representation of the latent heat capacity of both the PCMs.

$$c_{p,comp}(T) = c_{p,conc}(T) * v_{conc} + c_{p,pcm}(T) * v_{pcm} \quad \text{(Eq. 9-6)}$$

$$k_{comp}(T) = k_{conc}(T) * v_{conc} + k_{pcm}(T) * v_{pcm} \quad \text{(Eq. 9-7)}$$

where v_{conc} is the volume fraction of concrete and v_{pcm} is the volume fraction of PCM in the PCM-incorporated concrete. In Equation 9-6, $c_{p,comp}(T)$ is the specific heat capacity of the PCM incorporated concrete, $c_{p,conc}(T)$ is the specific heat capacity of plain concrete (given in Equation 9-3), and $c_{p,pcm}(T)$ is the specific heat capacity of the PCM (from Figure 9-1 (a)). Similarly, in Equation 9-7, $k_{comp}(T)$, $k_{conc}(T)$ and $k_{pcm}(T)$ respectively are the thermal

conductivities of PCM incorporated concrete, plain concrete (given in Equation 9-2) and the PCM. The thermal conductivity of PCM, $k_{pcm}(T)$ is a function of temperature and is taken to be as 0.25, 0.20 and 0.15 W/m/K respectively when PCM is in the solid phase, latent transition phase, and liquid phase (Zalba et al. 2003; Abhat 1983; Sarı and Karaipekli 2007). The heat generated from cement hydration (q' in Equation 9-1) is given as (Anton K. Schindler and Folliard 2003):

$$q'(t_e) = H_u * C_c * \alpha(t_e) * \frac{\beta}{t_e} * \left(\frac{\tau}{t_e}\right)^{\beta} * \exp\left(\frac{E_a}{R}.\left(\frac{1}{T_r} - \frac{1}{T}\right)\right) \quad \text{(Eq. 9-8)}$$

where H_u is the heat generated at complete hydration ($J.kg^{-1}$), C_c is the amount of cementitious materials in the mixture ($kg.m^{-3}$), E_a is the activation energy ($J.mol^{-1}$), R is the universal gas constant ($J.mol^{-1}K^{-1}$), and T_r is the reference temperature (298 K). β and τ were defined before. H_u and E_a can be calculated using the chemical composition of the binding materials as described elsewhere (Anton K. Schindler and Folliard 2005). For a Type I/II OPC concrete with the composition chosen for simulations (explained in Section 2.3), H_u, E_a, α_u, τ and β were obtained as 460 $kJ.kg^{-1}$, 36.2 $kJ.mol^{-1}$, 0.78, 12.9 hours, and 0.77 respectively. For concrete containing PCM as cement paste replacement, the amount of cementitious materials (C_c) is adjusted based on the composition of the mixture. Since PCM has no effect on the heat generation during hydration, all other parameters remain unchanged.

Equation 9-1 was solved to calculate the temperature in the pavement as a function of depth and time using an explicit finite difference approach. The pavement model consisting of the

hydrating concrete layer and the base/sub-base was discretized into a number of layers. The number of layers and time step were selected to obtain convergence in results. In this study, 50 layers each were considered for the concrete pavement as well as the base/sub-base, which translated into layer thicknesses of 6 mm and 30 mm respectively for these components. The time step used was 10 seconds. Figure 9-2 shows a schematic of the finite difference model with the environmental factors that influence the early-age temperature development in a hydrating concrete pavement.

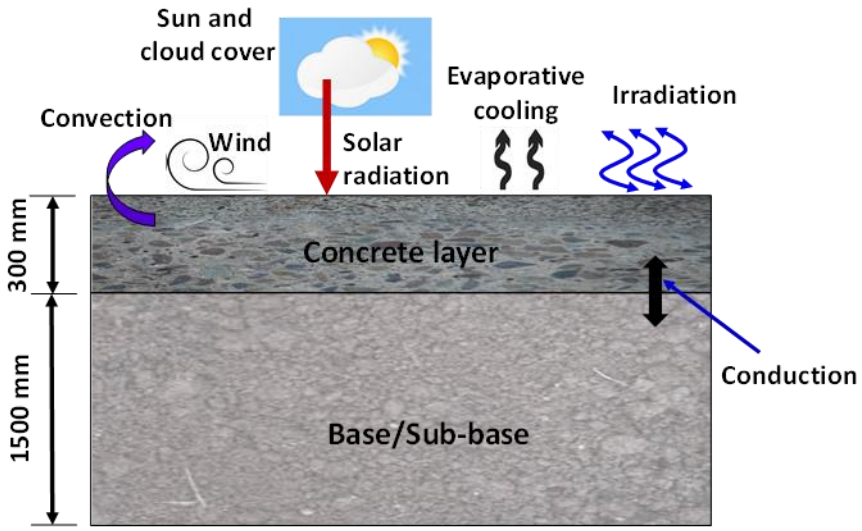

Figure 9-2 – Schematic model of a concrete pavement subjected to environmental effects at early ages

Equations 9-9, 9-10 and 9-12 depict the top, bottom, and the concrete-base/sub-base boundary conditions adopted for the model. The top surface boundary condition (Equation 9-9) captures the effects of the environmental phenomena such as evaporative cooling, incident solar radiation, irradiation, and convection to-and-from the surface. These are

functions of the temperature, wind speed, cloud cover and relative humidity (Anton Karel Schindler 2011).

$$-k_{comp}\frac{\partial T(0,t)}{\partial x} = h_0(T(0,t) - T_0) + \varepsilon\sigma(T_0^4 - T(0,t)^4) - \beta_s q_s$$

(Eq. 9-9)

The first term on the RHS of the top surface boundary condition represents the convective heat transfer. Here, h_0 is the surface convection coefficient, which is a function of the wind speed and the concrete curing method adopted in the field (ASTM Standard, n.d., 680; Riding et al. 2007). T_0 is the ambient temperature and T(0,t) represents the concrete surface temperature. The second term corresponds to the radiative heat transfer, where ε is the surface emissivity of concrete and σ is the Stefan-Boltzmann constant. The final term characterizes the solar absorption through the solar absorptivity β_s and the instantaneous solar radiation q_s.

The bottom surface boundary condition (in this case, at a depth of 1800 mm from the surface of the concrete pavement) can be stated as:

$$T(x, -L) = T_g$$

(Eq. 9-10)

where T_g is the constant ground temperature (°C). Also, the initial temperature across the pavement as well as the base/sub-base is assumed to be equal to T_g, which is calculated using the average annual temperature T_{aa} (°C) from the climatic data for the specific region as (Yoshitake et al. 2002):

$$T_g(t) = 0.83 * T_{aa}(t) + 3.7$$

(Eq. 9-11)

The continuity of heat flux through the pavement and base/sub-base leads to the third boundary condition at the pavement-base/sub-base interface (Equation 9-12).

$$k_{comp}\frac{\partial T(L,t)}{\partial x} = k_{soil}\frac{\partial T_{soil}(L,t)}{\partial x} \quad \text{(Eq. 9-12)}$$

The numerical simulations reported in this study were carried out using climate datasets from 2010 for Phoenix AZ, and San Francisco, CA, obtained from the website of the National Centers for Environmental Information ("Welcome to National Centers for Environmental Information (NCEI)" n.d.). These two locations were chosen to highlight the importance of PCM type/dosage as a function of the local climate. Phoenix has a hot and dry weather around the year with average annual temperature of 24°C (highs up to 50°C), whereas San Francisco is located in a colder and humid region with an average annual temperature of 14°C ("Climate Phoenix - Arizona and Weather Averages Phoenix" n.d.; "Climate San Francisco - California and Weather Averages San Francisco" n.d.). The climate data used for the simulations included hourly averages of temperature, cloud cover, relative humidity and wind speed. Since the least count for the finite difference model is 10 s, the required values were obtained using linear interpolation from the hourly averages.

9.2.2 Predicting Strength Development

Since thermal stresses are responsible for early age cracking of concrete pavements, it is important to understand the time when the stress exceeds the material strength, which is a function of the mixture composition and exposure conditions. As is generally implemented, the compressive strength of hydrating concrete is modeled as a function of the ultimate

compressive strength $f_{c\text{-}ult}$, as shown in Equation 9-13 (Springenschmid 1994). τ_s and β_s are the fit parameters.

$$f_c(t_e) = f_{c-ult}\exp\left(-\left(\frac{\tau_s}{t_e}\right)^{\beta_s}\right)$$

(Eq. 9-13)

The tensile strength and elastic modulus at time t_e are functions of the compressive strength at the particular time (Raphael 1984; Committee, Institute, and Standardization 2008, 318–08) and are represented using Equations 9-14 and 9-15.

$$f_t = l * (f_c(t_e)^m$$

(Eq. 9-14)

$$E = k.(f_c(t_e)^{0.5}$$

(Eq. 9-15)

'l' and 'm' are parameters that obtained by fitting the experimental tensile strength and compressive strength data for the chosen mixture proportion. For an ultimate compressive strength $f_{c\text{-}ult}$ of 40 MPa, the different fit parameters have been obtained as: τ_s = 27.8 hours, β_s = 0.72, l = 0.35, m = 0.67, and k = 3.88 x 10^6 $Pa^{0.5}$.

9.2.3 Mixture Compositions Containing PCMs

PCMs can be incorporated in concretes either by replacing a fraction of the fine aggregate (sand) or a fraction of cement (i.e., cement paste). Both these strategies are evaluated in the simulations. Previous studies have shown that replacing a small fraction of sand by microencapsulated PCM does not result in strength reductions, even though the elastic modulus is reduced owing to the replacement of stiff material (quartz sand) by a soft inclusion (PCM) (Aguayo et al. 2016). However, when a fraction of the cement paste is

replaced by PCM, both strength and elastic modulus are compromised. In the simulations performed here, 5% to 20% of sand or cement paste by volume are replaced in the concrete mixture. That translates to 1.2% to 5.5% by volume of the concrete, as shown in Figure 9-3. The plain concrete used in the simulations has a cement content of 341 $kg.m^{-3}$, a fine aggregate content of 666 $kg.m^{-3}$, a coarse aggregate content of 1121 $kg.m^{-3}$ and a water content of 148 $kg.m^{-3}$. A 20% replacement of cement paste by PCM (by volume) is equivalent to a 13.5% replacement of cement (by mass) by the PCM, whereas a 20% volume replacement of sand is equivalent to a 14.7% of replacement of sand (by mass) by the PCM.

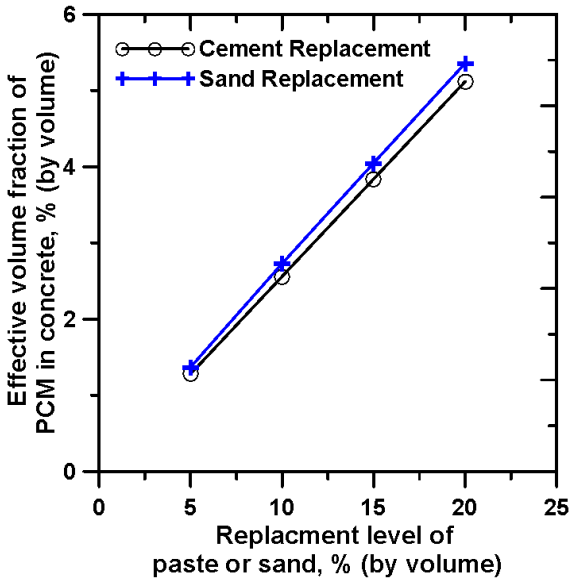

Figure 9-3 – Relating replacement levels of cement paste or fine aggregates by PCM (by volume) to the total PCM content in the concrete (by volume)

9.3. NUMERICAL SIMULATION OF EARLY AGE RESPONSE: RESULTS AND ANALYSIS

9.3.1 Pavement Temperature Profile at Early Ages

The hydration of cementitious materials generates heat for several days after placement of the concrete members. The exothermic hydration reaction, coupled with the imposed daily temperatures induce temperature differentials across the pavement section. While the surface heats up or cools rapidly in response to the ambient temperature variation, the internal temperature changes at a slower rate. The early age temperature development is predicted by solving the one-dimensional heat diffusion equation (Equation 9-1). The simulated pavement is located in Phoenix, AZ, and the placement is considered to occur either in the month of March or July. The corresponding ambient 8-day temperatures are shown in Figure 9-4. In order to keep the discussions succinct, this section discusses primarily the cases where the pavement was placed in March, where a PCM with a phase transition temperature of 24°C was used.

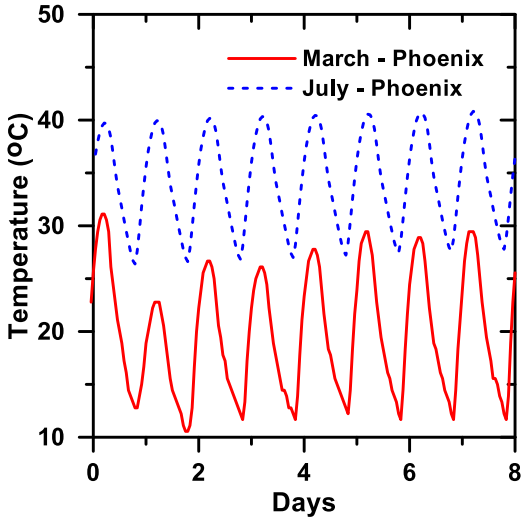

Figure 9-4 – Ambient 8-day temperature profiles for pavements cast in March and July in Phoenix, AZ

The temperature profile for a plain OPC concrete pavement located in Phoenix, AZ, placed in the month of March, is shown in Figure 9-5 (a), at different depths from the surface of the pavement. The temperature differential between the ambient and the interior of the concrete is higher for the first 48 hours due to significant internal heat generated from cement hydration. After 48 hours, the heat generation reduces significantly, resulting in the calculated temperature profile for the first layer being similar to the imposed external temperature. The temperature differentials for the internal layers also reduce with time. Figure 9-5(b) shows the maximum and minimum temperature profiles for the pavement section along with the temperature profile at the center of the pavement. The maximum temperature in the pavement section is critical, since it has a direct bearing on the internal stresses, and consequently the propensity of the pavement to crack at early ages.

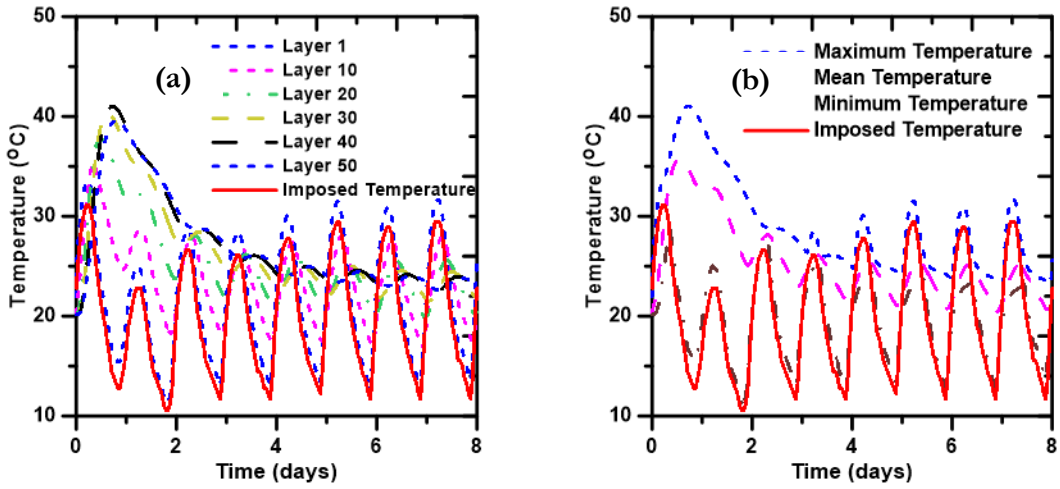

Figure 9-5 - (a) Predicted temperature profile for a plain OPC concrete pavement. Layer 1 corresponds to the top surface exposed to the atmosphere and Layer 50 corresponds to the bottom surface, which is in contact with the base, and (b) temporal variation of maximum, minimum and mean temperatures for the plain OPC concrete pavement.

When microencapsulated PCMs of appropriate phase transition temperature are incorporated into the mixture, their latent heat storage capacity results in reduced section temperatures. The maximum temperature in the pavement as a function of time, where PCM inclusions replace either a part of the cement paste or fine aggregates, are plotted in Figures 9-6 (a) and (b) respectively. The phase transition temperature of the PCM is 24°C. Both the replacement scenarios are designed to result in a PCM volume fraction between 1.25% and 5.5% in concrete. As noticed from Figure 9-6, the early age surge in the temperature development in concrete is significantly reduced by the incorporation of PCMs. The magnitude of temperature reduction increases with increasing PCM content as expected. When the concrete contains 5% of PCM by volume, there is an approximately 10°C reduction in the peak hydration temperature under the exposure conditions chosen, when cement paste is replaced by the PCM, and an approximately 6°C reduction when a similar volume of PCM replaces sand. These are significant in reducing the cracking propensity of the concrete, as elucidated in a later section. The latent heat storage by the PCM also delays the occurrence of the peak temperature, and slows down the cool down rate, both of which are instrumental in regulating the thermal strains within the hydrating concrete member. When PCM replaces part of the cement paste, the latent heat storage by PCM is supplemented by the reduced rate of heat generation (which depends on the replacement level), whereas when PCM replaces part of the fine aggregate, the thermal storage capacity of the PCM is solely responsible for reduction in maximum section temperatures.

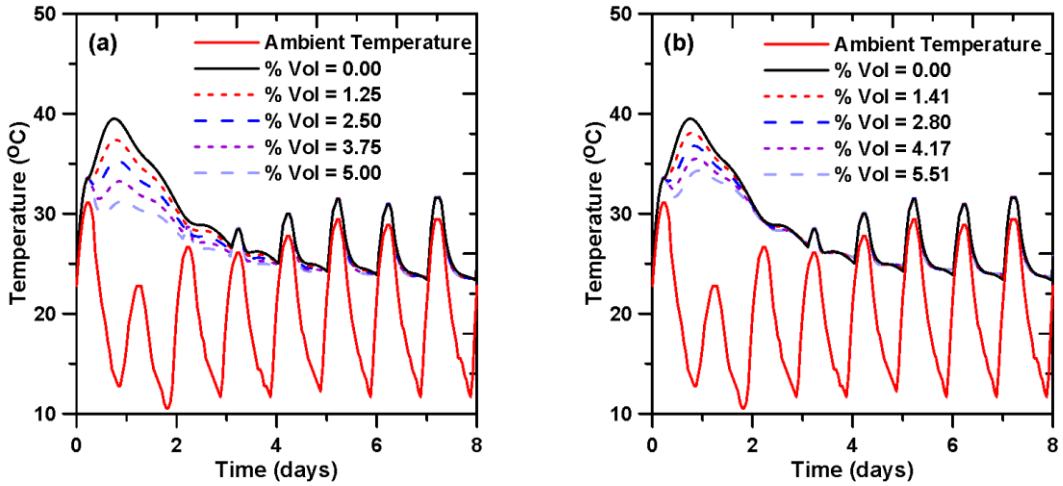

Figure 9-6 – Comparison of maximum section temperatures: (a) PCM replacing cement paste, and (b) PCM replacing fine aggregates. The volume fraction of PCMs in concrete is shown in the graphs.

A commonly adopted approach to reduce excessive early age temperature rise in hydrating concrete members is the use of fly ash as a partial cement replacement. Fly ash incorporation reduces the peak temperature in concrete at early ages due to the dilution effect. Figure 9-7 compares the predicted temperature profiles when 20% of cement (mass-based) is replaced by fly ash (which translates to 2.34% of fly ash by volume of concrete) or 10% by volume of sand is replaced by PCM (which translates to 2.8% of the volume of concrete). Note that at early ages, fly ash does not react in a cementitious system and can be considered as a filler material. This enables rational comparison of the early-age response of systems containing similar volumes of fly ash or PCM. A similar reduction in maximum section temperatures, as compared to the plain OPC pavement, is noticed. However, when fly ash replaces cement in concrete, the effectiveness in reducing the temperature differential is limited to early ages since the dilution effect dominates during this period. Hence, the presence of fly ash

primarily influences the heat generation term in Equation 9-1. On the other hand, there is no dilution in the cement content when PCM replaces fine aggregate, and the temperature reduction is solely attributed to the latent heat storage capacity of the PCM.

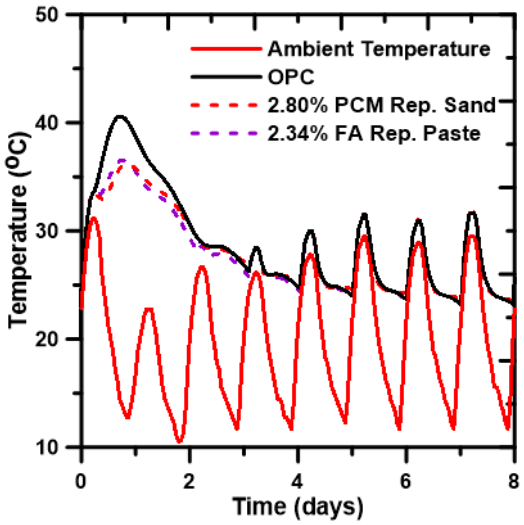

Figure 9-7 – Comparison of maximum section temperature as a function of time at early ages for concretes containing comparable volumes of fly ash or PCM.

While the maximum section temperatures shown in Figure 9-7 reflect the temperature difference between the systems during very early periods of hydration, it is instructive to examine the temperature profiles at the mid-section of the pavement during the first 8 days. This is shown in Figure 9-8 for all the three concrete compositions discussed in Figure 9-7, for the same imposed temperature profile. The temperature profiles at the mid-section are used here, since, for the imposed temperature loading and the PCM type chosen, the mid-section temperatures during early ages lie in the phase transition region of the chosen PCM, thereby allowing for a clear understanding of the influence of the PCM. It can be observed that the temperature profiles for concrete containing fly ash or PCM are similar for the first

48 hours. In other words, the heat storage capacity of 10% of PCM (by volume) that replaces sand in concrete is equivalent to the reduction in heat generation accomplished by a replacement of 20% (mass-based) of cement by fly ash, during the initial 48 hours. Beyond this time, the rate of heat generation from cement hydration decreases significantly, consequently decreasing the effectiveness of fly ash in reducing section temperatures. This is shown in the magnified region in Figure 9-8. However, the concrete containing PCM shows a lower temperature at the mid-section, attributed to the fact that there is thermal energy storage by PCM, which increases the heat capacity of the concrete mixture. Also significant is the change in slope of the heating and cooling rates of concrete containing PCM (cool down rates, in particular), in addition to the reduced magnitude of temperature peaks, which is influential in reducing the thermal cracking risk of concrete.

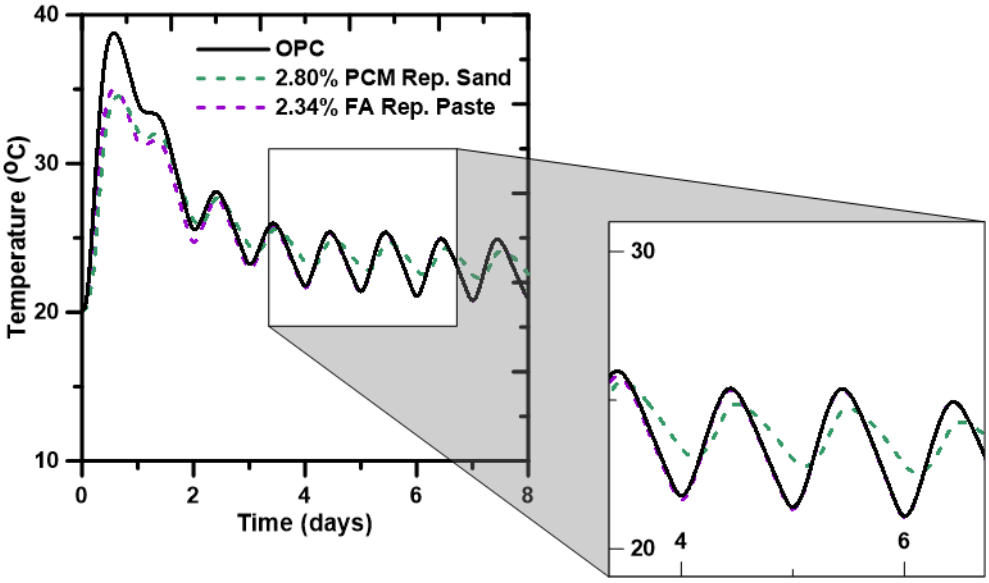

Figure 9-8 –Temperature profiles at the center of the concrete pavement, for fly ash and PCM containing mixtures

9.3.2 Early Age Stress Development

The influence of PCM incorporation on the thermal stress development in pavements is discussed in this section. The axial thermal strains are calculated using the average temperature difference between the current temperature of the pavement layer and the temperature of the layer at final set (Saetta, Scotta, and Vitaliani 1995).

$$\Delta T_{axial} = \frac{\sum_{z=0}^{h}[(T_{z,current} - T_{z,final-set})\Delta z]}{h} \quad \text{(Eq. 9-16)}$$

Here, 'h' is the total thickness of the slab, $T_{z,current}$ is the temperature of the slab at depth 'z' at the given time step, $T_{z,final\text{-}set}$ is the temperature of the slab at depth 'z' at time of final set and 'Δz' is the increment at which the temperature is calculated. The calculation for axial thermal strain (ε_{axial}) and axial thermal stress (σ_{axial}) is given as:

$$\varepsilon_{axial}(t) = \alpha_{comp}(t).\Delta T_{axial}(t) \quad \text{(Eq. 9-17)}$$

$$\sigma_{axial}(t) = E(t).\varepsilon_{axial}(t) \quad \text{(Eq. 9-18)}$$

α_{comp} is the coefficient of thermal expansion of the composite concrete (i.e., PCMs embedded into the conventional concrete), calculated using a series rule of mixtures by accounting for the coefficients of thermal expansion and volume fractions of the concrete and PCM phases in the composite concrete.

The coefficient of thermal expansion (CTE) of hardened concrete is a function of the CTE of the constituent materials in concrete. The CTE of concrete changes as the hydration progresses, and it has been found that the CTE of fresh concrete is 8-10 times that of

hardened concrete (Schöppel and Springenschmid 1995). However, the CTE attains a stable value post final-set (Hashida and Yamazaki 2002). Therefore, a constant value for CTE of concrete (α_{conc}) is used in the calculation of axial thermal strains at early ages, and is given as:

$$\alpha_{conc} = \alpha_{ca} v_{ca} + \alpha_{fa} v_{fa} + \alpha_p v_p \quad \text{(Eq. 9-19)}$$

Here, α_{ca} is the CTE of coarse aggregate (10 x 10^{-6} $^{o}C^{-1}$), α_{fa} is the CTE of fine aggregate (11 x 10^{-6} $^{o}C^{-1}$), α_p is the CTE of cement paste (10.8 x 10^{-6} $^{o}C^{-1}$) (Emanuel and Hulsey 1977), and v_{ca}, v_{fa}, v_p are the volume fractions of the corresponding concrete constituents, as obtained from the mixture proportions.

Figure 9-9 shows the axial thermal stress profiles for the plain OPC concrete, and the concrete mixtures containing 20% by volume of fly ash or 10% by volume of PCM (replacing either the cement paste or sand) at different times during the early hydration period. The axial stresses shown here are the elastic stresses, obtained as the product of the axial thermal strains and the time-dependent elastic modulus (Equation 9-15) of the hydrating concrete. It is found that there is significant reduction in the early age axial thermal stresses when fly ash (as a cement replacement material) or PCMs (as paste or sand replacement) are incorporated in the concrete. Further, it is also observed that even at low replacement levels, concrete pavements containing PCM demonstrate reduced axial tensile stresses as compared to those containing fly ash as a cement replacement material. For cases where PCM replaces cement paste or sand, the stresses are generally comparable. The significant reduction in axial tensile stresses in the pavement provides justification for the

use of PCMs in concrete even if the early age property development must be marginally compromised.

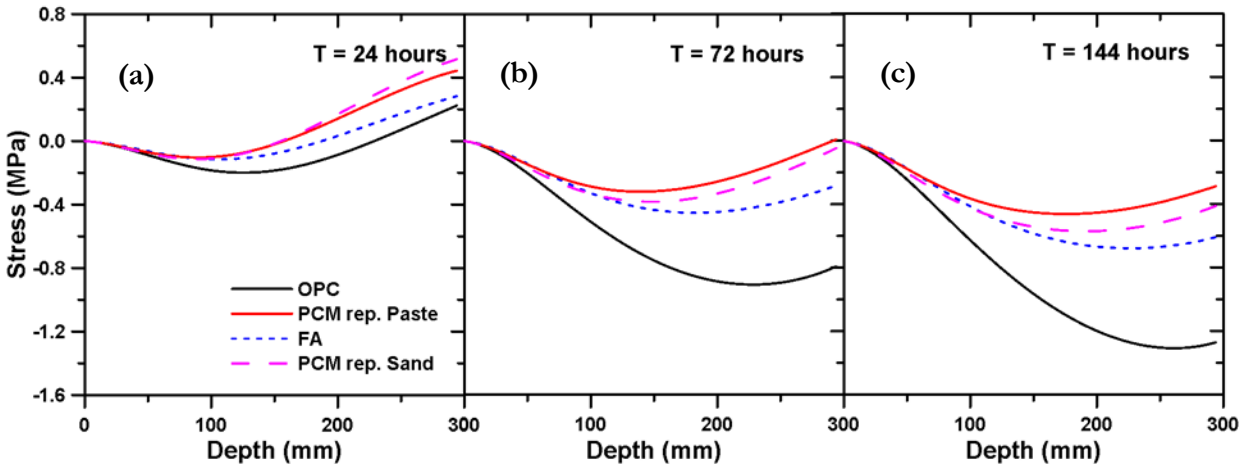

Figure 9-9 – Axial stress profiles at different times during early hydration for plain OPC concrete pavement, and those containing fly ash or PCM (as cement paste or sand replacement): (a) 1 day of hydration, (b) 3 days of hydration, and (c) 7 days of hydration.

The top surface of a pavement is exposed to a wide range of temperatures while the bottom surface is relatively insulated. The resulting temperature gradient across the cross section causes the cooler portions to contract more as compared to warmer portions that restrain the contraction, thereby resulting in curling. The curling stress calculation in this study is based on a modified form of Westergaard's equation (Westergaard 1927; Bradbury 1938). The temperature gradient for curling stress calculation (ΔT_{curl}) is given in Equation 9-20.

$$\Delta T_{curl} = (T_{top,current} - T_{bottom,current}) - (T_{top,final-set} - T_{bottom,final-set}) \quad \text{(Eq. 9-20)}$$

Here, $T_{top,current}$ and $T_{bottom,current}$ are the temperatures at the top and bottom surface of the concrete pavement respectively at the considered time. Similarly, $T_{top,final\text{-}set}$ and $T_{bottom,final\text{-}set}$ are respectively the temperatures at the top and bottom surface at the time of final set. The curling stress is calculated as:

$$\sigma_{curl} = \frac{\alpha_{comp} \cdot \Delta T_{curl} \cdot E}{2(1-\nu^2)} (C_{max} + \nu C_{min})$$

(Eq. 9-21)

Here, C_{max} and C_{min} are maximum and minimum values of Bradbury's coefficient, which is a function of the slab geometry, and calculated using the approach given in (Bradbury 1938). The restraint factor represents the level of axial restraint due to slab-base friction (Xin, Zollinger, and James 1992). The upper bound for restraint factor is 1.0 which represents a base course with infinite friction, i.e., no free movement would occur in this case. The strain would fully translate into an internal stress in this case, equal to the product of the free strain and the modulus of elasticity. Lower bound for the restraint factor is 0, which represents a frictionless base, in which case no stresses would develop. These conditions are never experienced in reality and the actual values lie somewhere in between, varying non-linearly through the thickness of the pavement. However, for simplicity in stress calculation, the restraint factor is considered to vary from a value of 1.0 at the bottom of the subbase to 0 at the top of the concrete pavement. Since the objective of this analysis is to compare the influence of PCMs on stress development, the choice of restraint factors is not very consequential.

The critical stress is calculated as the maximum tensile stress using a combination of the free strains, restraint factor, elastic modulus and the curling stresses as shown in Equation 9-22

(HIPERPAV, n.d.). The location of critical stress changes during early ages due to the combined effects of imposed temperature and cement hydration. Although, it would be in the interior of the slab, the position of critical stress along the depth of the slab varies with time as the slab curls upward or downward through the daily temperature cycles.

$$\sigma_{critical} = MAX_{tensile} \begin{cases} \varepsilon_{axial,top} \times R_F(top) \times E + \sigma_{curl,top} \\ \varepsilon_{axial,z} \times R_F(z) \times E \\ \varepsilon_{axial,bottom} \times R_F(bottom) \times E + \sigma_{curl,bottom} \\ 0 \end{cases}$$

(Eq. 9-22)

Here $R_F(z)$ represents the restraint factor at depth 'z' in the pavement.

The early age critical thermal stress development, along with the tensile strength development for the four different pavement mixtures considered earlier in Figure 9-9, are shown in Figures 9-10 and 9-11. When the pavement is placed in the month of March in Phoenix, AZ, the critical stresses never exceed the tensile strength of the mixtures during the first week of hydration (Figure 9-10). Note that the tensile strength development has been adjusted based on the composition of the mixture. When placed in the month of July, it can be observed that the critical stress in a plain OPC pavement exceeds its tensile strength at about 4 days, thereby presenting a very high risk of early age cracking (Figure 9-11). The impact of increased ambient placement temperatures on thermal stress development can also be quantified through a comparison of Figures 9-10 and 9-11. The effectiveness of PCMs or fly ash in reducing the cracking risk can be inferred from Figures 9-11(b)-(d).

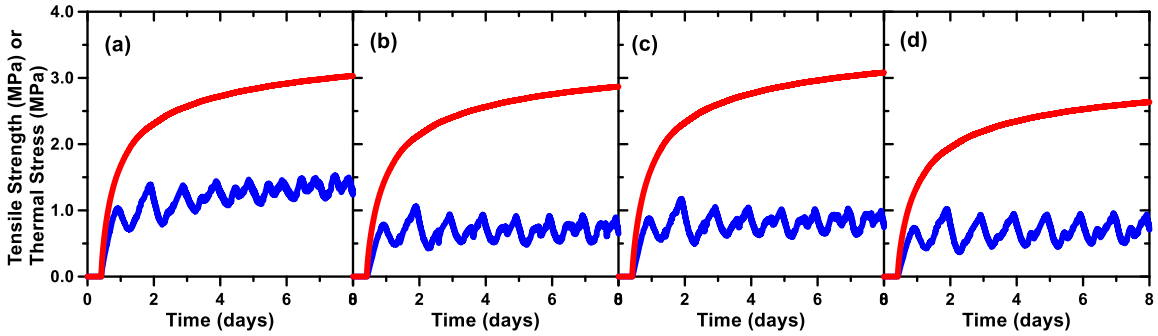

Figure 9-10 – Critical thermal stress and tensile strength development for: (a) OPC concrete, (b) concrete with 10% PCM replacing cement paste, (c) concrete with 10% PCM replacing fine aggregate, and (d) concrete with 20% fly ash replacing cement paste. The monotonically increasing curve corresponds to the strength development. The pavement is placed in Phoenix, AZ in the month of March, and the PCM has a phase transition temperature around 24°C.

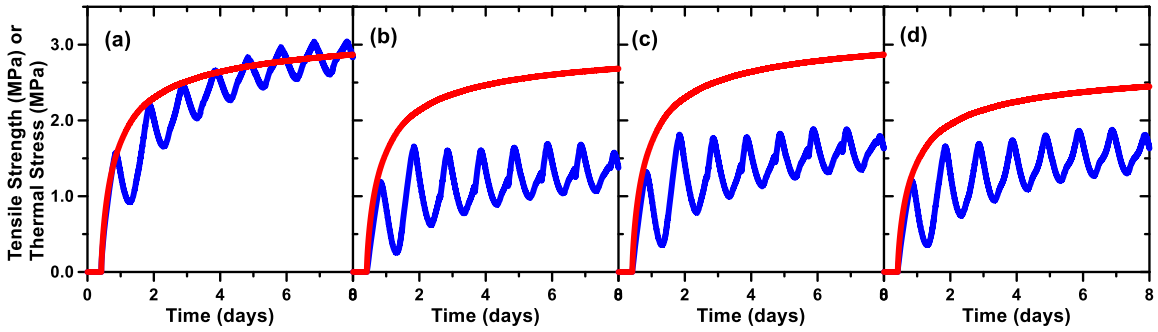

Figure 9-11 - Critical thermal stress and tensile strength development for: (a) OPC concrete, (b) concrete with 10% PCM replacing cement paste, (c) concrete with 10% PCM replacing fine aggregate, and (d) concrete with 20% fly ash replacing cement paste. The monotonically increasing curve corresponds to the strength development. The pavement is placed in Phoenix, AZ in the month of July, and the PCM has a phase transition temperature around 35°C.

9.3.3 Predicting the Likelihood of Early Age Cracking

The likelihood of thermal cracking at any time depends on the ratio of the calculated thermal stress at that time to the corresponding tensile strength of concrete. The stress-to-strength

ratio of the member depends on the ambient temperature that the member is subjected to, as well as the degree of hydration of concrete. To calculate the probability of cracking (P_c), different weights were assigned for different thermal stress-to-tensile strength ratios (S_r) as shown in Equation 9-23. The stress-to-strength ratios were determined based on Figures 9-10 and 9-11. For instance, a S_r less than 0.1 indicates a very low probability of cracking with a weighting factor of 0, whereas a S_r greater than 0.75 indicates severe cracking probability, which is assigned a weight of 1.0. Such an approach has been employed in previous studies (Riding et al. 2014).

$$P_c = \begin{cases} VERY\ LOW\ (=0.0),\ S_r \le 0.1 \\ LOW\ (=0.2),\ 0.10 < S_r \le 0.20 \\ MEDIUM\ (=0.4),\ 0.20 < S_r \le 0.30 \\ HIGH\ (=0.6),\ 0.30 < S_r \le 0.50 \\ VERY\ HIGH\ (=0.8),\ 0.50 < S_r \le 0.75 \\ SEVERE\ (=1.0),\ 0.75 < S_r \end{cases} \quad \text{(Eq. 9-23)}$$

The cracking probabilities at different times during the first 8 days of hydration ($0 < P_c \le 1$) were averaged to determine an average cracking probability for the considered concrete mixtures. Figure 9-12 shows the average cracking probabilities under the two different imposed temperature scenarios considered for Phoenix, AZ (moderate weather in March, and hot conditions in July), along with the ratios of the maximum thermal stress to the tensile strength at the corresponding age. The cracking probabilities for all the four mixture types (plain OPC concrete, concretes where fly ash replaces 10% or 20% of the cement by mass, or concretes where PCM replaces 10% or 20% of fine aggregate or cement paste by

volume) are shown in this figure. The incorporation of PCMs, either as a replacement for cement paste or fine aggregates, significantly reduces the early age cracking probability of concrete pavements, which scales with the PCM content in the concrete. For the simulation conditions and PCM types chosen, it is noticed that the use of PCMs with phase transition temperature lying within the range of the imposed temperature (see Figure 9-4) will significantly reduce the propensity of early-age cracking when used at a dosage rate of 5% by volume of the concrete (or approximately 20% by volume of sand or cement paste). The ratios of the maximum thermal stress to the corresponding tensile strength, also plotted in Figure 9-12 as symbols, provide an additional means of evaluating the efficiency of the PCMs in reducing early age thermal cracking. Cracking is certain if this ratio reaches or exceeds 1.0. This representation overcomes the averaging effects in calculating probabilities (such as the case of OPC placed in July, where the averaged P_c is only ~0.85, but cracking is certain since there are multiple occurrences where S_r is equal to or greater than 1.0 as seen in Figure 9-12).

While replacing a part of the cement paste with PCM is the most effective strategy to reduce cracking probability based on this analysis because of the added advantage of reduction in cement content (and consequently heat of hydration), partially replacing sand with PCM is likely a better strategy to ensure desirable early-age property development and mitigate any potential strength loss at later ages (Aguayo et al. 2016). However, an economic analysis favors the cement paste replacement approach.

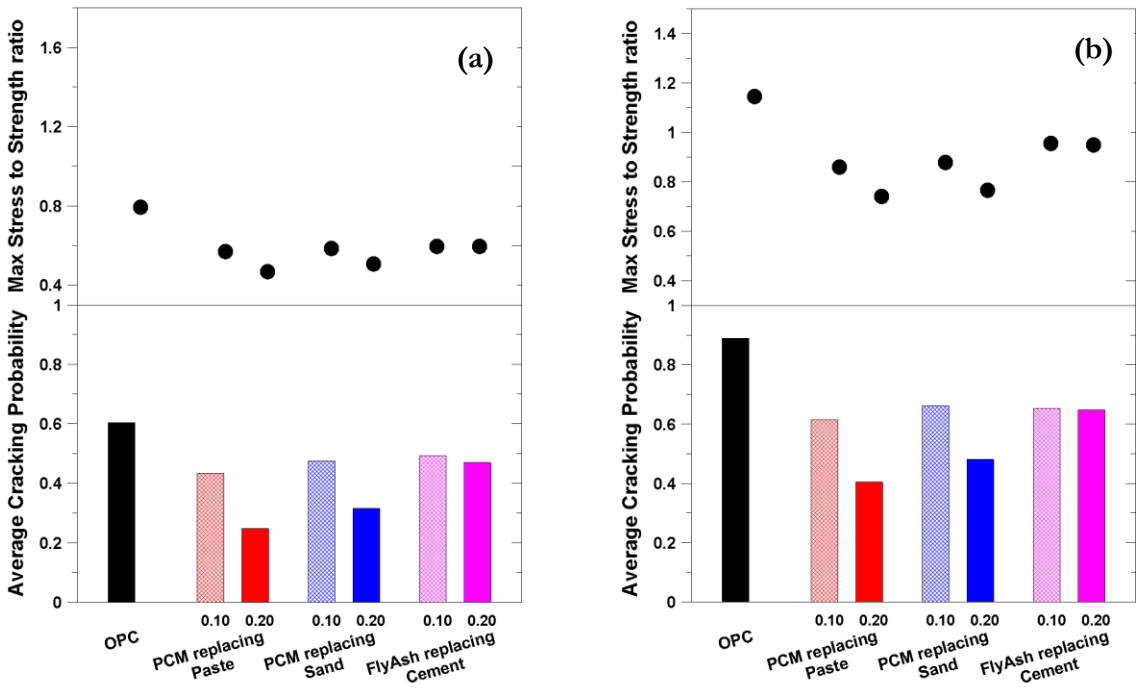

Figure 9-12 – Maximum stress-to strength ratios and cracking probabilities of pavement concrete mixtures placed in Phoenix, AZ: (a) concrete placement in March, and PCM with a phase transition temperature of 24°C is used, and (b) concrete placement in July and PCM with a phase transition temperature of 35°C is used. The X-axis is common for the top and bottom plots.

9.4. SIMULATING LONG TERM THERMAL RESPONSE

Beyond 28 days, cement hydration can be considered to have reached a steady state and the heat generation term in Equation 9-1 can be neglected. For plain OPC concrete, it can be safely assumed that the thermal conductivity and specific heat attain their ultimate values at complete hydration, i.e., at 28 days. For concrete containing PCM, the specific heat and thermal conductivity values of the composite material at later ages are determined using the same approach mentioned in Section 2.0. It has been reported that concrete gains 10-to-20% strength between 28 days and 3 years (Neville 1995). This strength development depends on

the type of cement, mixture composition, and exposure conditions. The strength development beyond 28 days is accounted for in this study by applying a time dependent multiplier, $\beta_t(t)$, to the 28-day strength $f_t(28)$ as shown in Equation 9-24 (HIPERPAV, n.d.). The multiplier $\beta_t(t)$ is expressed as shown in Equation 9-25, where 's' is a constant which is a function of the cement type (0.25 for normal and rapid hardening cements), and 't' is the time in days.

$$f_t(t) = f_t(28) * \beta(t) \quad \text{(Eq. 9-24)}$$

$$\beta(t) = \exp\{s\left[1 - \left(\frac{28}{t}\right)^{1/2}\right]\} \quad \text{(Eq. 9-25)}$$

The concrete pavement is subjected to an imposed climate data for one year (obtained from the national climate database) for a given location (here, Phoenix AZ, or San Francisco, CA with very different climate patterns) and the spatial and temporal variation in the pavement temperature is determined using the finite difference approach. The boundary conditions and initial conditions used are the same as reported in Section 2.1 for early-age response. Figure 9-13 shows a one-year temperature profile calculated for a plain OPC concrete pavement subjected to thermal loading in Phoenix, AZ, during the time period Jan 1 2010 – Dec 31 2010.

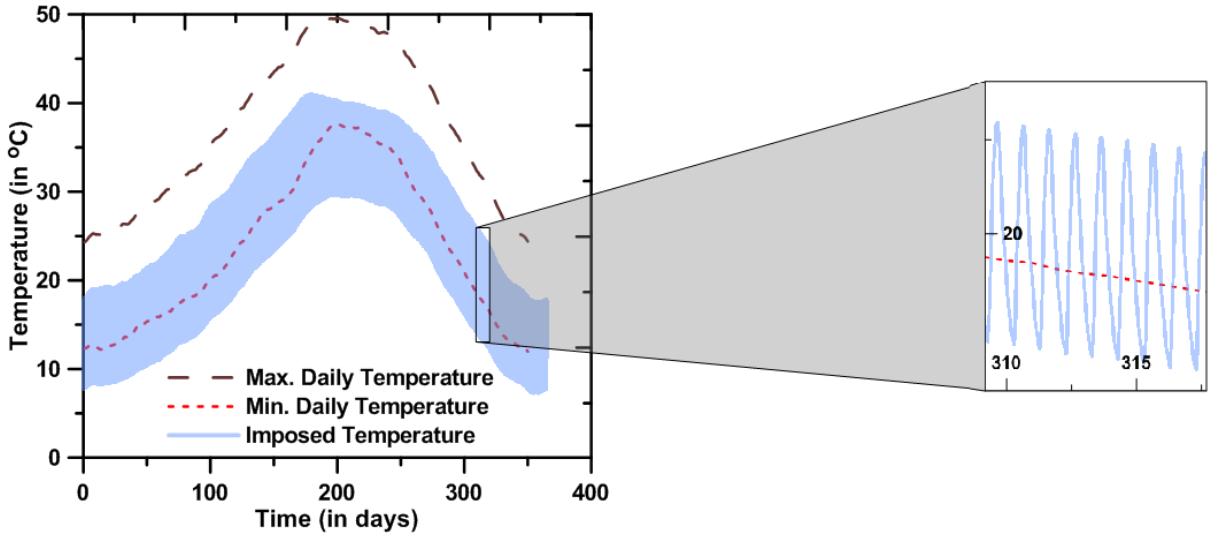

Figure 9-13 – Maximum and minimum temperatures in a plain OPC concrete pavement in Phoenix, AZ for a thermal loading duration of one year (Jan 1 2010 to Dec 31 2010). The magnified plot shows the actual variation in the imposed daily temperature.

The daily variation of external temperature is sinusoidal in nature, and that coupled with the overall seasonal variation during the year causes the imposed annual temperature to appear as a band as shown in Figure 9-13. A magnified view of a small time period is also shown to demonstrate the actual daily temperature variation. The seasonal variation over a period of several years will also follow this pattern. It is noted that the calculated maximum daily temperature in the concrete pavement is usually about 5°C-to-10°C higher than the maximum imposed daily temperature, as has been reported in other studies also (Ge 2005; A. K. Schindler et al. 2004). Since the incorporation of fly ash in the concrete mixture has minimal influence on the thermal response of the pavement at later ages, as demonstrated in Figure 9-8, only a plain OPC concrete and concrete in which PCM replaces cement paste (for a total volume fraction of 5% in concrete) are the only compositions considered for

later age thermal analysis. Concrete where PCM replaces fine aggregate also would behave similar in later age modeling to the one where cement paste is replaced, provided the volume fractions of the PCM are the same. Hence only the former is used in this section for detailed analysis.

9.4.1 Annual Concrete Temperature Profiles

Figures 9-14 and 9-15 show the comparison between temperature profiles at different depths for an OPC concrete pavement and one containing 5% of PCM by volume. For both cases, the pavement is subjected to the same externally imposed temperature as shown in Figure 9-13. In Figure 9-14, 5% of the overall volume of concrete contains a PCM with a phase change temperature of 24°C whereas in Figure 9-15, the results are for the pavement containing PCM with a phase change temperature of 35°C. The height of the temperature profiles at different depths in the pavement is indicative of the temperature range that the pavement is subjected to, at that particular depth. The temperature differential (difference between maximum and minimum) decreases with increasing depth, which is attributed to the constant boundary condition at the bottom of the pavement. It is noted from Figure 9-14 that the PCM with a phase change temperature of 24°C reduces the amplitude of the daily temperature variation within the concrete pavement over a certain range of temperatures that lie in the latent heat storage/release range of the PCM, particularly between 15°C and 27°C. This is the active temperature range for the 24°C PCM, as can be identified from the DSC plot shown in Figure 9-1(a). When used in Phoenix, AZ, this PCM is particularly effective from November through April (when the ambient and concrete temperature is in this range), as can be observed from Figure 9-14. Similarly, it is noted from Figure 9-15 that

the 35°C PCM is active in the temperature range of 30°C to 44°C. This renders this PCM highly efficient in reducing the concrete pavement temperature and gradient in the hot summer months of May through September in Phoenix, AZ. The simulations shown here establish the influence of PCMs in reducing the peak temperature and temperature differentials in concrete pavements, thereby facilitating an increase in thermal fatigue life.

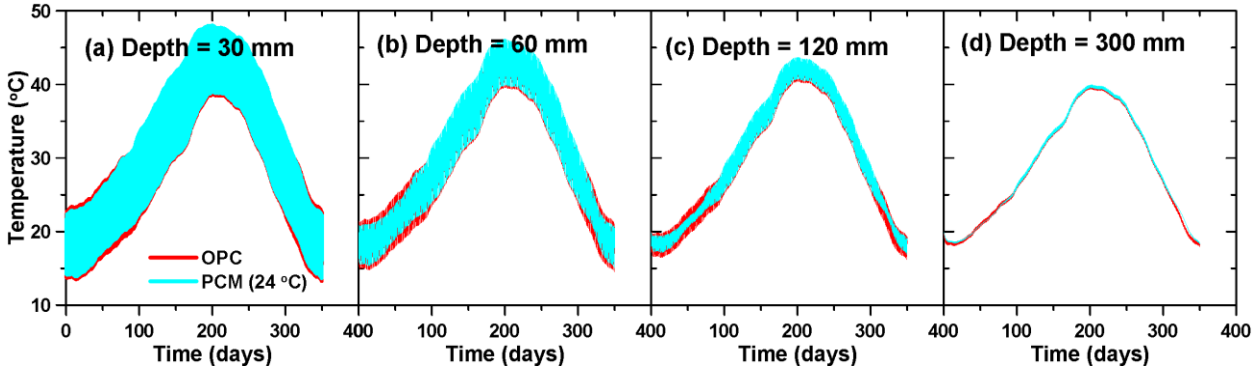

Figure 9-14 - Comparison of temperature profiles over a year (Jan 1 2010 to Dec 31 2010) for plain OPC and 24°C PCM-incorporated concrete pavements located in Phoenix, Arizona.

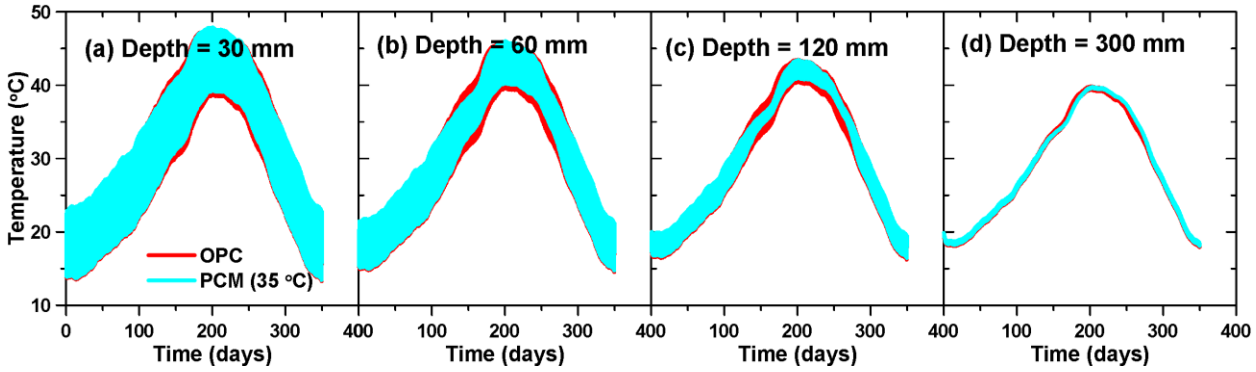

Figure 9-15 - Comparison of temperature profiles over a year (Jan 1 2010 to Dec 31 2010) for plain OPC and 35°C PCM-incorporated concrete pavements located in Phoenix, Arizona.

The temperature profiles shown in Figures 9-14 and 9-15 provide a strong case for using a combination of both the 24°C and 35°C PCMs in the same concrete mixture when placed in Phoenix, AZ. This choice, indeed, depends on the climatic conditions of the region in which the PCMs are used. Since both PCMs have different latent heat transition phases, incorporating both in the concrete mixture would ensure reduced temperature differentials for most part of the year for a concrete pavement in Phoenix. Simulations were carried out on concrete mixtures containing 2.5% by volume of each of these PCMs, adding to a total of 5% of PCM by volume of concrete. Figure 9-16 shows the temperature profiles of plain OPC concrete and the hybrid PCM concrete mixture. Beneficial temperature differential reduction is observed for most part of the year.

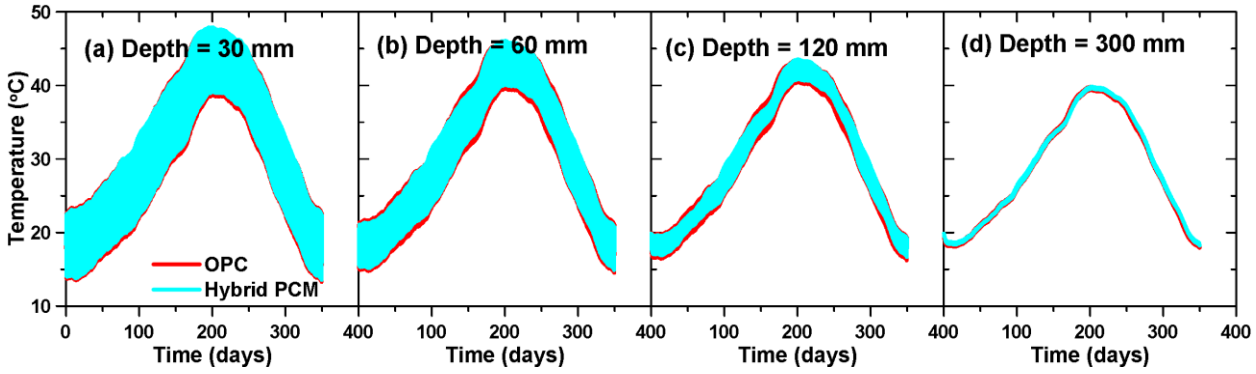

Figure 9-16 - Comparison of temperature profiles over a year (Jan 1 2010 to Dec 31 2010) for plain OPC and hybrid (24°C and 35°C) PCM-incorporated concrete pavements located in Phoenix, Arizona.

Since thermal stresses are strongly related to the temperature gradient in the concrete members, a reduced temperature profile would certainly give rise to lower stresses, thereby

increasing the life of the pavement. The maximum temperature differential at any location along the depth of the pavement is calculated as the difference between the maximum and the minimum temperatures at that particular depth during a given 24-hour cycle. Figure 9-17 shows a comparison of the daily maximum temperature differentials experienced at different depths along the pavement for the plain OPC concrete and the one containing 5% by volume of either the 24°C or the 35°C PCM. The figure is a result of simulations carried out for a year corresponding to the imposed temperatures in Phoenix, AZ, and San Francisco, CA. Of particular note is the fact that, for San Francisco, the use of a 35°C PCM is not beneficial at all since the ambient temperature hardly gets to that level. The 24°C PCM is capable of providing year round reductions in temperature differentials for San Francisco as can be noticed from Figure 9-17. Regarding Phoenix, each of the PCMs are effective during certain times of the year, as discussed earlier. Simulations such as this can be implemented for local climates, providing the possibility to use individual or hybrid PCMs in order to gain maximum benefit towards thermal fatigue life cycle enhancement of concrete pavements.

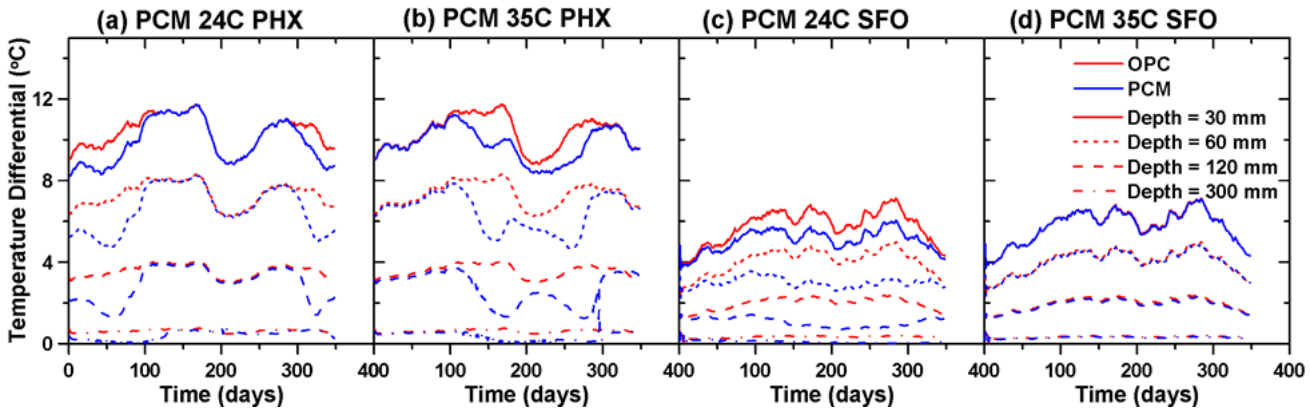

Figure 9-17 – Maximum daily temperature differentials at different depths for plain OPC concrete and concrete containing 5% of PCM by volume. The simulations were carried out for a year (Jan 1 2010 to Dec 31 2010).

9.4.2 Annual Stress Profiles

The temperature gradient between the top and bottom of the pavement causes it to curl upwards or downwards. For rigid pavements, curling stresses due to thermal gradients are a major concern since they are significantly higher compared to the axial thermal stresses (Belshe et al. 2011; Tutumluer, Al-Qadi, and others 2009). Therefore, the axial thermal stresses are neglected here for simplicity. The external restraint on the pavement due to the base friction causes temperature-induced tensile stresses, which may lead to cracking of the pavement. While Westergaard's theory (Westergaard 1927) considers curling stress in the pavement as a function of the temperature of the top and bottom surface, it has been shown that the shape of the temperature profile is also important in dictating the internal stresses. Since the temperature profile is a non-linear function of the depth, the temperature gradient is calculated using the approach suggested in (Mohamed and Hansen 1997). The equivalent temperature gradient, ΔT_{eq} is defined as:

$$\Delta T_{eq} = -\frac{12M^*}{\alpha_{comp} h^2}$$

(Eq. 9-26)

$$M^* = \int_{-h/2}^{h/2} \varepsilon(z).\, z.\, dz$$

Here , where h is the depth of the pavement, and ε(z) is the strain at distance z from the center of the pavement. α_{comp} is the coefficient of thermal expansion of

the concrete. The calculated equivalent temperature gradient is then used in Equation 9-21 to calculate the curling stresses in the pavement. Figure 9-18 shows the comparison of curling stresses experienced by a plain OPC concrete pavement and one containing 5% PCM by volume, for a one-year exposure in Phoenix, AZ. Since the objective here is to compare curling stresses for a concrete pavement with and without PCM inclusions, only thermal loading on the pavement was considered (i.e., no traffic loading was considered). It is assumed here, for the sake of comparison, that the stresses caused by thermally induced curling strains and traffic loading are independent. It is observed from Figure 9-18 that the inclusion of PCM causes the curling stresses in the pavement to reduce. It is also noted that both the PCMs are effective at different times of the year depending on the internal temperature profile of the pavement, as expected. It should also be noted that a part of the reduction in the stresses in the PCM-incorporated concrete is also due to a slight reduction in the stiffness of the pavement. In both these cases, the tensile stresses due to curling alone are not sufficient to cause fatigue cracking, however, they are likely to be significant when considered along with the traffic loading.

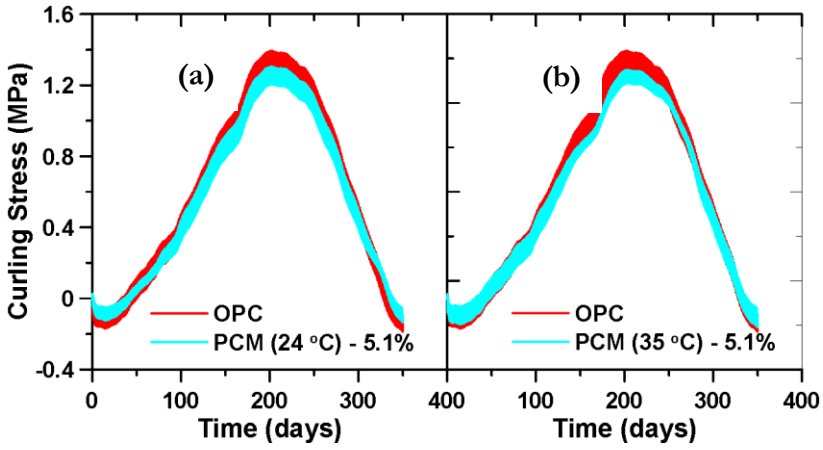

Figure 9-18 – Curling stresses in a plain OPC concrete pavement and one containing 5% PCM, in Phoenix, Arizona: (a) 24°C PCM, and (b) 35°C PCM.

9.5. CONCLUSIONS

A detailed numerical simulation approach to quantify the early- and later-age benefits of using PCMs in concrete pavements was outlined in this chapter. Concrete pavement mixtures containing microencapsulated PCMs (of phase change temperatures in the vicinity of 24°C and 35°C) replacing either a fraction of the cement paste or fine aggregate (1.25% to 5.5% of the total volume of concrete) were simulated under exposure conditions corresponding to Phoenix, AZ or San Francisco, CA. The temporal change of temperature inside the pavement under imposed environmental loading was calculated by solving the second-order heat diffusion equation. The temperature profiles along the pavement depth, and the corresponding stress development were extracted based on the data obtained from the model and are used to quantify the efficiency of PCMs in mitigating thermal cracking risks in concrete. Well-reported time-dependent models were used for concrete property development. Significant reductions in early-age hydration heat release were observed when PCMs were incorporated in the pavement concretes, either as replacement for the cement paste or fine aggregates. The simulations predicted a 6°C-to-10°C reduction in peak temperature when the concrete contained approximately 5% by volume of PCM, either as a replacement of fine aggregates or of the cement paste. The cement dilution effect when PCM replaces cement paste is supplemented by the latent heat storage of the PCM, which resulted in enhanced peak temperature reductions. The PCMs were also found to influence

the slopes of the heating and cooling rates, which enhances their efficiency in mitigating the risk of thermal cracking. The axial and curling strains due to the temperature gradients were calculated and combined with a restraint factor, to determine the critical stress in the pavement slab during hydration. The early-age critical stress development, along with the tensile strength development was used to determine the probability of cracking. Using the specific examples of concrete placement in the months of March and July in Phoenix, AZ, the influence of PCMs of appropriate phase transition temperatures in significantly reducing the cracking probabilities were elucidated.

The numerical model was also used to predict the pavement temperatures and curling stresses for a longer duration, well after the major effects of cement hydration had subsided. The ambient annual temperature history for Phoenix, AZ resulted in a combination of PCMs with phase transition temperatures of 24°C and 35°C being more effective for year-round reduction in pavement temperatures whereas for San Francisco, CA, only the 24°C PCM was needed. The reduction in pavement temperature reduces cracking probability and improves the durability of concrete pavements. The simulations reported in this chapter, when implemented for local climates, help engineers and designers choose the appropriate type and quantity of PCMs (individual or hybrid) in order to gain maximum benefits towards thermal fatigue life cycle enhancement of concrete pavements.

CHAPTER 10

MATRICES - A SOFTWARE PACKAGE FOR ANALYSIS AND MODELING OF THERMAL STRESSES IN CONCRETE STRUCTURES

10.1. Overview

MATRICEs (Modeling and Analysis of Thermal stResses In ConcrEtes) version 1.0 is a software package designed to model and analyze heat flow in concrete members subjected to climatic conditions in the form of solar radiation, cloud cover, wind currents and relative humidity. The software is a one-dimensional numerical heat flow solver which is equipped to consider the internal heat generated in a newly cast concrete member because of the hydration process, in addition to the analysis of a mature concrete member which has already achieved a certain level of hydration. Version 1.0 of MATRICEs is suitable to analyze two different types of concrete member geometries – Pavements and Bridge Decks. The model considers the basic material properties and mixture proportions in concrete and couples them with the weather conditions to solve for the internal temperature and stress profile of the concrete member. The software is particularly useful owing to its capability to simulate the temperature and stress profile of a concrete member containing thermal energy storage materials or phase change materials (PCMs).

The heat released during the hydration of cement at early-ages is well understood to be a reason for early-age cracking of restrained concrete elements such as pavements and bridge-decks, while diurnal changes in temperature can cause thermal fatigue and associated cracking in mature concrete at later ages. Previous studies have shown that the use of microencapsulated PCMs in concrete effectively reduces the adverse effects of heat of

hydration by reducing the peak temperature rise and the rate of heat evolution/release during cement hydration (Fernandes et al. 2014; Arora, Sant, and Neithalath 2017). It has also been shown that small volume fractions (in the range of 5-to-10% by volume of concrete) of such PCMs can be well dispersed in concrete with little influence on the resulting mechanical properties (Aguayo et al. 2016).

10.2. Model Description

MATRICEs version 1.0 evaluates the temperature development in a concrete member subjected to external variations in climatic conditions using the second-order heat-diffusion equation (Reynolds and Perkins 1977; Springenschmid 1994) given as:

$$\nabla.(k\nabla T) + \dot{q} = \rho c_p \frac{\partial T}{\partial t} \qquad \text{(Eq. 10-1)}$$

Here k is the thermal conductivity of the concrete ($W.m^{-1}K^{-1}$), T(x,y,z) is the scalar temperature field (K), q` corresponds to the heat generated from the cement hydration reactions (W), ϱ is the density of concrete ($kg.m^{-3}$), c_p is the specific heat capacity of concrete ($J.kg^{-1}K^{-1}$), and t is the time (s). For hydrating cementitious systems (i.e., at early ages), the thermal conductivity and specific heat capacity are dependent on the degree of hydration.

10.2.1 Boundary Conditions Implementation

The temperature development in concrete is calculated as a function of time and depth by numerically solving equation 10-1. The temperature profile is used to calculate the evolution of thermal stresses in concrete with time. The coefficient of thermal expansion (CTE) of hardened concrete is a function of the CTE of the constituent materials in concrete. The

CTE of concrete changes as the hydration progresses, and it has been found that the CTE of fresh concrete is 8-10 times that of hardened concrete (Schöppel and Springenschmid 1995). However, the CTE attains a stable value post final-set (Hashida and Yamazaki 2002). Therefore, a constant value for CTE of concrete (α_{conc}) is used in the calculation of axial thermal strains at early ages. The development of mechanical properties of concrete in tension and compression is modeled using the concrete maturity model (Springenschmid 1994). The simulated thermal stress profile is compared with the modeled strength development of concrete to determine the likelihood of early age cracking in the concrete member.

10.3. MATRICEs Implementation

10.3.1 Software Architecture

MATRICEs version 1.0 has been built as a standalone Java desktop application in Java 8.0.45. It is a one-dimensional explicit numerical heat flow solver which evaluates the spatio-temporal temperature profile in a concrete member. MATRICEs has a six-step framework with which it takes the user input regarding the materials, mix design and property development models/parameters. The framework is shown in Figure 10-1.

Figure 10-1 – Six-step software architecture framework

10.3.2 Member Geometry

Version 1.0 of MATRICEs is equipped to handle two concrete geometries – Bridge deck and Pavement. Both the geometries have distinct boundary conditions that will be described later. For either type of concrete member, user input is required for the dimensions of the member. In case of a concrete bridge deck, the dimensions required are the length, width and depth of the bridge deck. For a concrete pavement, dimensions required are length, width and depth of the concrete section, as well as the depth of the subgrade below the concrete pavement. The two geometries are shown in Figure 10-2.

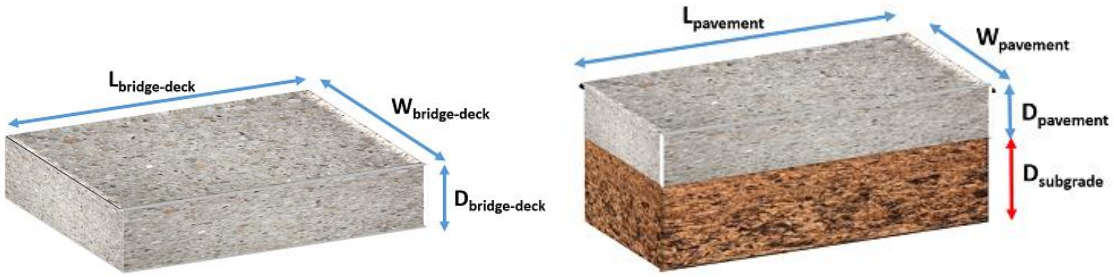

Figure 10-2 – Member geometries available in MATRICEs version 1.0 (a) Bridge Deck (b) Pavement

The finite difference analysis is carried out spatially along the depth of the member, so the number of finite elements required depends on the depth of the member. The top surface of the concrete member is taken as the reference (z = 0) for the numerical model. The length and width of the pavement are used to evaluate the moment of inertia and the radius of relative stiffness for the member. These quantities are used to capture the influence of curling of the concrete member due to the presence of a temperature gradient between the top and bottom surface.

10.3.3 Environmental Conditions

Temperature, wind speed, cloud cover and relative humidity are imported from a climate database as inputs for the climate model in MATRICEs. Hourly values of these parameters are obtained and linearly interpolated as necessary depending on the time step of the solver. These conditions control the top and bottom boundary conditions for the concrete member. Figure 10-3 shows the software user interface to obtain these inputs.

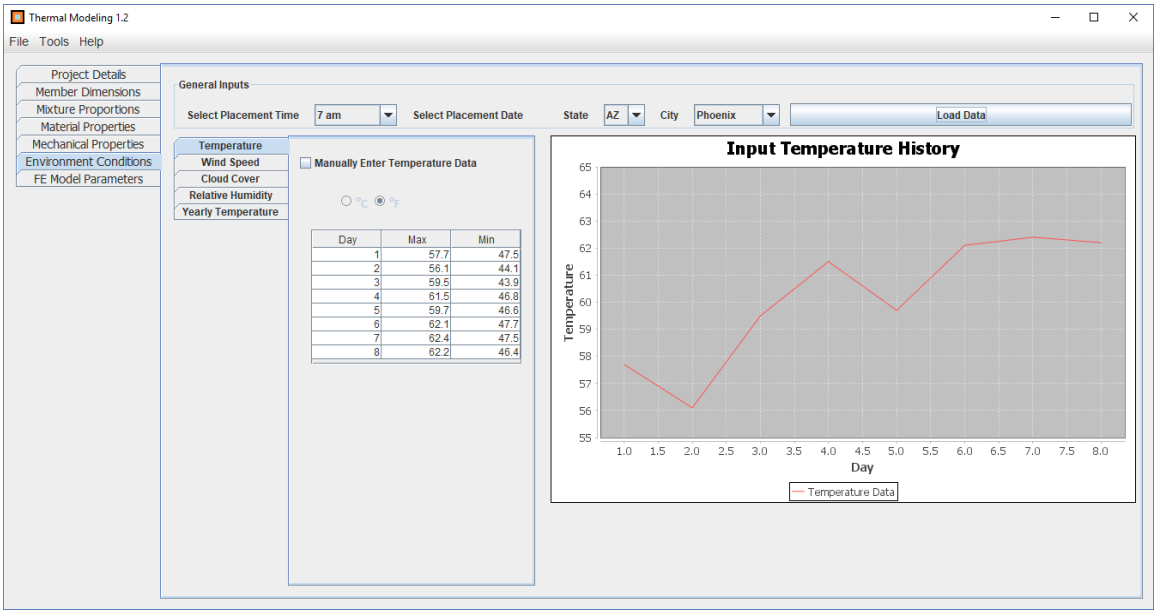

Figure 10-3 – Screenshot of MATRICEs v1.0 showing the environmental conditions step

Figure 10-4 shows the schematic models of concrete members defined in MATRICEs v1.0 highlighting the different processes that govern the boundary conditions.

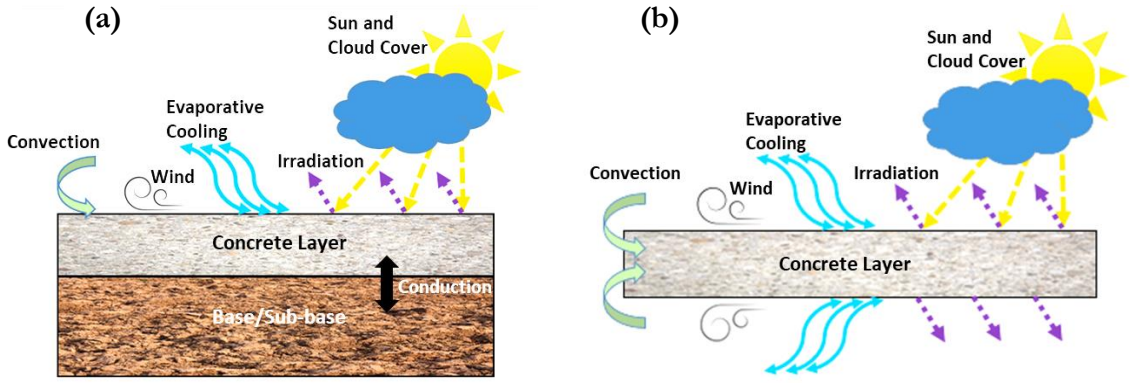

Figure 10-4 - Schematic model of (a) concrete pavement and (b) concrete bridge deck subjected to climatic factors

The incident solar energy on the member is a function of the percent cloud cover (Equation 10-2). Here, β_s is the solar absorptivity and q_s (W/m^2) is the instantaneous incident solar radiation and CC is the percent cloud cover.

$$q_{solar} = -\beta_s q_s \times (1 - CC/100) \quad \text{(Eq. 10-2)}$$

The irradiation because of the difference in the surface temperature of the concrete member and the ambient temperature is given by Equation 10-3. Here, ε is the surface emissivity of concrete, σ is the Stefan-Boltzmann constant, $T_0(t)$ is the ambient temperature at time 't' and T(0,t) represents the concrete surface temperature at any time 't'.

$$q_{irradiation} = \varepsilon\sigma(T_0(t)^4 - T(0,t)^4) \quad \text{(Eq. 10-3)}$$

The convective heat transfer is given by Equation 10-4. Here, h_0 is the surface convection coefficient, which is a function of the wind speed ('w' m/s) and the concrete curing method adopted in the field given by the empirical relationship (Riding et al. 2007) in Equation 10-5.

$$q_{convection} = h_0(T(0,t) - T_0(t)^4) \quad \text{(Eq. 10-4)}$$

$$h_0 = -0.0022 * w^2 + 0.6522 * w + 1.9521 \quad \text{(Eq. 10-5)}$$

The boundary condition of the top and bottom surface is given by Equation 10-6 and 10-7 respectively. Here k_{comp} is the thermal conductivity (W/m/K) of the concrete member.

$$\text{Top Surface}: \; -k_{comp}\frac{\partial T(0,t)}{\partial x} = q_{solar} + q_{irradiation} + q_{convection} \quad \text{(Eq. 10-6)}$$

$$\text{Bottom Surface}: \; -k_{comp}\frac{\partial T(D_{bridge-deck},t)}{\partial x} = q_{irradiation} + q_{convection} \quad \text{(Eq.10-7)}$$

For modeling a concrete member such as a concrete pavement, the annual average temperature of the climatic region is used to define the constant ground temperature of the soil. A similar assumption would be valid for modeling a concrete foundation as well. The temperature profile at time (t=0) is the initial condition required to solve the heat equation. This is considered as the ambient temperature at the time of the start of analysis for any concrete member. While this is perfectly appropriate for a freshly cast concrete member, it needs some time (3-4 days) to equilibrate for analysis of a concrete member at later ages.

10.3.4 Mixture Proportions and Material Properties

The chemical and physical properties of the concrete member are evaluated based on the properties of its constituents – cement paste and aggregate. Figure 10-5 shows the software user interface to obtain inputs for the concrete mix design.

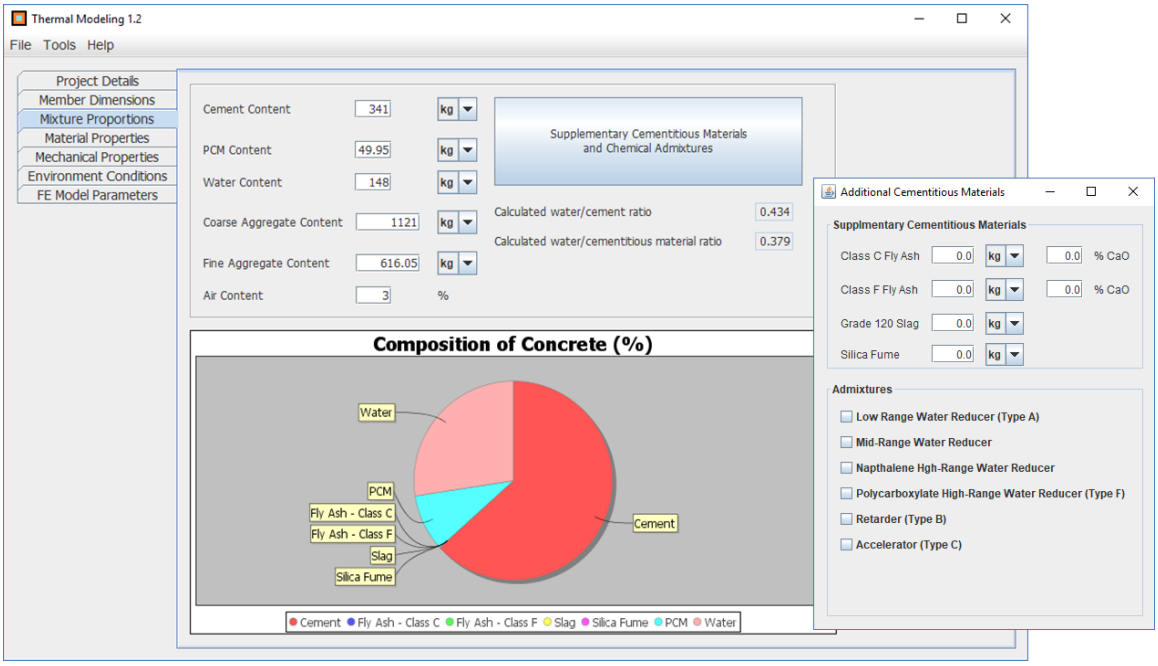

Figure 10-5 – Screenshot of MATRICEs v1.0 showing the mixture proportions step

Supplementary cementitious materials and admixtures used, if any, may be specified as well. The software then calculates and displays the water to cement ratio and the water to binder ratio. A pie-chart description of cementitious components is also provided to provide visual aid and enhance user experience.

For a fresh concrete member, the time dependent parameters - internal heat generated as a result of the hydration of cement paste, activation energy and the degree of hydration are calculated as a function of the constituents using empirical relationships established in (Anton K. Schindler 2004; Anton K. Schindler and Folliard 2005; Pane and Hansen 2002; Anton K. Schindler and Folliard 2003). Figure 10-6 shows the software user interface to obtain inputs for material properties of cement and SCMs.

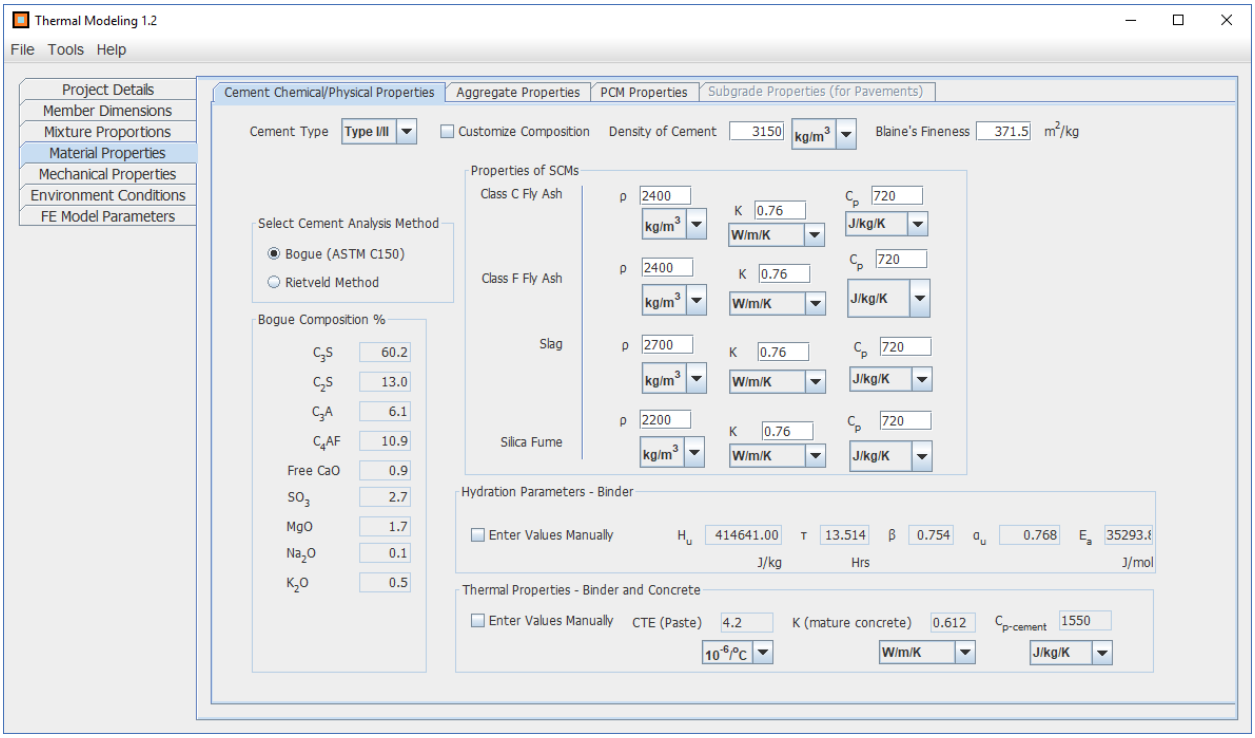

Figure 10-6 – Screenshot of MATRICEs v1.0 showing the material properties step for cement and SCMs

Equation 10-8 shows the calculation of the heat of hydration H_{cem} (J/kg). All quantities in the RHS of Equation 10-8 are the volume fractions of constituents in cement powder obtained from the Bogue formulation.

$$H_{cem} = 500C_3S + 260C_2S + 866C_3A + 420C_4AF + 624SO_3 + 1186Ca_{free} + 850MgO$$

(Eq. 10-8)

In the presence of supplementary cementitious materials such as Fly Ash, Slag, Silica Fume, the ultimate heat of hydration H_u (Anton K. Schindler and Folliard 2003) is calculated using Equation 10-9. The volume fractions of cement, slag, fly ash class F, fly ash class C and silica fume are given by v_{cem}, v_{slag}, v_{FFA}, v_{CFA} and v_{SF} respectively. $v_{FFA-CaO}$ and $v_{CFA-CaO}$ are the volume fractions corresponding to calcium oxide in class F and class C fly ash respectively.

$$H_u = H_{cem} * v_{cem} + 550v_{slag} + 1800v_{FFA}v_{FFA-CaO} + 1800v_{CFA}v_{CFA-CaO} + 330v_{SF}$$

(Eq. 10-9)

The degree of hydration is calculated as a function of time and temperature using equation 10-10 (Pane and Hansen 2002). $\alpha(t_e)$ is the degree of hydration at equivalent age t_e, α_u is the ultimate degree of hydration, τ is the hydration time parameter (hours), and β is the slope parameter. These parameters may be determined using calorimetric techniques by fitting the experimental degree of hydration to equation 10-10.

$$\alpha(t_e) = \alpha_u * \exp\left(-\left(\frac{\tau}{t_e}\right)^{\beta}\right)$$

(Eq. 10-10)

Alternatively, the hydration parameters may be calculated as a function of the mix composition using equations 10-11 to 10-13. All quantities on the RHS in equations 10-11 to 10-13 are volume fractions. The effect of admixtures has also been considered and the subscripts ACCL, LRWR, MRWR, CHRWR, NHRWR refer to accelerator, low range water reducer, mid-range water reducer, polycarboxylate high range water reducer and naphthalene high range water reducer respectively. 'wc' is the effective water to binder ratio of the mixture.

$$\tau = \exp(1.266 - 0.757C_3S * v_{cem} + 98.8Na_2O_{eq} * v_{cem} + 1.44v_{slag} + 4.12v_{FFA}v_{FFA-CaO} + 4.12v_{CFA}v_{CFA-CaO} - 11.4v_{ACCL})$$

(Eq. 10-11)

$$\beta = \exp(-0.4636 + 3.41C_3A * v_{cem} - 0.8463v_{slag} + 33.8v_{LRWR} + 15.7v_{MRWR} + 38.3v_{CHRWR} + 8.97v_{NHRWR})$$

(Eq. 10-12)

$$\alpha_u = 1.031wc/(0.194 + wc) + \exp(-0.0885 - 13.7C_4AF * v_{cem} - 283Na_2O * v_{cem} - 9.90v_{FFA}v_{FFA-CaO} - 9.90v_{FFA}v_{FFA-CaO} - 95.4v_{PCHRWR})$$

(Eq. 10-13)

The equivalent age t_e in equation 10-10 considers the effect of temperature on the degree of hydration. A higher temperature would shift the degree of hydration plot to the left and vice versa. Equation 10-14 defines the equivalent age (t_e) of concrete in terms of the activation energy (E_a), the reference temperature (298 K) and concrete temperature 'T'.

$$t_e(T) = \int_0^t \exp\left(\frac{E_a}{R}.\left(\frac{1}{T_r} - \frac{1}{T}\right)\right)dt$$

(Eq. 10-14)

The activation energy E_a in the equation 10-14 is calculated using the empirical relationship given in equation 10-15.

$$E_a = 41230 + 832700 * (C_3A + C_4AF) * v_{CEM} * SO_3 * v_{cem} - 347000Na_2O_{eq} - 19.8Blaine + 29634v_{FFA}v_{FFA-CaO} + 29634v_{CFA}v_{CFA-CaO} + 16200v_{slag} - 51600v_{SF} - 344613v_{ACCL}$$

(Eq. 10-15)

After calculation of all these parameters, the time dependent heat generated during cement hydration is given by Equation 10-16.

$$q'(t_e) = H_u * C_c * \alpha(t_e) * \frac{\beta}{t_e} * \left(\frac{\tau}{t_e}\right)^{\beta} * \exp\left(\frac{E_a}{R}.\left(\frac{1}{T_r} - \frac{1}{T}\right)\right)$$ (Eq. 10-16)

For a Type I/II OPC concrete H_u, E_a, α_u, τ and β were calculated as 460 kJ.kg^{-1}, 36.2 kJ.mol^{-1}, 0.78, 12.9 hours, and 0.77 respectively. In addition to the hydration parameters, thermal properties of concrete significantly affect the heat transfer. The effective thermal conductivity (k_c) and specific heat capacity (c_{p-c}) of the concrete member are key inputs to the governing heat transfer equation within concrete and depend on the degree of hydration (α) of concrete (Equation 10-17 and 10-18) (Reinhardt, Blaauwendraad, and Jongedijk 1982). k_{uc} is the ultimate thermal conductivity of concrete at maximum hydration (α_u) (taken as 0.612 W.m^{-1}K^{-1}) and c_{p-uc} is the ultimate heat capacity of concrete (910 J.kg^{-1}K^{-1}). The values for k_{uc} and c_{p-uc} are modified in the presence of SCMs and admixtures and may be determined using ASTM C1470 ("Standard Guide for Testing the Thermal Properties of Advanced Ceramics" 2013).

$$k_c(t,T) = k_{uc} * (2 - \alpha(t,T))$$ (Eq. 10-17)

$$c_{p-c}(t,T) = c_{p-uc} * (1.25 - 0.25 * \alpha(t,T)) \quad \text{(Eq. 10-18)}$$

In the presence of PCMs in concrete, the thermal conductivity and specific heat capacity depend significantly on the concrete temperature. The above equations are then modified to include the volume fraction of concrete (v_{conc}) and PCM (v_{pcm}).

$$k_c(t,T) = k_{uc} * (2 - \alpha(t,T)) * v_{conc} + k_{pcm}(T) * v_{pcm} \quad \text{(Eq. 10-19)}$$

$$c_{p-c}(t,T) = c_{p-uc} * \left(1.25 - 0.25 * \alpha(t,T)\right) + c_{p,pcm}(T) * v_{pcm} \quad \text{(Eq. 10-20)}$$

Figure 10-7 shows the software user interface to obtain inputs for the properties of PCMs. The specific heat capacity and thermal conductivity of PCM may be specified either as a step function or in the form of a continuous plot. Both quantities are plotted as a xy-line plot in the same window as user input is received.

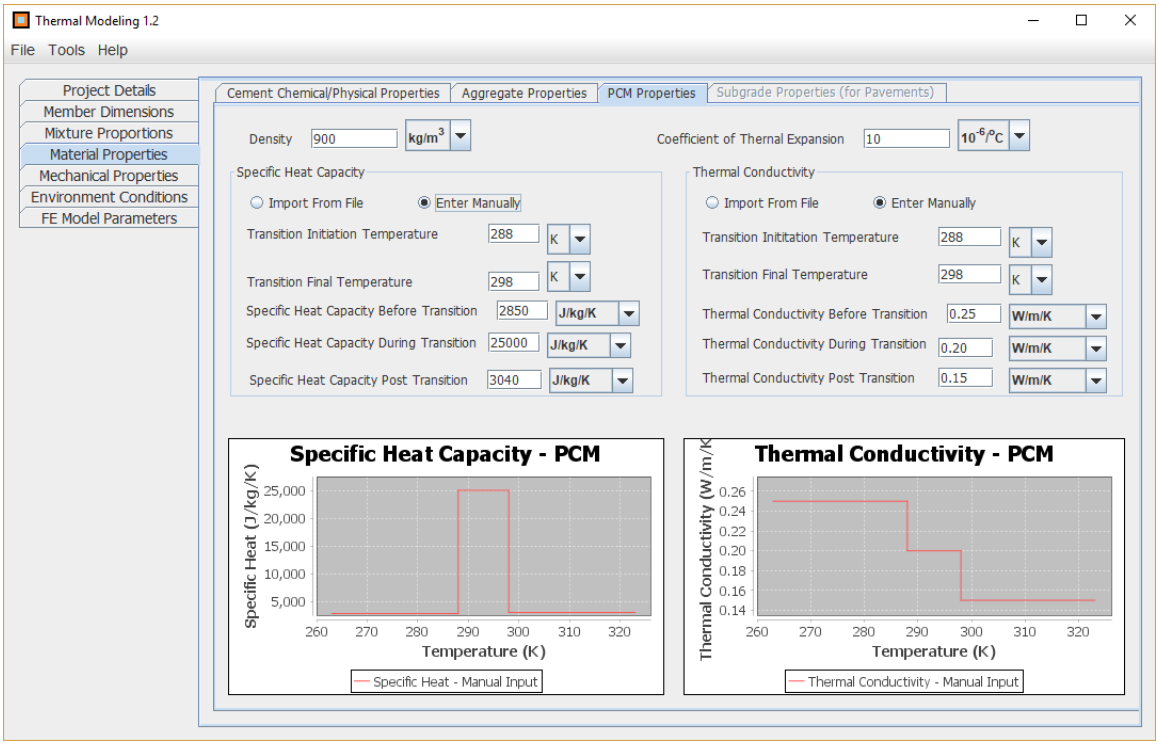

Figure 10-7 – Screenshot of MATRICEs v1.0 showing the material properties step for PCM

The coefficient of thermal expansion of concrete is used in post-processing to calculate the thermal stresses from the measured thermal strains and is calculated using Equation 10-21.

$$\alpha_{conc} = \alpha_{ca} v_{ca} + \alpha_{fa} v_{fa} + \alpha_{p} v_{p} + \alpha_{pcm} v_{pcm} \quad \text{(Eq. 10-21)}$$

Figure 10-8 shows the software user interface to obtain inputs for the properties of coarse and fine aggregates in the concrete mix design.

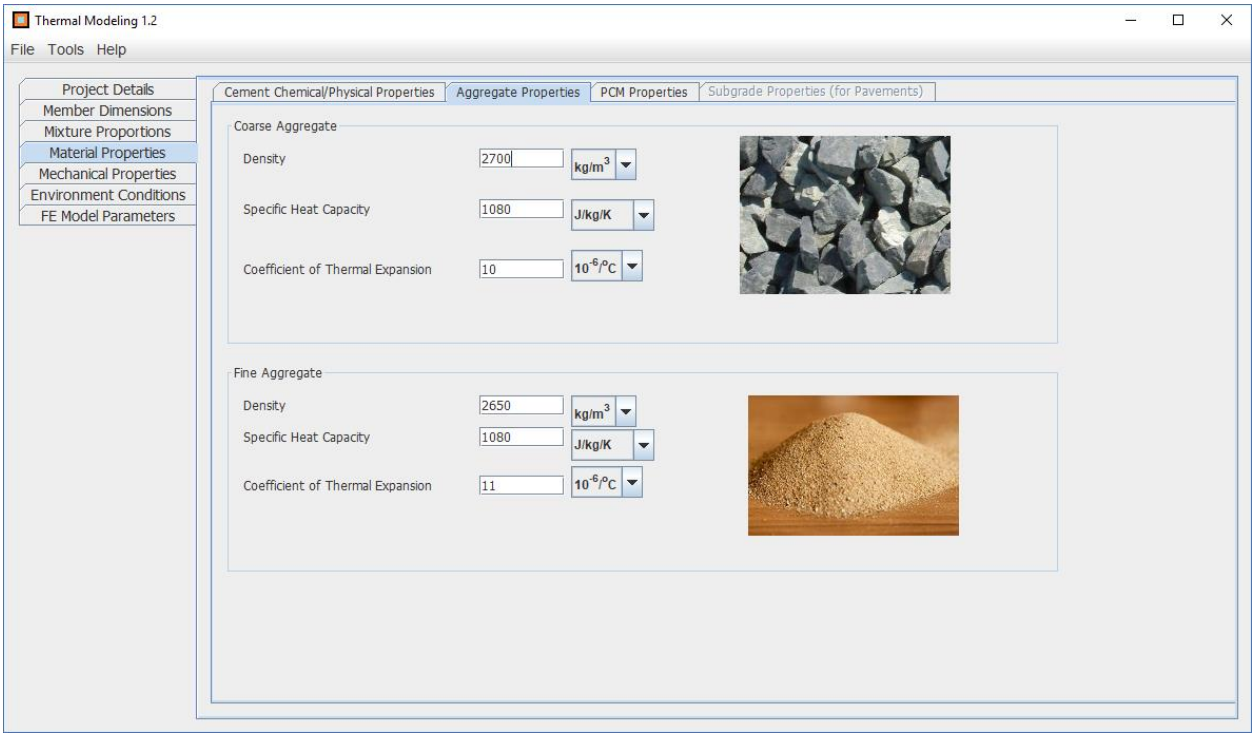

Figure 10-8 – Screenshot of MATRICEs v1.0 showing the material properties step for aggregates

10.3.5 Mechanical Properties

Several models are available to evaluate the development of strength and elastic modulus in fresh concrete as a function of time.

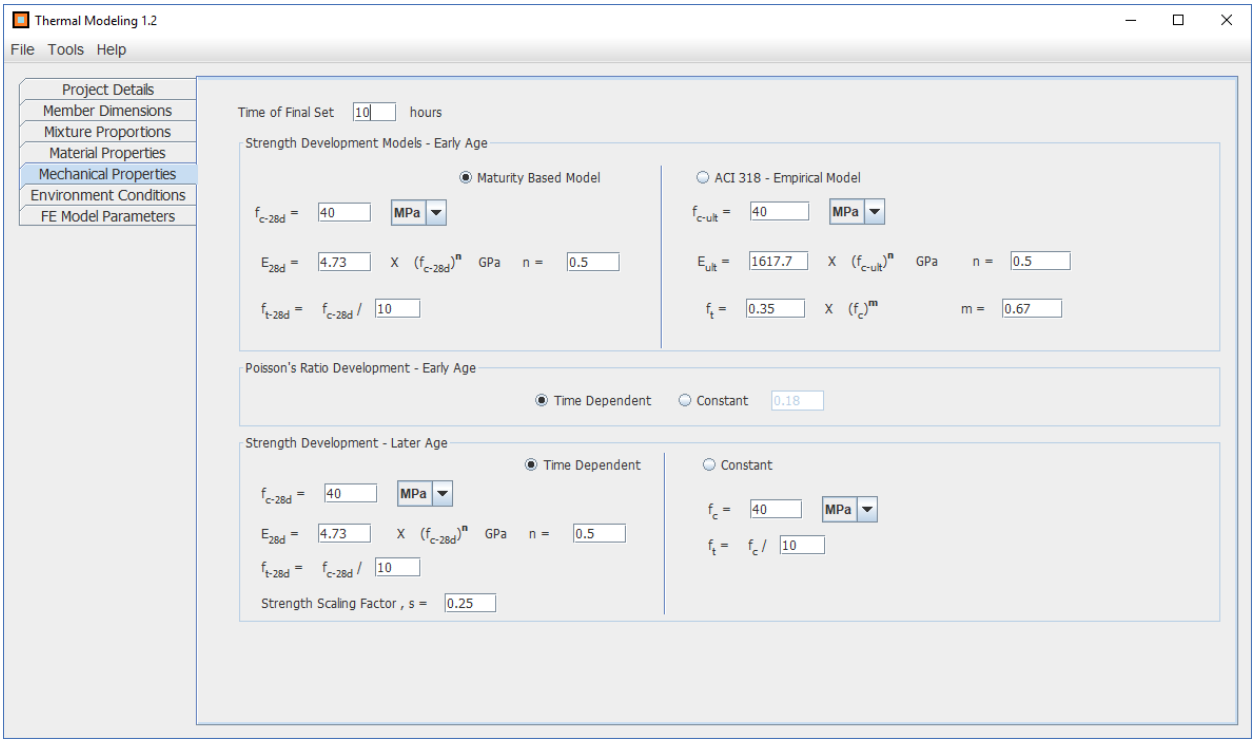

Figure 10-9 – Screenshot of MATRICEs v1.0 showing the mechanical properties step

Two models are available in MATRICEs v1.0 – maturity-based model (Carino and Lew n.d.), and ACI 318 empirical model (Committee, Institute, and Standardization 2008). Equations 10-22 to 10-23 show both the calculation of compressive strength, elastic modulus and tensile strength using the maturity-based model. This model relies on a linear relationship between the mechanical properties and the degree of hydration of the concrete.

Maturity Based Model

$$E_{28} = 4.73 * (f_{c-28})^{0.5};\ \ E(t) = E_{28} * \frac{\alpha(t) - \alpha_{final-set}}{\alpha_{28} - \alpha_{final-set}} \quad \text{(Eq. 10-22)}$$

$$f_{t-28} = \frac{f_{c-28}}{10};\ f_t(t) = f_{t-28} * \frac{\alpha(t) - \alpha_{final-set}}{\alpha_{28} - \alpha_{final-set}} \quad \text{(Eq. 10-23)}$$

Equations 10-24 to 10-26 show the calculation of mechanical properties based on the ACI 318 model. As opposed to the maturity-based model, this model is empirical in nature and several constants used here are only valid for regular concrete mixes. For specialized concrete mixture compositions including SCMs, non-traditional aggregates, low water-cement ratio, the exponents may need to be adjusted in the formulation based on experimental results. Such capability is provided in MATRICEs (see Figure 10-9).

ACI 318 Model

$$f_c(t) = f_{c-ult}\left(\exp\left(-\left(\frac{\tau}{t_e}\right)^{\beta}\right) - \exp\left(-\left(\frac{\tau}{t_{e-final-set}}\right)^{\beta}\right)\right) \quad \text{(Eq. 10-24)}$$

$$E(t) = 1617.7 * (f_c(t))^{0.5} \quad \text{(Eq. 10-25)}$$

$$f_t(t) = 0.35 * f_c(t)^{0.67} \quad \text{(Eq. 10-26)}$$

The time dependent Poisson's ratio is computed using Equation 10-27 (De Schutter and Taerwe 1996).

$$\nu = 0.18 * \sin\left(\frac{\pi\alpha}{2}\right) + 0.5 * e^{-10\alpha} \quad \text{(Eq. 10-27)}$$

Since concrete develops strength even beyond 28 days, therefore a time-dependent model has been implemented in MATRICEs to account for later age mechanical strength development (Equation 10-28). Here, 's' is a constant that depends on the cement type (s = 0.25 for normal and rapid hardening cements) and $f_t(28)$ is the tensile strength at 28 days which may be calculated using either of the methods described in equations 10-23 and 10-26.

$$f_t(t) = f_t(28) * exp\left(s\left(1 - \left(\frac{28}{t}\right)^{0.5}\right)\right) \quad \text{(Eq. 10-28)}$$

10.3.6 Finite Difference Model

MATRICEs has an in-built one-dimensional finite difference model which solves for the temperature profile of the concrete member at every time step using the heat diffusion equation. The user software interface for the model is shown in Figure 10-10. The computation speed is related to the time step selected internally to solve the finite difference scheme. Three standard options are provided to the user to control the time required for computation. For running large scale simulations (for example simulations for one year or longer), the user also has an option to select the frequency at which data is stored in order to generate output file and for post-processing.

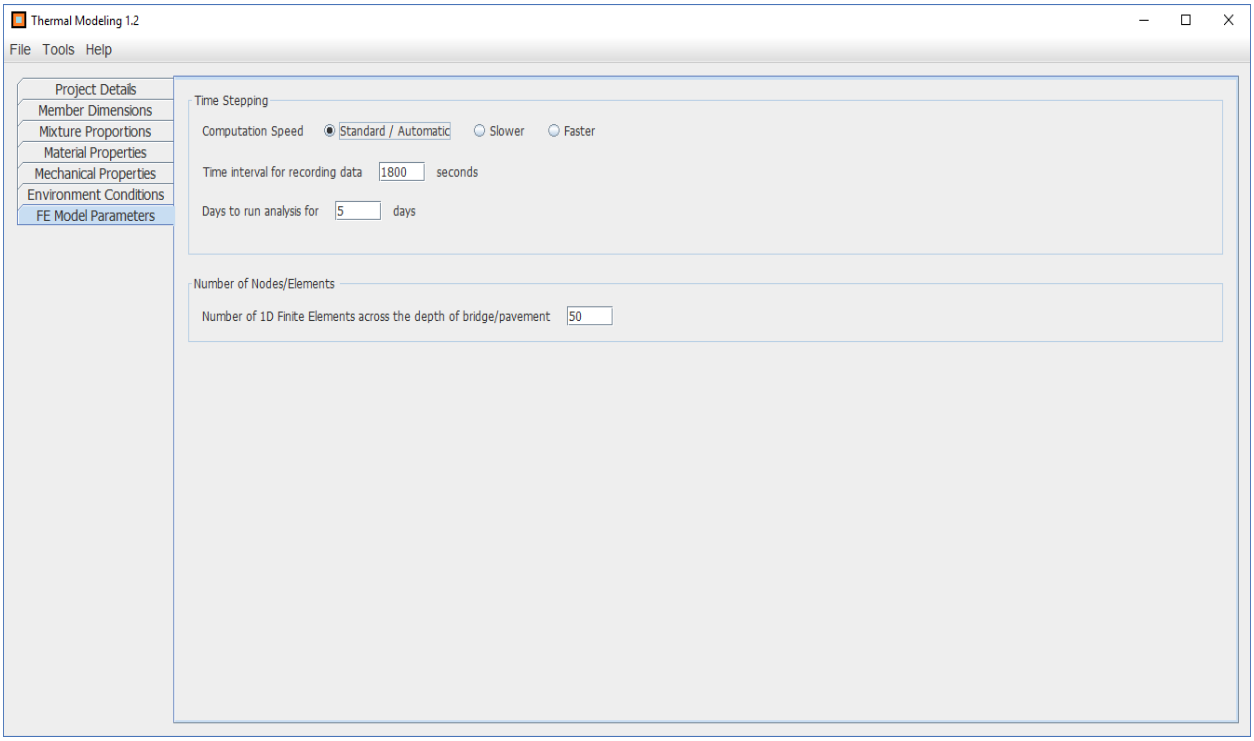

Figure 10-10 – Screenshot of MATRICEs v1.0 showing the FD model parameters step

The simplified version of the diffusion equation in one-dimension is given in Equation 10-29. Here '$\varkappa$' is the diffusivity of the concrete member.

$$\kappa \frac{\partial^2 T}{\partial x^2} + \frac{\dot{q}}{\rho c_p} = \frac{\partial T}{\partial t} \qquad \text{(Eq. 10-29)}$$

Equation 10-29 is discretized using an explicit finite difference scheme, where the temperature of the concrete member at time step 'n+1' is dependent explicitly on the temperature at time step 'n'. The discretized heat equation is given in Equation 10-30.

$$\kappa \frac{T_{i+1}^n - 2T_i^n + T_{i-1}^n}{\Delta x^2} + \frac{\dot{q}}{\rho c_p} = \frac{T_i^{n+1} - T_i^n}{\Delta t} \qquad \text{(Eq. 10-30)}$$

For equation 10-30, T_i^{n+1} can be calculated, since all other values are known. Here, it is important that the spatial and time steps are selected such that the stability criteria given in Equation 10-31 are satisfied.

$$0 < \frac{\kappa \Delta t}{\Delta x^2} < 0.5 \qquad \text{(Eq. 10-31)}$$

For hydrating concrete, the constant terms in the above equation $\varkappa$, ϱ, c_p and q are also functions of time and are evaluated at each time step for every element in the finite difference scheme.

10.3.7 Solver and Post-Processing

The solver integrates the six-step framework and solves the finite difference scheme to generate the spatio-temporal temperature profile of the concrete member. The user software interface showing the output from MATRICEs solver is shown in Figure 10-11. The result

here shows the temperature profile corresponding to all the elements in the finite difference scheme. The user has the option to select/de-select certain layers and output selected data to a file. For a fresh concrete system containing PCM, the simulation takes about 60 seconds to run for seven days on a 3.5 GHz 8-core processor. For a later age concrete system containing PCM, the simulation takes about 10-20 minutes to run for 365 days. The temperature profile for every finite difference element is recorded and can be output from MATRICEs into an excel sheet for further analysis. The specific heat capacity pertaining to each layer can also be mapped for every finite difference element.

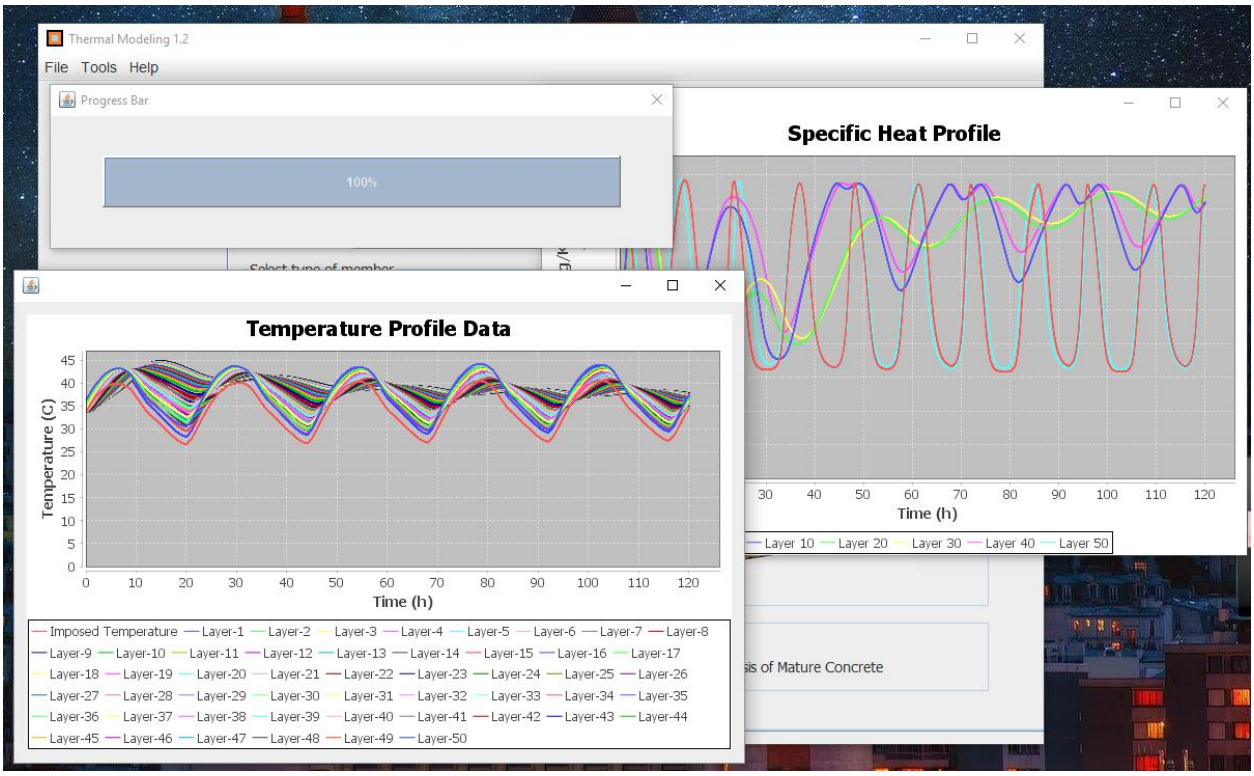

Figure 10-11 – Temperature and Specific Heat profiles

The temperature profile obtained is used to calculate the thermal stress development in the concrete member. The axial thermal strain is computed for a finite difference element using the difference between the temperature of the concrete member at time 't' and the temperature at the time of final set (Equation 10-32). For later age analysis, when the temperature at the time of final set is not known, it is replaced by the temperature at the time of the beginning of the analysis and relative thermal strains are computed.

$$\varepsilon_{axial} = \alpha_{comp}.\Delta T_{axial} \quad \text{(Eq. 10-32)}$$

Here, ΔT_{axial} is the temperature gradient computed as described above (Equation 10-33).

$$\Delta T_{axial} = \frac{\sum_{z=0}^{h}\left[\left(T_{z,current} - T_{z,final-set}\right)\Delta z\right]}{h} \quad \text{(Eq. 10-33)}$$

Here, 'h' is the total thickness of the slab, $T_{z,current}$ is the temperature of the slab at depth 'z' at the given time step, $T_{z,final\text{-}set}$ is the temperature of the slab at depth 'z' at time of final set and 'Δz' is the increment at which the temperature is calculated.

The temperature gradient across the top and bottom of the concrete member results in a curling stress (σ_{curl}) (Belshe et al. 2011) in the member which is computed using a modified Westergaard formulation (Equation 10-34 and 10-35) (Westergaard 1927). Here, E and ν are the elastic constants for the concrete member, α_{comp} is the concrete composite coefficient of thermal expansion, C_{max} and C_{min} are the maximum and minimum values of the Bradbury's coefficients (Bradbury 1938) derived from the the radius of relative stiffness of the concrete member, which is a function of the Poisson's ratio, elastic modulus, and geometry of the member.

$$\sigma_{curl} = \frac{\alpha_{comp} \cdot \Delta T_{curl} \cdot E}{2(1-\nu^2)} (C_{max} + \nu C_{min}) \quad \text{(Eq. 10-34)}$$

$$\Delta T_{curl} = (T_{top,current} - T_{bottom,current}) - (T_{top,final-set} - T_{bottom,final-set}) \quad \text{(Eq. 10-35)}$$

Finally, the overall thermal stress component is calculated as a combination of the curling and axial stress (Equation 10-36). Here, R_F is a restraint factor imposed on the thermal strain component to evaluate the thermal stress (Mohamed and Hansen 1997). In the absence of any restraint in the member, there would be no stresses and the member would be able to expand and contract freely under the imposed temperature. However, due to differential strength development along the depth as well as boundary constraints, every layer in the concrete member experiences a certain degree of restraint which leads to the presence of axial thermal stresses. The value of restraint factor can vary from 0.0 to 1.0, with a value of zero representing no restraint and consequently no stresses and a value of unity representing infinite restraint and complete stress transfer. A linear variation for the restraint factor is considered in MATRICEs starting from an initial value given by the user at the bottom of the member (bridge deck or pavement) and a value of zero at the top of the member.

$$\sigma_{total} = \varepsilon_{axial,z} \times E \times R_F(z) + \sigma_{curl,z} \quad \text{(Eq. 10-36)}$$

The overall thermal stress is compared to the tensile strength of fresh concrete to determine the probability of thermal cracking at early ages. For concrete members at later ages, the value of the total thermal stress may be added to the value of mechanical stresses generated as a result of live loads acting on the member. Figure 10-12 shows the post-processed stress versus time plot for two different fresh concrete compositions – (a) regular OPC concrete,

and (b) concrete containing 2.80% PCM. It is observed that thermal stresses in the concrete containing PCM are significantly lower than the tensile strength which contributes to a low cracking probability. On the other hand, the regular concrete member is prone to high degree of cracking since the thermal stresses exceed the tensile strength.

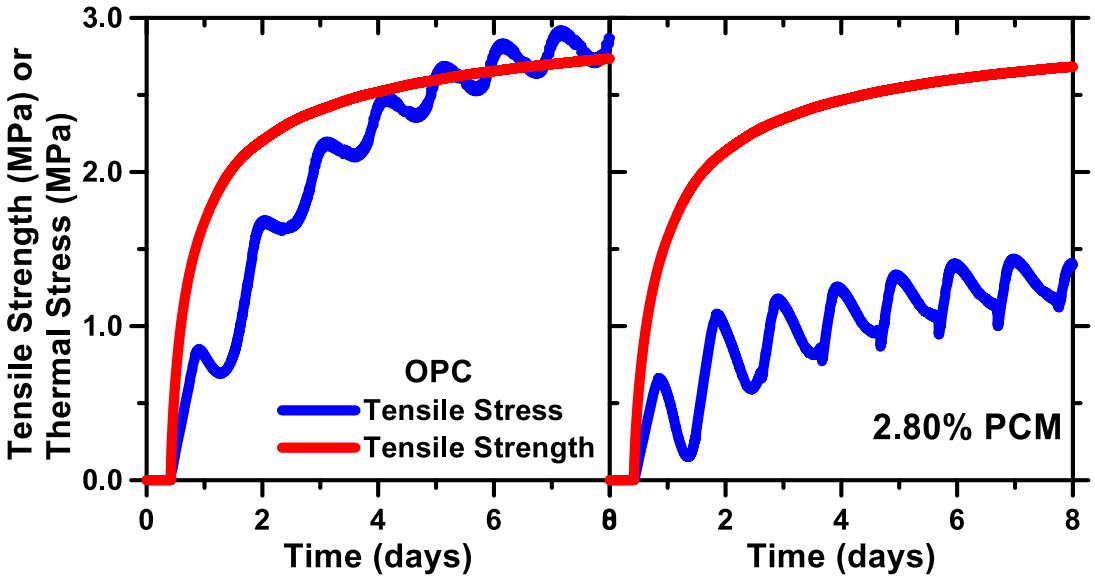

Figure 10-12 – Comparison of thermal stress and tensile strength development in a fresh concrete pavement with two different mixture compositions

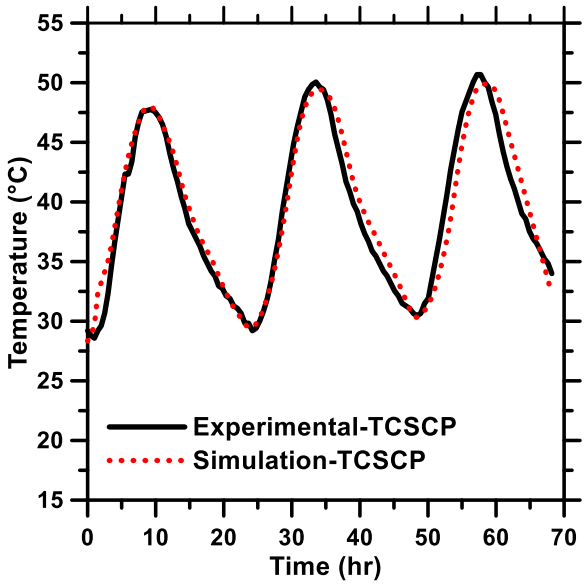

Figure 10-13 – Experimental validation for MATRICEs conducted on a concrete pavement slab

A field validation of MATRICEs was carried out by embedding RFID sensors containing thermocouples inside a fresh concrete pavement slab. The experimentally measured temperature profile for three days was compared against the temperature profile predicted by MATRICEs. The results are shown in Figure 10-13. Results show a good agreement between measured and predicted values.

CHAPTER 11

CONCLUSIONS

A comprehensive investigation on multi-component cementitious composites has been presented in three parts in this thesis. The first part is focused on the understanding of the behavior of interground limestone systems and their interaction with alumina based materials. The second part sets ground over ultra-high performance concrete – a novel type of concrete with extremely high mechanical strength and durability characteristics. A novel framework to design ultra-high performance binders and concrete based on microstructure, rheology and aggregate optimization has been developed and implemented. Mechanical and durability investigations on the developed UHPC mixtures have been conducted. The last part of the study goes over the numerical modeling of phase change materials in concrete. Following are the conclusions of this thesis.

- Limestone is either interground or blended with cement powder to be used as a partial replacement material. It is found that interground systems consistently outperform the blended systems in terms of compressive strength, porosity and reaction kinetics.
- Particle-size matched blended limestone cements created are compared with the interground limestone-based cements at the same level of limestone replacement. The size matching ensures the same particle size distributions for the composite powder and neutralizes the effect of surface area. Comparing between the interground and blended systems shows that interground systems show enhanced early age hydration properties as noted from the calorimetric heat evolution curves.

- The interground limestone systems show a higher degree of carbonate consumption indicating the participation of limestone in the formation of hydration products, and not just acting as a filler material.
- The interground limestone systems show a significantly refined pore-structure with a lower critical pore diameter. At the same time, the interground systems demonstrate a higher value of compressive strength as compared to the blended systems. This is attributed to the presence of relatively finer limestone in the interground systems.
- The enhanced properties of the interground limestone systems over the particle size matched blended limestone systems is intriguing. The hypothesis that limestone is finer in the interground systems was confirmed in a following study conducted to determine the exact distribution of limestone and cement in the interground systems. A novel method has been proposed since conventional methods are found to be insufficient.
- The novel method is an optimization approach based on the (a) characteristic diameter and (b) shape parameter obtained from Rosin-Rammler distribution of the blended and interground powders, and (c) surface area of powders obtained using their particle size distributions. It is found that limestone present in the interground systems is significantly finer than the limestone present in the blended systems. The reason for this is the differential grinding of cement and limestone due to different material hardness. Limestone, being the softer phase, is ground to a much smaller

size as compared to cement clinker. Such a method is useful to help achieve performance equivalence to the interground systems.

- The interaction of interground and blended limestone systems with alumina containing blast furnace slag has been investigated in Chapter 5. Three different mixture categories – pure slag, interground limestone containing slag, blended limestone containing slag, were created to replace cement at a volume fraction of 20% to 50%.
- The synergistic effect of limestone and slag has been brought out. The hydration of slag was accelerated in the presence of limestone, with the finer limestone in interground systems providing increased acceleration than the blended ones, as determined from isothermal calorimetry measurements. At the same time, the consumption of limestone was found to increase with increase in the slag content of the mixture.
- The hydration product corresponding to the presence of limestone, AFmc or carboaluminate phase was quantified using thermos-gravimetric measurements. A linear correlation was identified between the consumption of carbonates and the formation of the AFmc phase. The effect was more pronounced in interground limestone containing slag systems, due to the presence of finer limestone.
- The synergistic effect of limestone and slag was found to achieve similar compressive strength values as compared to pure cement at all replacement levels. The critical

pore diameter was found to decrease in the presence of slag and limestone, indicating pore size refinement in these systems.

- A first principles-based design of ultra-high performance binders and concrete has been proposed. Rational methodologies for the design of UHP concretes were derived from the fundamental understanding of the characteristics of the component paste phase at the microstructure level and component aggregate phase at the mesostructure level. The ideal binder formulation suitable to exhibit ultra-high performance was selected from several binary, ternary, and quaternary blends using a stepwise algorithm that considered the effect of both microstructural packing as well as rheological properties of the binder.
- The proposed methodology allows the user to select mixtures based on acceptable ranges of microstructural packing and workability demanded by the application. The selected binder formulations were evaluated for the compressive strengths and 28-day compressive strengths close to 100 MPa were obtained for all binders.
- A compressible packing model was used for the packing of coarse and fine aggregates in UHPC and to determine the optimum aggregate composition to achieve the maximum packing density. 28-day compressive strengths in excess of 150 MPa were obtained. 28-day flexural strengths more than 10 MPa were obtained. Significantly improved resistance to ionic transport as compared to conventional or high performance concretes was also observed, validating the material design procedure.

- In the final part of this study, a numerical simulation approach was carried out to quantify the effect of phase change materials in concrete infrastructure. Phase change materials are high latent heat capacity materials which can change phase reversibly at room temperatures, and as a result store or release heat energy. A comprehensive software tool MATRICEs was developed to analyze the thermal stresses in concretes as a result of concrete hydration as well as daily and seasonal climatic variations.
- Phase change materials with transition temperatures of 24 °C and 35 °C were simulated in concrete pavements and bridge decks. The concrete members were subjected to climatic conditions obtained from historical climate database and their temperature profiles were determined by solving the second-order heat diffusion equation using a finite difference scheme.
- It was found that presence of PCMs at 5% by volume reduced the peak temperature by 6 °C to 10 °C in hydrating fresh concretes. The thermal stresses were determined using the temperature profiles and compared with the tensile strength development to determine the probability and severity of thermal cracking in the concrete members. Concretes containing PCMs showed significantly reduced cracking probabilities.
- The selection of phase change material to be used under different climatic conditions was explored. Long term simulations for concrete pavements containing PCMs were carried out for Phoenix, AZ and San Francisco, CA weather. It was found that 24 C PCM was more effective for San Francisco, a hybrid combination of 24 °C and 35

°C PCM resulted in higher effectiveness in thermal stresses for Phoenix climate, thus reducing thermal fatigue and life cycle costs.

- Experimental validation of the model developed in MATRICEs was carried out on a concrete pavement located in Phoenix, AZ. Excellent agreement between measured and predicted temperature profiles was obtained.

REFERENCES

Abbas, Safeer, Ahmed M. Soliman, and Moncef L. Nehdi. 2015. "Exploring Mechanical and Durability Properties of Ultra-High Performance Concrete Incorporating Various Steel Fiber Lengths and Dosages." *Construction and Building Materials* 75 (January): 429–41. https://doi.org/10.1016/j.conbuildmat.2014.11.017.

Abhat, A. 1983. "Low Temperature Latent Heat Thermal Energy Storage: Heat Storage Materials." *Solar Energy* 30 (4): 313–32. https://doi.org/10.1016/0038-092X(83)90186-X.

Aguayo, Matthew, Sumanta Das, Cesar Castro, Nihat Kabay, Gaurav Sant, and Narayanan Neithalath. 2017. "Porous Inclusions as Hosts for Phase Change Materials in Cementitious Composites: Characterization, Thermal Performance, and Analytical Models." *Construction and Building Materials* 134 (March): 574–84. https://doi.org/10.1016/j.conbuildmat.2016.12.185.

Aguayo, Matthew, Sumanta Das, Amit Maroli, Nihat Kabay, James C. E. Mertens, Subramaniam D. Rajan, Gaurav Sant, Nikhilesh Chawla, and Narayanan Neithalath. 2016. "The Influence of Microencapsulated Phase Change Material (PCM) Characteristics on the Microstructure and Strength of Cementitious Composites: Experiments and Finite Element Simulations." *Cement and Concrete Composites* 73 (October): 29–41. https://doi.org/10.1016/j.cemconcomp.2016.06.018.

Ahlborn, Theresa M., Erron J. Peuse, and Donald Li Misson. 2008. "Ultra-High-Performance-Concrete for Michigan Bridges Material Performance – Phase I," November. https://trid.trb.org/view/934652.

Ahmad, Maha, André Bontemps, Hébert Sallée, and Daniel Quenard. 2006. "Thermal Testing and Numerical Simulation of a Prototype Cell Using Light Wallboards Coupling Vacuum Isolation Panels and Phase Change Material." *Energy and Buildings* 38 (6): 673–81. https://doi.org/10.1016/j.enbuild.2005.11.002.

Aim, R. Ben, and P. Le Goff. 1969. "Porosité Des Mélanges Binaires de Sphères et d'objets à Symétrie Cylindrique." *Powder Technology* 2 (3): 169–74. https://doi.org/10.1016/0032-5910(69)80006-9.

Aldahdooh, M. A. A., N. Muhamad Bunnori, and M. A. Megat Johari. 2013. "Evaluation of Ultra-High-Performance-Fiber Reinforced Concrete Binder Content Using the Response Surface Method." *Materials & Design* 52 (December): 957–65. https://doi.org/10.1016/j.matdes.2013.06.034.

Alkaysi, Mo, Sherif El-Tawil, Zhichao Liu, and Will Hansen. 2016. "Effects of Silica Powder and Cement Type on Durability of Ultra High Performance Concrete (UHPC)."

Cement and Concrete Composites 66 (February): 47–56. https://doi.org/10.1016/j.cemconcomp.2015.11.005.

Alsalman, Ali, Canh N. Dang, and W. Micah Hale. 2017. "Development of Ultra-High Performance Concrete with Locally Available Materials." *Construction and Building Materials* 133 (February): 135–45. https://doi.org/10.1016/j.conbuildmat.2016.12.040.

Alsalman, Ali, Canh N. Dang, Gary S. Prinz, and W. Micah Hale. 2017. "Evaluation of Modulus of Elasticity of Ultra-High Performance Concrete." *Construction and Building Materials* 153: 918–928.

Aoude, Hassan, Frederic P. Dagenais, Russell P. Burrell, and Murat Saatcioglu. 2015. "Behavior of Ultra-High Performance Fiber Reinforced Concrete Columns under Blast Loading." *International Journal of Impact Engineering* 80 (June): 185–202. https://doi.org/10.1016/j.ijimpeng.2015.02.006.

Ariño, Antonio M., and Barzin Mobasher. 1999. "Effect of Ground Copper Slag on Strength and Toughness of Cementitious Mixes." *ACI Materials Journal* 96 (1). https://asu.pure.elsevier.com/en/publications/effect-of-ground-copper-slag-on-strength-and-toughness-of-cementi.

Arora, A., K. Vance, G. Sant, and N. Neithalath. 2016. "A Methodology to Extract the Component Size Distributions in Interground Composite (Limestone) Cements." *Construction and Building Materials* 121: 328–37. https://doi.org/10.1016/j.conbuildmat.2016.06.006.

Arora, Aashay, Matthew Aguayo, Hannah Hansen, Cesar Castro, Erin Federspiel, Barzin Mobasher, and Narayanan Neithalath. 2018. "Microstructural Packing- and Rheology-Based Binder Selection and Characterization for Ultra-High Performance Concrete (UHPC)." *Cement and Concrete Research* 103 (January): 179–90. https://doi.org/10.1016/j.cemconres.2017.10.013.

Arora, Aashay, Asim Almujaddidi, Farrokh Kianmofrad, Barzin Mobasher, and Narayanan Neithalath. n.d. "Particle Packing-Based Design of Economical Ultra-High Performance Concrete (UHPC) and Evaluation of Their Properties (Under Review)." *Cement and Concrete Research*.

Arora, Aashay, Gaurav Sant, and Narayanan Neithalath. 2016. "Ternary Blends Containing Slag and Interground/Blended Limestone: Hydration, Strength, and Pore Structure." *Construction and Building Materials* 102, Part 1 (January): 113–24. https://doi.org/10.1016/j.conbuildmat.2015.10.179.

———. 2017. "Numerical Simulations to Quantify the Influence of Phase Change Materials (PCMs) on the Early- and Later-Age Thermal Response of Concrete Pavements." *Cement and Concrete Composites* 81 (August): 11–24. https://doi.org/10.1016/j.cemconcomp.2017.04.006.

ASTM, C. 2011. "1074, Standard Practice for Estimating Concrete Strength by the Maturity Method. ASTM International, West Conshohocken (USA)."

"ASTM C109 / C109M - 12 Standard Test Method for Compressive Strength of Hydraulic Cement Mortars (Using 2-in. or [50-Mm] Cube Specimens)." 2012. In . ASTM International, West Conshohocken, PA.

"ASTM C109 / C109M - 12 Standard Test Method for Compressive Strength of Hydraulic Cement Mortars (Using 2-in. or [50-Mm] Cube Specimens). ASTM International, West Conshohocken, PA; 2012." n.d.

"ASTM C150 / C150M - 12. Standard Specification for Portland Cement." 2012. In . ASTM International, West Conshohocken, PA.

"ASTM C305-13 Standard Practice for Mechanical Mixing of Hydraulic Cement Pastes and Mortars of Plastic Consistency." 2013. In . ASTM International, West Conshohocken, PA.

"ASTM C305-13 Standard Practice for Mechanical Mixing of Hydraulic Cement Pastes and Mortars of Plastic Consistency. ASTM International, West Conshohocken, PA; 2013." n.d.

"ASTM C568 / C568M - 10. Standard Specification for Limestone Dimension Stone." 2012. In . ASTM International, West Conshohocken, PA.

"ASTM C595 / C595M - 16 Standard Specification for Blended Hydraulic Cements." n.d. Accessed April 11, 2016. about:reader?url=http%3A%2F%2Fwww.astm.org%2FStandards%2FC595.htm.

"ASTM C1157/C1157M-11 Standard Performance Specification for Hydraulic Cement." 2013. In . ASTM International, West Conshohocken, PA.

"ASTM C1202 - 12. Standard Test Method for Electrical Indication of Concrete's Ability to Resist Chloride Ion Penetration." 2012. *ASTM International, West Conshohocken, PA (2012)*.

ASTM C1260. 2014. "ASTM C1260 - 14. Standard Test Method for Potential Alkali Reactivity of Aggregates (Mortar-Bar Method)." *ASTM International, West Conshohocken, PA (2014)*.

ASTM C1585. 2013. "ASTM C1585 - 13. Standard Test Method for Measurement of Rate of Water by Hydraulic-Cement Concretes." *ASTM International, West Conshohocken, PA (2013)*.

"ASTM C1611/C1611M-14 Standard Test Method for Slump Flow of Self-Consolidating Concrete." 2014. West Conshohocken, PA: ASTM International.

ASTM Standard. n.d. "C680-10, Standard Practice for Estimate of the Heat Gain or Loss and the Surface Temperatures of Insulated Flat, Cylindrical, and Spherical Systems by Use of Computer Programs."

Baetens, Ruben, Bjørn Petter Jelle, and Arild Gustavsen. 2010. "Phase Change Materials for Building Applications: A State-of-the-Art Review." *Energy and Buildings* 42 (9): 1361–68. https://doi.org/10.1016/j.enbuild.2010.03.026.

Bágel, L. 1998. "Strength and Pore Structure of Ternary Blended Cement Mortars Containing Blast Furnace Slag and Silica Fume." *Cement and Concrete Research* 28 (7): 1011–22. https://doi.org/10.1016/S0008-8846(98)00078-7.

Bager, Dirch H., and Erik J. Sellevold. 1975. "Mercury Porosimetry of Hardened Cement Paste: The Influence of Particle Size." *Cement and Concrete Research* 5 (2): 171–177.

Bakhshi, Mehdi, Christopher Barsby, and Barzin Mobasher. 2014. "Comparative Evaluation of Early Age Toughness Parameters in Fiber Reinforced Concrete." *Materials and Structures* 47 (5): 853–72. https://doi.org/10.1617/s11527-013-0098-1.

Banthia, Nandakumar, and N. Nandakumar. 2003. "Crack Growth Resistance of Hybrid Fiber Reinforced Cement Composites." *Cement and Concrete Composites* 25 (1): 3–9.

Barcelo, Laurent, Michael D. A. Thomas, Kevin Cail, Anik Delagrave, and Bruce Blair. 2013. "Portland Limestone Cement Equivalent Strength Explained." *Concrete International* 35 (11): 41–47.

Belshe, Mark, Michael S. Mamlouk, Kamil E. Kaloush, and Maria Rodezno. 2011. "Temperature Gradient and Curling Stresses in Concrete Pavement with and without Open-Graded Friction Course." *Journal of Transportation Engineering* 137 (10): 723–29. https://doi.org/10.1061/(ASCE)TE.1943-5436.0000254.

Bencardino, Francesco, Lidia Rizzuti, Giuseppe Spadea, and Ramnath N. Swamy. 2008. "Stress-Strain Behavior of Steel Fiber-Reinforced Concrete in Compression." *Journal of Materials in Civil Engineering* 20 (3): 255–63. https://doi.org/10.1061/(ASCE)0899-1561(2008)20:3(255).

Benson, David K., C. B. Christensen, and R. W. Burrows. 1985. "New Phase-Change Thermal Energy Storage Materials for Buildings." Solar Energy Research Inst., Golden, CO (USA).

Bentz, D., E. F Irassar, B. Bucher, and W. J Weiss. 2009. "Limestone Fillers Conserve Cement: Part 1: An Analysis Based on Powers Model." *Concrete International* 31 (11): 41–46.

Bentz, D. P. 2006. "Modeling the Influence of Limestone Filler on Cement Hydration Using CEMHYD3D." *Cement and Concrete Composites* 28 (2): 124–29. https://doi.org/10.1016/j.cemconcomp.2005.10.006.

Bentz, Dale P., Edward J. Garboczi, Claus J. Haecker, and Ole M. Jensen. 1999. "Effects of Cement Particle Size Distribution on Performance Properties of Portland Cement-Based Materials." *Cement and Concrete Research* 29 (10): 1663–71. https://doi.org/10.1016/S0008-8846(99)00163-5.

Bentz, Dale P., Gaurav Sant, and Jason Weiss. 2008. "Early-Age Properties of Cement-Based Materials. I: Influence of Cement Fineness." *Journal of Materials in Civil Engineering* 20 (7): 502–508.

Bentz, D.P. 2005. "Replacement of 'Coarse' Cement Particles by Inert Fillers in Low w/c Ratio Concretes: II. Experimental Validation." *Cement and Concrete Research* 35 (1): 185–88. https://doi.org/16/j.cemconres.2004.09.003.

Berry, Michael. 2015. "Feasibility of Non-Proprietary Ultra-High Performance Concrete (UHPC) for Use in Highway Bridges in Montana."

Beushausen, Hans, Mark Alexander, and Yunus Ballim. 2012. "Early-Age Properties, Strength Development and Heat of Hydration of Concrete Containing Various South African Slags at Different Replacement Ratios." *Construction and Building Materials* 29 (April): 533–40. https://doi.org/10.1016/j.conbuildmat.2011.06.018.

Bobko, Christopher P., Benjamin Gathier, J. Alberto Ortega, Franz-Josef Ulm, Lavinia Borges, and Younane N. Abousleiman. 2011. "The Nanogranular Origin of Friction and Cohesion in Shale—a Strength Homogenization Approach to Interpretation of Nanoindentation Results." *International Journal for Numerical and Analytical Methods in Geomechanics* 35 (17): 1854–1876.

Bonavetti, V., H. Donza, G. Menéndez, O. Cabrera, and E. F. Irassar. 2003. "Limestone Filler Cement in Low w/c Concrete: A Rational Use of Energy." *Cement and Concrete Research* 33 (6): 865–71. https://doi.org/16/S0008-8846(02)01087-6.

Bonavetti, V. L., V. F. Rahhal, and E. F. Irassar. 2001. "Studies on the Carboaluminate Formation in Limestone Filler-Blended Cements." *Cement and Concrete Research* 31 (6): 853–59. https://doi.org/16/S0008-8846(01)00491-4.

Bradbury, R. D. 1938. *Reinforced Concrete Pavements*. Washington, D.C.: Wire Reinforcement Institute.

Brühwiler, Eugen, and Emmanuel Denarié. 2013. "Rehabilitation and Strengthening of Concrete Structures Using Ultra-High Performance Fibre Reinforced Concrete." *Structural Engineering International* 23 (4): 450–57. https://doi.org/10.2749/101686613X13627347100437.

Bullard, Jeffrey W., Hamlin M. Jennings, Richard A. Livingston, Andre Nonat, George W. Scherer, Jeffrey S. Schweitzer, Karen L. Scrivener, and Jeffrey J. Thomas. 2011. "Mechanisms of Cement Hydration." *Cement and Concrete Research* 41 (12): 1208–1223.

Burroughs, Jedadiah F., Jay Shannon, Todd S. Rushing, Kevin Yi, Quinn B. Gutierrez, and Danny W. Harrelson. 2017. "Potential of Finely Ground Limestone Powder to Benefit Ultra-High Performance Concrete Mixtures." *Construction and Building Materials* 141 (June): 335–42. https://doi.org/10.1016/j.conbuildmat.2017.02.073.

Cabeza, Luisa F., Cecilia Castellón, Miquel Nogués, Marc Medrano, Ron Leppers, and Oihana Zubillaga. 2007. "Use of Microencapsulated PCM in Concrete Walls for Energy Savings." *Energy and Buildings* 39 (2): 113–19. https://doi.org/10.1016/j.enbuild.2006.03.030.

Cai, M, P. K Kaiser, Y Tasaka, T Maejima, H Morioka, and M Minami. 2004. "Generalized Crack Initiation and Crack Damage Stress Thresholds of Brittle Rock Masses near Underground Excavations." *International Journal of Rock Mechanics and Mining Sciences* 41 (5): 833–47. https://doi.org/10.1016/j.ijrmms.2004.02.001.

Cam, Hieu T., and Narayanan Neithalath. 2010. "Moisture and Ionic Transport in Concretes Containing Coarse Limestone Powder." *Cement and Concrete Composites* 32 (7): 486–96. https://doi.org/10.1016/j.cemconcomp.2010.04.002.

Camiletti, J., A. M. Soliman, and M. L. Nehdi. 2012. "Effects of Nano- and Micro-Limestone Addition on Early-Age Properties of Ultra-High-Performance Concrete." *Materials and Structures* 46 (6): 881–98. https://doi.org/10.1617/s11527-012-9940-0.

Carino, Nicholas J., and H. S. Lew. n.d. "The Maturity Method: From Theory to Application." In *Structures 2001*, 1–19. American Society of Civil Engineers. Accessed August 27, 2016. http://ascelibrary.org/doi/abs/10.1061/40558%282001%2917.

Cariou, Sophie, Franz-Josef Ulm, and Luc Dormieux. 2008. "Hardness–Packing Density Scaling Relations for Cohesive-Frictional Porous Materials." *Journal of the Mechanics and Physics of Solids* 56 (3): 924–952.

Castell, A., I. Martorell, M. Medrano, G. Pérez, and L. F. Cabeza. 2010. "Experimental Study of Using PCM in Brick Constructive Solutions for Passive Cooling." *Energy and Buildings* 42 (4): 534–40. https://doi.org/10.1016/j.enbuild.2009.10.022.

Chan, K. W., and A. K. H. Kwan. 2014. "Evaluation of Particle Packing Models by Comparing with Published Test Results." *Particuology* 16 (Supplement C): 108–15. https://doi.org/10.1016/j.partic.2013.11.008.

Cheng, Yang-Tse, and Che-Min Cheng. 2004. "Scaling, Dimensional Analysis, and Indentation Measurements." *Materials Science and Engineering: R: Reports* 44 (4–5): 91–149.

Chiara F., Ferraris, Jeffrey W. Bullard, and Vincent Hackley. n.d. "Particle Size Distribution by Laser Diffraction Spectrometry: Application to Cementitious Powders." *Proceedings of the 5th World Congress on Particle Technology, Orlando. 2006*. http://ciks.cbt.nist.gov/garbocz/monograph/FerrarisBullard_Sulfate.pdf.

Chiara F Ferraris, Vincent A. Hackley. 2011. "Analysis of the ASTM Round-Robin Test on Particle Size Distribution of Portland Cement: Phase I1."

Choi, Myoung Sung, Jung Soo Lee, Keum Seong Ryu, Kyung-Taek Koh, and Seung Hee Kwon. 2016. "Estimation of Rheological Properties of UHPC Using Mini Slump Test." *Construction and Building Materials* 106 (March): 632–39. https://doi.org/10.1016/j.conbuildmat.2015.12.106.

Chu, T. C., W. F. Ranson, and Mr A. Sutton. 1985. "Applications of Digital-Image-Correlation Techniques to Experimental Mechanics." *Experimental Mechanics* 25 (3): 232–244.

"Climate Phoenix - Arizona and Weather Averages Phoenix." n.d. Accessed August 27, 2016. http://www.usclimatedata.com/climate/phoenix/arizona/united-states/usaz0166.

"Climate San Francisco - California and Weather Averages San Francisco." n.d. Accessed August 27, 2016. http://www.usclimatedata.com/climate/san-francisco/california/united-states/usca0987.

Collier, R. K., and D. P. Grimmer. 1979. "Experimental Evaluation of Phase Change Material Building Walls Using Small Passive Test Boxes." Los Alamos Scientific Lab., NM (USA).

Committee, A. C. I., American Concrete Institute, and International Organization for Standardization. 2008. "Building Code Requirements for Structural Concrete (ACI 318-08) and Commentary." In . American Concrete Institute. https://books.google.com/books?hl=en&lr=&id=c6yQszMV2-EC&oi=fnd&pg=PT10&dq=ACI+318%E2%80%9308.+Building+code+requirements+for+structural+concrete+and+commentary%3B+2008.&ots=nWSmKX0yKJ&sig=ERlBHdXNtUDCy5ftRM00TuoxQx0.

Constantinides, Georgios, and Franz-Josef Ulm. 2007. "The Nanogranular Nature of C–S–H." *Journal of the Mechanics and Physics of Solids* 55 (1): 64–90.

Cook, Raymond A., and Kenneth C. Hover. 1993. "Mercury Porosimetry of Cement-Based Materials and Associated Correction Factors." *Construction and Building Materials* 7 (4): 231–40. https://doi.org/10.1016/0950-0618(93)90007-Y.

———. 1999. "Mercury Porosimetry of Hardened Cement Pastes." *Cement and Concrete Research* 29 (6): 933–943.

Courard, Luc, and Frédéric Michel. 2014. "Limestone Fillers Cement Based Composites: Effects of Blast Furnace Slags on Fresh and Hardened Properties." *Construction and Building Materials* 51 (January): 439–45. https://doi.org/10.1016/j.conbuildmat.2013.10.076.

D. P. Bentz. 2005. "CEMHYD3D: A Three-Dimensional Cement Hydration and Microstructure Development Modeling Package. Version 3.0. NISTIR 7232." *US Department of Commerce*.

Damidot, D., B. Lothenbach, D. Herfort, and F. P. Glasser. 2011. "Thermodynamics and Cement Science." *Cement and Concrete Research*, Special Issue: 13th International Congress on the Chemistry of Cement, 41 (7): 679–95. https://doi.org/10.1016/j.cemconres.2011.03.018.

Darweesh, H. H. M. 2004. "Limestone as an Accelerator and Filler in Limestone-Substituted Alumina Cement." *Ceramics International* 30 (2): 145–50. https://doi.org/16/S0272-8842(03)00073-7.

Das, Sumanta, Matthew Aguayo, Vikram Dey, Robert Kachala, Barzin Mobasher, Gaurav Sant, and Narayanan Neithalath. 2014. "The Fracture Response of Blended Formulations Containing Limestone Powder: Evaluations Using Two-Parameter Fracture Model and Digital Image Correlation." *Cement and Concrete Composites* 53 (October): 316–26. https://doi.org/10.1016/j.cemconcomp.2014.07.018.

Das, Sumanta, Matthew Aguayo, Gaurav Sant, Barzin Mobasher, and Narayanan Neithalath. 2015. "Fracture Process Zone and Tensile Behavior of Blended Binders Containing

Limestone Powder." *Cement and Concrete Research* 73 (July): 51–62. https://doi.org/10.1016/j.cemconres.2015.03.002.

De Larrard, Francois. 1999. *Concrete Mixture Proportioning: A Scientific Approach*. CRC Press.

De Schutter, Geert, and Luc Taerwe. 1996. "Degree of Hydration-Based Description of Mechanical Properties of Early Age Concrete." *Materials and Structures* 29 (6): 335.

De Weerdt, K., M. Ben Haha, G. Le Saout, K. O. Kjellsen, H. Justnes, and B. Lothenbach. 2011. "Hydration Mechanisms of Ternary Portland Cements Containing Limestone Powder and Fly Ash." *Cement and Concrete Research* 41 (3): 279–91. https://doi.org/10.1016/j.cemconres.2010.11.014.

De Weerdt, K., K. O. Kjellsen, E. Sellevold, and H. Justnes. 2011. "Synergy between Fly Ash and Limestone Powder in Ternary Cements." *Cement and Concrete Composites* 33 (1): 30–38. https://doi.org/10.1016/j.cemconcomp.2010.09.006.

DELAGRAMMATIKAS, G., and S. TSIMAS. 2004. "Grinding Process Simulation Based on Rosin-Rammler Equation." *Chemical Engineering Communications* 191 (10): 1362–78. https://doi.org/10.1080/00986440490472625.

Dewar, Joe. 2002. *Computer Modelling of Concrete Mixtures*. CRC Press.

Dhir, R. K., M. C. Limbachiya, M. J. McCarthy, and A. Chaipanich. 2007. "Evaluation of Portland Limestone Cements for Use in Concrete Construction." *Materials and Structures* 40 (5): 459–473.

Diamond, Sidney. 2000. "Mercury Porosimetry: An Inappropriate Method for the Measurement of Pore Size Distributions in Cement-Based Materials." *Cement and Concrete Research* 30 (10): 1517–1525.

Dubey, Ashish, and Nemkumar Banthia. 1998. "Influence of High-Reactivity Metakaolin and Silica Fume on the Flexural Toughness of High-Performance Steel Fiber Reinforced Concrete." *Materials Journal* 95 (3): 284–92. https://doi.org/10.14359/372.

El-Dieb, Amr S. 2009. "Mechanical, Durability and Microstructural Characteristics of Ultra-High-Strength Self-Compacting Concrete Incorporating Steel Fibers." *Materials & Design* 30 (10): 4286–92. https://doi.org/10.1016/j.matdes.2009.04.024.

Elrahman, Mohamed Abd, and Bernd Hillemeier. 2014. "Combined Effect of Fine Fly Ash and Packing Density on the Properties of High Performance Concrete: An Experimental Approach." *Construction and Building Materials* 58: 225–233.

Emanuel, Jack H., and J. Leroy Hulsey. 1977. "Prediction of the Thermal Coefficient of Expansion of Concrete." *Journal Proceedings* 74 (4): 149–55.

Emborg, Mats, and Stig Bernander. 1994. "Assessment of Risk of Thermal Cracking in Hardening Concrete." *Journal of Structural Engineering* 120 (10): 2893–2912. https://doi.org/10.1061/(ASCE)0733-9445(1994)120:10(2893).

Escalante, J. I, L. Y Gómez, K. K Johal, G Mendoza, H Mancha, and J Méndez. 2001. "Reactivity of Blast-Furnace Slag in Portland Cement Blends Hydrated under Different Conditions." *Cement and Concrete Research* 31 (10): 1403–9. https://doi.org/10.1016/S0008-8846(01)00587-7.

Farmer, Robert W., and James R. Beckman. 1984. "Particle Size Distribution Analysis of Blended Solids by a Modified Andreasen Pipet Method." *Industrial & Engineering Chemistry Process Design and Development* 23 (2): 341–43. https://doi.org/10.1021/i200025a027.

Feng, X., E. J. Garboczi, D. P. Bentz, P. E. Stutzman, and T. O. Mason. 2004. "Estimation of the Degree of Hydration of Blended Cement Pastes by a Scanning Electron Microscope Point-Counting Procedure." *Cement and Concrete Research* 34 (10): 1787–93. https://doi.org/10.1016/j.cemconres.2004.01.014.

Fernandes, Fabio, Shilpa Manari, Mathew Aguayo, Kevin Santos, Tandre Oey, Zhenhua Wei, Gabriel Falzone, Narayanan Neithalath, and Gaurav Sant. 2014. "On the Feasibility of Using Phase Change Materials (PCMs) to Mitigate Thermal Cracking in Cementitious Materials." *Cement and Concrete Composites* 51 (August): 14–26. https://doi.org/10.1016/j.cemconcomp.2014.03.003.

"Fillers in Action: How to Achieve High Particle Loadings." 2015. *Polymer Innovation Blog* (blog). December 7, 2015. http://polymerinnovationblog.com/fillers-action-achieve-high-particle-loadings/.

Flatt, Robert J., and Paul Bowen. 2006. "Yodel: A Yield Stress Model for Suspensions." *Journal of the American Ceramic Society* 89 (4): 1244–56. https://doi.org/10.1111/j.1551-2916.2005.00888.x.

———. 2007. "Yield Stress of Multimodal Powder Suspensions: An Extension of the YODEL (Yield Stress MODEL)." *Journal of the American Ceramic Society* 90 (4): 1038–44. https://doi.org/10.1111/j.1551-2916.2007.01595.x.

Frohnsdorff, Geoffrey. 1986. *Blended Cements: A Symposium*. ASTM International.

Fu, G., and W. Dekelbab. 2003. "3-D Random Packing of Polydisperse Particles and Concrete Aggregate Grading." *Powder Technology* 133 (1): 147–55. https://doi.org/10.1016/S0032-5910(03)00082-2.

Gallucci, E., P. Mathur, and K. Scrivener. 2010. "Microstructural Development of Early Age Hydration Shells around Cement Grains." *Cement and Concrete Research* 40 (1): 4–13.

Ge, Zhi. 2005. "Predicting Temperature and Strength Development of the Field Concrete." http://lib.dr.iastate.edu/rtd/1730/.

Gesoglu, Mehmet, Erhan Güneyisi, Guler Fakhraddin Muhyaddin, and Diler Sabah Asaad. 2016. "Strain Hardening Ultra-High Performance Fiber Reinforced Cementitious Composites: Effect of Fiber Type and Concentration." *Composites Part B: Engineering* 103 (October): 74–83. https://doi.org/10.1016/j.compositesb.2016.08.004.

Ghafari, Ehsan, Mahdi Arezoumandi, Hugo Costa, and Eduardo Júlio. 2015. "Influence of Nano-Silica Addition on Durability of UHPC." *Construction and Building Materials* 94 (September): 181–88. https://doi.org/10.1016/j.conbuildmat.2015.07.009.

Ghafari, Ehsan, Hugo Costa, and Eduardo Júlio. 2015. "Statistical Mixture Design Approach for Eco-Efficient UHPC." *Cement and Concrete Composites* 55 (January): 17–25. https://doi.org/10.1016/j.cemconcomp.2014.07.016.

Ghafari, Ehsan, Hugo Costa, Eduardo Júlio, António Portugal, and Luisa Durães. 2012. "Optimization of UHPC by Adding Nanomaterials." In *Proceedings of 3rd International Symposium on Ultra-High-Performance Concrete and Nanotechnology for High Performance Construction Materials Kassel (Germany)*, 71–8. https://books.google.com/books?hl=en&lr=&id=LufCDwJ-sacC&oi=fnd&pg=PA71&dq=optimization+of+UHPC+by+adding+nanomaterials&ots=b3vHtOtO4s&sig=ukL-ei9dcXN5s36Sl4JpzeEk17Y.

———. 2014. "The Effect of Nanosilica Addition on Flowability, Strength and Transport Properties of Ultra High Performance Concrete." *Materials & Design* 59 (July): 1–9. https://doi.org/10.1016/j.matdes.2014.02.051.

Goltermann, Per, Vagn Johansen, and Lars Palbøl. 1997. "Packing of Aggregates: An Alternative Tool to Determine the Optimal Aggregate Mix." *Materials Journal* 94 (5): 435–43. https://doi.org/10.14359/328.

Graybeal, B. 2011. "FHWA TECHNOTE: Ultra High Performance Concrete." *FHWA Publication No: FHWA-HRT-11-038: Federal Highway Administration*.

Graybeal, Ben. 2011. "Ultra-High Performance Concrete." *Technote*, March. https://trid.trb.org/view.aspx?id=1104239.

Graybeal, Benjamin A. 2006. "Material Property Characterization of Ultra-High Performance Concrete," August. https://trid.trb.org/view.aspx?id=798080.

———. 2010. "Behavior of Field-Cast Ultra-High Performance Concrete Bridge Deck Connections under Cyclic and Static Structural Loading." United States. Federal Highway Administration.

———. 2011. "Fatigue Response in Bridge Deck Connection Composed of Field-Cast Ultra-High-Performance Concrete." *Transportation Research Record*, no. 2251: 93–100. https://doi.org/10.3141/2251-10.

———. 2012. *Ultra-High Performance Concrete Composite Connections for Precast Concrete Bridge Decks*. US Department of Transportation, Federal Highway Administration.

Graybeal, Benjamin, and Jussara Tanesi. 2007. "Durability of an Ultrahigh-Performance Concrete." *Journal of Materials in Civil Engineering* 19 (10): 848–54. https://doi.org/10.1061/(ASCE)0899-1561(2007)19:10(848).

Grünewald, Steffen. 2004. *Performance-Based Design of Self-Compacting Fibre Reinforced Concrete*. TU Delft, Delft University of Technology. http://repository.tudelft.nl/view/ir/uuid:07a817aa-cba1-4c93-bbed-40a5645cf0f1/.

Guillermo Puerta-Falla, Magdalena Balonis, Gwenn Le Saout, Gabriel Falzone, Aditya Kumar, Carolyn Zhang, Narayanan Neithalath, and Gaurav Sant. 2015. "The Influence of the Aluminous Source on Enhancing Limestone Reactivity in Cementitious Materials." *Journal of the American Ceramic Society*.

Habel, Katrin, Marco Viviani, Emmanuel Denarié, and Eugen Brühwiler. 2006. "Development of the Mechanical Properties of an Ultra-High Performance Fiber Reinforced Concrete (UHPFRC)." *Cement and Concrete Research* 36 (7): 1362–70. https://doi.org/10.1016/j.cemconres.2006.03.009.

Hakala, M., H. Kuula, and J. A. Hudson. 2007. "Estimating the Transversely Isotropic Elastic Intact Rock Properties for in Situ Stress Measurement Data Reduction: A Case Study of the Olkiluoto Mica Gneiss, Finland." *International Journal of Rock Mechanics and Mining Sciences* 44 (1): 14–46. https://doi.org/10.1016/j.ijrmms.2006.04.003.

Hakala, Matti, and Esa Heikkilä. 1997. "Summary Report-Development of Laboratory Tests and the Stress-Strain Behaviour of Olkiluoto Mica Gneiss." Posiva Oy.

Hallbauer, D. K., H. Wagner, and N. G. W. Cook. 1973. "Some Observations Concerning the Microscopic and Mechanical Behaviour of Quartzite Specimens in Stiff, Triaxial Compression Tests." *International Journal of Rock Mechanics and Mining Sciences &*

Geomechanics Abstracts 10 (6): 713–26. https://doi.org/10.1016/0148-9062(73)90015-6.

Han, Sang-Hun, and Jin-Keun Kim. 2004. "Effect of Temperature and Age on the Relationship between Dynamic and Static Elastic Modulus of Concrete." *Cement and Concrete Research* 34 (7): 1219–27. https://doi.org/10.1016/j.cemconres.2003.12.011.

Hariri, A. S., and I. C. Ward. 1988. "A Review of Thermal Storage Systems Used in Building Applications." *Building and Environment* 23 (1): 1–10. https://doi.org/10.1016/0360-1323(88)90011-X.

Hashida, Hiroshi, and Nobuyuki Yamazaki. 2002. "Deformation Composed of Autogenous Shrinkage and Thermal Expansion Due to Hydration of High-Strength Concrete and Stress in Reinforced Structures." *Proc. of Self-Desiccation and Its Importance in Concrete Technology*, 77–92.

Hassan, A. M. T., S. W. Jones, and G. H. Mahmud. 2012. "Experimental Test Methods to Determine the Uniaxial Tensile and Compressive Behaviour of Ultra High Performance Fibre Reinforced Concrete (UHPFRC)." *Construction and Building Materials*, Non Destructive Techniques for Assessment of Concrete, 37 (December): 874–82. https://doi.org/10.1016/j.conbuildmat.2012.04.030.

Hawes, D. W., D. Banu, and D. Feldman. 1990. "Latent Heat Storage in Concrete. II." *Solar Energy Materials* 21 (1): 61–80.

Hawes, D. W., D. Feldman, and D. Banu. 1993. "Latent Heat Storage in Building Materials." *Energy and Buildings* 20 (1): 77–86. https://doi.org/10.1016/0378-7788(93)90040-2.

Hawkins, Peter, Paul Tennis, and Rachel Detwiler. n.d. "The Use of Limestone in Portland Cement: A State-of-the-Art Review." http://cement.org/astmc01/EB227.pdf.

Hearn, Nataliya. 1999. "Effect of Shrinkage and Load-Induced Cracking on Water Permeability of Concrete." *Materials Journal* 96 (2): 234–41. https://doi.org/10.14359/450.

HIPERPAV, II. n.d. *High Performance Concrete Paving Software, Transtec Inc., Austin, Tex., July 2007*.

Honarvar, Ebadollah, Sri Sritharan, Jon Matthews Rouse, and Sriram Aaleti. 2016. "Bridge Decks with Precast UHPC Waffle Panels: A Field Evaluation and Design Optimization." *Journal of Bridge Engineering* 21 (1): 04015030. https://doi.org/10.1061/(ASCE)BE.1943-5592.0000775.

Huang, Huanghuang, Xiaojian Gao, Hui Wang, and Huan Ye. 2017. "Influence of Rice Husk Ash on Strength and Permeability of Ultra-High Performance Concrete." *Construction and Building Materials* 149 (Supplement C): 621–28. https://doi.org/10.1016/j.conbuildmat.2017.05.155.

Huang, Wei, Hadi Kazemi-Kamyab, Wei Sun, and Karen Scrivener. 2017a. "Effect of Replacement of Silica Fume with Calcined Clay on the Hydration and Microstructural Development of Eco-UHPFRC." *Materials & Design* 121: 36–46.

———. 2017b. "Effect of Cement Substitution by Limestone on the Hydration and Microstructural Development of Ultra-High Performance Concrete (UHPC)." *Cement and Concrete Composites* 77 (March): 86–101. https://doi.org/10.1016/j.cemconcomp.2016.12.009.

Hwang, C.L., and C.Y. Lin. 1986. "STRENGTH DEVELOPMENT OF BLENDED BLAST FURNACE SLAG CEMENT MORTARS." In , 2:1323–40.

Ingram, Kevin D., and Kenneth E. Daugherty. 1991. "Special Issue on Blended CementsA Review of Limestone Additions to Portland Cement and Concrete." *Cement and Concrete Composites* 13 (3): 165–70. https://doi.org/10.1016/0958-9465(91)90016-B.

Irassar, E. F., D. Violini, V. F. Rahhal, C. Milanesi, M. A. Trezza, and V. L. Bonavetti. 2011. "Influence of Limestone Content, Gypsum Content and Fineness on Early Age Properties of Portland Limestone Cement Produced by Inter-Grinding." *Cement and Concrete Composites* 33 (2): 192–200. https://doi.org/10.1016/j.cemconcomp.2010.10.001.

Jones, R., and I. Fącąoaru. 1969. "Recommendations for Testing Concrete by the Ultrasonic Pulse Method." *Matériaux et Constructions* 2 (4): 275–84. https://doi.org/10.1007/BF02475162.

Khayat, K. H. 1999. "Workability, Testing, and Performance of Self-Consolidating Concrete." *Materials Journal* 96 (3): 346–53. https://doi.org/10.14359/632.

Khudhair, Amar M., and Mohammed M. Farid. 2004. "A Review on Energy Conservation in Building Applications with Thermal Storage by Latent Heat Using Phase Change Materials." *Energy Conversion and Management* 45 (2): 263–75. https://doi.org/10.1016/S0196-8904(03)00131-6.

Kim, Min Sik, Yubin Jun, Changha Lee, and Jae Eun Oh. 2013. "Use of CaO as an Activator for Producing a Price-Competitive Non-Cement Structural Binder Using Ground Granulated Blast Furnace Slag." *Cement and Concrete Research* 54 (December): 208–14. https://doi.org/10.1016/j.cemconres.2013.09.011.

Kirk Vance, Narayanan Neithalath, and Gaurav Sant. 2013. "Hydration and Strength Development in Ternary Portland Cement Blends Containing Limestone and Fly Ash or Metakaolin." *Under Review*.

Kolani, B., L. Buffo-Lacarrière, A. Sellier, G. Escadeillas, L. Boutillon, and L. Linger. 2012. "Hydration of Slag-Blended Cements." *Cement and Concrete Composites* 34 (9): 1009–18. https://doi.org/10.1016/j.cemconcomp.2012.05.007.

Komloš, K., S. Popovics, T. Nürnbergerová, B. Babál, and J. S. Popovics. 1996. "Ultrasonic Pulse Velocity Test of Concrete Properties as Specified in Various Standards." *Cement and Concrete Composites* 18 (5): 357–64. https://doi.org/10.1016/0958-9465(96)00026-1.

Kumar, Aditya, Tandre Oey, Guillermo Puerta Falla, Ryan Henkensiefken, Narayanan Neithalath, and Gaurav Sant. 2013. "A Comparison of Intergrinding and Blending Limestone on Reaction and Strength Evolution in Cementitious Materials." *Construction and Building Materials* 43 (June): 428–35. https://doi.org/10.1016/j.conbuildmat.2013.02.032.

Kumar, Aditya, Tandre Oey, Seohyun Kim, Davis Thomas, Sondos Badran, Jialin Li, Fabio Fernandes, Narayanan Neithalath, and Gaurav Sant. 2013. "Simple Methods to Estimate the Influence of Limestone Fillers on Reaction and Property Evolution in Cementitious Materials." *Cement and Concrete Composites* 42 (September): 20–29. https://doi.org/10.1016/j.cemconcomp.2013.05.002.

Kumar, Rakesh, and B. Bhattacharjee. 2003a. "Study on Some Factors Affecting the Results in the Use of MIP Method in Concrete Research." *Cement and Concrete Research* 33 (3): 417–424.

Kumar, Rakesh, and B Bhattacharjee. 2003b. "Study on Some Factors Affecting the Results in the Use of MIP Method in Concrete Research." *Cement and Concrete Research* 33 (3): 417–24. https://doi.org/10.1016/S0008-8846(02)00974-2.

Kwan, A. K. H., and W. W. S. Fung. 2009. "Packing Density Measurement and Modelling of Fine Aggregate and Mortar." *Cement and Concrete Composites* 31 (6): 349–57. https://doi.org/10.1016/j.cemconcomp.2009.03.006.

Lamond, Jf, and Jh Pielert, eds. 2006. *Significance of Tests and Properties of Concrete and Concrete-Making Materials*. 100 Barr Harbor Drive, PO Box C700, West Conshohocken, PA 19428-2959: ASTM International. http://www.astm.org/doiLink.cgi?STP169D-EB.

Lange, F., H. Mörtel, and V. Rudert. 1997. "Dense Packing of Cement Pastes and Resulting Consequences on Mortar Properties." *Cement and Concrete Research*, Materials Research Society Symposium on Structure-Property Relationships in Hardened Cement Paste

and Composites, 27 (10): 1481–88. https://doi.org/10.1016/S0008-8846(97)00189-0.

Larrard, F. de, and T. Sedran. 1994a. "Optimization of Ultra-High-Performance Concrete by the Use of a Packing Model." *Cement and Concrete Research* 24 (6): 997–1009. https://doi.org/10.1016/0008-8846(94)90022-1.

———. 1994b. "Optimization of Ultra-High-Performance Concrete by the Use of a Packing Model." *Cement and Concrete Research* 24 (6): 997–1009. https://doi.org/10.1016/0008-8846(94)90022-1.

Le, Ha Thanh, Matthias Müller, Karsten Siewert, and Horst-Michael Ludwig. 2015. "The Mix Design for Self-Compacting High Performance Concrete Containing Various Mineral Admixtures." *Materials & Design* 72 (May): 51–62. https://doi.org/10.1016/j.matdes.2015.01.006.

Le Hoang, An, and Ekkehard Fehling. 2017. "Influence of Steel Fiber Content and Aspect Ratio on the Uniaxial Tensile and Compressive Behavior of Ultra High Performance Concrete." *Construction and Building Materials* 153 (Supplement C): 790–806. https://doi.org/10.1016/j.conbuildmat.2017.07.130.

Lecomte, André. 2006a. "The Measurement of Real and Virtual Packing Density of Soft Grains." *Materials and Structures* 39 (1): 63–80.

———. 2006b. "The Measurement of Real and Virtual Packing Density of Soft Grains." *Materials and Structures* 39 (1): 63–80.

Lee, N. K., K. T. Koh, S. H. Park, and G. S. Ryu. 2017. "Microstructural Investigation of Calcium Aluminate Cement-Based Ultra-High Performance Concrete (UHPC) Exposed to High Temperatures." *Cement and Concrete Research* 102 (Supplement C): 109–18. https://doi.org/10.1016/j.cemconres.2017.09.004.

Li, Wengui, Zhengyu Huang, Fangliang Cao, Zhihui Sun, and Surendra P. Shah. 2015. "Effects of Nano-Silica and Nano-Limestone on Flowability and Mechanical Properties of Ultra-High-Performance Concrete Matrix." *Construction and Building Materials* 95 (October): 366–74. https://doi.org/10.1016/j.conbuildmat.2015.05.137.

Li, Zhengqi, Harish Kizhakkumodom Venkata, and Prasada Rao Rangaraju. 2015. "Influence of Silica Flour–Silica Fume Combination on the Properties of High Performance Cementitious Mixtures at Ambient Temperature Curing." *Construction and Building Materials* 100 (Supplement C): 225–33. https://doi.org/10.1016/j.conbuildmat.2015.09.042.

Liabastre, Albert A, and Clyde Orr. 1978. "An Evaluation of Pore Structure by Mercury Penetration." *Journal of Colloid and Interface Science* 64 (1): 1–18. https://doi.org/10.1016/0021-9797(78)90329-6.

Lothenbach, Barbara, Karen Scrivener, and R. D. Hooton. 2011. "Supplementary Cementitious Materials." *Cement and Concrete Research*, Conferences Special: Cement Hydration Kinetics and Modeling, Quebec City, 2009 & CONMOD10, Lausanne, 2010, 41 (12): 1244–56. https://doi.org/10.1016/j.cemconres.2010.12.001.

Lothenbach, Barbara, and Frank Winnefeld. 2006. "Thermodynamic Modelling of the Hydration of Portland Cement." *Cement and Concrete Research* 36 (2): 209–26. https://doi.org/10.1016/j.cemconres.2005.03.001.

Macedo, Vanessa Cruz, André Luis Faria e Silva, and Luis Roberto Marcondes Martins. 2010. "Effect of Cement Type, Relining Procedure, and Length of Cementation on Pull-out Bond Strength of Fiber Posts." *Journal of Endodontics* 36 (9): 1543–1546.

Magureanu, Cornelia, Ioan Sosa, Camelia Negrutiu, and Bogdan Heghes. 2012. "Mechanical Properties and Durability of Ultra-High-Performance Concrete." *Materials Journal* 109 (2): 177–84.

Markovic, Ivan. 2006. "High-Performance Hybrid-Fibre Concrete: Development and Utilisation." TU Delft, Delft University of Technology. http://repository.tudelft.nl/view/ir/uuid:44ed51cd-fc27-4353-ab81-cf8348f52443/.

Martin, C. D., and N. A. Chandler. 1994. "The Progressive Fracture of Lac Du Bonnet Granite." *International Journal of Rock Mechanics and Mining Sciences & Geomechanics Abstracts* 31 (6): 643–59. https://doi.org/10.1016/0148-9062(94)90005-1.

Matschei, T., B. Lothenbach, and F. P. Glasser. 2007a. "The AFm Phase in Portland Cement." *Cement and Concrete Research* 37 (2): 118–30. https://doi.org/10.1016/j.cemconres.2006.10.010.

———. 2007b. "The Role of Calcium Carbonate in Cement Hydration." *Cement and Concrete Research* 37 (4): 551–58. https://doi.org/10.1016/j.cemconres.2006.10.013.

Matschei, T., B. Lothenbach, and F.P. Glasser. 2007c. "The Role of Calcium Carbonate in Cement Hydration." *Cement and Concrete Research* 37 (4): 551–58. https://doi.org/16/j.cemconres.2006.10.013.

Maya, L. F., and B. Graybeal. 2017. "Experimental Study of Strand Splice Connections in UHPC for Continuous Precast Prestressed Concrete Bridges." *Engineering Structures* 133 (Supplement C): 81–90. https://doi.org/10.1016/j.engstruct.2016.12.018.

Menéndez, G, V Bonavetti, and E. F Irassar. 2003. "Strength Development of Ternary Blended Cement with Limestone Filler and Blast-Furnace Slag." *Cement and Concrete Composites* 25 (1): 61–67. https://doi.org/10.1016/S0958-9465(01)00056-7.

Meng, Weina, and Kamal H. Khayat. 2016. "Mechanical Properties of Ultra-High-Performance Concrete Enhanced with Graphite Nanoplatelets and Carbon Nanofibers." *Composites Part B: Engineering* 107 (December): 113–22. https://doi.org/10.1016/j.compositesb.2016.09.069.

Minard, Hélène, Sandrine Garrault, Laure Regnaud, and André Nonat. 2007. "Mechanisms and Parameters Controlling the Tricalcium Aluminate Reactivity in the Presence of Gypsum." *Cement and Concrete Research* 37 (10): 1418–1426.

Mobasher, B., and Cheng Yu Li. 1996. "Effect of Interfacial Properties on the Crack Propagation in Cementitious Composites." *Advanced Cement Based Materials* 4 (3): 93–105. https://doi.org/10.1016/S1065-7355(96)90078-4.

Mohamed, Ashraf, and Will Hansen. 1997. "Effect of Nonlinear Temperature Gradient on Curling Stress in Concrete Pavements." *Transportation Research Record: Journal of the Transportation Research Board* 1568 (January): 65–71. https://doi.org/10.3141/1568-08.

Molina, Larissa. 1992. *On Predicting the Influence of Curing Conditions on the Degree of Hydration*. Cement och Betong Institututet.

Mooney, M. 1951. "The Viscosity of a Concentrated Suspension of Spherical Particles." *Journal of Colloid Science* 6 (2): 162–70. https://doi.org/10.1016/0095-8522(51)90036-0.

Moro, F., and H. Böhni. 2002a. "Ink-Bottle Effect in Mercury Intrusion Porosimetry of Cement-Based Materials." *Journal of Colloid and Interface Science* 246 (1): 135–149.

———. 2002b. "Ink-Bottle Effect in Mercury Intrusion Porosimetry of Cement-Based Materials." *Journal of Colloid and Interface Science* 246 (1): 135–49. https://doi.org/10.1006/jcis.2001.7962.

Moser, B, C Pfeifer, and J Stark. 2009. "Durability and Microstructural Development during Hydration in Ultra-High Performance Concrete." *London, UK: Taylor and Francis Group*, 87–88.

Muhd Norhasri, M. S., M. S. Hamidah, A. Mohd Fadzil, and O. Megawati. 2016. "Inclusion of Nano Metakaolin as Additive in Ultra High Performance Concrete (UHPC)." *Construction and Building Materials* 127 (November): 167–75. https://doi.org/10.1016/j.conbuildmat.2016.09.127.

Naaman, Antoine E., George G. Namur, Jamil M. Alwan, and Husam S. Najm. 1991. "Fiber Pullout and Bond Slip. I: Analytical Study." *Journal of Structural Engineering* 117 (9): 2769–2790.

Nauman, E. Bruce, and Timothy J. Cavanaugh. 1998. "Method of Calculating True Particle Size Distributions from Observed Sizes in a Thin Section." *Microscopy and Microanalysis* 4 (02): 122–127. https://doi.org/10.1017/S1431927698980102.

Navi, Parviz, and Christian Pignat. 1996. "Simulation of Cement Hydration and the Connectivity of the Capillary Pore Space." *Advanced Cement Based Materials* 4 (2): 58–67. https://doi.org/10.1016/S1065-7355(96)90052-8.

Neithalath, Narayanan, and Jitendra Jain. 2010. "Relating Rapid Chloride Transport Parameters of Concretes to Microstructural Features Extracted from Electrical Impedance." *Cement and Concrete Research* 40 (7): 1041–51. https://doi.org/10.1016/j.cemconres.2010.02.016.

Neville, Adam M. 1995. *Properties of Concrete*. https://trid.trb.org/view.aspx?id=454875.

Ngab, Ali S., Floyd O. Slate, and Arthur H. Nilson. 1981. "Microcracking and Time-Dependent Strains in High Strength Concrete." *Journal Proceedings* 78 (4): 262–68. https://doi.org/10.14359/6923.

Odler, Ivan. 2003. *Special Inorganic Cements*. CRC Press.

Oey, Tandré, Aditya Kumar, Jeffrey W. Bullard, Narayanan Neithalath, and Gaurav Sant. 2013. "The Filler Effect: The Influence of Filler Content and Surface Area on Cementitious Reaction Rates." *Journal of the American Ceramic Society* 96 (6): 1978–90. https://doi.org/10.1111/jace.12264.

Olhero, S. M, and J. M. F Ferreira. 2004. "Influence of Particle Size Distribution on Rheology and Particle Packing of Silica-Based Suspensions." *Powder Technology* 139 (1): 69–75. https://doi.org/10.1016/j.powtec.2003.10.004.

Olivier, Jos G.J., Greet Janssens-Maenhout, Marilena Muntean, and Jeroen A.H.W. Peters. 2016. "Trends in Global CO2 Emissions: 2016 Report." PBL Netherlands Environmental Assessment Agency.

Osborne, G. J. 1999. "Durability of Portland Blast-Furnace Slag Cement Concrete." *Cement and Concrete Composites* 21 (1): 11–21. https://doi.org/10.1016/S0958-9465(98)00032-8.

Pal, S. C, A Mukherjee, and S. R Pathak. 2003. "Investigation of Hydraulic Activity of Ground Granulated Blast Furnace Slag in Concrete." *Cement and Concrete Research* 33 (9): 1481–86. https://doi.org/10.1016/S0008-8846(03)00062-0.

Pan, Bing, Kemao Qian, Huimin Xie, and Anand Asundi. 2009. "Two-Dimensional Digital Image Correlation for in-Plane Displacement and Strain Measurement: A Review." *Measurement Science and Technology* 20 (6): 062001. https://doi.org/10.1088/0957-0233/20/6/062001.

Pane, Ivindra, and Will Hansen. 2002. "Concrete Hydration and Mechanical Properties under Nonisothermal Conditions." *Materials Journal* 99 (6): 534–42.

———. 2005. "Investigation of Blended Cement Hydration by Isothermal Calorimetry and Thermal Analysis." *Cement and Concrete Research* 35 (6): 1155–64. https://doi.org/10.1016/j.cemconres.2004.10.027.

Park, Jung Jun, Su Tae Kang, Kyung Taek Koh, and Sung Wook Kim. 2008. "Influence of the Ingredients on the Compressive Strength of UHPC as a Fundamental Study to Optimize the Mixing Proportion." In *Proceedings of the International Symposium on Ultra-High Performance Concrete, Structural Materials and Engineering Series*, 105–12.

Pasupathy, A., L. Athanasius, R. Velraj, and R. V. Seeniraj. 2008. "Experimental Investigation and Numerical Simulation Analysis on the Thermal Performance of a Building Roof Incorporating Phase Change Material (PCM) for Thermal Management." *Applied Thermal Engineering* 28 (5): 556–65. https://doi.org/10.1016/j.applthermaleng.2007.04.016.

Pedersen, J. S. 1994. "Determination of Size Distribution from Small-Angle Scattering Data for Systems with Effective Hard-Sphere Interactions." *Journal of Applied Crystallography* 27 (4): 595–608. https://doi.org/10.1107/S0021889893013810.

Pichler, Bernhard, and Christian Hellmich. 2011. "Upscaling Quasi-Brittle Strength of Cement Paste and Mortar: A Multi-Scale Engineering Mechanics Model." *Cement and Concrete Research* 41 (5): 467–76. https://doi.org/10.1016/j.cemconres.2011.01.010.

Pommersheim, James M., and James R. Clifton. 1979. "Mathematical Modeling of Tricalcium Silicate Hydration." *Cement and Concrete Research* 9 (6): 765–70. https://doi.org/10.1016/0008-8846(79)90072-3.

Poon, C. S., S. C. Kou, and L. Lam. 2006. "Compressive Strength, Chloride Diffusivity and Pore Structure of High Performance Metakaolin and Silica Fume Concrete." *Construction and Building Materials* 20 (10): 858–65. https://doi.org/10.1016/j.conbuildmat.2005.07.001.

Popovics, J. S., J. Zemajtis, and I. Shkolnik. 2008. "A Study of Static and Dynamic Modulus of Elasticity of Concrete." *ACI-CRC Final Report*.

Pötschke, Petra, Katrin Wallheinke, Andreas Janke, Cornelia Bellmann, Herbert Stutz, and Walter Heckmann. 1999. "Determination of Particle Size in Multiphase Blends by Different Methods." *Journal of Macromolecular Science, Part B* 38 (5–6): 527–39. https://doi.org/10.1080/00222349908248118.

Prem, Prabhat Ranjan, Avadhanam Ramachandra Murthy, and Bhajantri H. Bharatkumar. 2015. "Influence of Curing Regime and Steel Fibres on the Mechanical Properties of UHPC." *Magazine of Concrete Research* 67 (18): 1400333. https://doi.org/10.1680/macr.14.00333.

Puerta-Falla, Guillermo, Magdalena Balonis, Gwenn Le Saout, Gabriel Falzone, Carolyn Zhang, Narayanan Neithalath, and Gaurav Sant. 2015. "Elucidating the Role of the Aluminous Source on Limestone Reactivity in Cementitious Materials." *Journal of the American Ceramic Society* 98 (12): 4076–4089.

Randl, N., T. Steiner, S. Ofner, E. Baumgartner, and T. Mészöly. 2014. "Development of UHPC Mixtures from an Ecological Point of View." *Construction and Building Materials*, Concrete Sustainability, 67, Part C (September): 373–78. https://doi.org/10.1016/j.conbuildmat.2013.12.102.

Raphael, Jerome M. 1984. "Tensile Strength of Concrete." *Journal Proceedings* 81 (2): 158–65.

Reda, M. M, N. G Shrive, and J. E Gillott. 1999. "Microstructural Investigation of Innovative UHPC." *Cement and Concrete Research* 29 (3): 323–29. https://doi.org/10.1016/S0008-8846(98)00225-7.

Reinhardt, H. W., J. Blaauwendraad, and J. Jongedijk. 1982. "Temperature Development in Concrete Structures Taking Account of State Dependent Properties." In *International Conference on Concrete at Early Ages*. Vol. 1.

Reynolds, William C, and Henry C Perkins. 1977. *Engineering Thermodynamics*. New York: McGraw-Hill. http://books.google.com/books?id=m9FSAAAAMAAJ.

Richardson, I. G., and G. W. Groves. 1992. "Microstructure and Microanalysis of Hardened Cement Pastes Involving Ground Granulated Blast-Furnace Slag." *Journal of Materials Science* 27 (22): 6204–12. https://doi.org/10.1007/BF01133772.

Riding, Kyle A., Jonathan L. Poole, Anton K. Schindler, Maria C. G. Juenger, and Kevin J. Folliard. 2014. "Statistical Determination of Cracking Probability for Mass Concrete." *Journal of Materials in Civil Engineering* 26 (9): 04014058. https://doi.org/10.1061/(ASCE)MT.1943-5533.0000947.

Riding, Kyle A., Jonathan L. Poole, Anton K. Schindler, Maria CG Juenger, and Kevin J. Folliard. 2007. "Temperature Boundary Condition Models for Concrete Bridge Members." *ACI Materials Journal* 104 (4): 379.

Roquier, G. 2016. "The 4-Parameter Compressible Packing Model (CPM) Including a New Theory about Wall Effect and Loosening Effect for Spheres." *Powder Technology* 302 (Supplement C): 247–53. https://doi.org/10.1016/j.powtec.2016.08.031.

Rosin, P., and E. Rammler. 1933. "The Laws Governing the Fineness of Powdered Coal." *J. Inst. Fuel.* 7: 29–36.

Rouquerol, J., D. Avnir, C. W. Fairbridge, D. H. Everett, J. M. Haynes, N. Pernicone, J. D. F. Ramsay, K. S. W. Sing, and K. K. Unger. 1994. "Recommendations for the Characterization of Porous Solids (Technical Report)." *Pure and Applied Chemistry* 66 (8): 1739–1758.

Roussel, N., C. Stefani, and R. Leroy. 2005. "From Mini-Cone Test to Abrams Cone Test: Measurement of Cement-Based Materials Yield Stress Using Slump Tests." *Cement and Concrete Research* 35 (5): 817–22. https://doi.org/10.1016/j.cemconres.2004.07.032.

Russell, Henry G., and Benjamin A. Graybeal. 2013. "Ultra-High Performance Concrete: A State-of-the-Art Report for the Bridge Community."

Saetta, Anna, Roberto Scotta, and Renato Vitaliani. 1995. "Stress Analysis of Concrete Structures Subjected to Variable Thermal Loads." *Journal of Structural Engineering* 121 (3): 446–57. https://doi.org/10.1061/(ASCE)0733-9445(1995)121:3(446).

Saleem, Muhammad Azhar, Amir Mirmiran, Jun Xia, and Kevin Mackie. 2011. "Ultra-High-Performance Concrete Bridge Deck Reinforced with High-Strength Steel." *Aci Structural Journal* 108 (5): 601–9.

Sarı, Ahmet, and Ali Karaipekli. 2007. "Thermal Conductivity and Latent Heat Thermal Energy Storage Characteristics of Paraffin/Expanded Graphite Composite as Phase Change Material." *Applied Thermal Engineering* 27 (8–9): 1271–77. https://doi.org/10.1016/j.applthermaleng.2006.11.004.

Šavija, Branko, and Erik Schlangen. 2016. "Use of Phase Change Materials (PCMs) to Mitigate Early Age Thermal Cracking in Concrete: Theoretical Considerations." *Construction and Building Materials* 126 (November): 332–44. https://doi.org/10.1016/j.conbuildmat.2016.09.046.

Schachinger, Ingo, Karl Schmidt, Detlef Heinz, and Peter Schiebl. 2002. "Early-Age Cracking Risk and Relaxation by Restrained Autogenous Deformation of Ultra High

Performance Concrete." In *Proc. of the 6 International Symposium on Utilization of High Strength / High Performance Concrete*, 16–20. Leipzig.

Schindler, A. K., J. M. Ruiz, R. O. Rasmussen, G. K. Chang, and L. G. Wathne. 2004. "Concrete Pavement Temperature Prediction and Case Studies with the FHWA HIPERPAV Models." *Cement and Concrete Composites*, Early Age Concrete - Properties and Performance, 26 (5): 463–71. https://doi.org/10.1016/S0958-9465(03)00075-1.

Schindler, Anton K. 2004. "Effect of Temperature on Hydration of Cementitious Materials." *Materials Journal* 101 (1): 72–81.

Schindler, Anton K., and Kevin J. Folliard. 2003. "Influence of Supplementary Cementing Materials on the Heat of Hydration of Concrete." In *Advances in Cement and Concrete IX Conference, Copper Mountain Conference Resort in Colorado*. https://www.researchgate.net/profile/Kevin_Folliard/publication/228593908_Influence_of_supplementary_cementing_materials_on_the_heat_of_hydration_of_concrete/links/0c9605329b61bf03fd000000.pdf.

———. 2005. "Heat of Hydration Models for Cementitious Materials." *Materials Journal* 102 (1): 24–33.

Schindler, Anton Karel. 2011. "Concrete Hydration, Temperature Development, and Setting at Early-Ages." https://utexas-ir.tdl.org/handle/2152/11145.

Schöppel, K., and R. Springenschmid. 1995. "The Effect of Thermal Deformation, Chemical Shrinkage and Swelling on Restraint Stresses in Concrete at Early Ages." In *RILEM PROCEEDINGS*, 213–213. CHAPMAN & HALL.

Schossig, P., H. -M. Henning, S. Gschwander, and T. Haussmann. 2005. "Micro-Encapsulated Phase-Change Materials Integrated into Construction Materials." *Solar Energy Materials and Solar Cells*, EuroSun2004EuroSun2004, 89 (2–3): 297–306. https://doi.org/10.1016/j.solmat.2005.01.017.

Sezera, Inan, O. Çopuroglu, and K. Ramyar. 2010. "Microstructure of 2 and 28-Day Cured Portland Limestone Cement Pastes," 289–94.

Shafieifar, Mohamadreza, Mahsa Farzad, and Atorod Azizinamini. 2017. "Experimental and Numerical Study on Mechanical Properties of Ultra High Performance Concrete (UHPC)." *Construction and Building Materials* 156 (Supplement C): 402–11. https://doi.org/10.1016/j.conbuildmat.2017.08.170.

Shapiro, M. M., D. Feldman, D. Hawes, and DPCM Banu. 1987. "Thermal Storage in Drywall Using Organic Phase-Change Material." *Passive Sol. J.;(United States)* 4 (4).

Shi, Dexiang, and Douglas N. Winslow. 1985. "Contact Angle and Damage during Mercury Intrusion into Cement Paste." *Cement and Concrete Research* 15 (4): 645–54. https://doi.org/10.1016/0008-8846(85)90064-X.

Shilei, Lv, Zhu Neng, and Feng Guohui. 2006. "Impact of Phase Change Wall Room on Indoor Thermal Environment in Winter." *Energy and Buildings* 38 (1): 18–24. https://doi.org/10.1016/j.enbuild.2005.02.007.

Skazlić, Marijan, Marijana Serdar, and Dubravka Bjegović. 2008. "Influence of Test Specimen Geometry on Compressive Strength of Ultra High Performance Concrete." In . http://bib.irb.hr/prikazi-rad?rad=326094.

Sobolev, Konstantin. 2004. "The Development of a New Method for the Proportioning of High-Performance Concrete Mixtures." *Cement and Concrete Composites* 26 (7): 901–7. https://doi.org/10.1016/j.cemconcomp.2003.09.002.

Sobuz, H. R., P. Visintin, M. S. Mohamed Ali, M. Singh, M. C. Griffith, and A. H. Sheikh. 2016. "Manufacturing Ultra-High Performance Concrete Utilising Conventional Materials and Production Methods." *Construction and Building Materials* 111 (May): 251–61. https://doi.org/10.1016/j.conbuildmat.2016.02.102.

Soliman, N. A., and A. Tagnit-Hamou. 2016. "Development of Ultra-High-Performance Concrete Using Glass Powder – Towards Ecofriendly Concrete." *Construction and Building Materials* 125 (October): 600–612. https://doi.org/10.1016/j.conbuildmat.2016.08.073.

Soliman, Nancy A., and Arezki Tagnit-Hamou. 2017. "Using Glass Sand as an Alternative for Quartz Sand in UHPC." *Construction and Building Materials* 145 (Supplement C): 243–52. https://doi.org/10.1016/j.conbuildmat.2017.03.187.

Sorelli, Luca, Georgios Constantinides, Franz-Josef Ulm, and François Toutlemonde. 2008. "The Nano-Mechanical Signature of Ultra High Performance Concrete by Statistical Nanoindentation Techniques." *Cement and Concrete Research* 38 (12): 1447–1456.

Soroka, I., and N. Setter. 1977. "The Effect of Fillers on Strength of Cement Mortars." *Cement and Concrete Research* 7 (4): 449–456.

Springenschmid, R. 1994. *Thermal Cracking in Concrete at Early Ages: Proceedings of the International RILEM Symposium*. CRC Press.

"Standard Guide for Testing the Thermal Properties of Advanced Ceramics." 2013.

Stovall, T., F. De Larrard, and M. Buil. 1986. "Linear Packing Density Model of Grain Mixtures." *Powder Technology* 48 (1): 1–12.

Stovall, T., F. de Larrard, and M. Buil. 1986. "Linear Packing Density Model of Grain Mixtures." *Powder Technology* 48 (1): 1–12. https://doi.org/10.1016/0032-5910(86)80058-4.

Stroeven, Piet, and Martijn Stroeven. 1999. "Assessment of Packing Characteristics by Computer Simulation." *Cement and Concrete Research* 29 (8): 1201–6. https://doi.org/10.1016/S0008-8846(99)00020-4.

Su, Nan, Kung-Chung Hsu, and His-Wen Chai. 2001. "A Simple Mix Design Method for Self-Compacting Concrete." *Cement and Concrete Research* 31 (12): 1799–1807. https://doi.org/10.1016/S0008-8846(01)00566-X.

Tafraoui, Ahmed, Gilles Escadeillas, Soltane Lebaili, and Thierry Vidal. 2009. "Metakaolin in the Formulation of UHPC." *Construction and Building Materials* 23 (2): 669–74. https://doi.org/10.1016/j.conbuildmat.2008.02.018.

Tafraoui, Ahmed, Gilles Escadeillas, and Thierry Vidal. 2016. "Durability of the Ultra High Performances Concrete Containing Metakaolin." *Construction and Building Materials* 112 (June): 980–87. https://doi.org/10.1016/j.conbuildmat.2016.02.169.

Taylor, H. F. W. 1997. *Cement Chemistry*. Thomas Telford.

Tazarv, Mostafa, and M. Saiid Saiidi. 2015. "UHPC-Filled Duct Connections for Accelerated Bridge Construction of RC Columns in High Seismic Zones." *Engineering Structures* 99 (Supplement C): 413–22. https://doi.org/10.1016/j.engstruct.2015.05.018.

Thomas, Jeffrey J., Joseph J. Biernacki, Jeffrey W. Bullard, Shashank Bishnoi, Jorge S. Dolado, George W. Scherer, and Andreas Luttge. 2011. "Modeling and Simulation of Cement Hydration Kinetics and Microstructure Development." *Cement and Concrete Research*, Conferences Special: Cement Hydration Kinetics and Modeling, Quebec City, 2009 & CONMOD10, Lausanne, 2010, 41 (12): 1257–78. https://doi.org/10.1016/j.cemconres.2010.10.004.

Thomas, Jeffrey J., Hamlin M. Jennings, and Jeffrey J. Chen. 2009. "Influence of Nucleation Seeding on the Hydration Mechanisms of Tricalcium Silicate and Cement." *The Journal of Physical Chemistry C* 113 (11): 4327–4334.

Toufar, W., M. Born, and E. Klose. 1976. "Contribution of Optimisation of Components of Different Density in Polydispersed Particles Systems." *Freiberger Booklet A* 558: 29–44.

Tsivilis, S., G. Batis, E. Chaniotakis, Gr. Grigoriadis, and D. Theodossis. 2000. "Properties and Behavior of Limestone Cement Concrete and Mortar." *Cement and Concrete Research* 30 (10): 1679–83. https://doi.org/10.1016/S0008-8846(00)00372-0.

Tsivilis, S., E. Chaniotakis, E. Badogiannis, G. Pahoulas, and A. Ilias. 1999. "A Study on the Parameters Affecting the Properties of Portland Limestone Cements." *Cement and Concrete Composites* 21 (2): 107–16. https://doi.org/16/S0958-9465(98)00031-6.

Tutumluer, Erol, A. L. Al-Qadi, and others. 2009. "Bearing Capacity of Roads, Railways and Airfields (BCR2A'09)." In *International Conference on the Bearing Capacity of Roads, Railways and Airfields, 8th, 2009, Urbana, Illinois, USA*. https://trid.trb.org/view.aspx?id=1152387.

Van Tuan, Nguyen, Guang Ye, Klaas van Breugel, and Oguzhan Copuroglu. 2011. "Hydration and Microstructure of Ultra High Performance Concrete Incorporating Rice Husk Ash." *Cement and Concrete Research* 41 (11): 1104–11. https://doi.org/10.1016/j.cemconres.2011.06.009.

Vance, Kirk. 2014. "Early Age Characterization and Microstructural Features of Sustainable Binder Systems for Concrete." PhD Dissertation, Tempe, AZ: Arizona State University.

Vance, Kirk. 2014. "Early Age Characterization and Microstructural Features of Sustainable Binder Systems for Concrete." PhD Dissertation, Tempe, AZ: Arizona State University.

Vance, Kirk, Matthew Aguayo, Tandre Oey, Gaurav Sant, and Narayanan Neithalath. 2013. "Hydration and Strength Development in Ternary Portland Cement Blends Containing Limestone and Fly Ash or Metakaolin." *Cement and Concrete Composites* 39: 93–103.

Vance, Kirk, Aashay Arora, Gaurav Sant, and Narayanan Neithalath. 2015. "Rheological Evaluations of Interground and Blended Cement–Limestone Suspensions." *Construction and Building Materials* 79 (March): 65–72. https://doi.org/10.1016/j.conbuildmat.2014.12.054.

Vance, Kirk, Aditya Kumar, Gaurav Sant, and Narayanan Neithalath. 2013. "The Rheological Properties of Ternary Binders Containing Portland Cement, Limestone, and Metakaolin or Fly Ash." *Cement and Concrete Research* 52 (October): 196–207. https://doi.org/10.1016/j.cemconres.2013.07.007.

Vance, Kirk, Gaurav Sant, and Narayanan Neithalath. 2015. "The Rheology of Cementitious Suspensions: A Closer Look at Experimental Parameters and Property Determination Using Common Rheological Models." *Cement and Concrete Composites* 59 (May): 38–48. https://doi.org/10.1016/j.cemconcomp.2015.03.001.

Vendroux, G., and W. G. Knauss. 1998. "Submicron Deformation Field Measurements: Part 2. Improved Digital Image Correlation." *Experimental Mechanics* 38 (2): 86–92. https://doi.org/10.1007/BF02321649.

Vikan, Hedda, and Harald Justnes. 2007. "Rheology of Cementitious Paste with Silica Fume or Limestone." *Cement and Concrete Research* 37 (11): 1512–17. https://doi.org/10.1016/j.cemconres.2007.08.012.

Vítek, Jan L., Robert Coufal, and David Čítek. 2013. "UHPC – Development and Testing on Structural Elements." *Procedia Engineering*, CONCRETE AND CONCRETE STRUCTURES 2013 - 6th International Conference, Slovakia, 65 (Supplement C): 218–23. https://doi.org/10.1016/j.proeng.2013.09.033.

Voglis, N., G. Kakali, E. Chaniotakis, and S. Tsivilis. 2005. "Portland-Limestone Cements. Their Properties and Hydration Compared to Those of Other Composite Cements." *Cement and Concrete Composites*, Cement and Concrete Research in Greece, 27 (2): 191–96. https://doi.org/10.1016/j.cemconcomp.2004.02.006.

Vuk, T., V. Tinta, R. Gabrovšek, and V. Kaučič. 2001. "The Effects of Limestone Addition, Clinker Type and Fineness on Properties of Portland Cement." *Cement and Concrete Research* 31 (1): 135–39. https://doi.org/10.1016/S0008-8846(00)00427-0.

W. Chen, H. J. H. Brouwers. 2007. "The Hydration of Slag, Part 2: Reaction Models for Blended Cement." *Journal of Materials Science* 42 (2): 444–64. https://doi.org/10.1007/s10853-006-0874-1.

Wallevik, Jon Elvar. 2009. "Rheological Properties of Cement Paste: Thixotropic Behavior and Structural Breakdown." *Cement and Concrete Research* 39 (1): 14–29. https://doi.org/10.1016/j.cemconres.2008.10.001.

Wang, Aiqin, Chengzhi Zhang, and Ningsheng Zhang. 1997. "Study of the Influence of the Particle Size Distribution on the Properties of Cement." *Cement and Concrete Research* 27 (5): 685–95. https://doi.org/10.1016/S0008-8846(97)00060-4.

Wang, Chong, Changhui Yang, Fang Liu, Chaojun Wan, and Xincheng Pu. 2012. "Preparation of Ultra-High Performance Concrete with Common Technology and Materials." *Cement and Concrete Composites* 34 (4): 538–44. https://doi.org/10.1016/j.cemconcomp.2011.11.005.

Washburn, Edward W. 1921a. "Note on a Method of Determining the Distribution of Pore Sizes in a Porous Material." *Proceedings of the National Academy of Sciences of the United States of America*, 115–116.

———. 1921b. "Note on a Method of Determining the Distribution of Pore Sizes in a Porous Material." *Proceedings of the National Academy of Sciences of the United States of America* 7 (4): 115–16.

"Welcome to National Centers for Environmental Information (NCEI)." n.d. National Centers for Environmental Information (NCEI). Accessed August 27, 2016. https://www.ncei.noaa.gov/node.

Westergaard, H. M. 1927. "ANALYSIS OF STRESSES IN CONCRETE PAVEMENTS DUE TO VARIATIONS OF TEMPERATURE." *Highway Research Board Proceedings* 6. https://trid.trb.org/view.aspx?id=105055.

Wille, K., and C. Boisvert-Cotulio. 2013. "Development of Non-Proprietary Ultra-High Performance Concrete for Use in the Highway Bridge Sector." *Report No. PB2013-110587, National Technical Information Service, Springfield, VA*.

Wille, Kay, and Christopher Boisvert-Cotulio. 2015. "Material Efficiency in the Design of Ultra-High Performance Concrete." *Construction and Building Materials* 86 (July): 33–43. https://doi.org/10.1016/j.conbuildmat.2015.03.087.

Wille, Kay, Dong Joo Kim, and Antoine E. Naaman. 2011. "Strain-Hardening UHP-FRC with Low Fiber Contents." *Materials and Structures* 44 (3): 583–98. https://doi.org/10.1617/s11527-010-9650-4.

Wille, Kay, Antoine E. Naaman, Sherif El-Tawil, and Gustavo J. Parra-Montesinos. 2011. "Ultra-High Performance Concrete and Fiber Reinforced Concrete: Achieving Strength and Ductility without Heat Curing." *Materials and Structures* 45 (3): 309–24. https://doi.org/10.1617/s11527-011-9767-0.

Wille, Kay, Antoine E. Naaman, and Gustavo J. Parra-Montesinos. 2011. "Ultra-High Performance Concrete with Compressive Strength Exceeding 150 MPa (22 Ksi): A Simpler Way." *Materials Journal* 108 (1): 46–54.

Williamson, R. B. 1972. "Solidification of Portland Cement." *Progress in Materials Science* 15 (3): 189–286. https://doi.org/10.1016/0079-6425(72)90001-1.

Windslow, Douglas, and Sidney Diamond. 1969. "A Mercury Porosimetry Study of the Evolution of Porosity in Portland Cement : Technical Publication." *JTRP Technical Reports*, January. https://doi.org/10.5703/1288284314510.

Winslow, Douglas N., and S. Diamond. 1970. "A MERCURY POROSIMETRY STUDY OF THE POROSITY IN PORTLAND CEMENT." *Journal of Materials*. http://trid.trb.org/view.aspx?id=96627.

Wolfsdorf, T. L., W. H. Bender, and P. W. Voorhees. 1997. "The Morphology of High Volume Fraction Solid-Liquid Mixtures: An Application of Microstructural Tomography." *Acta Materialia* 45 (6): 2279–2295.

Worrell, E., L. Price, N. Martin, C. Hendriks, and L.O. Meida. 2001. "Carbon Dioxide Emissions from the Global Cement Industry." *Annual Review of Energy and the Environment* 26: 303–29. https://doi.org/10.1146/annurev.energy.26.1.303.

Wu, X., D. M. Roy, and C. A. Langton. 1983. "Early Stage Hydration of Slag-Cement." *Cement and Concrete Research* 13 (2): 277–86. https://doi.org/10.1016/0008-8846(83)90111-4.

Wu, Xuequan, Weimin Jiang, and D. M. Roy. 1990. "Early Activation and Properties of Slag Cement." *Cement and Concrete Research* 20 (6): 961–74. https://doi.org/10.1016/0008-8846(90)90060-B.

Xin, Dapeng, Dan G. Zollinger, and Ray W. James. 1992. "One-Dimensional Model for Analysis of CRC Pavement Growth." *Journal of Transportation Engineering* 118 (4): 557–75. https://doi.org/10.1061/(ASCE)0733-947X(1992)118:4(557).

Xu, Xu, Yinping Zhang, Kunping Lin, Hongfa Di, and Rui Yang. 2005. "Modeling and Simulation on the Thermal Performance of Shape-Stabilized Phase Change Material Floor Used in Passive Solar Buildings." *Energy and Buildings* 37 (10): 1084–91. https://doi.org/10.1016/j.enbuild.2004.12.016.

Yang, S. L., S. G. Millard, M. N. Soutsos, S. J. Barnett, and T. T. Le. 2009. "Influence of Aggregate and Curing Regime on the Mechanical Properties of Ultra-High Performance Fibre Reinforced Concrete (UHPFRC)." *Construction and Building Materials* 23 (6): 2291–98. https://doi.org/10.1016/j.conbuildmat.2008.11.012.

Yazıcı, Halit, Hüseyin Yiğiter, Anıl Ş Karabulut, and Bülent Baradan. 2008. "Utilization of Fly Ash and Ground Granulated Blast Furnace Slag as an Alternative Silica Source in Reactive Powder Concrete." *Fuel* 87 (12): 2401–2407.

Yi, Na-Hyun, Jang-Ho Jay Kim, Tong-Seok Han, Yun-Gu Cho, and Jang Hwa Lee. 2012. "Blast-Resistant Characteristics of Ultra-High Strength Concrete and Reactive Powder Concrete." *Construction and Building Materials* 28 (1): 694–707. https://doi.org/10.1016/j.conbuildmat.2011.09.014.

Yoo, Doo-Yeol, and Nemkumar Banthia. 2016. "Mechanical Properties of Ultra-High-Performance Fiber-Reinforced Concrete: A Review." *Cement and Concrete Composites* 73 (October): 267–80. https://doi.org/10.1016/j.cemconcomp.2016.08.001.

Yoo, Doo-Yeol, Joo-Ha Lee, and Young-Soo Yoon. 2013. "Effect of Fiber Content on Mechanical and Fracture Properties of Ultra High Performance Fiber Reinforced Cementitious Composites." *Composite Structures* 106 (December): 742–53. https://doi.org/10.1016/j.compstruct.2013.07.033.

Yoo, Doo-Yeol, and Young-Soo Yoon. 2015. "Structural Performance of Ultra-High-Performance Concrete Beams with Different Steel Fibers." *Engineering Structures* 102 (November): 409–23. https://doi.org/10.1016/j.engstruct.2015.08.029.

Yoshitake, Isamu, Senji Nagai, Toshio Tanimoto, and Sumio Hamada. 2002. "Simple Estimation of the Ground Water Temperature and Snow Melting Process." In *Proceedings of the 11th International Road Weather Conference*. https://www.researchgate.net/profile/Isamu_Yoshitake2/publication/266868665_Simple_Estimation_of_the_Ground_Water_Temperature_and_Snow_Melting_Process/links/5441114d0cf2a76a3cc731ac.pdf.

Yu, R., P. Spiesz, and H. J. H. Brouwers. 2014a. "Mix Design and Properties Assessment of Ultra-High Performance Fibre Reinforced Concrete (UHPFRC)." *Cement and Concrete Research* 56 (February): 29–39. https://doi.org/10.1016/j.cemconres.2013.11.002.

———. 2014b. "Effect of Nano-Silica on the Hydration and Microstructure Development of Ultra-High Performance Concrete (UHPC) with a Low Binder Amount." *Construction and Building Materials* 65 (August): 140–50. https://doi.org/10.1016/j.conbuildmat.2014.04.063.

———. 2015. "Development of an Eco-Friendly Ultra-High Performance Concrete (UHPC) with Efficient Cement and Mineral Admixtures Uses." *Cement and Concrete Composites* 55 (January): 383–94. https://doi.org/10.1016/j.cemconcomp.2014.09.024.

Zalba, Belén, José M Marı n, Luisa F. Cabeza, and Harald Mehling. 2003. "Review on Thermal Energy Storage with Phase Change: Materials, Heat Transfer Analysis and Applications." *Applied Thermal Engineering* 23 (3): 251–83. https://doi.org/10.1016/S1359-4311(02)00192-8.

Zelić, J., D. Jozić, and D. Krpan-Lisica. 2009. "Synergistic Action of a Ternary System of Portland Cement – Limestone – Silica Fume in Concrete." In *Nanotechnology in Construction 3*, edited by Zdeněk Bittnar, Peter J. M. Bartos, Jiří Němeček, Vít Šmilauer, and Jan Zeman, 425–34. Springer Berlin Heidelberg. https://doi.org/10.1007/978-3-642-00980-8_59.

Zeng, Qiang, Kefei Li, Teddy Fen-Chong, and Patrick Dangla. 2012. "Analysis of Pore Structure, Contact Angle and Pore Entrapment of Blended Cement Pastes from

Mercury Porosimetry Data." *Cement and Concrete Composites* 34 (9): 1053–60. https://doi.org/10.1016/j.cemconcomp.2012.06.005.

Zhou, D., C. Y. Zhao, and Y. Tian. 2012. "Review on Thermal Energy Storage with Phase Change Materials (PCMs) in Building Applications." *Applied Energy* 92 (April): 593–605. https://doi.org/10.1016/j.apenergy.2011.08.025.

Zohrevand, Pedram, and Amir Mirmiran. 2011. "Behavior of Ultrahigh-Performance Concrete Confined by Fiber-Reinforced Polymers." *Journal of Materials in Civil Engineering* 23 (12): 1727–1734.

BIOGRAPHICAL SKETCH

Aashay Arora attended the Indian Institute of Technology, Kharagpur and graduated with a Bachelor of Technology (H.) in Civil Engineering in 2013. He submitted his bachelors' thesis titled "Finite Element modelling of stress analysis of concrete gravity dams under dynamic loading" working under the direction of Professor Dhrubajyoti Sen. Immediately following his graduation, he began his doctoral studies in Structures and Materials Engineering at Arizona State University in 2013. He pursued his research in the area of multi-component novel cementitious composites under the direction of Dr. Narayanan Neithalath. He has been the recipient of the prestigious National Talent Search Scholarship awarded by the government of India, Kishor Vaigyanik Protsahan Yojana (KVPY) fellowship awarded by the Indian Institute of Sciences and the Merit-cum-Means scholarship awarded by the Indian Institute of Technology, Kharagpur. Aashay has worked and collaborated on several academic projects during his undergraduate and graduate career. Some of his works include the development of a graphical user interface for distributed rainfall-runoff modeling working for an Indian Space Research Organization sponsored project, internship with the Water Resources Institute at South Dakota State University to work on the application of geographical information systems (GIS) for agricultural, climatological and environmental applications, working with Arizona Department of Transportation on developing ultra-high performance concrete mix designs for Arizona bridge element connections. He was awarded the best paper award at the Sixth International Conference on the Durability of Concrete Structures, 2018 for his paper "First Principles-Based Design of Economical Ultra-High Performance Concrete".

The following publications were a result of work conducted during his doctoral study.

- Arora, Aashay, Pu Yang, Barzin Mobasher, Christian G. Hoover, Narayanan Neithalath. "Application of Micro-Indentation and DEM to Predict the Mechanical Response of Ultra-High Performance Concrete (UHPC)". (To be submitted)
- Arora, Aashay, Yiming Yao, Farrokh Kianmofrad, Khaled Al Bannai, Barzin Mobasher, Narayanan Neithalath. "Fundamental Insights into the Compressive and Flexural Response of Binder- and Aggregate-Optimized Ultra-High Performance Concrete (UHPC)." (Under Review), Journal of Cement and Concrete Research.
- Arora, Aashay, Asim Almujaddidi, Farrokh Kianmofrad, Barzin Mobasher, Narayanan Neithalath. "Material Design of Economical Ultra-High Performance Concrete (UHPC) and Evaluation of their Properties." (Under Review), Journal of Cement and Concrete Composites.

- Arora, Aashay, Matthew Aguayo, Yiming Yao, Barzin Mobasher, Narayanan Neithalath. "SPR 745 – Developing Ultra-High-Performance Concrete Mix Designs for Arizona Bridge Element Connections." Arizona Department of Transportation
- Arora, Aashay, Matthew Aguayo, Farrokh Kianmofrad, Yiming Yao, Barzin Mobasher, Narayanan Neithalath. "First Principles-Based Design of Economical Ultra-High Performance Concrete." Sixth International Conference on the Durability of Concrete Structures, 2018.
- Arora, Aashay, Matthew Aguayo, Hannah Hansen, Cesar Castro, Erin Federspiel, Barzin Mobasher, and Narayanan Neithalath. "Microstructural packing-and rheology-based binder selection and characterization for Ultra-high Performance Concrete (UHPC)." *Cement and Concrete Research* 103 (2018): 179-190.
- Arora, Aashay, Gaurav Sant, and Narayanan Neithalath. "Numerical simulations to quantify the influence of phase change materials (PCMs) on the early-and later-age thermal response of concrete pavements." *Cement and Concrete Composites* 81 (2017): 11-24.
- Arora, Aashay, Kirk Vance, Gaurav Sant, and Narayanan Neithalath. "A methodology to extract the component size distributions in interground composite (limestone) cements." *Construction and Building Materials* 121 (2016): 328-337.
- Arora, Aashay, Gaurav Sant, and Narayanan Neithalath. "Ternary blends containing slag and interground/blended limestone: Hydration, strength, and pore structure." *Construction and Building Materials* 102 (2016): 113-124.
- Aguayo, Matthew, Aashay Arora, Narayanan Neithalath. "Thermal Control in Pavements using Phase Change Materials (PCM) and Smart Monitoring". (To be submitted)
- Nair, Sooraj, Hussam Alghamdi, Aashay Arora, Iman Mehdipour, Gaurav Sant, Narayanan Neithalath. "Linking Fresh Paste Microstructure, Rheology and Extrusion Characteristics of Cementitious Binders for 3D Printing." (Under Review), Journal of American Ceramic Society.
- Yao, Yiming, Aashay Arora, Narayanan Neithalath, and Barzin Mobasher. "Ultra high Performance Concrete-Materials Formulations and Serviceability based Design." In *HAC 2018. V Congreso Iberoamericano de hormigón autocompactable y hormigones especiales*, pp. 1-13. Editorial Universitat Politècnica de València, 2018.
- Vance, Kirk, Aashay Arora, Gaurav Sant, and Narayanan Neithalath. "Rheological evaluations of interground and blended cement–limestone suspensions." *Construction and Building Materials* 79 (2015): 65-72.